Discovery potential and mass measurement of a MSSM charged Higgs produced in top decays with the ATLAS detector[1]

Mireia Dosil i Bonmatí
Universitat Autònoma de Barcelona
Departament de Física
Edifici Cn E-08193 Bellaterra (Barcelona)

June 2003

[1]Ph.D. Dissertation

A l'Ignasi i a la
meva família de Besalú.

Acknowledgments

First of all I would like to thank sincerely the help I obtained from Catherine Biscarat. Without her, this work would not have been possible (or may be yes, but in a much longer timescale!!). Together with Catherine, the advises of Martine were really useful. I could learn not only from their physics knowledge but also from their great personality.

I am also very grateful to Elzbieta, Fabio, Donatella, Ketevi and Karl, from the ATLAS Higgs working group. They always gave me a prompt reply to the questions I had concerning my analysis.

Coming to the senior people at IFAE, I would like to thank Enrique for giving me the opportunity to work in high energy physics at the institute. I also should not forget Mokhtar, who is always ready to invite me for a coffee, and Federico, with whom I discussed some aspects of this thesis. Special acknowledgments go to Matteo, for letting me travel so that I could attend to conferences and meetings and learn a little bit more about the big world of particle physics. And I would like to thank also the other seniors I did not work directly with.

I ara arriba el torn dels estudiants (i alguns, no tant estudiants!). Primer de tot, voldria agrair a la Sílvia, el Gonzalo i a l'Hugo (un gran company de pis!) el seu humor i les seves bromes quan jo em posava pesada queixant-me del pes d'aquesta tesi així com les estones i els sopars compartits. També, es clar, em van ajudar a resoldre alguns dubtes que se'm plantejaven tot sovint. I l'Oscar, que va escoltar estoicament els cacaus mentals que de tant en tant m'entervolien el cap. I qui més? El Xavi Espinal, un molt bon company de despatx, sempre apunt per ajudar en el que fos, El Xavi Portell (que no l'he pogut ajudar tant com voldria) l'Olga i l'Eva, companyes d'alguns dimarts freds d'hivern :-), el Lluís Jané, que sempre m'ha ajudat en els meus problemes logístics, i a més, és un bon amic, i tants altres: el Dennis, la Carmen, el Pepe, el Javi, l'Esther, l'altra Esther, la Carolina, l'Oriol, l'Ana, el Markus i els que em pugui endescuidar. Pel que fa a la branca teòrica, voldria mencionar el Daniel (que apart d'un bon amic és un expert en LaTeX), l'Oriol, el Santi i el Francesc.

Voldria agrair també l'ajuda dels "sister managers"+ Andreu + Miquel que em solucionaven els problemes informàtics que m'anava trobant.

I com no, voldria agrair a la Barbara (una gran cuinera i amiga) i al Tito la seva hospitalitat cada vegada que pujava al CERN.

Ah! I els companys de l'IFIC de València, el Santi, el Paco, la Farida i el Pablo per les estones compartides al CERN i als winter meetings.

Uff! Me n'adono que hi ha tanta gent que directament o indirectament han contribuït en aquest treball...

Ara és el torn de la gent que vaig conèixer durant la carrera (ja fa molt temps d'això!): el Jordi Arnabat, el Marc i la Marta, el Roger, el Martí, el Jaume, el Gus, l'Enric metereòleg i en Josep Gispert.

I no voldria endescuidar-me de la Teresa, per les nostres converses sovint tant divertides, i dels meus amics de Besalú que veig tant poc sovint.

Ara arriba el torn de la meva família, que sempre han estat al meu costat: la mama, el papa, la Laia, l'Iris i la iaia. I l'avi, del qual tant ens enrecordem.

I finalment, unes gràcies molt especials per l'Ignasi, sobretot per la paciència que ha tingut amb mi en tot moment i pel seu suport incondicional, que per molts anys puguem seguir caminant plegats!

Contents

List of Figures

List of Tables

Chapter 1

Introduction

The observation of one or several Higgs bosons will be of capital importance in order to understand the electroweak symmetry breaking mechanism. In the Standard Model (SM), one scalar doublet is responsible for the electroweak symmetry breaking giving as a result only one Higgs boson.

However, the SM has serious drawbacks which are difficult to solve within the theory itself. This problems find a solution in Supersymmetric (SUSY) models. The Minimal Supersymmetric Standard Model (MSSM) is the simplest SUSY extension of the SM. The MSSM Higgs sector is made of two Higgs doublets which lead to five Higgs particles (three neutral and a charged pair) after electroweak symmetry breaking.

The discovery of the MSSM charged Higgs would be a clear sign of new physics beyond the SM. MSSM charged Higgs could be copiously produced at the LHC (Large Hadron Collider) in top decays. In the present work, the sensitivity of the ATLAS detector to the discovery of the charged Higgs in the low luminosity running conditions is studied in detail. Moreover, a method to extract the charged Higgs mass and to determine its expected precision is also described.

In chapter 2, an introduction to the SM and the MSSM is presented. It is not intended as an in depth description of both theories, but rather tries to underline the main concepts that are important to understand the charged Higgs studies exposed in this work.

In chapter 3, the LHC project and more specifically, the ATLAS experiment are briefly summarized, with particular emphasis on the subdetectors and their performances that

are more relevant for the studies presented in this thesis.

Next, in chapter 4, the ATLAS trigger system is thoroughly described focusing on the ATLAS trigger menus which will be decisive to select the charged Higgs signature. Moreover, a study on the performances for such signature is described.

Chapter 5 contains a description of the software tools that were used for the physics and detector simulations: both Fortran and C++ used programs are briefly summarized. In addition, the parameters used for the event reconstruction are also listed.

Then, in chapter 6 the motivations that gave rise to this analysis are given and the discovery potential of the MSSM charged Higgs produced in top decays with the ATLAS detector is exposed in detail from a SM perspective first and a MSSM perspective afterwards.

Finally, before the conclusions, the charged Higgs mass is extracted by means of a maximum likelihood method. In addition, the expected precision on the charged Higgs mass is also discussed.

At the end of the present work, the effects of the new trigger thresholds on the discovery potential of the charged Higgs signature are described in an appendix.

Chapter 2

Theoretical framework and status of the MSSM $H^{\pm}$ searches

This chapter covers the relevant theoretical concepts which are needed for the understanding of the present work as well as the experimental situation of the MSSM $H^{\pm}$ recent searches.

In section 2.1, the basis of the Standard Model (SM) theory are briefly reviewed focusing on the spontaneous symmetry breaking mechanism. Next, in section 2.2, the principles of Supersymmetry (SUSY) and in particular, of the Minimal Supersymmetric Standard Model (MSSM) are outlined. Finally, in section 2.3, the recent MSSM charged Higgs boson searches are commented and the present exclusion limits are also given.

2.1 The Standard Model

The Standard Model [1] is an unified quantum gauge theory which describes electromagnetic and weak interactions, with a Quantum Chromodynamics (QCD) [2] sector for the description of strong interactions.

In a quantum field theory, the elementary particle interactions are expressed in terms of particle exchanges. There are two types of particles: the basic building blocks of matter, known as matter particles and the intermediate interaction particles. The matter particles are fermions (particles with spin $S = \frac{1}{2}$). They are classified into leptons, which

do not respond to strong interactions, and quarks, which do. Both quarks and leptons are divided in three families (see Table 2.1).

Family	Leptons		Quarks	
	Particle	e. charge	Particle	e. charge
1	ν_e	0	u	2/3
	e	-1	d	-1/3
2	ν_μ	0	c	2/3
	μ	-1	s	-1/3
3	ν_τ	0	t	2/3
	τ	-1	b	-1/3

Table 2.1: Matter fermions.

The interaction among fermions is mediated by spin-1 gauge bosons: one massless photon (γ) and eight massless gluons (g_1,...,g_8) for the electromagnetic and strong interactions respectively, and three massive bosons ($W^{\pm}$ and Z) for the weak interaction.

2.1.1 The electroweak interaction

The model for electroweak (EW) interactions is based on the gauge group $SU(2)_L \otimes U(1)_Y$. $SU(2)_L$ has three generators: $t_i = \frac{\sigma_i}{2}$ (i=1,2,3), where σ_i are the Pauli matrices. The generator of $U(1)_Y$ is the hypercharge $Y = 2Q - T^3$, where Q is the electric charge and T^3 the weak isospin. The symmetry group of electromagnetic interactions, $U(1)_{em}$ is a subgroup of $SU(2)_L \otimes U(1)_Y$. Hence, the electromagnetic and weak interactions are unified. The gauge fields corresponding to each generator are: W^1_μ, W^2_μ, W^3_μ from $SU(2)_L$ and a neutral field B_μ associated to $U(1)_Y$.

The left-handed fermions transform as doublets under $SU(2)_L$, while the right handed ones transform as singlets:

$$f^i_L = \begin{pmatrix} \nu^i_L \\ l^i_L \end{pmatrix}, \begin{pmatrix} u^i_L \\ d^i_L \end{pmatrix} \qquad i = 1,2,3 \tag{2.1}$$

$$f^i_R = l^i_R, u^i_R, d^i_R$$

where i is the family index.

The SM electroweak Lagrangian is obtained requiring invariance under a local gauge transformations in order to obtain an interacting field theory. This is done by replacing the derivatives of the fields by the corresponding covariant derivatives. For a generic fermion field f, its covariant derivative corresponding to the $SU(2)_L \otimes U(1)_Y$ gauge symmetry is:

$$D_\mu f = (\partial\mu - ig\vec{T}\vec{W}_\mu - ig\prime\frac{Y}{2}B_\mu)f \tag{2.2}$$

where g and $g\prime$ are the coupling constants corresponding to $SU(2)_L$ and $U(1)_Y$ respectively.
The total electroweak Lagrangian can be written as a sum of different terms:

$$\mathcal{L}_{SM} = \mathcal{L}_f + \mathcal{L}_G + \mathcal{L}_{SBS} + \mathcal{L}_{YW} \tag{2.3}$$

The first term corresponds to the fermion Lagrangian:

$$\mathcal{L}_f = \sum_{f=l,q} \overline{f}\, i\not{D} f \tag{2.4}$$

The Lagrangian for the gauge fields is given by:

$$\mathcal{L}_G = -\frac{1}{4}W^i_{\mu\nu}W_i^{\mu\nu} - \frac{1}{4}B_{\mu\nu}B^{\mu\nu} + \mathcal{L}_{GF} + \mathcal{L}_{FP} \tag{2.5}$$

which is written in terms of the field strength tensors,

$$\begin{aligned} W^i_{\mu\nu} &= \partial_\mu W^i_\nu - \partial_\nu W^i_\mu + g\epsilon^{ijk}W^j_\mu W^k_\nu \\ B_{\mu\nu} &= \partial_\mu B_\nu - \partial_\nu B_\mu \end{aligned} \tag{2.6}$$

$\mathcal{L}_{GF}$ and $\mathcal{L}_{FP}$ are the gauge fixing and Faddeev Popov Lagrangians respectively that are needed in any theory[3]. Here they are omitted for brevity.

The last two terms, $\mathcal{L}_{SBS}$ and $\mathcal{L}_{YW}$ are the symmetry breaking sector Lagrangian and the Yukawa Lagrangian respectively. They will be discussed in the section 2.1.3.

The physical gauge bosons $W_{\mu}^{\pm}$, Z_{μ} and A_{μ} (photon field) are obtained from the electroweak interaction eigenstates by the following expressions:

$$\begin{aligned} W_{\mu}^{\pm} &= \frac{1}{\sqrt{2}}(W_{\mu}^{1} \mp iW_{\mu}^{2}) \\ Z_{\mu} &= \cos\theta_W W_{\mu}^{3} - \sin\theta_W B_{\mu} \\ A_{\mu} &= sin\theta_W W_{\mu}^{3} + \cos\theta_W B_{\mu} \end{aligned} \tag{2.7}$$

where $\cos\theta_W = \frac{g}{\sqrt{g'^2+g^2}}$ is the weak mixing angle.

However, mass terms such as $M_W^2 W_\mu W^\mu$, $\frac{1}{2}M_Z^2 Z_\mu Z^\mu$ and $m_f \bar{f} f$ are forbidden by $SU(2)_L \otimes U(1)_Y$ gauge invariance. The needed gauge boson masses must be generated in a gauge invariant way. The spontaneous breaking of the $SU(2)_L \otimes U(1)_Y$ symmetry and the Higgs Mechanism provide this mass generation as it will be shown in section 2.1.3.

2.1.2 The strong interaction

As it was already pointed out, QCD is the gauge theory that describes the strong interaction and it is based on the local color transformations that leave its Lagrangian invariant. The gauge symmetry group that is generated by these color transformations is the non-abelian Lie group $SU(3)_C$, where C refers to colors and 3 refers to the three possible color states of the quarks which are assumed to be in the fundamental representation of the group having dimension 3. The gluons g_α with $i = 1, ..., 8$ are the gauge boson particles associated to this gauge generators and are the mediators of the strong interactions among quarks.

The building of the QCD invariant Lagrangian is done by following the same steps as in the electroweak case. In particular, one applies the gauge principle together with the particularities of the non-abelian group $SU(3)$ taken into account. The derivative of the quark fields in the Lagrangian is replaced by its covariant derivative which in the QCD case is:

$$D_\mu q \equiv (\partial_\mu - ig_S(\frac{\lambda_\alpha}{2})A_\mu^\alpha)\, q \tag{2.8}$$

where,

$$
\begin{aligned}
q &= \begin{pmatrix} q_1 \\ q_2 \\ q_3 \end{pmatrix} \\
q_i &= \quad quark\ fields; \qquad i = 1,2,3 \\
g_S &= \quad strong\ coupling\ constant \\
\frac{\lambda_\alpha}{2} &= \quad SU(3)\ generators \\
A^\alpha_\mu &= \quad gluon\ fields;\ \alpha = 1, ..., 8
\end{aligned}
\tag{2.9}
$$

The QCD Lagrangian is then written in terms of the quarks and their covariant derivatives and contains in addition the kinetic term for the gluon fields,

$$\mathcal{L}_{QCD} = \sum_q \bar{q}(x)(i \not{D} - m_q)q(x) - \frac{1}{4}F^\alpha_{\mu\nu}(x)F^{\mu\nu}_\alpha(x) \tag{2.10}$$

where $F^\alpha_{\mu\nu}(x)$ is the gluon field strength given by,

$$F^\alpha_{\mu\nu}(x) = \partial_\mu A^\alpha_\nu(x) - \partial_\nu A^\alpha_\mu(x) + g_S f^{\alpha\beta\gamma} A_{\mu\beta} A_{\nu\gamma} \tag{2.11}$$

and $f^{\alpha\beta\gamma}$ are the structure constants of the $SU(3)_C$ group.

The gauge interactions among the quarks and gluons are contained in the $\bar{q}i \not{D} q$ term,

$$\bar{q} g_S \frac{\lambda^\alpha}{2} A^\alpha_\mu \gamma^\mu q$$

In addition, the $F^\alpha_{\mu\nu}F^{\mu\nu}_\alpha$ term in the Lagrangian contains a three gluons term and a four gluons term. These are the self-interaction gluon vertices which are characteristic of a non-abelian theory.

2.1.3 Spontaneous Symmetry Breaking and the Higgs Mechanism

The gauge symmetry of SM forbids mass terms in the Lagrangian leading to massless fermions and bosons. The simplest way to generate particle masses while preserving the renormalizability of the theory is the Higgs Mechanism of Spontaneous Symmetry Breaking (SSB) [4].

A field represented by a complex $SU(2)_L$ doublet:

$$\Phi = \begin{pmatrix} \phi^+ \\ \phi_0 \end{pmatrix} \tag{2.12}$$

with hypercharge $Y(\Phi) = 1$ and the potential given by the relation:

$$V(\Phi) = \mu \Phi^\dagger \Phi + \lambda (\Phi^\dagger \Phi)^2 \tag{2.13}$$

is defined. One can find that, if $\lambda > 0$ and $\mu^2 < 0$, the potential $V(\Phi)$ has a minimum for:

$$\Phi^\dagger \Phi = -\frac{\mu^2}{2\lambda} \equiv \frac{v^2}{2} \tag{2.14}$$

This implies that the true vacuum corresponds to a non-zero vacuum expectation value (VEV) for the field Φ, i.e. $< 0|\Phi|0 > \neq 0$. This is shown schematically in Fig. 2.1. Because the scalar field is complex, the above relation has an infinite number of solutions. By choosing one particular solution the gauge symmetry is broken. The coupling of this field (called Higgs field) to particles provides masses to bosons and fermions.

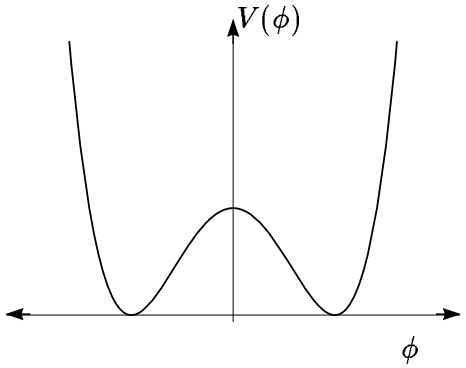

Figure 2.1: A 2-dimensional slice of the spontaneous symmetry breaking Higgs potential.

The two missing terms in the SM Lagrangian of Eq. (2.3), i.e. $\mathcal{L}_{SBS}$ and $\mathcal{L}_{YW}$ are given by:

$$\mathcal{L}_{SBS} = (D_\mu \Phi)^\dagger (D^\mu \Phi) + \mu^2 \Phi^\dagger \Phi - \lambda (\Phi^\dagger \Phi)^2 \tag{2.15}$$

and

$$\mathcal{L}_{YW} = \lambda_e \bar{l}_L \Phi e_R + \lambda_u \bar{q}_L \tilde{\Phi} u_R + \lambda_d \bar{q}_L \Phi d_R + \text{h.c.} + 2^{nd} \text{ and } 3^{rd} \text{ families} \tag{2.16}$$

Here,

$$l_L = \begin{pmatrix} \nu_L \\ e_L \end{pmatrix} ; \qquad q_L = \begin{pmatrix} u_L \\ d_L \end{pmatrix} ; \qquad \tilde{\Phi} = i\sigma_2 \Phi^* \tag{2.17}$$

By substituting the Higgs field expansion around the vacuum state:

$$\Phi = \frac{1}{\sqrt{2}} \begin{pmatrix} 0 \\ v + H \end{pmatrix} \tag{2.18}$$

in the $\mathcal{L}_{YW}$ and $\mathcal{L}_{SBS}$ expressions, one can obtain the mass terms for fermions, gauge bosons and Higgs boson at tree level prediction:

$$\begin{aligned} M_W &= \frac{gv}{2} ; \qquad M_Z = \frac{\sqrt{g^2 + g'^2} v}{2} \\ M_H &= \sqrt{2}\mu \\ m_e &= \lambda_e \frac{v}{\sqrt{2}} ; \qquad m_u = \lambda_u \frac{v}{\sqrt{2}} ; \qquad m_d = \lambda_d \frac{v}{\sqrt{2}} ; .... \end{aligned} \tag{2.19}$$

Finally one can rewrite $\mathcal{L}_{YW}$ and $\mathcal{L}_{SBS}$ in terms of the physical scalar fields, and get not just the mass terms but also the kinetic interaction terms for the Higgs sector. Thus, one gets the trilinear Higgs self-coupling and the Higgs-gauge and Higgs-fermion interaction strengths:

$$\lambda_{HHH} = 3\frac{M_H^2}{M_Z^2} ; \qquad \lambda_{HVV} = 2\sqrt{2G_F} M_V^2 ; \qquad \lambda_{Hff} = 2\sqrt{2G_F} m_f \tag{2.20}$$

where $V = W, Z$ and G_F is the Fermi constant.

The vacuum expected value v is determined experimentally from μ decay. By identifying the predictions of the partial width $\Gamma(\mu \to \nu_\mu \bar{\nu}_e e)$ in the SM to low energies ($q^2 \ll M_W^2$), one gets:

$$\frac{G_F}{\sqrt{2}} = \frac{g^2}{8M_W^2} = \frac{1}{2v^2} \tag{2.21}$$

and from here, the electroweak scale is obtained:

$$v = (\sqrt{2}G_F)^{-\frac{1}{2}} = 246\ GeV \tag{2.22}$$

The electroweak symmetry breaking of the Standard Model has also the special feature that it can provide limits to the SM Higgs mass. The argument follows from the scattering

of longitudinally polarized gauge bosons [5]. By applying some unitarity conditions (i.e. the probability of scattering from a particular state to another one grows with energy till it becomes 1) and for a light Higgs boson, one has the theoretical limit:

$$M_H < 860\ GeV \tag{2.23}$$

Besides, the final results of the LEP search for the SM Higgs were published in [6] and the 95% Confidence Level lower limit on M_H was set to 111.5 GeV.

Thus, the scientific community is waiting for the LHC startup to continue the search of the SM Higgs.

The SM has been very successful in its predictions: mass values of W and Z bosons were predicted well before their discovery at CERN (the European Laboratory for Particle Physics) in 1983 [7]. Moreover, there is a remarkable agreement between the SM prediction and the precision measurements of electroweak observables performed at LEP (Large Electron Positron) [8, 9] and SPS experiments at CERN. However, the scalar sector of the SM is not yet experimentally confirmed as the Higgs boson is the only particle that has not been yet observed by the experiments so far. Also, as it will be discussed in the next section, the SM has several shortfalls.

2.1.4 Problems of the Standard Model

The Standard Model provides a remarkably successful description of presently known phenomena. Still, it seems quite clear that the SM is a *work in progress* and it will have to be extended to describe physics at arbitrarily high energies. Furthermore, even if one accepts the rather odd set of group representations and hypercharges that it requires, the SM contains at least 19 parameters. Moreover, many more parameters are required if one wishes to accommodate non-accelerator observations.

The questions raised by the SM are organized into several broad categories:

⇒ **Mass problem:** Do particle masses really originate from a Higgs boson?

⇒ **Hierarchy problem:** if so, why are these masses not much closer to the Planck mass $m_P \simeq 10^{19} GeV$? Or, can the validity of the SM be extended to large masses and energy scales?

⇒ **Unification problem:** Can all particle interactions be unified in a simple gauge group, and, if so, does it predict observable new phenomena such as baryon decay and/or neutrino masses? Does it also predict relations between parameters of SM such as gauge couplings or fermion masses?

⇒ **Flavour problem:** What is the origin of the three flavours each of quarks and leptons, and what explain their weak charged current mixing and CP violation?

2.1.5 The hierarchy problem

One of the most serious drawbacks of the SM is the problem of mass and, as a consequence, the hierarchy problem [10], that appears when one tries to extend the validity of the SM to large masses and energy scales. From measurements of the properties of the weak interactions together with perturbative unitarity arguments [11], it can be deduced that the squared Higgs mass is of the order of $M_H^2 \sim (100\text{GeV})^2$. However, M_H^2 receives enormous quantum corrections from the virtual effects of every particle which couples to the Higgs field. The one-loop diagrams contributing to the corrections are shown in Fig. 2.2.

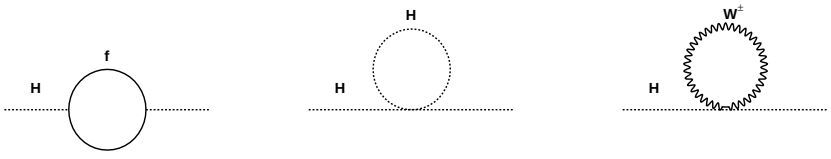

(a) (b) (c)

Figure 2.2: One-loop quantum corrections to M_H^2 in the SM.

If one considers the case of Fig. 2.2(a), the diagram containing a 1-loop fermion yields a correction:

$$\Delta M_H^2 = \frac{\lambda_f^2}{16\pi^2}\left[-2\Lambda^2 + \mathcal{O}\left(m_f^2 \ln\left(\frac{\Lambda}{m_f}\right)\right)\right] \tag{2.24}$$

where λ_f is a Yukawa coupling of fermion f. Λ is an energy cutoff which is interpreted as the energy scale at which new physics enters and changes the high-energy behavior of the theory. That is, if the SM is embedded in a Grand Unified Theory (GUT), Λ

is M_{GUT}. Then the quantum correction to M_H^2 is about 30 orders of magnitude larger than $M_H \sim 100$ GeV! And this means that the square of the bare Higgs mass and other contributions to M_H^2 each of order 10^{30} GeV , have to combine to yield $\sim 10^4 \mathrm{GeV}^2$, and this cancellation is clearly unnatural.

Furthermore, the unstability of the mass to radiative corrections is intrinsic to scalar fields only. Because of their chiral and gauge symmetries, fermions and gauge bosons are protected respectively from these quadratic radiative corrections to their masses. However, since the quarks, leptons and the W and Z bosons acquire mass due to the Higgs VEV's v, the whole mass spectrum is sensitive to the cutoff Λ.

2.2 Supersymmetry and Minimal Supersymmetric Standard Model

A possible solution to the hierarchy problem is offered by Supersymmetry, a symmetry which relates masses and couplings of fermions and scalars [12].

A supersymmetry transformation turns a bosonic state into a fermionic state and vice versa. The Q operator generating such transformations must be an anticommuting spinor with:

$$Q|Boson>=|Fermion> \qquad Q|Fermion>=|Boson> \tag{2.25}$$

Spinors are intrinsically complex objects, so $Q^{\dagger}$ is also a symmetry generator. This generators are fermionic in nature ($S = 1/2$) and form, together with the four-momentum and the Lorentz transformation generators, a so-called graded Lie algebra[13]. Defining relations between the generators of the algebra have fundamental consequences in the theory: when SUSY is realized locally, it contains the graviton among its gauge fields and includes Einstein's theory of the general relativity. Thus, SUSY seems to be a good candidate for a theory of all interactions.

Coming back to the hierarchy problem, SUSY provides the cancellation of the dangerous contributions to M_H^2 given by Eq. (2.26) in a natural way: the scalar SUSY partner S of a fermion f couples to the Higgs as well, and its corresponding correction to the Higgs boson mass is:

$$\Delta M_H^2 = \frac{\lambda_S^2}{16\pi^2}\left[-2\Lambda^2 + \mathcal{O}\left(m_S^2 \ln\left(\frac{\Lambda}{m_S}\right)\right)\right] \tag{2.26}$$

and since each of the quarks and leptons of the SM is accompanied by two scalars with the same couplings as their SM companion, $\lambda_f = \lambda_S$, the Λ^2 contributions of Eqs. (2.24) and (2.26) are nicely canceled [14].

The single-particle states of a supersymmetric theory fall naturally into irreducible representations of the SUSY algebra which are called *supermultiplets*. Each supermultiplet contains both fermions and bosons which are called *superpartners* of each other. The (mass^2) operator $-P^2$ commutes with the Q and $Q^\dagger$ operators, and with all space-time rotation and translation operators. This means that those particles belonging to a same irreducible supermultiplet must have equal eigenvalues of $-P^2$, and therefore equal masses. The same happens with the electric charge, the weak isospin and the color degrees of freedom which are the same for all particles belonging to the same supermultiplet. In addition, the number of bosonic and fermionic degrees of freedom in a supermultiplet must be also the same, $n_B = n_F$ [15].

The simplest supermultiplet which satisfies the above requirements contains a single Weyl fermion (with two helicity states, so $n_F = 2$) and two real scalars (each with $n_B = 1$). This combination is called a *chiral supermultiplet*. The next simplest possibility for a supermultiplet contains a massless spin-1 vector boson (with two helicity states, so the number of bosonic degrees of freedom is $n_B = 2$), and its superpartner, a massless spin-1/2 Weyl fermion (again with two helicity states, so $n_F = 2$). These fermions, called gauginos, must have the same gauge transformation properties for left-handed and for right-handed components. Such a combination of spin-1/2 gauginos and spin-1 gauge bosons is called a *gauge supermultiplet*.

In a SUSY extension of the SM, each of the known fundamental particles must be either in a chiral or in a gauge supermultiplet and have a superpartner with spin differing by one half. The SM fermions can only be placed in chiral supermultiplets together with their SUSY partners: *scalar quarks* and *scalar leptons* or *squarks* and *sleptons*. The left-handed and right-handed states of the quarks and leptons are two-component separated Weyl fermions with different gauge transformation properties in the SM, so each must have its own complex scalar partner, $\tilde{f}_L$ and $\tilde{f}_R$. As will be discussed later, the gauge interactions of each of these squark and slepton fields are the same as for the corresponding SM fermions. For instance, a left-handed squark $\tilde{u}_L$ will couple to the W boson while $\tilde{u}_R$ not.

The Higgs boson must reside in a chiral supermultiplet since it has spin 0. But it turns

out that one Higgs supermultiplet is not enough: if so, the electroweak gauge symmetry would suffer a so-called triangle gauge anomaly, and would be inconsistent as a quantum theory [15]. This can be avoided if there are two Higgs supermultiplets, one with each of $Y = \pm 1/2$. Moreover, both of these are also necessary for another completely different reason: because of the structure of supersymmetric theories, only a $Y = +\frac{1}{2}$ Higgs chiral supermultiplet can have the Yukawa couplings necessary to give masses to up-type quarks, and only a $Y = -\frac{1}{2}$ Higgs can have the Yukawa couplings necessary to give masses to down-type quarks and to charged leptons. Thus, there are two $SU(2)_L$-doublet complex scalar fields, H_u and H_d. The weak isospin components of H_u with $I_3 = (+1/2, -1/2)$ are denoted (H_u^+, H_u^0). Similarly, the H_d field has weak isospin components (H_d^0, H_d^-) with $I_3 = (+1/2, -1/2)$.

The simplest SUSY extension of the SM is the **Minimal Supersymmetric Standard Model** [16]. The MSSM has the smallest number of new particles and couplings.

The chiral supermultiplets of a MSSM classified according to their transformation properties under the SM gauge group $SU(3)_C \otimes SU(2)_L \otimes U(1)_Y$, are summarized in Table 2.2. The standard convention is that all chiral supermultiplets are defined in terms of left-handed Weyl spinors, so that the only *conjugates* of the right-handed quarks and leptons and their superpartners appear in this Table.

Names		**spin 0**	**spin $\frac{1}{2}$**	$SU(3)_C$, $SU(2)_L$, $U(1)_Y$
squarks, quarks (x 3 families)	Q	$(\tilde{u}_L\ \tilde{d}_L)$	$(u_L\ d_L)$	$(3, 2, \frac{1}{6})$
	$\bar{U}$	$\tilde{u}_R^*$	$\tilde{u}_R^\dagger$	$(\bar{3}, 1, -\frac{2}{3})$
	$\bar{D}$	$\tilde{d}_R^*$	$\tilde{d}_R^\dagger$	$(\bar{3}, 1, \frac{1}{3})$
sleptons, leptons (x 3 families)	L	$(\tilde{\nu}\ \tilde{e}_L)$	$(\nu\ e_L)$	$(1, 2, -\frac{1}{2})$
	$\bar{E}$	$\tilde{e}_R^*$	$\tilde{e}_R^\dagger$	$(1, 1, 1)$
Higgs, higgsinos	H_u	$(H_u^+\ H_u^0)$	$(\tilde{H}_u^\dagger\ \tilde{H}_u^0)$	$(1, 2, +\frac{1}{2})$
	H_d	$(H_d^0\ H_d^-)$	$(\tilde{H}_d^0\ \tilde{H}_d^-)$	$(1, 2, -\frac{1}{2})$

Table 2.2: Chiral supermultiplets in the MSSM. Symbols for each of the chiral supermultiplets as a whole are indicated in the second column. The bar on $\bar{U}$, $\bar{D}$, $\bar{E}$ is part of the name, and does not denote any kind of conjugation.

The vector bosons of the SM introduced in section 2.1.1 are grouped into gauge supermultiplets. Their fermionic superpartners are called gauginos. The gauge bosons W^1,

W^2, W^3 and B, have associated spin-1/2 superpartners $\tilde{W}^1$, $\tilde{W}^2$, $\tilde{W}^3$ and $\tilde{B}$, called *winos* and *binos*. After electroweak symmetry breaking, the W^3 and the B gauge eigenstates mix to give the mass eigenstates Z^0 and γ. The corresponding gaugino mixtures of $\tilde{W}^3$ and $\tilde{B}$ are called *zino* ($\tilde{Z}^0$) and *photino* ($\tilde{\gamma}$). The $SU(3)_C$ color gauge interactions of QCD are mediated by the gluon whose spin-1/2 color-octet supersymmetric partner is the gluino $\tilde{g}$. In Table 2.3 the gauge supermultiplets are summarized, which together with the chiral supermultiplets of Table 2.2, they compose the particle content of the MSSM.

Names	**spin $\frac{1}{2}$**	**spin 1**	$\boldsymbol{SU(3)_C,\ SU(2)_L,\ U(1)_Y}$
gluino, gluon	$\tilde{g}$	g	(8, 1, 0)
winos, W bosons	$\tilde{W}^1\ \tilde{W}^2\ \tilde{W}^3$	$W^1\ W^2\ W^3$	(1, 3, 0)
bino, B boson	$\tilde{B}$	B	(1, 1, 0)

Table 2.3: Gauge supermultiplets in the MSSM.

2.2.1 MSSM Lagrangian and R-parity

By requiring gauge and SUSY invariance, the supersymmetric Lagrangian in terms of the component fields takes the following form [17]:

$$\begin{aligned}\mathcal{L} = &\sum_i (D_\mu S_i)^\dagger (D^\mu S_i) + \frac{i}{2}\sum_i \bar{\psi}_i \gamma^\mu D_\mu \psi_i \\ &- \frac{1}{4}\sum_A F_{\mu\nu A} F_A^{\mu\nu} + \frac{i}{2}\sum_A \bar{\lambda}_A \gamma^\mu D_\mu \lambda_A \\ &- \sqrt{2}\sum_{i,A}\left[S_i^\dagger (g_\alpha\ t_{\alpha A})\bar{\psi}_i \frac{1-\gamma_5}{2}\lambda_A + h.c.\right] \\ &- \frac{1}{2}\sum_A \left[\sum_i S_i^\dagger g_\alpha t_{\alpha A} S_i\right]^2\end{aligned} \tag{2.27}$$

Here, $S_i(\psi_i)$ is the scalar (fermion) component of the i^{th} chiral superfield, $F_{\mu\nu A}$ is the Yang-Mills gauge field, and λ_A is the gaugino superpartner of the corresponding gauge boson. The $\sum_i$ is over all fermion fields of the SM, ψ_i, and their scalar partners, S_i, and also over the 2 Higgs doublets with their fermion partners. The $\sum_A$ is over the $SU(3)_C$, $SU(2)_L$ and $U(1)_Y$ gauge fields with their fermion partners, the gauginos.

The first two lines of the Lagrangian (2.27) are the gauge invariant kinetic energies for the components of the chiral and gauge superfields. These terms completely determine how all particles interact with gauge bosons. They also contain the SM Lagrangian. The derivatives that appear in (2.27) are gauge covariant derivatives appropriate to the particular representation to which the field belongs.

The third line describes interactions of gauginos with matter and Higgs multiplets. These interactions are also determined by the gauge couplings. Here, $t_{\alpha A}$ is the matrix representation of the group generators and g_α are the corresponding gauge coupling constants.

The fourth line in (2.27) describes the quartic couplings of scalar matter.

So, the interactions between the chiral superfields of Table 2.2 and gauge fields and gauginos of Table 2.3 are completely specified by the gauge symmetries and by Supersymmetry, as are the quartic interactions of the scalars, and the interaction strengths are fixed in terms of the SM coupling constants.

The only freedom in constructing the supersymmetric Lagrangian, once the superfields and the gauge symmetries are chosen, is the *superpotential*, $\mathcal{W}$ [15]. The superpotential is an analytic function of the chiral superfields $\hat{S} = Q, \bar{U}, \bar{D}, L, \bar{E}, H_u, H_d$. It needs to be at most cubic in the superfields since higher terms would yield non-renormalizable interactions in the Lagrangian. The $SU(3)_C \otimes SU(2)_L \otimes U(1)_Y$ invariant superpotential has the following form:

$$\begin{aligned}\mathcal{W} =& \epsilon_{ij}\mu H_u^i H_d^j + \epsilon_{ij}\Big[\lambda_L H_d^i \bar{L}^j \bar{E} + \lambda_D H_d^i Q^j \bar{D} + \lambda_U H_u^j Q^i \bar{U}\Big] \\ &+ \epsilon_{ij}\Big[\lambda_1 L^i L^j \bar{E} + \lambda_2 L^i Q^j \bar{D}\Big] + \lambda_3 \bar{U}\bar{D}\bar{D}\end{aligned} \tag{2.28}$$

where i and j are $SU(2)_L$ doublet indices and $\epsilon_{ij} = -\epsilon_{ji}$ (with $\epsilon_{12} = 1$) contracts the $SU(2)_L$ doublet fields. The superpotential is written in terms of the fields of the first generation. The λ_i $(i = 1, 2, 3)$ are matrices which mix the interactions of the 3 generations.

When introducing this into the supersymmetric Lagrangian one has:

$$\mathcal{L}_{\mathcal{W}} = -\sum_i \left|\frac{\partial \mathcal{W}}{\partial S_i}\right|^2 - \frac{1}{2}\sum_{i,j}\left\{\bar{\psi}_i\left[\frac{1-\gamma_5}{2}\right]\left(\frac{\partial^2 \mathcal{W}}{\partial S_i \partial S_j}\right)\psi_j + h.c.\right\} \tag{2.29}$$

where $\mathcal{S}_i$ is a chiral superfield. This form of the Lagrangian is required by SUSY and it is renormalizable. $\mathcal{L}_{\mathcal{W}}$ describes both the scalar potential and the Yukawa interactions of

fermions with scalars: the $\mu H_u^i H_d^j$ term in $\mathcal{W}$ gives mass terms for the Higgs bosons when applying $\frac{\partial \mathcal{W}}{\partial S}$, and μ is often called the higgsino mass parameter. The terms of superpotential proportional to λ_L, λ_D and λ_U give the usual Yukawa interactions of fermions with the Higgs bosons from the second term of Eq. (2.29). Furthermore, these coefficients are determined in terms of the fermion masses and the Vacuum Expectation Values (VEV's) of the neutral members of the scalar components of the Higgs doublets. Thus, in the SUSY Lagrangian, up to this point, there is only one additional free parameter with respect to the SM:

$$\tan\beta \equiv \frac{v_2}{v_1} \tag{2.30}$$

where $v_1 = \langle H_d^0 \rangle$ and $v_2 = \langle H_u^0 \rangle$ which are the VEV's of the neutral components of the two Higgs doublets.

The terms proportional to λ_1, λ_2 and λ_3 in the second line of Eq. (2.28), contribute to lepton and baryon number violating interactions. They can, for example, give proton decay at tree level through the exchange of the scalar partner of the down quark. But there are several possible solutions to avoid the lepton and baryon number violating interactions. The trivial one would be to make the coefficients λ_1, λ_2 and λ_3 small enough to satisfy the experimental limits [18]. Another possible solution would be to make either the lepton number violating interactions, λ_1 and λ_2 or the baryon number violating interaction, λ_3, zero, while allowing the others to be non-zero, so that the proton decay is suppressed. However, there is not much theoretical motivation for either of these approaches.

The solution is to require that this lepton and baryon number violating terms are forbidden by a symmetry, called *R-parity* [19]. R-parity can be defined as a multiplicative quantum number such that all SM particles have R-parity +1, while their SUSY partners have R-parity -1. R-parity is defined as:

$$R = (-1)^{3(B-L)+2s} \tag{2.31}$$

where B and L are the baryon and lepton quantum numbers and s is the spin of the particle.

The assumption of R-parity conservation forbids the lepton and baryon number violating terms in Eq. (2.28). This R-parity conservation has also very important phenomenological consequences: there can be no mixing between the sparticles and the $P_R = +1$ particles; SUSY particles can only be pair produced in the collisions of SM particles; a

SUSY particle decays to SM particle(s) and SUSY ones, and at the end of the chain the lightest SUSY particle (LSP) is produced; and the LSP must be stable and neutral.

2.2.2 Supersymmetry breaking

It was already shown that SUSY gives a solution to the hierarchy problem. However, the Lagrangians of Eqs. (2.27) and (2.29) have no mass terms for the particles (fermions, scalars and gauge fields). On the other hand, if the broken SUSY needs to provide a solution to the hierarchy problem, the splitting between superpartner masses should not be much larger than the electroweak scale [16, 20], so that terms proportional to $m^2 \ln(\frac{\Lambda}{m})$ in Eqs. (2.24) and (2.26) do not lead to a correction which is much higher than 10^4 GeV^2.

The usual approach is to assume that the MSSM, which is the theory at the electroweak scale, is an effective low energy theory [21]. It is also assumed that the SUSY breaking occurs at a high scale, and perhaps results from some complete theory encompassing gravity. This is in agreement with the fact that up to now, no sparticles have been discovered.

The Supersymmetry breaking is implemented by including *soft* mass terms [22] for the scalar members of the chiral supermultiplets and for the gaugino members of the vector supermultiplets in the Lagrangian. This interactions are named soft because they do not re-introduce the quadratic divergences which motivated the introduction of SUSY, and naturally maintain a hierarchy between the electroweak scale and the Planck (or some other very large) mass scale. The dimension of soft operators in the Lagrangian must be 3 or less, which means that the possible soft operators are mass terms, bi-linear mixing terms ("B" terms), and tri-linear scalar mixing terms ("A" terms). The usual strategy is to add to the Lagrangian all of the mass and mixing terms which are allowed by the gauge symmetries and R-parity conservation. Then the complete SUSY breaking Lagrangian for the first generation is given by [17, 22]:

$$\begin{aligned}
\mathcal{L}_{soft} =& m_1^2|H_d|^2 + m_2^2|H_u|^2 - B\mu\epsilon_{ij}(H_d^i H_u^j + h.c.) + \\
& M_Q^2 \bar{Q}_i Q^i + M_U^2 \bar{U}U + M_D^2 \bar{D}D + M_L^2 \bar{L}^i L^i + M_E^2 \bar{E}E + \\
& \frac{1}{2}\left[M_1\, \bar{\tilde{B}}\tilde{B}^0 + M_2\, \bar{\tilde{W}}^a \tilde{W}^a + M_3 \bar{\tilde{g}}\tilde{g}\right] + \\
& \frac{g_2\epsilon_{ij}}{\sqrt{2}M_W}\left[\frac{m_d}{\cos\beta} A_d H_d^i Q^j \tilde{d}_R^* + \frac{m_u}{\sin\beta} A_u H_u^j Q^i \tilde{u}_R^* + \frac{m_e}{\cos\beta} A_e H_d^i L^j \tilde{e}_R^* + h.c.\right]
\end{aligned} \tag{2.32}$$

where i and j are the $SU(2)_L$ doublet indices. This Lagrangian has arbitrary masses for the scalars and gauginos and also arbitrary tri-linear and bi-linear mixing terms. The scalar and gaugino mass terms have the desired effect of breaking the mass degeneracy between the particles and their SUSY partners. The tri-linear A terms affect primarily the particles of the third generation. The $B\mu$ term mixes the scalar components of the two Higgs doublets. The origin of all these terms is left unspecified. In the most general case, all of the mass and interaction terms of Eq. (2.32) are matrices involving all three generators.

Besides, $\mathcal{L}_{soft}$ introduces new supersymmetric parameters [23], 104 in total, whereas in the Lagrangian of unbroken SUSY there's only one new parameter, $\tan\beta$.

2.2.3 The Higgs potential and the Higgs boson masses

SUSY also provides a mechanism to electroweak symmetry breaking. The Higgs scalar potential is derived from the superpotential and the relevant soft terms in $\mathcal{L}_{soft}$. After carrying out $SU(2)_L$ transformations which allow to rotate away possible VEV's of the charge components of the scalar fields, the Higgs potential acquires the form:

$$\begin{aligned} V_H =&(|\mu|^2 + m_1^2)|H_d|^2 + (|\mu|^2 + m_2^2)|H_u|^2 - \mu B\epsilon_{ij}(H_d^i H_u^j + h.c.)+ \\ &\frac{g_1^2 + g_2^2}{8}(|H_d|^2 - |H_u|^2)^2 + \frac{1}{2}g_2^2|H_d^* H_u|^2 \end{aligned} \tag{2.33}$$

In the usual Renormalization Group Equation (RGE) approach, the m_1^2 and m_2^2 are evolved from GUT scale down to electroweak scale. The RGEs get large Yukawa coupling contributions which can cause one or both mass-square terms become negative and thereby provide the correct pattern for generation of Spontaneous Symmetry Breaking. In SUSY the electroweak symmetry breaking is produced in a natural way [24], whereas in the SM it is put *by hand*. As in the SM case, the symmetry is broken when the neutral components of the Higgs doublets get vacuum expectation values, $v_1 =< H_d^0 >$ and $v_2 =< H_u^0 >$.

After electroweak symmetry breaking occurs, 5 physical Higgs particles are obtained [1]: two neutral CP-even $\boldsymbol{h}$ and $\boldsymbol{H}$ ($m_h < m_H$), a neutral CP-odd $\boldsymbol{A}$ and a pair of charged

[1]Before the symmetry was broken, the 2 complex $SU(2)_L$ Higgs doublets had 8 degrees of freedom. Three of these were absorbed to give the $W^\pm$ and the Z gauge bosons their masses, leaving 5 physical degrees of freedom.

Higgses $H^{\pm}$. Their tree-level masses [2] are given by:

$$m_A^2 = \frac{2|\mu B|}{\sin 2\beta} \tag{2.34}$$

$$m_{H^{\pm}}^2 = m_A^2 + M_W^2 \tag{2.35}$$

$$m_{h,H}^2 = \frac{1}{2}\left[m_A^2 + M_Z^2 \mp \sqrt{(m_A^2 + M_Z^2)^2 - 4m_A^2 M_Z^2 \cos 2\beta^2}\right] \tag{2.36}$$

From Eq. (2.36) it follows that the lightest neutral Higgs is lighter than $M_Z|\cos 2\beta|$. However, m_h is subject to large radiative corrections and after taking them into account, the upper bound on m_h can be pushed up to about 150 GeV [26].

On the other hand, the charged Higgs mass at tree level given by Eq. (2.35) is less sensitive to radiative corrections [27], for example, if $1 \lesssim \tan\beta \lesssim m_{top}/m_b$, the charged Higgs boson mass shift is less than 10 GeV over nearly the entire range of the low-energy supersymmetric parameter space [28].

There are also experimental bounds to the charged Higgs mass that come mainly from the $H^{\pm}$ searches at LEP and Tevatron. Those searches were able to set lower limits on $m_{H^{\pm}}$ as it is going to be explained in section 2.3. Other experimental bounds come from processes where the charged Higgs enters as a virtual particle. One of this processes is the $b \to s\gamma$ decay, where indirect limits on $m_{H^{\pm}}$ are obtained from the measurement of the decay rate [29]. However, these bounds are strongly model dependent (see [30] and [31]). In [30] it is stated that a charged Higgs boson lighter than 450 GeV is strongly disfavoured in Two-Higgs Doublet Models (2HDM) of Type II [3]. This limit is not valid if there are other particles in the loop, such as the case of the MSSM (which is a Type II 2HDM), in which the chargino and the $H^{\pm}$ tend to cancel each other.

Concerning the electroweak gauge bosons, they also get masses which are fixed by $v^2 = v_1^2 + v_2^2$:

$$M_W = \frac{1}{\sqrt{2}} g_2 v \qquad\qquad M_Z = \frac{1}{\sqrt{2}}\sqrt{g_1^2 + g_2^2 v} \tag{2.37}$$

[2] For higher order corrections see [25].

[3] In this models, one Higgs doublet is coupled to the up-type quarks and neutrinos and the other one is coupled to the down-type quarks and leptons, whereas in Type I 2HDM only one of the Higgs doublets is coupled to the fermionic sector.

2.2.4 The Higgs Yukawa couplings and the fermion masses

Regarding the Yukawa couplings at tree level, the following relations can be derived from Eq. (2.32):

$$\begin{aligned} \lambda_L &= \frac{g_2 m_l}{\sqrt{2} M_W \cos\beta} \\ \lambda_U &= \frac{g_2 m_u}{\sqrt{2} M_W \sin\beta} \\ \lambda_D &= \frac{g_2 m_d}{\sqrt{2} M_W \cos\beta} \end{aligned} \tag{2.38}$$

Therefore, the masses of the quarks and leptons are determined by the Yukawa couplings of the superpotential and the parameter $\tan\beta$. This is because the top, charm and up quarks get masses proportional to $v_2 =< H_u^0 >= v \sin\beta$ and the bottom, strange and down quarks and the charged leptons get masses proportional to $v_1 =< H_d^0 >= v \cos\beta$. Thus, at tree level one has:

$$\begin{aligned} \lambda_t &= \frac{g_2 m_{top}}{\sqrt{2} M_W \sin\beta} \\ \lambda_b &= \frac{g_2 m_b}{\sqrt{2} M_W \cos\beta} \\ \lambda_\tau &= \frac{g_2 m_\tau}{\sqrt{2} M_W \cos\beta} \end{aligned} \tag{2.39}$$

These relations hold for the t, b and τ running masses rather than the physical pole masses which are significantly larger [15]. Including those corrections, one can relate the Yukawa couplings to $\tan\beta$. Even if $m_b, m_\tau \ll m_{top}$, one should not neglect the Higgs couplings of bottom and τ, λ_b and λ_τ. To a first approximation:

$$\begin{aligned} \frac{\lambda_b}{\lambda_t} &= \frac{m_b}{m_{top}} \tan\beta \\ \frac{\lambda_\tau}{\lambda_t} &= \frac{m_\tau}{m_{top}} \tan\beta \end{aligned} \tag{2.40}$$

so that if $\tan\beta \gg 1$, those couplings have to be taken into account. Hence, in the MSSM, the couplings to bottom quarks and to tau leptons are enhanced with respect to the SM.

If one tries to make $\sin\beta$ too small, λ_t will become non perturbatively large. Requiring that λ_t does not blow up above the electroweak scale, one finds that $\tan\beta \gtrsim 1.2$ or so,

depending on the mass of the top quark, the QCD couplings and other fine details. In principle, one can also determine a lower bound on $\cos\beta$ and thus, an upper bound on $\tan\beta$ by requiring that λ_b and λ_τ are non perturbatively large. This gives a rough upper bound of $\tan\beta \lesssim 65$. However, this is complicated by the fact that the bottom quark mass gets significant one-loop corrections in the large $\tan\beta$ limit [32].

2.3 $H^{\pm}$ boson searches

The $H^{\pm}$ search is of capital importance. Among the 5 physical Higgs bosons -the two neutral scalars (h and H), a pseudoscalar (A) and a pair of charged Higgs bosons ($H^{\pm}$)- the charged Higgs carries an unequivocal signature of a two Higgs doublet model and consequently, of the Supersymmetric Higgs sector.

2.3.1 $H^{\pm}$ decay modes

Assuming that all supersymmetric particles are heavy enough[4] not to play an important role in the phenomenology of $H^{\pm}$ decay (see next subsection), the MSSM charged Higgs will only decay into SM particles. These decays are given by the Yukawa couplings to up- and down-type fermions given by Eqs. (2.38) and (2.39). In addition, the value of $\tan\beta$ determines to a large extent the decay pattern of the charged Higgs bosons as it was shown in the previous section.

For large $\tan\beta$ values, as a result of the strong enhancement of the couplings to down-type fermions, $H^{\pm}$ with $m_{H^{\pm}} > m_{top}$ will decay into tb pairs with a branching ratio of almost 85% and into $\tau\nu$ pairs with a branching ratio of 15%, for a large enough $m_{H^{\pm}}$ values. For $H^{\pm}$ with $m_{H^{\pm}} < m_{top}$, the most important decay channel is $H^+ \to \tau\nu$ with a branching ratio of $\sim 100\%$.

On the other hand, for small $\tan\beta$ values, $\tan\beta \lesssim 5$, the pattern is more complicated. For $m_{H^{\pm}} > m_{top}$, charged Higgs will decay mainly into tb. In addition, decays into Wh final states play also an important role since they can reach the level of several ten percent for certain m_{H^+} values, leading to a significant reduction of the dominant branching ratio into $\tau\nu$ states. For $H^{\pm}$ with $m_{H^{\pm}} < m_{top}$, the main decay mode is $H^+ \to \tau\nu$ and the $H^+ \to cs$ channel starts being non negligible.

[4] Otherwise called heavy SUSY spectrum.

The $H^{\pm}$ branching ratios are summarized in Fig. 2.3 for the values $\tan\beta = 1.5$ and $\tan\beta = 30$.

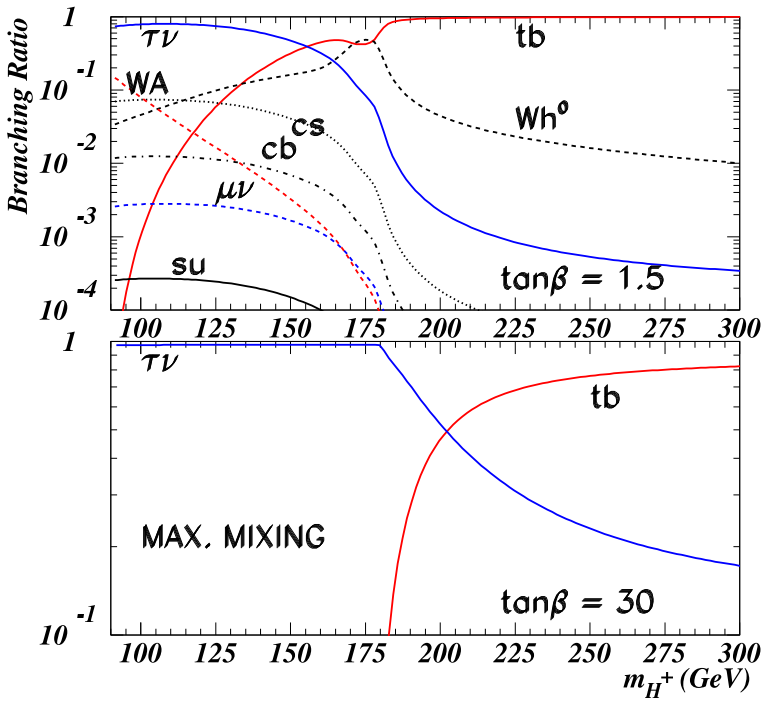

Figure 2.3: Branching ratios of H^+ decays as a function of m_{H^+} for $\tan\beta = 1.5$ and 30 computed by the HDECAY program. Taken from [33].

2.3.2 MSSM scenarios

Within the MSSM, the mass of the CP-even h Higgs boson is calculable in terms of the other MSSM parameters. At tree level, m_h is bounded from above according to $m_h \leqq m_Z$ (see Eq. (2.36)). As it was already pointed out, if radiative corrections are added [26], the m_h upper bound is increased up to $m_h \leqq 135$ GeV [5].

At LEP, the search of the lightest MSSM neutral Higgs boson has been performed in three benchmark scenarios [34] which give a constraint to the large number of free parameters in the MSSM:

[5] This value holds for $m_{top} = 175$ GeV and a SUSY scale $M_{SUSY} = 1$ TeV. If m_{top} is raised by 5 GeV, then the m_h limit is increased by about 5 GeV; using $M_{SUSY} = 2$ TeV increases the limit by about 2 GeV.

- **Maximal Mixing scenario**
  This scenario yields the theoretical upper bound of m_h in the MSSM as a function of $\tan\beta$ for fixed m_{top} and M_{SUSY} (i.e. the SUSY scale at which heavy sparticles decouple from Higgs). It therefore allows to derive conservative constraints on $\tan\beta$ from the h search.

- **No Mixing scenario**
  In this scenario, the mixing in the scalar top sector[6] is chosen to be zero, while the other parameters are the same as in the Maximal Mixing scenario.

- **Large μ scenario**
  This benchmark scenario is characterized by a relatively large value of $|\mu|$ (the Higgs mass parameter given in Eq. (2.32)) compared to M_{SUSY}. A relatively small value of M_{SUSY} is adopted and a moderate mixing in the scalar top sector is proposed.

The MSSM parameters in the three different benchmark scenarios are given in Table 2.4. Thus, for each scenario a different radiative correction to m_h is obtained. For example, in the No Mixing scenario, the lowest upper limit for the h mass is obtained, $m_h \sim 115$ GeV, and in the Maximal Mixing scenario, one gets the highest possible upper limit for this mass, $m_h \sim 122$ GeV.

Scenario	μ	$X_t \equiv A_t - \mu\cot\beta$	A_b	M_{SUSY}	$m_{\tilde{g}}$
No Mixing	-0.2	0	A_t	1.0	0.8
Maximal Mixing	-0.2	$\sqrt{6}M_{SUSY}$	A_t	1.0	0.8
Large μ	1	-0.3	A_t	0.4	0.2

Table 2.4: MSSM parameters in TeV for the three benchmark scenarios. X_t is the $\tilde{t}$ mixing parameter, A_t is the three-linear Higgs-stop coupling, A_b denotes the Higgs-sbottom coupling and $m_{\tilde{g}}$ is the gluino mass. The gaugino mass parameter M_2 is set to 0.2 TeV.

Nevertheless, for any of the three scenarios, the charged Higgs boson mass and couplings remain practically the same. For the studies presented in this thesis, in order to be

[6] The tri-linear scalar A_i terms in Eq. (2.32) allow the scalar superpartners of the left- and right-handed fermions to mix to form mass eigenstates. If one assumes that these A_i terms are of similar size, the mixing effects will be proportional to the quark mass. Therefore, the mixing will be only relevant in the scalar superpartners of the top and the bottom quarks, i.e. $\tilde{t}$ and $\tilde{b}$. For more information see [35].

consistent with previous charged Higgs searches (see section 2.3.5), the Maximal Mixing scenario was used.

2.3.3 $H^{\pm}$ searches at LEP

Charged Higgs bosons would have been produced at LEP through the process $e^+e^- \rightarrow H^+H^-$ as shown in Fig. 2.4. The production rate depends only on $m_{H^{\pm}}$ in the general two Higgs doublet model.

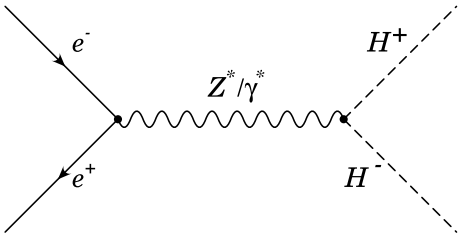

Figure 2.4: Feynman diagram of charged Higgs pair production at LEP.

In the MSSM and at tree level, the $H^{\pm}$ mass is constrained to be heavier than the $W^{\pm}$ mass, giving a rather difficult scenario for $H^{\pm}$ discovery at LEP2, but for specific choices of the MSSM parameters, the loop corrections can lower this mass.

The LEP $H^{\pm}$ searches [36] where carried out under the assumption that the two decays $H^+ \rightarrow c\bar{s}$ and $H^+ \rightarrow \tau^+\nu$ exhaust the H^+ decay width, but the relative branching ratio is free. Thus, they searched for the following H^+H^- final states: $(c\bar{s})(\bar{c}s)$, $(\tau^+\nu)(\tau^-\bar{\nu})$ and the mixed mode $(c\bar{s})(\tau^-\bar{\nu}) + (\bar{c}s)(\tau^+\nu)$. Since they did not obtain any signal, they could give mass limits as a function of the branching ratio $B(H^+ \rightarrow \tau^+\nu)$. The limit at 95 % confidence level on the charged Higgs as a function of $B(H^+ \rightarrow \tau^+\nu)$ obtained by ALEPH experiment can be seen in Fig. 2.5.

The most general lower limit, valid at the 95% confidence level for any value of the branching ratio is **78.6 GeV/c^2**.

2.3.4 $H^{\pm}$ searches at Tevatron

One of the main goals of the Tevatron Higgs Working Group is to examine the potential for the upgraded Tevatron to extend the LEP2 MSSM Higgs search [38]. The Tevatron is

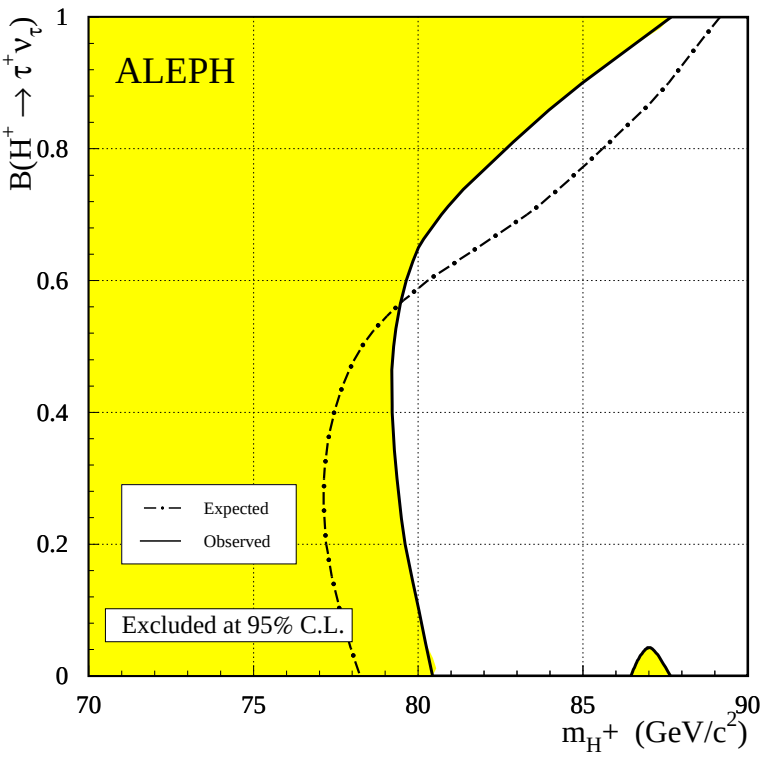

Figure 2.5: Limit at 95% C. L. on the charged Higgs boson mass as a function of $B(H^+ \to \tau^+\nu)$. Taken from [37] .

expected to deliver an integrated luminosity of $\mathcal{L} = 2\ fb^{-1}$ in the first two years (Run II a) and $\mathcal{L} = 13\ fb^{-1}$ in the subsequent years (Run II b) until the LHC starts. The CDF and D$\emptyset$ experiments Run IIa upgrades [39] where successfully installed in spring 2001 and are currently taking data from $p\bar{p}$ collisions.

If $m_{H^\pm} < m_{top} - m_b$, the charged Higgs boson could be produced at Tevatron in $t\bar{t}$ production via $t \to bH^+$ (and $\bar{t} \to \bar{b}H^-$) decay channel, which would compete with the dominant SM decay mode, $t \to bW^+$, depending on the value of $\tan\beta$. The $BR(t \to bH^+) + BR(t \to bW^+) = 1$ assumption was used. Moreover, they study the $H^\pm$ production within the two Higgs Doublet Model (H2DM) (the MSSM Higgs sector is a Type II 2HDM [40]).

In a recent D$\emptyset$ publication [41], the results of a direct search for $H^\pm$ were exposed. The $t\bar{t}$ events for that analysis were obtained from $p\bar{p}$ collisions at $\sqrt{s} = 1.8$ TeV and for an integrated luminosity of 62.2 ± 3.1 pb^{-1}. The considered channels were both

$t\bar{t} \to H^+H^-b\bar{b}$ and $t\bar{t} \to H^{\pm}W^{\mp}b\bar{b}$. At small $\tan\beta$ the $H^{\pm} \to c\bar{s}$ decay mode is quite important, while at large $\tan\beta$, $H^{\pm}$ decays into $\tau^+\nu$. Because at small $\tan\beta$ there is background from multijet production, the search was concentrated on large $\tan\beta$ and $t\bar{t} \to \tau^-\tau^+\nu_\tau\bar{\nu}_\tau$+2 b jets and $t\bar{t} \to \tau\nu_\tau qq\prime$ (from $W^{\pm}$ decay)+ 2 b jets final states were considered with τ decaying hadronically. Since the experimental signature for $t \to bH^+$ is nearly identical to that for $t \to bW^+$, and since $BR(t \to bH^+) > BR(t \to bW^+)$ in this region of the parameter space, they search for an increase of the absolute yield of τ leptons at high $\tan\beta$ to differentiate between the two decay modes. The obtained results were in agreement with the SM predictions, and it showed no evidence for a signal for $m_{H^{\pm}} < 150$ GeV. They concluded that charged Higgs boson is excluded at 95 % CL for $BR(t \to H^+b) > 0.36$ in the region 0.3< $\tan\beta < 150$ and $m_{H^{\pm}} < 160$ GeV. These results are summarized in Fig. 2.6.

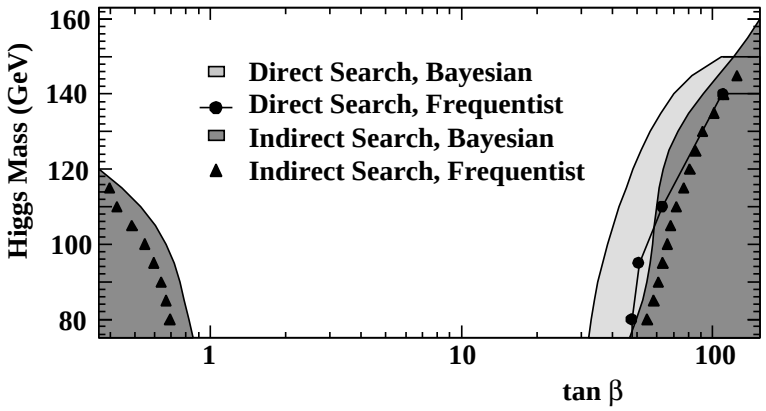

Figure 2.6: Region of exclusions at 95% C. L. in $(m_{H^{\pm}}, \tan\beta)$ for $m_{top} = 175$ GeV and $\sigma(t\bar{t}) = 5.5\ pb$. Taken from [41].

In the $m_{H^{\pm}} > m_{top} - m_b$ case, the charged Higgs boson production occurs mainly through radiation of a third generation quark: $gb \to tH^-$; $gg, q\bar{q} \to t\bar{b}H^-$. However, the cross section for this inclusive charged Higgs production is too small to be seen at the upgraded Tevatron if $m_{H^{\pm}} \gtrsim m_{top}$.

2.3.5 $H^{\pm}$ searches at LHC

The sensitivity of the ATLAS and CMS detectors at the LHC to the discovery of the charged Higgs boson was investigated in detail in [42] for the ATLAS Technical Design

Report and in [43] for the CMS Technical Proposal assuming that the mass scale of supersymmetric partners of ordinary matter is above the charged Higgs boson mass, so that $H^{\pm}$ decays into SUSY partners are forbidden.

If the charged Higgs is lighter than the top quark, top quark decays would be a good source of charged Higgs production with $pp \to t\bar{t}$, $t \to H^{+}b$, since top quarks will be produced with very large rates at the LHC [42]. In this mass range, the decay channel $H^{\pm} \to \tau\nu$ is the dominant decay mode. For low $\tan\beta$, this decay channel is complemented by $H^{\pm} \to cs$ decay, but the later suffers from huge QCD backgrounds.

The $H^{\pm} \to \tau\nu$ channel was studied in detail in [44] for the ATLAS detector, using full simulation Monte Carlo (which provides a detailed description of the detector geometry and simulates accurately the interactions of particles with the different detector materials) for $m_{H^{\pm}} < m_{top}$. The experimental signature for the Higgs production would be the measurement of a significant excess of events with an isolated τ with respect to the rate predicted by the SM. The signal process considered in this analysis is:

$$
pp \to t\bar{t}
\begin{cases}
t \to H^{+}b \;\; ; & H^{+} \to \tau^{+}\nu_{\tau} \;\; ; & \tau^{+} \to hadrons\ \bar{\nu_{\tau}} \\
\text{with 3 possibilities for the } \bar{t} \text{ decay:} & & \\
\bar{t} \to W^{-}b \;\; ; & W^{-} \to l\nu_{l} \;\; (l = e, \mu) & \\
\bar{t} \to W^{-}b \;\; ; & W^{-} \to \tau\nu_{\tau}; & \tau \to l\nu_{l}\nu_{\tau} \;\; (l = e, \mu) \\
\bar{t} \to H^{-}b \;\; ; & H^{-} \to \tau\nu_{\tau}; & \tau \to l\nu_{l}\nu_{\tau} \;\; (l = e, \mu)
\end{cases}
$$

The expected 5σ discovery contour curve for this channel in the $(m_A, \tan\beta)$ plane for an integrated luminosity of $30 fb^{-1}$ (i.e. for 3 years of running at low luminosity) is shown in Fig. 2.7. This analysis is going to be further commented in section 6.1.2. In this thesis, these results will be complemented by the study of the hadronic decay of the W boson.

In the case of $m_{H^{\pm}} > m_{top}$, the charged Higgs boson would be produced through the $2 \to 3$ process $gg \to tbH^{\pm}$ and $2 \to 2$ process $gb \to tH^{\pm}$ as shown in Fig. 2.8.

In this region, the $H^{\pm} \to tb$ decay mode becomes dominant. A detailed study of this channel for the ATLAS experiment is presented in [46]. They searched for one top decaying leptonically to trigger the experiment and the other one hadronically. The background process for this reaction was $t\bar{t}b$ and $t\bar{t}q$ productions. Above $m_{H^{\pm}} = 300$ GeV, the reduced signal rate and the combinatorial background make the observation of this channel diffi-

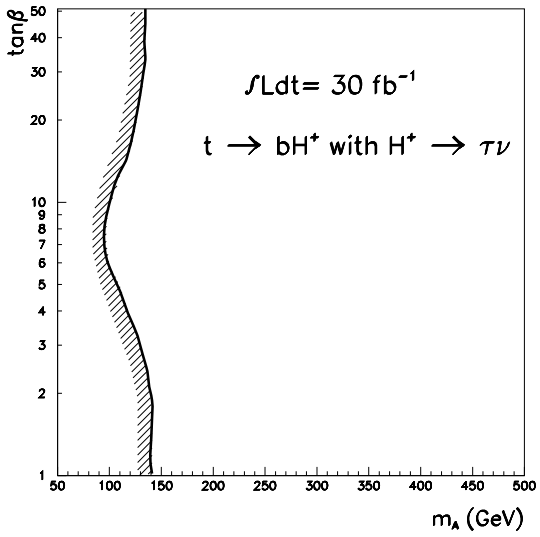

Figure 2.7: 5σ discovery contour plot for $H^{\pm} \to \tau\nu$ channel with $m_{H^{\pm}} < m_{top}$ in the $(m_A, \tan\beta)$ plane for and integrated luminosity of 30 fb^{-1} and a top quark mass of $m_{top} = 175$ GeV . Taken from [42].

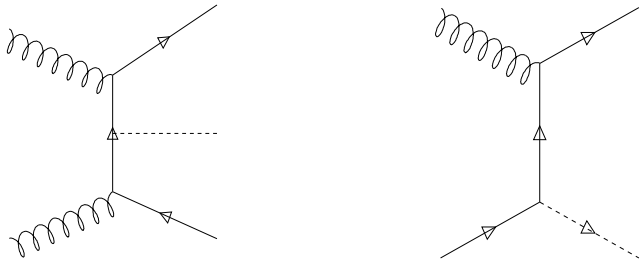

(a) $gg \to tH^+b$ (b) $gb \to tH^+$

Figure 2.8: Charged Higgs production at the LHC through the $gg \to tbH^{\pm}$ and $gb \to tH^{\pm}$ channels.

cult. Below the charged Higgs mass of 300 GeV, this channel may be observed above the $t\bar{t}b$ and the $t\bar{t}q$ backgrounds. At high $\tan\beta$ values, sensitivity is expected up to $m_{H^{\pm}} \sim$ 400 GeV. In the intermediate $\tan\beta$ region, the $H^{\pm} \to tb$ channel suffers from large combinatorial backgrounds due to a wrong (tb) pairing out of all the possible candidates, and the $H^{\pm}$ discovery in this region is no more possible.

The $\tau\nu$ decay channel was also studied for $m_{H^{\pm}} > m_{top}$ and $\tan\beta > 10$ in [47]. The events were produced through the channel $gb \to tH^{\pm}$ and the associated top quark was

required to decay hadronically, $t \to jjb$. The charged Higgs decayed into $\tau\nu$ and only the hadronic decays of the τ lepton were considered. Significances greater than 5σ could be achieved at $\tan\beta$ values lower than in the $H^{\pm} \to tb$ channel in the high $\tan\beta$ region, since this channel does not suffer the large irreducible backgrounds present in the other one. However, in the low $\tan\beta$ region, and for $m_{H^{\pm}} > m_{top}$, the $\tau\nu$ channel offers no sensitivity for the charged Higgs discovery since the $H^{\pm} \to \tau\nu$ branching ratio vanishes.

The channel $H^{\pm} \to W^{\pm}h^0$ is only relevant in a tiny range of the MSSM parameter space, although it represents a unique test for MSSM and it may be sensitive to a singlet extension to MSSM, i.e., NMSSM [33, 45]. In [33] it was seen that in the LEP allowed regions of the MSSM parameter space, this channel presents no significant discovery potential for the charged Higgs.

In Fig. 2.9, the combined ATLAS and CMS charged Higgs 5σ discovery plot is shown for 30 fb^{-1} of integrated luminosity together with the LEP 2000 exclusion limit. Below the top quark mass, $H^{\pm}$ is produced from top decay, and the $H^{\pm} \to \tau^{\pm}\nu_{\tau}$ channel provides coverage for most $\tan\beta$ below ~160 GeV (this 5σ line is the one already shown in Fig. 2.7). Above the top quark mass, the $H^{+} \to tb$ channel covers the low and high $\tan\beta$ region while the $H^{\pm} \to \tau^{\pm}\nu_{\tau}$ channel extends the discovery reach to high Higgs boson mass and to lower $\tan\beta$ in the high $\tan\beta$ region.

In Fig. 2.10, the ATLAS 5σ discovery contours for all the MSSM Higgs bosons (h, H, A, H^{+}, H^{-}) is shown for one year of running at low luminosity (10 fb^{-1})[7]. One can easily observe that one or more Higgs could be observed in most of the parameter space except for a small region around $\tan\beta \sim 10$. The coverage of this region is one of goals of the work presented in this thesis.

[7]In this thesis, one assumes that one year of running at low luminosity corresponds to 10 fb^{-1} of integrated luminosity. However, in some ATLAS publications and talks, one year of low luminosity stands for 2 ·10 fb^{-1}.

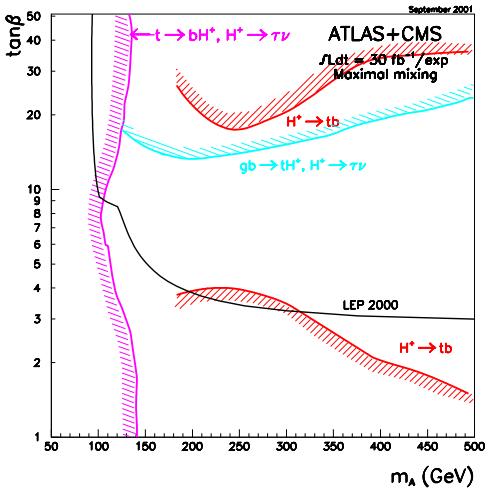

Figure 2.9: Combined ATLAS and CMS 5σ discovery plot for a MSSM charged Higgs in the Maximal Mixing Scenario and for 3 years of running at low luminosity ($\int \mathcal{L}dt = 30$ fb^{-1}). LEP 2000 exclusion limits where also added. Taken from [48].

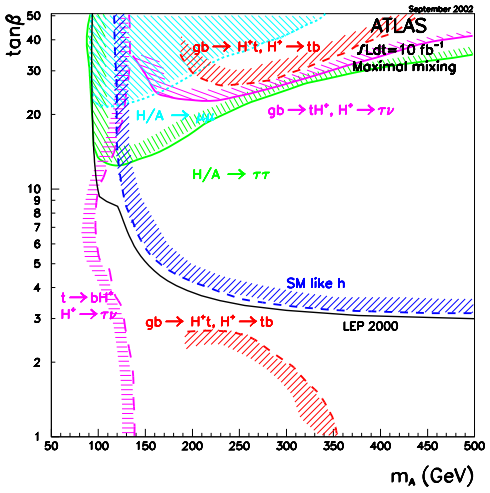

Figure 2.10: ATLAS and 5σ discovery contours for the MSSM Higgs bosons (h, H, A, H^+, H^-) obtained with different decay channels for 1 year of running at low luminosity ($\int \mathcal{L}dt = 10$ fb^{-1}). Maximal Mixing scenario was used. Taken from [48].

Chapter 3

The ATLAS experiment

ATLAS (**A** **T**oroidal **L**hc **A**pparatu**S**) is a general purpose pp detector designed to exploit the full discovery potential of the **L**arge **H**adron **C**ollider (LHC), the next generation collider at CERN. In section 3.1, the main characteristics of the collider are outlined. In section 3.2 the design requirements of the ATLAS detector are exposed followed by a description of the different subsystems. Finally, in section 3.3 some physics aspects relevant for the analysis presented in this thesis are introduced.

3.1 The LHC

The LHC is now being constructed by CERN in the tunnel which housed the Large Electron Positron (LEP) [8, 9] collider on the outskirts of Geneva. The 27 km circular tunnel lies on average 100m below ground, between lake Leman and the Jura mountains. The LEP collider was removed after October 2000 and it gave us a preview of exciting discoveries that may be made at higher energies. The LHC has been designed to seek answers to profound questions and investigate new physics at those higher energies. It will be operative in April 2007.

3.1.1 Design

The LHC is a high-energy, high-luminosity proton-proton collider. It will collide beams of 7 TeV and its design luminosity is $10^{34} cm^{-2} s^{-1}$. Before particles are injected into the

LHC ring they are accelerated up to a given energy by a chain of preaccelerators. First of all the LINAC (LINear ACcelerator) accelerates the protons up to 50 MeV and then the Booster increases this energy up to 1 GeV. Furthermore, the PS (Proton Synchrotron) and the SPS (Super Proton Synchrotron) increase the energy up to 26 GeV and 450 GeV respectively, for the final injection into the LHC (see Fig. 3.1).

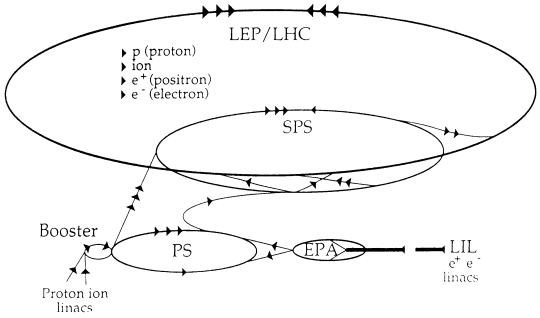

Figure 3.1: The LEP/LHC injector system.

The basic layout of the machine can be seen in Fig. 3.2. This layout mirrors that of LEP, with eight straight sections, each approximately 528m long, available for experimental insertions or utilities. As it can be seen in Fig. 3.2, ATLAS (A Toroidal LHC Apparatus) will be placed at point 1, and CMS (Compact Muon Solenoid) will be placed at point 5. Two more experimental insertions are located at point 2, ALICE (A Large Ion Collider Experiment) and at point 8, LHCb. The later straight sections also contain the injection systems. The rings cross only at this 4 locations.

The LHC will have two separate beam lines since it will collide particle beams of the same charge. Thus, the direction of the magnetic field in one beam-line must be opposite to that of the other beam line. This is accomplished by using a magnet design that combines the two guide fields into a single magnet as shown in Fig. 3.3. This option was chosen over the one using two separated magnets due to space restrictions in the LEP tunnel. See [49] for more details.

In order to meet the LHC energy requirements, 1296 superconducting magnets (cooled with super fluid helium) with a length of 12.2 meters and a field strength of 8.6 Tesla will be installed. However, dipole bending magnets are not the only superconducting magnets needed for the LHC ring; 3.1 meter, 6.9 Tesla superconducting quadrupole magnets are also needed for beam focusing.

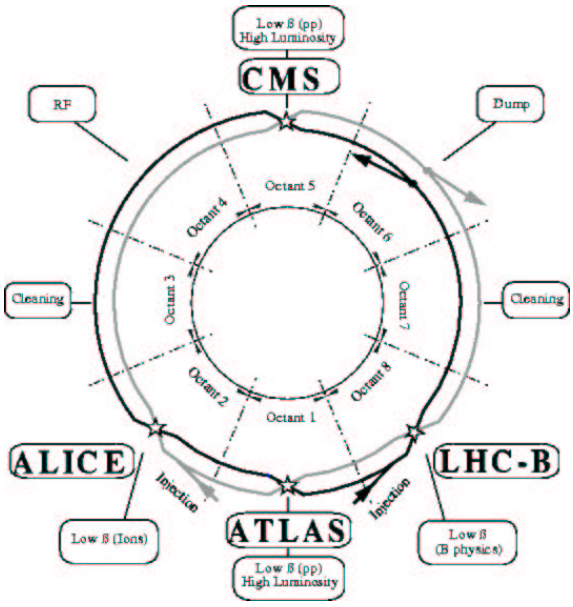

Figure 3.2: The LHC schematic layout.

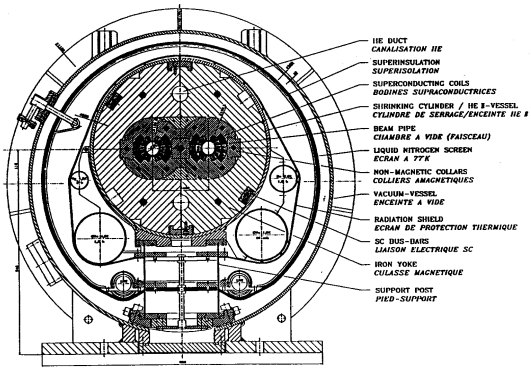

Figure 3.3: Frontal view of an standard LHC two-in-one dipole and its cryostat.

3.1.2 Machine performance

The upper limit of the energy which can be reached at the LHC is imposed by geometrical and magnetic constraints. The highest operational magnetic field for affordable super-

conducting magnets is 8.65 Tesla which together with the requirement that LHC has to fit inside the existing LEP tunnel gives the maximum energy of 7 TeV per beam. However, another way to increase the rate of events of interesting physics is to increase the luminosity:

$$n_x = \sigma_x \cdot \mathcal{L} \tag{3.1}$$

where n_x is the event rate of the specific process, σ_x its cross section and $\mathcal{L}$ the luminosity, which is related to the parameters of the collider. This relation is given by:

$$\mathcal{L} = \frac{1}{4\pi} \cdot \frac{N^2 f}{t A_T} \tag{3.2}$$

where N is the number of protons in each bunch, t the time between individual bunches, A_T the transverse dimension of the bunches at the interaction points and f the fraction of bunch positions actually containing protons.

The time between bunches is limited by the fact that there should be no additional interactions on each side of the interaction region and the time resolution of the experiment. The bunch crossing rate for the LHC will be 25 ns corresponding to approximately 23 interactions per bunch. The transverse dimensions of the beam at the interaction point will be of the order of a few μm. Besides, to be able to fill new bunches into the LHC and to operate the beam dump, it is necessary to order the proton bunches in bunch trains followed by some empty bunches. In total 2835 of the 3557 available positions with 25 ns separation will contain protons corresponding to $f = 0.80$. Thus, the only way left to increase the luminosity is to increase the number of protons per bunch, but this is limited by electromagnetic forces. The nominal luminosity is fixed at $\mathcal{L} = 10^{34}$ cm^{-2}s^{-1} but for the first years of operations it is foreseen to run at a lower luminosity, $\mathcal{L} = 10^{33}$ cm^{-2}s^{-1} and increase it gradually to the nominal value.

The high requirement on luminosity is the reason for the choice of a proton-proton collider. While a proton-antiproton machine has the advantage that both counter rotating beams can be kept in the same beam pipe, producing these enormous amounts of antiprotons required for the high luminosity is not realistic, and it would be more expensive than the proton-proton solution with separated beam pipes.

The total inelastic, non-diffractive cross section at the LHC energies and during high luminosity operation will be about 100 mb corresponding to an interaction rate of 10^9Hz. As it was already mentioned above, with a bunch crossing rate of 40 MHz (period 25

ns), about 23 interactions will happen in each bunch crossing ("pile-up") resulting in about ∼10000 tracks in the detector within 100 ns, the typical duration of a pulse in the detectors. This situations impose stringent requirements to the design and performance of the LHC detectors: they must be rather fast, in order to integrate the signals from the pile-up events over many bunch crossings, and highly granular, in order to minimize the contribution of pile-up in a given detector cell. The LHC performance parameters are shown in Table 3.1.

Machine performances	
Energy per beam	7 TeV
Dipole field	8.6 Tesla
Coil aperture	56 mm
Distance between apertures	194 mm
Design Luminosity	10^{34} cm^{-2}s^{-1}
Beam-beam parameter	0.0034
Injection energy	450 GeV
Circulating current/beam	0.54 A
Bunch spacing	25 ns
Particles per bunch	10^{11}
Stored beam energy	334 MJ
Normalized transverse emittance	3.75 μm rad
r.m.s. bunch length	0.075 m
β-values at I. P. in collision	0.5 m
Full crossing angle	200 μrad
Beam lifetime	22 h
Luminosity lifetime	10 h
Energy loss per turn	6.7 KeV
Critical photon energy	44.1 eV
Total radiated power per beam	3.6 kW

Table 3.1: LHC performance parameters.

3.1.3 Physics Interests

As it was already pointed out, the primary purpose of the LHC is to search for and to study new physics. Although with the LEP results the Standard Model is tested sometimes to better than 1% level, some fundamental questions are still open. In particular, one hopes to understand the origin of electroweak symmetry breaking (masses of W and Z *bosons*) looking primarily for one or more Higgs bosons, for example. The LHC can also be used to search for SUSY particles, which (in case they exist) will be produced in some cases with large rates. The MSSM charged Higgs studied in this thesis could be a good example. Some other possibilities for new physics that could be studied at the LHC are: quark compositeness, leptoquarks and heavy vector bosons (W', Z'). And last but not least, with the new energy regime that opens, there is always room for the unexpected.

Moreover, experiments at LHC will be able to provide many measurements related to known physics, such as top decay properties, B-physics and numerous cross section measurements (W, Z, γ and jet production, for example). The B physics program will include studies of CP violation which will allow testing of the Standard Model, in which CP violation is parametrised within the so called *CKM matrix*. It will also include the measurement of B_s^0 oscillations, the search for rare B decays such as $B_s^0 \to \mu^+\mu^-(X)$ and the study of doubly-heavy hadrons such as B_c.

The LHC can also be used to collide beams of heavy ions (e.g. lead ions) with a center of mass energy of about 6 TeV per nucleon, but with lower luminosity (10^{27} cm^{-2}s^{-1}) and interaction rate of $\sim 10^4$s^{-1} for p-p collisions. The heavy-ion program has as its primary objective the search for the quark-gluon plasma. One will try to investigate different stages in the production of the plasma before the formation of the normal hadronic matter: the initial conditions, the quark-gluon plasma, the phase transition and the hadronic matter.

In Fig. 3.4 the cross sections for many interesting new physics processes at the LHC as well as expected Standard Model processes are shown. It can be seen there that for many potentially interesting physics processes, overall the LHC cross section is very high compared to previous machines. However, the total cross section of interesting physics channels such as SM Higgs production, is several orders of magnitude smaller. This means that the LHC detectors will have to be flexible enough to detect a wide range of physics processes despite a very large background.

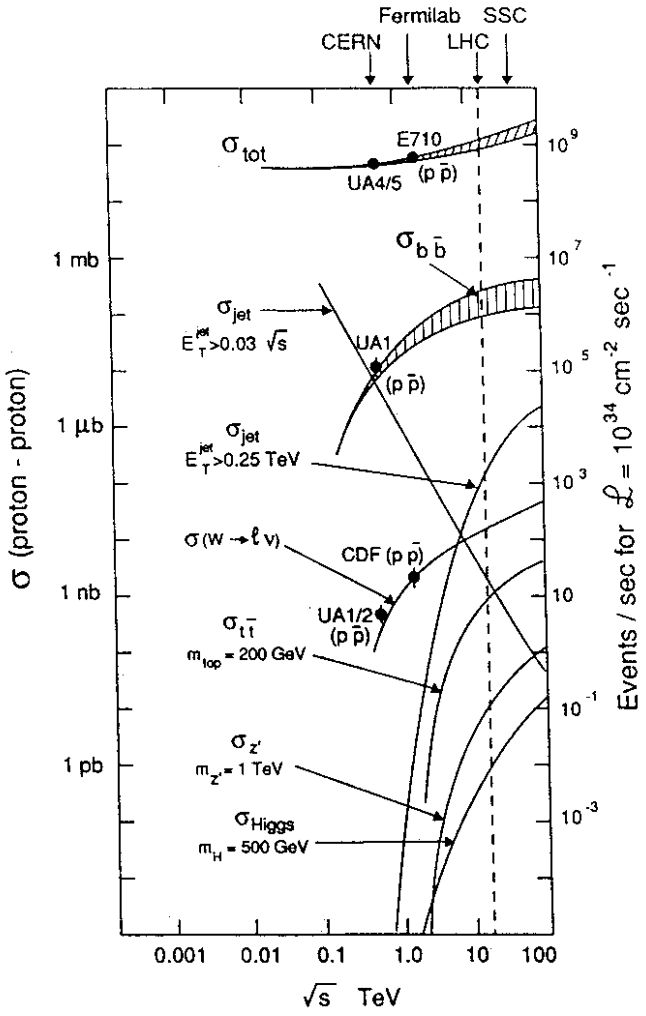

Figure 3.4: Expected proton-proton cross section as a function of the energy in the center of mass system at the LHC.

3.2 The ATLAS detector

ATLAS is a general purpose p-p spectrometer designed to exploit the full discovery potential of the LHC. The detector concept and its physics potential were presented in the Technical Proposal [50] in 1994 and in different Technical Design Reports[51, 42]. Since then, the design has evolved guided by detailed physics performance studies, experience

from a rigorous and broad R&D program, and the necessity to stay within cost-effective technologies.

The ATLAS experiment is designed, constructed and operated by a world-wide collaboration of scientists and engineers (~1800 members) from 146 institutions of 33 countries. Spain is contributing with three Institutes and about 4.1% of the ATLAS members.

The overall detector layout as shown in Fig. 3.5 has a cylindrical symmetry with a total length of 42 m and a radius of 11 m. The total weight of the detector is ~7000 Tons, mainly due to the calorimetry system.

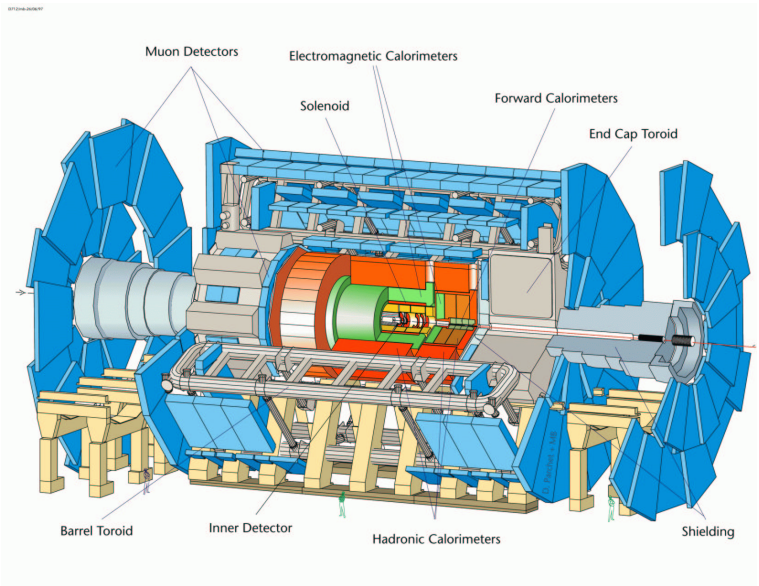

Figure 3.5: General overview of the ATLAS detector.

The detector is optimized for a long range of known and hypothetical processes. The observable cross section for most of the processes is small over a large part of energy range (see Fig. 3.4), hence it is an important design consideration to operate at high luminosity and to maximize the detectable rates above backgrounds by high resolution measurements. The basic design criteria of the detector include the following:

- Very good electromagnetic calorimetry for electron and photon identification and measurements, complemented by a full-coverage hadronic calorimetry for accurate jet and missing transverse energy (E_{Tmiss}) measurements.

- High-precision muon measurements, with the capability to guarantee accurate measurements at the highest luminosity using the external muon spectrometer alone.
- Efficient tracking at high luminosity for high transverse lepton momentum (p_T) measurement, electron and photon identification, τ lepton and heavy flavour identification, and full event reconstruction capability at lower luminosity.
- Large acceptance in pseudo-rapidity ($\eta \equiv -log\ tan\frac{\theta}{2}$) with almost full azimuthal angle (ϕ) coverage everywhere (ϕ is measured around the beam axis).
- Triggering and measurements of particles at low p_T thresholds, providing high efficiencies for most physics processes of interest at the LHC.

The following sections summarize the physics scope, performance and design of the individual subdetectors.

3.2.1 The Inner Detector

The Inner Detector (ID) [52, 53] is designed to reconstruct tracks and decay vertices in any event with high efficiency. Using additional information from the calorimeter and muon systems, the Inner Detector also contributes to electron, photon, and muon identification, and supplies extra signatures for short-lived particle decay vertices. Important physics considerations for the design of the Inner Detector are:

- Excellent momentum and impact parameter resolution for tracks with $p_T > 0.5$ GeV up to very high momentum
- Tracking coverage over the range $|\eta| < 2.5$
- High efficiency keeping high noise rejection
- Identification of the charge of high p_T tracks
- Tagging of b-jets originating from b-quarks
- Reconstruction of soft electrons and secondary vertices from b and τ decays
- Identification of the primary vertex

- Electron identification capability
- Identification of a high p_T track to reduce the level 1 electromagnetic cluster trigger rate from jet events

The magnetic field configuration of the ID is based on an inner thin super-conducting solenoid surrounding the Inner Detector cavity with a radius of 1.2 m and a length of 5.3 m. It provides an axial magnetic field of 2 T in the center of the tracking volume.

The momentum and vertex resolution requirements from physics call for high-precision measurements to be made with fine granularity detectors, given the very large track density expected at the LHC. The layout of the Inner Detector is shown in Fig. 3.6. The outer radius of the ID cavity is 115 cm. It consists of three units: a barrel section extending over $\pm$ 80 cm, and two identical end-caps covering the rest of the cylindrical part. In the barrel region, high-precision detector layers are arranged on concentric cylinders around the beam axis, while the end-cap detectors are mounted on disks perpendicular to the beam axis.

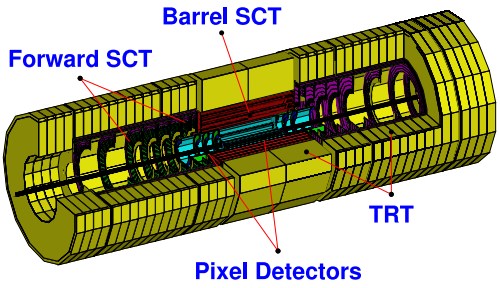

Figure 3.6: Three dimensional cut-away view of the ATLAS Inner Detector.

The highest granularity around the vertex region is provided by semi-conductor pixel and strip detectors, the later employed in the Semiconductor Tracker (SCT). The basic principle of the semiconductor detectors is that the passage of ionizing radiation creates electron-hole pairs in the semiconductor which are collected by an electrical field. The difference between strips and pixels is mainly geometry, pixels being closely spaced pads

capable of good two dimensional reconstruction while strips give a better spacial resolution in one coordinate than the other.

The pixel layers are segmented in $R\phi$ and z, while SCT detector uses small angle (40 mrad) stereo strips to measure both coordinates, with one set of strips in each layer measuring ϕ. The pixel detector is much more radiation tolerant than the silicon strip tracker.

To improve momentum reconstruction, pattern recognition and electron identification a straw-tube Transition Radiation Tracker (TRT) is placed, which provides 36 points per track (> 7 points/track for *electron-identification*).

The basic layout parameters and the expected measurement resolutions are summarized in Table 3.2. The layout provides full tracking coverage over $|\eta| \leq 2.5$, including impact parameter measurements and vertexing for heavy-flavour and τ-tagging. The secondary vertex measurement performance is enhanced by the innermost layer of pixels, at a radius of about 4cm, as close as is practical to the beam pipe. The lifetime of such a detector will be limited by radiation damage, and may need replacement after a few years, the exact time depending on the luminosity profile. A large amount of interesting physics can be done with this detector during the initial low luminosity running, especially in the B sector, but physics studies have demonstrated the value of good b-tagging performance during all phases of the LHC operation, for example in the case of Higgs and Supersymmetry searches. It is therefore considered very important that this innermost pixel layer (or B-layer) can be replaced to maintain the highest possible performance throughout the experiments's lifetime. The mechanical design of the pixel system allows the possibility of replacing this B-layer.

The three different detector technologies are summarized in the following subsections.

3.2.1.1 Pixel detector

The ATLAS Pixel Detector [54] is designed to provide a very high-granularity and high-precision set of measurements as close to the interaction point as possible. The system consists of three barrels at a radii of 5.05 cm[1], 8.85 cm, and 12.25 cm respectively, and five rings on each side, with 11 cm inner radius and 20 cm out outer radius, which complete

[1]In [54], the innermost pixel layer was designed to have 4 cm radius but this was later moved to 5 cm to accommodate larger beam-pipe.

System	Position	Area (m^{-2})	Resolution $\sigma(\mu$m)	Channels (10^6)	η coverage
Pixels	1 removable barrel layer (B-layer)	0.2	$R\phi = 12, z = 66$	16	$\pm$ 2.5
	2 barrel layers	1.4	$R\phi = 12, z = 66$	81	$\pm$ 1.7
	5 endcap disks on each side	0.7	$R\phi = 12, R = 77$	43	1.7-2.5
Silicon strips	4 barrel layers	34.4	$R\phi = 16, z = 580$	3.2	$\pm$1.4
	9 endcap wheels on each side	26.7	$R\phi = 16, R = 580$	3.0	1.4-2.5
TRT	Axial barrel straws		170 (per straw)	0.1	$\pm$0.7
	Radial endcap straws		170 (per straw)	0.32	0.7-2.5

Table 3.2: Parameters of the Inner Detector. The resolutions quoted are typical values (the actual resolution in each detector depends on $|\eta|$.

the angular coverage. The thickness of each layer is expected to be about 1.7% of a radiation length (X_0) at normal incidence. It provides three precision measurements over the full acceptance, and mostly determines the impact parameter resolution.

The Pixel detector contains a total of 140 millions of detector elements, each 50 μm in the $r\phi$ plane and 400 μm in z, allowing the track origin to be reconstructed and secondary decay vertices to be found. This is very important for the identification of short-lived particles such as b quarks and τ leptons, which require the Inner Detector to reconstruct the decay point inside the beam pipe by extrapolating the tracks back to their origins. The impact parameter resolution for low luminosity B-physics studies is greatly improved by the presence of the inner-most pixel layer at 5.05 cm, the so-called B-layer.

The readout of the pixels requires the use of advanced techniques. The readout chips cover a large area, with individual circuits for each pixel element, including buffering to store the data while awaiting the level-1 trigger decision. In addition each chip must be radiation-hard to withstand something like 300 kGy of ionizing radiation and 5×10^{14} neutrons per cm^2 over ten years of operation of the experiment.

3.2.1.2 Semiconductor Tracker

The SemiConductor Tracker (SCT) system is designed to provide eight precision measurements per track in the intermediate radial range, contributing to the measurement

of momentum, impact parameter and vertex position, as well as providing good pattern recognition by the use of high granularity.

The SCT is an order of magnitude larger in surface area than previous generations of silicon microstrip detectors, and in addition it must face radiation levels which will alter the fundamental characteristics of the silicon wafers themselves.

The barrel SCT uses four layers of silicon microstrip detectors to provide precision points in the $r\phi$ and z coordinates, with a small stereo angle to obtain the z measurement. Each silicon detector is 6.36×6.40 cm^2 with 768 readout strips each with 80 μm pitch. The detector contains 61 m^2 of silicon detectors, with 6.2 million read-out channels.

3.2.1.3 Transition Radiation Tracker

The TRT is based on the use of straw detectors, which can operate at the very high rates needed, by virtue of their small diameter and the isolation of the sense wires within individual gas envelopes. Electron identification capability is added by employing xenon gas to detect transition-radiation photons created in a radiator between the straws. Each straw is 4 mm in diameter, giving a fast response and good mechanical properties for a maximum straw length of 150 cm. The barrel contains about 50000 straws, each divided in two at its center in order to reduce the occupancy and readout at each end. The endcaps contain 320000 radial straws, with the readout at the outer radius.

The total number of electronic channels is 420000. Each channel provides a drift-time measurement, giving a spatial resolution of 170 μm per straw, and two independent thresholds. These allow the detector to discriminate between tracking hits, which pass the lower threshold, and transition-radiation hits, which pas the higher.

3.2.2 Calorimeters

Unlike other detector subsystems, the intrinsic energy resolution of calorimeters improves with increasing energy, making them suitable for use at high energy colliders. Physics requirements on calorimeters at the LHC include:

- accurate measurement of energy and position of both electrons and photons,

- measurement of the energy and direction of jets,
- particle identification including the separation of electrons, photons and hadronic τ decays from jets,
- measurement of the missing transverse energy of events,
- event selection already at the first trigger level.

The system is divided into an electromagnetic sampling calorimeter with high resolution closest to the interaction point and a larger hadronic calorimeter behind with a coarser resolution. The electromagnetic calorimeter uses Liquid Argon (LAr) as active medium whereas in the hadronic calorimeter, different technologies are employed depending on the environmental constrains like radiation dose. The ATLAS calorimeters are shown in Fig. 3.7.

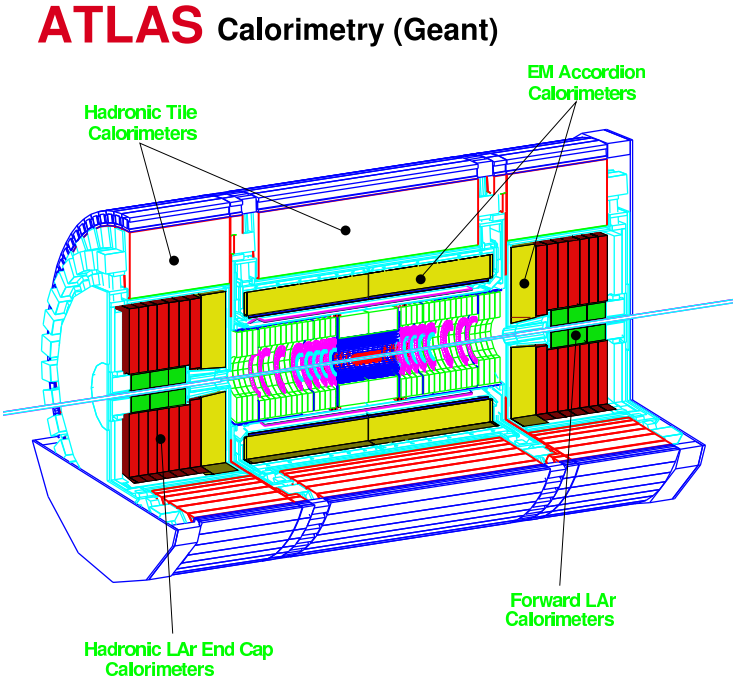

Figure 3.7: View of the ATLAS calorimetry.

The position of the central solenoid in front of the electromagnetic calorimeter demands a careful minimization of the material in order to achieve the desired calorimeter performance. As a consequence, the central solenoid and the LAr calorimeter share one common vacuum vessel, thereby eliminating two vacuum walls. The cryostat covers a pseudorapidity range of $|\eta| < 1.7$. The central solenoid is designed to be as thin as possible without sacrifying the operational safety and reliability. Two endcaps cryostats enclose the electromagnetic ($1.5 < |\eta| < 3.2$) and hadronic calorimeters ($|\eta| < 3.2$) as well as integrated forward calorimeters ($3.1 < |\eta| < 4.9$). The rapidity coverage and basic granularity of the calorimeters is summarized in Table 3.3.

System	**$\|\eta\|$ coverage**	**Granularity ($\Delta\eta \times \Delta\phi$)**
EM barrel	$\|\eta\| \leq 1.475$	0.03 x 0.1 (s1)
		0.025 x 0.025 (s2)
		0.05 x 0.025 (s3)
Presampler	$\|\eta\| \leq 1.8$	0.025 x 0.1
Hadronic barrel	$\|\eta\| \leq 1.8$	0.1 x 0.1
Hadronic endcap	$1.5 \leq \|\eta\| \leq 2.5$	0.1 x 0.1
	$2.5 \leq \|\eta\| \leq 3.2$	0.2 x 0.2
Forward Calo	$3.2 \leq \|\eta\| \leq 4.9$	-0.1 x 0.2

Table 3.3: The ATLAS calorimeter system.

3.2.2.1 Electromagnetic Calorimeter

The electromagnetic (EM) calorimeter is a Lead Liquid-Argon detector with accordion geometry [55]. The principle of the calorimeter is seen in Fig. 3.8.

In the pseudorapidity range $|\eta| \leq 1.8$ the EM calorimeter is preceded by a presampler detector, installed immediately behind the cryostat cold wall and used to correct the loss of energy in the material (Inner Detector, cryostats, coil) upstream the calorimeter. Its total thickness is $25X_0$ in the barrel and $26X_0$ in the endcaps, being X_0 the radiation length. The total number of channels is about 200000, and the segmentation of the calorimeter in $\Delta\eta \times \Delta\phi$ is 0.025 x 0.025.

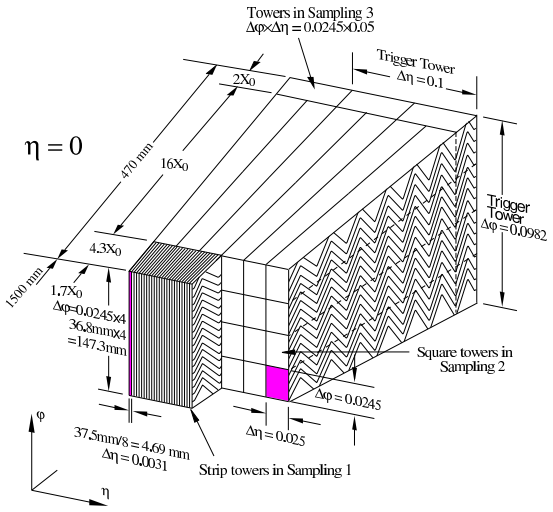

Figure 3.8: Sketch of the accordion structure of the electromagnetic calorimeter.

Apart from the energy measurement, the EM calorimeter will provide, thanks to its high granularity, powerful electron/photon identification and rejection of the jet background. The thin strips in the first sampling are the most important feature of this calorimeter. They allow π^0 rejection by a factor larger than 3 at 50 GeV of E_T. In total, the jet rejection, at 20 GeV or above, is expected to be about 5000. Such a rejection is required to eliminate the huge QCD background of the $H \to \gamma\gamma$ channel, for example.

The narrow strips contribute also to the photon angular measurement in the $|\eta|$ direction, with an accuracy of about 50 mrad/$\sqrt{E}$, an essential information in the reconstruction of the channel mentioned above.

Moreover, the EM calorimeter is also useful for identifying τ decays into hadrons. Combined with the tracker, a rejection of about 400 against jets is possible with about 30% efficiency, allowing to improve significantly the signal to background ratio in the search for MSSM Higgs bosons such as $H^{\pm}$ decaying into $\tau\nu$ and A/H decaying into $\tau\tau$ [56].

3.2.2.2 Tile Hadronic Calorimeter

The Tile Hadronic Calorimeter covers the range $|\eta| \leq 1.6$ and it consists of a central barrel and two extended barrel cylinders [57]. The hadronic barrel calorimeter is a cylinder with an inner radius of 2.28 m and an outer radius of 4.23 m. It is based on a sampling technique with plastic scintillator plates (tiles) embedded in an iron absorber matrix; the read out is performed by wavelength shifting fibers. The tiles are placed in the perpendicular plane to the beam axis and staggered in depth, simplifying the mechanical construction and the fiber routing. In Fig. 3.9, a full size extended barrel calorimeter module is shown during construction.

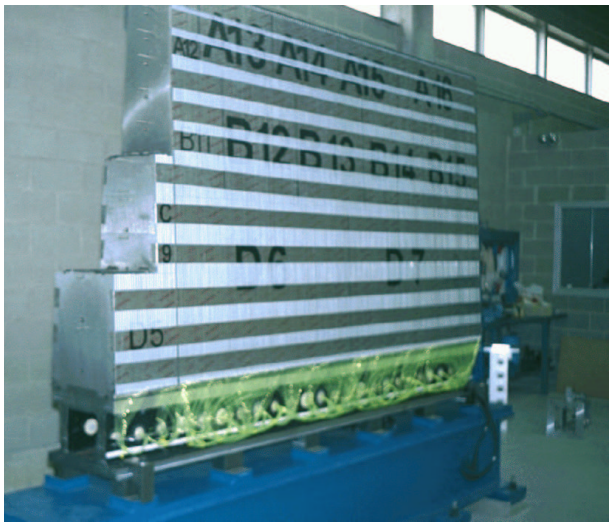

Figure 3.9: A Tile Calorimeter extended barrel module constructed in Barcelona.

The calorimeter is segmented in three layers, approximately 1.4, 4.0 and 1.8 absorption lengths (λ_{abs}) thick at $\eta = 0$. Azimuthally, the barrel and extended barrels are divided into 64 modules. Readout cells are built by grouping the optical fibers and routing them to the direction pointing to the photomultipliers; this gives the possibility to define pseudo-projective towers in the η direction pointing to the interaction region. The total number of channels is 10000. The tile calorimeter is placed behind the EM calorimeter ($1.2\lambda_{abs}$) and the solenoid coil, resulting in a total active calorimeter thickness (EM+Tile) of 9.2 λ_{abs} at $\eta = 0$ and a total amount of material in front of the muon system, including the

support structure of the tile calorimeter of 11 λ_{abs} also at $\eta = 0$.

3.2.2.3 Liquid Argon Hadronic Calorimeter

The LAr hadronic calorimeter covers the range $1.5 \leq |\eta| \leq 4.9$. The endcap hadronic calorimeter extends to $|\eta| = 3.2$ while the range $3.1 \leq |\eta| \leq 4.9$ is covered by the high density forward calorimeter. Both the hadronic endcap and the forward calorimeter are integrated in the same cryostat, housing also the EM endcaps. Each hadronic endcap calorimeter consists of two, equal diameter, independent wheels. The first wheel is built out out 25 mm copper plates, while the second one uses 50 mm plates; in both wheels the gap between consecutive copper plates is 8.5 mm, and is equipped with 3 electrodes that split it in 4 drift spaces of 1.8 mm each one. The wheels are divided in two longitudinal readout segments. The thickness of the active part of the endcap calorimeter is $\sim$12 λ_{abs}.

3.2.2.4 Forward Calorimeter

In ATLAS the Forward Calorimeter is integrated in the endcap cryostat, with the front face at about 5 meters from the interaction point. This makes the forward calorimeter a particular detector due to the high level of radiation. However, a clear benefit in terms of coverage continuity is obtained, because the effects of the crack in the transition region around $|\eta| = 3.1$ are reduced to the minimum, with advantages to the forward efficiency jet tagging and the reduction of the tails in the E_{Tmiss} distribution. The forward calorimeter has to accommodate at least 9 λ_{abs} of active detector in a rather short longitudinal space. Thus, it is a high density detector, consisting of three longitudinal sections, the first one made of copper, and the other two of tungsten. Each of them consists of a metal matrix with regularly spaced longitudinal channels filled with quartz rods. The sensitive medium is Liquid Argon and fills the gap between the quartz rod and copper matrix. The gaps are 250 microns wide in the first section and 375 (500) microns in the second (last) one. In the forward calorimeter the electronic noise for E_T in a jet cone of $\Delta R = 0.5$ is $\sim$1 GeV at $\eta = 3.2$ and drops quickly to 0.1 GeV at $\eta = 4.6$.

3.2.3 The Muon Spectrometer

High momentum final-state muons are among the signatures of LHC physics the most promising and robust. The discovery potential of the spectrometer has been optimized on the basis of selected benchmark processes, in particular Standard Model and supersymmetric Higgs decays and new vector bosons. The performance of the apparatus for low transverse momentum particles detection which are interesting for beauty physics and CP violation has also been studied. Important parameters that need to be optimized for maximum physics aims are: resolution, second-coordinate measurement, rapidity coverage of track reconstruction, trigger selectivity, trigger coverage and bunch crossing identification. To exploit this potential, the ATLAS collaboration has designed a high-resolution muon spectrometer with standalone triggering and momentum measurement capability covering a wide range of transverse momentum, pseudorapidity and azimuthal angle [58]. The view of the muon spectrometer is shown in Fig. 3.10.

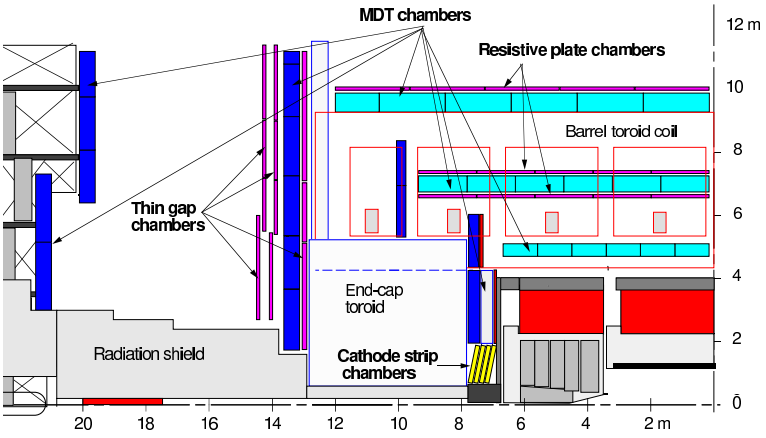

Figure 3.10: View of the ATLAS muon spectrometer.

3.2.3.1 Tracking System

The muon spectrometer exploits the magnetic deflection of muon tracks in a system of three large superconducting Arie-core toroid magnets (one barrel and two endcaps) instrumented with separate-function trigger and high-precision tracking chambers. In the pseudorapidity range $|\eta| \leq 1$, magnetic bending is provided by a large barrel magnet consisting of eight coils surrounding the hadron calorimeter. For $1.4 \leq |\eta| \leq 2.7$, muon tracks are bent in two smaller endcap magnets inserted into both ends of the barrel toroid. In the interval $1.0 \leq |\eta| \leq 1.4$, referred to as transition region, magnetic deflection is provided by a combination of barrel and endcap fields. This magnet configuration provides a field that is mostly orthogonal to the muon trajectories, and this minimizes the degradation of resolution due to multiple scattering.

Over most of the pseudorapidity range, a precise measurement of the track coordinates in the principal bending direction of the magnetic field is provided by **Monitored Drift Tubes (MDT)**. The basic detection elements are aluminum tubes of 30 mm diameter and 400 μm wall thickness, with a 50 μm diameter central W-Re wire. The tubes are operated with a non-flammable $ArCo_2$ mixture at 3 bar absolute pressure. The envisaged working point provides a non-linear spacetime relation with a maximum drift time of 700 ns, a small Lorentz angle and good ageing properties due to small gas amplification. The single-wire resolution is typically 80 μm. To improve the resolution of a chamber beyond the single wire limit and to achieve adequate redundancy for pattern recognition, the MDT chambers are constructed from 2 x 4 monolayers of drift tubes for the inner and 2 x 3 monolayers for the middle and outer stations. The tubes are arranged in multilayers of three or four monolayers, respectively, on either side of a rigid support structure. The construction of prototypes has demonstrated that they can be built with the required mechanical accuracy of 30 μm. Full size prototype modules have been built and tested in the beam, showing good performance within the specifications of ATLAS.

Cathode Strip Chambers (CSC) are used in the first station of the endcap region and for pseudorapidity $|\eta| \geq 2$ to provide the finner granularity which is required to cope with the demanding rate and background conditions. The CSC are multiwire proportional chambers with cathode strip readout and with a symmetric cell in which the anode-cathode spacing is equal to the anode wire pitch. The precision coordinate is obtained by measuring the charge induced on the segmented cathode by the avalanche formed on the anode wire. The anode wire pitch is 2.54 mm and the cathode readout pitch is 5.08 mm,

and r.m.s. resolutions better than 60 μm have been measured in several prototypes. Other important characteristics are: small electron drift times (30 ns), good time resolution (7 ns), good two-track resolution and low neutron sensitivity. The CSC are arranged in 2 x 4 layers. The design uses low-mass construction materials to minimize multiple scattering and detector weight.

3.2.3.2 Trigger Chambers

The Trigger Chambers for the ATLAS muon spectrometer serve a threefold purpose:

- Bunch crossing identification, requiring a time resolution better than the LHC bunch spacing of 25 ns
- A trigger with well defined p_T cut-off in moderate magnetic fields, requiring a granularity of the order of 1 cm
- Measurement of the second coordinate in a direction orthogonal to the one measured in the precision chambers with a typical resolution of 5-10 mm.

The proposed system employs two different types of detectors, **Resistive Plate Chambers (RPC)** in the barrel ($|\eta| \leq 1.4$) and **Thin Gap Chambers (TGC)** in the endcap region. The trigger chambers cover a total area of about 3650 m^2 in the barrel and 2900 m^2 in the endcap region, each chamber containing at least two detector layers. The total number of channels is about 350000 for the barrel and 440000 in the endcaps.

The RPC is a gaseous detector providing a typical space-time resolution of 1 cm x 1 ns with digital readout. The basic RPC unit is a narrow gas gap formed by two parallel resistive bakelite plates, separated by insulating spacers. The TGC chambers are designed in a way similar to multiwire proportional chambers, with the difference that the anode wire pitch is larger than the cathode-anode distance. A trigger chamber is made from two rectangular detector layers, each one read out by two orthogonal series of pick-up strips: the 'η strips' are parallel to the MDT wires and provide the bending view of the trigger detector; the 'ϕ strips', orthogonal to the MDT wires, provide the second-coordinate measurement which is also required for the offline pattern recognition.

The TGC are similar in design to multi-wire proportional chambers, with the difference that the anode wire pitch is larger than the cathode-anode distance. Signals from the anode wires, arranged parallel to the MDT wires, provide the trigger information together with readout strips arranged orthogonal to the wires. These readout strips are also used to measure the second coordinate.

The TGC are constructed in doublets and triplets of chambers. The inner station consists of one doublet and is only used to measure the second coordinate. The seven chamber layers in the middle station are arranged in one triplet and two doublets which provide the trigger signal and the second coordinate measurements.

To form a trigger signal, several anode wires are grouped and fed to a common readout channel. The number of wires per group varies between 4 and 20 depending on the desired granularity as a function of pseudorapidity.

3.2.4 Trigger and Data Acquisition systems

The task of the ATLAS trigger/DAQ system is to select interesting physics in an efficient and controlled way, and to move the data produced by the ATLAS detector for these events to permanent storage for later analysis. Starting from an initial bunch crossing rate of 40 MHz (interaction rate of $\sim 10^9$ Hz at a luminosity of 10^{34} cm^{-2}s^{-1}), the rate of events must be reduced to $\sim$ 200 Hz for permanent storage. To meet the required event rate reduction, of about 10^7, the event selection (trigger) function of the ATLAS trigger/DAQ system is organized in three levels (see Fig. 3.11):

- The level-1 trigger (**LVL1**) accepts data at the full LHC bunch-crossing rate of 40 MHz and provides a decision for each bunch crossing. The LVL1 trigger identifies the regions in the detector where interesting features were found, the so-called Regions of Interest (RoIs). The latency of the LVL1 trigger system (that is, the time taken to collect data, from the LVL1 trigger decision and distribute it) is $\sim$ 2 μs and all detector data are held in pipeline memories during this period. The maximum accept rate of the LVL1 trigger is set to $\sim$75 KHz and is determined by the capabilities of the subdetector readout system.

- The level-2 trigger (**LVL2**) has to reduce the acceptance rate to $\sim$2 KHz. The

ROLs (ReadOut Links) transport data fragments of LVL1 accepted events from the detectors' ReadOut Drivers (ROD) to the $\sim$ 1600 ReadOut Buffers (ROB). From here, requested data fragments from selected ROBs are served to the LVL2 trigger element. All the readout buffers are subsequently informed of the LVL2 trigger decision for the event and mark the data fragments for deletion or for event building accordingly. All this is done during the LVL2 trigger processing and the Event-Builder (EB) collection time. The LVL2 architecture is based on the use of the RoIs and uses full precision information from the inner tracking detectors, as well as from the calorimeters and muon detectors. The region-of-interest builder (RoIB) builds the RoI information from the various parts of the LVL1 trigger. These RoIs are then used to seed the LVL2 algorithms. The average decision time is estimated to be $\sim$10 ms.

- The level-3 trigger or Event Filter (**EF**) performs complete event reconstruction within $\sim$ 1 s. After an event is accepted by the LVL2 trigger, all the data for that event residing in the Event Builder, is sent to an EF processor via the Sub-Farm Interfaces (SFI). More sophisticated reconstruction and trigger algorithms, tools adapted from those of the offline, and more complete and detailed calibration information are used here to effect the selection. Events selected by the EF for final archiving in preparation for offline reconstruction and primary analysis are passed to permanent storage via the final element of the data-flow system, the Sub-Farm Output (SFO). The EF system must achieve a data-storage rate of the order of 100 Mbyte/s by reducing the event rate and/or the event size. This constrains the maximum event rate, which must be approximately 200 Hz.

The DAQ system handles the distribution of data from the ROD to mass storage and the overall monitoring and control of data taking. For this reason, the system has been factorized in two major components:

- The **Data Flow** provides the functionality of receiving and buffering detector data from ROD, distributing events to the High Level Triggers (HLT), that is, LVL2 and EF, and forwarding selected events to mass storage.
- The **Online Software System** controls the overall experiment: it provides run control, configuration of the HLT and DAQ systems and manages data taking partitions.

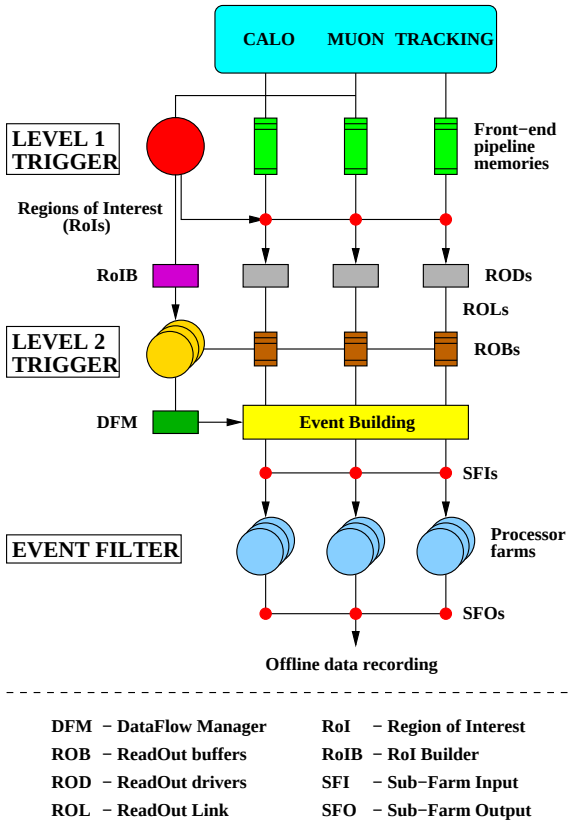

Figure 3.11: Three levels of the ATLAS trigger. Taken from [59].

The trigger system will be described in more detail in chapter 4, giving special attention to the trigger menus that are decisive for the selection of the MSSM $H^{\pm}$ signature.

3.3 Physics aspects

The physical quantities related to the overall detector performance that are relevant for the analysis presented in this thesis are: jet energy resolution, E_{Tmiss} measurement, jet energy scale, E_{Tmiss} scale, τ identification and b-tagging performance.

3.3.1 Jet energy resolution

There are several factors that play a role in the chain that goes from the initial parton produced in the hard-scattering process to the reconstructed jet in the calorimeter. Physics effects such as fragmentation, initial and final state radiation, and the co-existence of the underlying event or additional minimum-bias events are intrinsic properties of the $p-p$ collisions. On the other hand, detector effects such as different calorimeter response to charged and neutral hadrons, non-linearities, magnetic field, effects of death material, cracks between calorimeters, longitudinal leakage, lateral shower size and granularity, and electronic noise, are related to the performance of the detector, which can be optimized. All these effects play an important role when doing jet reconstruction.

In test beams, several algorithms for reconstructing the energy of pions were applied [51]. The performance of two algorithms, namely *the sampling-dependent weighting technique* [60], with weights applied to the different calorimeter compartments, and *the H1 based approach* [61], with weights applied directly to cell energies was studied. The data samples used were the fully simulated back-to-back di-jet events with quark energies E_0 equal to 20, 50, 200 and 1000 GeV at $|\eta| = 0.3$, contained in the Barrel Calorimeter. The cell electronic noise contribution to the EM calorimeter response was simulated applying the digital filtering method. The jets were reconstructed using the fixed-cone jet algorithm [62]. The jet seed threshold on the transverse energy in a tower was set to $E_s = 2$ GeV. The cone sizes used in this analysis were $\Delta R = 0.4$ and 0.7.

The energy resolutions were parametrised according to:

$$\frac{\sigma}{E} = \frac{a}{\sqrt{E}} \oplus b \tag{3.3}$$

The results obtained for the two cone sizes and the two calibration methods are given in Table 3.4 and Fig. 3.12. One can see there that the jet energy can be determined reliably without prior knowledge of jet energy at particle level using simple smooth functions to describe the energy dependence of the calibration coefficients. The results were obtained in the central barrel region, at $|\eta| = 0.3$.

	Sampling Method		H1 Method	
	Δ R=0.4	**Δ R=0.7**	**Δ R=0.4**	**Δ R=0.7**
a (% $\mathrm{GeV}^{1/2}$)	66.0 ± 1.5	61.2 ± 1.3	53.9 ± 1.3	51.5 ± 1.1
b (%)	1.2 ± 0.3	1.4 ± 0.2	1.3 ± 0.2	2.5 ± 0.2
χ^2 prob. (%)	1.6	0.8	27.3	66.7

Table 3.4: Parameter values obtained fitting the energy dependence of the jet energy resolution ($|\eta| = 0.3$). Taken from [51].

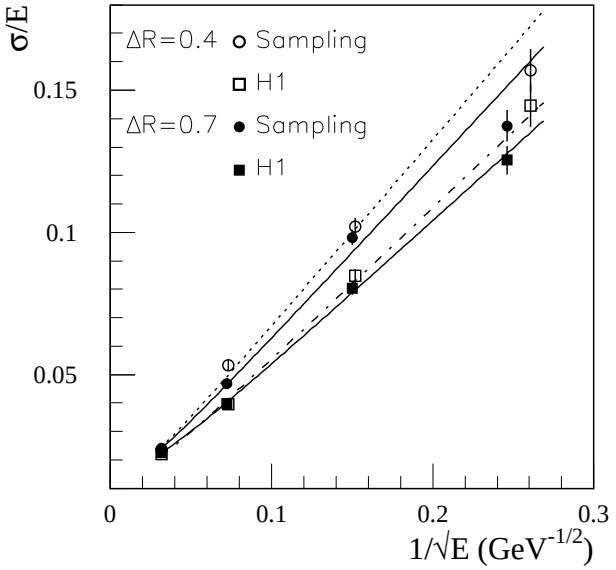

Figure 3.12: Jet energy resolutions obtained with the sampling and H1 methods for the two cone sizes: the full lines represent the fitted resolution for cone size $\Delta R = 0.7$ and the dashed lines for cone size $\Delta R = 0.4$. Taken from [51].

3.3.2 E_{Tmiss} measurement

There are two aspects that play an important role in the measurement of the missing transverse energy at the LHC. First of all, E_{Tmiss} is an important signal for new physics, for example, in the production and decay of SUSY particles such as $H^{\pm}$ in the $H^{\pm} \to \tau\nu$ channel, and of SM Higgs boson through the $H \to ZZ \to ll\nu\nu$ channel. Therefore, minimization of fake high-E_{Tmiss} tails produced by instrumental effects, such as jets badly measured in a calorimeter crack is mandatory in order to observe events characterized

by true missing transverse energy. Secondly, good E_{Tmiss} resolution is needed when reconstructing a narrow invariant mass distribution for new (heavy) particles involving neutrinos among their decay products. These two factors are closely related to the performance of the calorimeters: good energy resolution, good response, linearity and hermetic coverage are required.

The E_{Tmiss} resolution was studied in [63] with $A \to \tau\tau$ events, which have true E_{Tmiss} due to the presence of neutrinos, at low luminosity; and with minimum-bias events, which do not contain physical sources of E_{Tmiss}, at low and high luminosity.

The resolution $\sigma(p_{xy}^{miss})$ of each component of the E_{Tmiss} vector is defined as $\sigma(\Delta)$ where:

$$\Delta = \sum p_x(p_y)_{gen} - \sum p_x(p_y)_{rec} \tag{3.4}$$

The first term on the right hand side is the sum of the $x(y)$ components of the momenta of all generated particles (neutrinos and muons excluded) without any pseudorapidity restriction, and the second term is the sum of the $x(y)$ momenta as reconstructed from the calorimeters.

The dependence of $\sigma(p_{x,y}^{miss})$ on the total transverse energy measured in the calorimeters $\sum E_T$ for $A \to \tau\tau$ events at low luminosity is shown in Fig. 3.13.

The electronic noise of the EM calorimeter was also included, and a low-energy cut-off at 1.5 σ was applied to the transverse energy deposited in each cell. The resolution of the E_{Tmiss} components varies between about 5 and 10 GeV when m_A varies between 100 and 500 GeV, which allows a good mass resolution from the reconstructed $A \to \tau\tau$ spectrum.

The points shown in Fig. 3.13 can be fitted with the form:

$$\sigma(p_{xy}^{miss}) = 0.46 \cdot \sqrt{\sum E_T} \tag{3.5}$$

where E_T is expressed in GeV. This result includes the effect of both the energy resolution and the limited coverage of the detector.

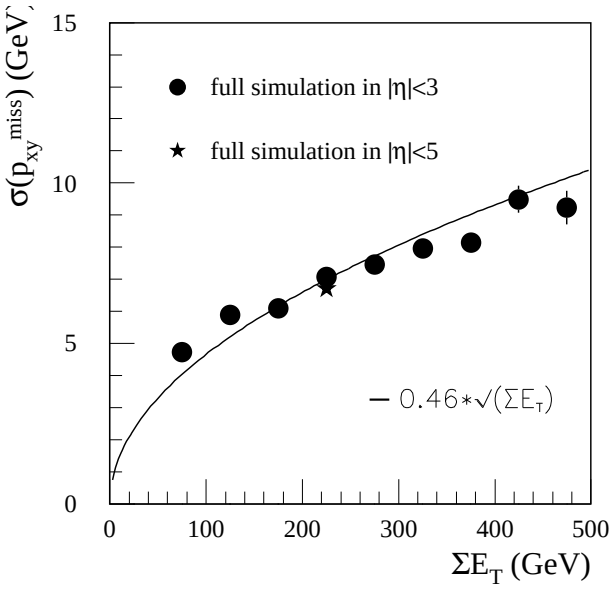

Figure 3.13: Resolution of the two components of the E_{Tmiss} vector, as a function of the total transverse energy in the calorimeters, for $A \to \tau\tau$ events with $m_A = 150$ GeV at low luminosity. Taken from [51].

3.3.3 Jet energy scale

The need for accurate experimental measurements of particle masses, such as W boson, top quark and SM Higgs, will provide overall constraints of the Standard Model an order of magnitude stronger than those available today. Moreover, if SUSY were to be discovered at the LHC, ATLAS would be able to perform a set of precision measurements of various supersymmetric particle masses [42]. Those physics goals derive to the following requirements concerning the absolute scale of energy and momentum measurements in ATLAS:

- In the case of e^- and μ^-, the scale should be known to an accuracy of $\sim$0.1%
- For hadronic jets, the scale should be known to an accuracy of $\sim$1% [2]

[2] In principle, it would be desirable to measure decays involving quarks with a similar accuracy to those involving leptons. However, it is clear that the fragmentation and hadronization of the original partons lead to uncertainties in the experimental measurements, which cannot be easily decreased below this level of 1%.

A large fraction of the ATLAS calorimeter modules will have been calibrated in beams of electrons, muons and pions, before installation into ATLAS. Moreover, *in situ* calibration of the absolute jet energy scale with data samples available at the LHC would guarantee an accurate and up-to-date inter-calibration between different modules and calorimeters:

- The very large statistics of $W \to jj$ decays from top quark decay will provide the best sample for understanding precisely the interplay between the jet energy scale and the mass scale of resonant jet-jet final states [3].
- Events containing a Z boson decaying into leptons and one high-p_T jet will be very useful to cross-check the calibration of the jet energy scale performed with $W \to jj$ decays, and will also provide constraints on the b-jet energy scale, which cannot be obtained directly from top quark decays.

It was shown in [51] that the high statistics $W \to jj$ decays reconstructed in inclusive $t\bar{t}$ events should provide an adequate tool to achieve an overall $\pm 1\%$ uncertainty on the absolute energy scale, over a range of jet transverse momenta from 50 GeV to several hundred of GeV, as it can be seen in Fig. 3.14. The lower and upper ends of this range will depend on how well residual systematic effects can be controlled with the data and the Monte Carlo simulation.

3.3.4 $\mathbf{E}_{Tmiss}$ scale

Once the absolute energy scale of the ATLAS Hadronic Calorimeter has been set to $\pm 1\%$ over the range $|\eta| < 3.2$, the knowledge of this absolute energy scale over the full pseudorapidity coverage (i.e. including forward calorimeters) is mainly of interest for physics involving an accurate measurement of the E_{Tmiss}, like in the analysis presented in this thesis.

As it was shown in [51], $Z \to \tau\tau$ events (with one leptonic τ decay and one single-prong hadronic decay) can be reconstructed rather accurately for events with $p_T^Z > 15$ GeV, since the expected mass resolution is about 9 GeV at low luminosity. For an integrated luminosity of 30 fb^{-1} (3 years at low luminosity), a sample of 3800 $Z \to \tau\tau$

[3] The W mass will be known to an accuracy of 30 MeV at the start-up of the LHC.

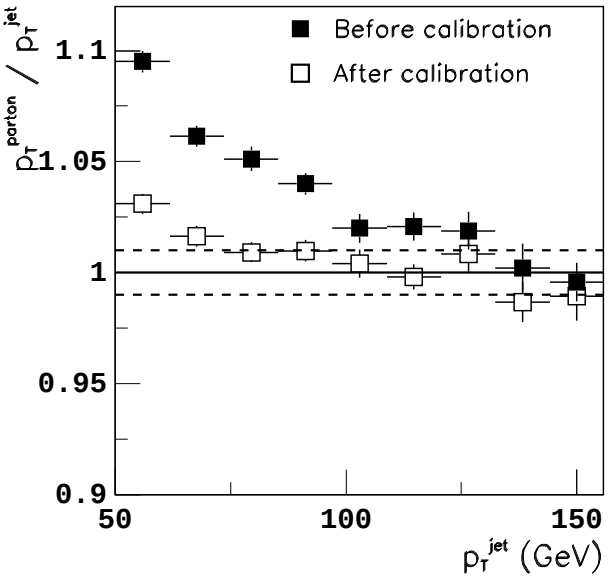

Figure 3.14: Ratio of the original parton p_T, p_T^{parton}, to the p_T of the reconstructed jet, p_T^{jet}, as a function of p_T^{jet} for $W \to jj$ decays reconstructed in inclusive $t\bar{t}$ events. The black squares correspond to the case without rescaling, whereas the open squares correspond to the result after rescaling the jet 4-vectors to obtain $m_{jj} = m_W$. The dashed horizontal lines represent the desired goal of a $\pm 1\%$ systematic uncertainty on the absolute jet energy scale. Taken from [51].

signal events is expected to be reconstructed above a total background of 200 events. This would lead to a statistical uncertainty of $\sim \pm$ 0.15 GeV on the measured Z mass, and therefore the overall error would be dominated completely by the 1% uncertainty on the absolute jet energy scale, which applies in this case to the high p_T hadronic jet from τ decay. In this study, a variation of $\pm$ 10 % of the E_{Tmiss} scale resulted in a shift of $\pm$ 2.5 % on the measured Z mass. Therefore, the E_{Tmiss} scale can be determined to $\pm$ 4% for an integrated luminosity of 30 fb^{-1}.

3.3.5 τ identification and measurement

The reconstruction and identification of all lepton species at the LHC is mandatory. Among them, tau leptons are the most difficult in that sense, since they produce neutrinos and hadrons among their decay products.

As it was already pointed out in sections 2.2.4 and 2.3.1, the heaviest Higgs bosons can

only be observed through their decays into τ leptons (e.g. $H^{\pm} \to \tau\nu$, $H/A \to \tau\tau$) over a large region of the MSSM space. Moreover, the sensitivity to this channels depend mainly on a good τ identification capability, since backgrounds from other jets are potentially very large.

The τ identification capability of ATLAS was evaluated in [64] and [65] by using fully-simulated events containing a MSSM Higgs boson A decaying into $\tau\tau$, where one of the τ decays hadronically and the other leptonically.

In this study, a jet was labeled as a τ-jet if the distance ΔR of the jet barycenter from the barycenter of the hadronic part of the τ decay (h_τ) computed at particle level, was less than 0.3. The tau jet energy was reconstructed from the calorimeter cell energies; its transverse momentum was defined as the p_T of the τ visible decay products; and the τ charge was calculated from the charge of the associated tracks: using the reconstructed tracks associated to the jet within a cone size of $\Delta R < 0.4$, the weighted jet charge was defined as the sign of $\sum_i |p_i| q_i$, where q_i is the charge of a track of momentum p_i.

Concerning the tau identification, jets from hadron τ decays and QCD jets can be distinguished by using the combined information of the calorimeters and the Inner Detector. Since hadronic τ decays are characterized by low multiplicity (in 77% of the cases only one charge track is produced), a τ-jet consists of a well collimated calorimeter cluster with a small number of associated charged tracks in the Inner Detector. According to this, three different variables were used to distinguish τ-jets from normal jets:

- R_{em}: jet radius computed using only the EM cells contained in the jet. It is defined as:

$$R_{em} = \frac{\sum_{i=1}^{n} E_T \cdot \sqrt{(\eta_i - \eta_{clus})^2 + (\phi_i - \phi_{clus})^2}}{\sum_{i=1}^{n} E_{Ti}} \tag{3.6}$$

- ΔE_T^{12}: fraction of transverse energy in the electromagnetic and hadronic calorimeters, which is contained in a region defined by $0.1 < \Delta R < 0.2$ around the cluster barycenter. This is an isolation criterion.

- N_{tr}: number of charged tracks with p_T above a given threshold (1, 2 and 5 GeV were used) pointing to the calorimeter cluster within $\Delta R = 0.3$.

It was shown in this study, that for a fixed set of selection cuts on the above listed variables, the τ identification efficiency increased with increasing p_T (from 15 to 130 GeV), and that this efficiency depends also on the pseudorapidity, being higher on the central region of acceptance.

Moreover, the jet rejection as a function of the τ identification efficiency was also studied using a selection criteria based on the variables R_{em}, ΔE_T^{12} and N_{tr} ($p_T > 2$ GeV). It was shown there that despite the τ efficiency increased with p_T, the jet rejection decreased. The total jet rejection, obtained with different p_T ranges, is shown in Fig. 3.15 as a function of the τ identification efficiency. As p_T increases, the curves shift towards larger τ efficiencies, for the same jet rejection.

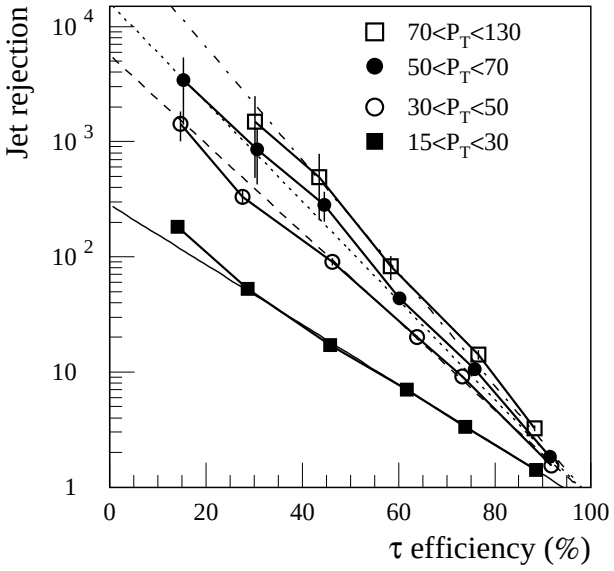

Figure 3.15: Jet rejection as a function of the τ efficiency, as obtained over the region $|\eta| < 2.5$ and in various p_T ranges. Straight-line fits are superimposed. Taken from [51].

3.3.6 *b*-tagging

Tagging the flavour of *b*-jets is very useful for the selection of events containing the top quark and SM or MSSM Higgs bosons, which couple preferentially to heavy objects.

In the study presented in [51], hadronic decays of SM Higgs were used for studies of the *b*-tagging capabilities of the Inner Detector. In particular, a comparison was done

between $H \to b\bar{b}$ and backgrounds $H \to x\bar{x}$, where x is a $u-$, $d-$, $s-$, $c-$ quark or gluon. The $H \to b\bar{b}$ decay was used as a 'factory' for producing high-p_T b-jets [4].

The following b-jet features where found:

- For both m_H = 100GeV and 400 GeV, 99% of charged particles produced from b-quark fragmentations were found to be in a cone of $\Delta R \leq 0.4$.
- The charged multiplicity of particles with $p_T > 1$ GeV in a cone of $\Delta R \leq 0.4$ was found to have a mean of 5.5 (10.0) for m_H = 100 GeV (400 GeV), 60% (40%) of which come from daughters of the B-hadron decay.

Moreover, the b-jet direction is not uniquely defined since b-quarks can radiate gluons (Final State Radiation, FSR) and therefore change direction. Thus, it is important to check the difference between the jet direction as measured by the calorimeters and the b-quark direction.

In order to tag b-quarks, the fact that b-hadrons have relatively long lifetimes ($c\tau \sim$ 470 μm) must be taken into account: b-hadron give rise to displaced vertices which may be tagged by either explicitly reconstructing the vertex or by examining the impact parameters of the daughters. Thus, the rejection of non b-jets is dependent on the fact that for light quarks, most of the stable particles which can be reconstructed in the Inner Detector come from the decay of short-lived objects, and hence appear to come from the primary vertex. This means that the impact parameter resolutions of the detector is very important in order to have a good b-tagging performance.

The rejection R_j for different background jets was compared to the ε_b for keeping b-jets with a likelihood ratio method. The results are shown in Fig. 3.16.

[4] A comparison with the performance calculated using b-jets from $t\bar{t}$ events was also made and the results were found to be the same.

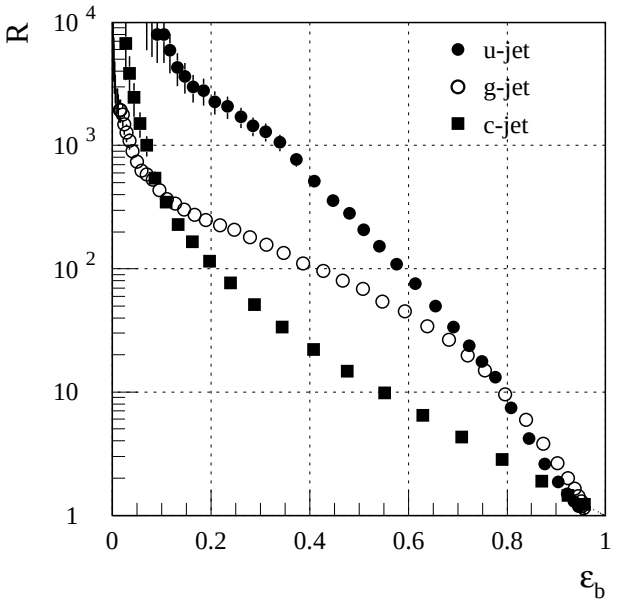

Figure 3.16: Background rejections as a function of the b-jet efficiency obtained by *xKalman* track finding algorithm [66]. Taken from [51].

Chapter 4

The ATLAS trigger system

As it was already pointed out in section 3.2.4, the high interaction rate of the LHC puts stringent requirements on the trigger and DAQ systems. The ATLAS trigger system must reduce the event rate from the bunch crossing rate of 40 MHz to around $\sim$ 200 Hz for recording onto mass storage. To achieve such challenging goals, the ATLAS trigger system is made of three levels of event selection: Level 1 trigger (LVL1), Level 2 trigger (LVL2) and Event Filter (EF).

In section 4.1, a description of the different trigger levels is presented. The trigger objects and the ATLAS trigger menus are summarized in section 4.2. Next, in section 4.3, the tau trigger in ATLAS is described in detail. Finally, in section 4.4, some aspects related to the jet+E_{Tmiss} and tau/hadr+E_{Tmiss} triggers are reviewed. Such triggers are decisive for the selection of the physics signature presented in this thesis.

4.1 Trigger system overview

Each one of the ATLAS trigger levels (LVL1, LVL2 and EF) contributes to a rate reduction of selected events consisting of data from the individual subdetectors, as it was shown in Fig. 3.11. At LVL1, special-purpose processors act on reduced-granularity data from a subset of detectors. LVL2 uses full-granularity, full-precision data from the detectors, but, for most triggers, examines only regions of the detector identified by the LVL1 trigger that contain interesting information. At the EF, the full event data are used together

with the last available calibration and alignment information to make the final selection of events to be recorded for offline analysis.

4.1.1 Level 1 trigger

The LVL1 trigger is a fast pipelined system for the selection of *interesting* physics with high efficiency. Its selectivity achieves an event rate reduction from the 40 MHz LHC bunch-crossing rate down to the first level acceptance of 75 kHz, which is the maximum rate at which the ATLAS front-end systems can accept LVL1 trigger. This is done by searching for isolated electrons and photons, hadrons, jets of particles, muons, and by calculating calorimeter global energy sums within 2.0 μs latency. This latency is taken up partly by cable delays. Hence, fast hard-wired algorithms implemented in application-specific integrated circuits (ASICs) and field programmable gate arrays (FPGAs) are required [67]. For that reason, the LVL1 trigger is also called the *hardware* trigger.

The LVL1 trigger is divided into three subsystems, the **Calorimeter Trigger**, the **Muon Trigger** and the **Central Trigger Processor (CTP)** as shown in Fig. 4.1.

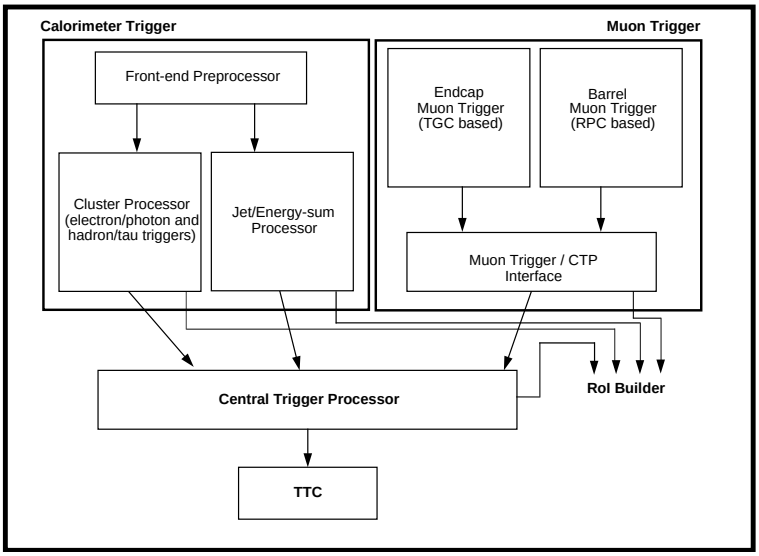

Figure 4.1: Block diagram of the LVL1 trigger system. Taken from [59].

4.1.1.1 Calorimeter Trigger

The Calorimeter Trigger gets analogue signals from trigger towers that have a typical granularity of $\Delta\eta \times \Delta\phi = 0.1 \times 0.1$. Separate tower signals are received from electromagnetic and hadronic calorimeters, corresponding to a total of $\sim$ 7200 analogue input signals that are transmitted electrically via twisted-pair cables from the detector to the LVL1 trigger electronics, located in the trigger cavern. The trigger towers are formed in the calorimeter front-end electronics by analogue summation over the corresponding calorimeter cells.

The trigger-tower signals are digitized using a dedicated ADC system. The **front-end Preprocessor** applies digital threshold to extract the transverse energy E_T for calorimeter pulses and to assign it to the correct bunch-crossing, since the shaped pulses from the calorimeters extend over several bunch-crossing periods.

The subsequent Calorimeter Trigger processing is fully digital, and is divided in two parts:

- **Cluster Processor:** it performs a search for high-p_T electrons/γ's and hadrons/τ's using the full-granularity trigger-tower information from the Preprocessor
- **Jet/Energy-sum Processor:** it searches for high-E_T jets and calculates the missing E_T (E_{Tmiss}) and total scalar-E_T values

For the electron/γ trigger, there are eight sets of thresholds that can be programmed independently; each set consists of a threshold on the E_T of the cluster, an isolation threshold on the surrounding E_T in the electromagnetic calorimeter, and a 'hadron-veto' threshold on the E_T in the associated hadron-calorimeter towers. Similarly, for the hadron/τ trigger, there are eight sets of thresholds that can be programmed independently; each set consists of a threshold on the E_T of the cluster and an isolation threshold for the surrounding E_T in the electromagnetic and hadronic calorimeters. For the jet trigger there are eight thresholds that can be programmed independently and to which the E_T in the so-called 'jet windows' is compared. The jet-window size is also programmable.

Summation is performed over the trigger towers to calculate the total scalar-E_T for the event and the E_{Tmiss} vector. Thresholding is performed, with eight threshold values for the E_{Tmiss} trigger (applied to the modulus of the E_{Tmiss} vector), and four for the scalar-E_T trigger.

The information is sent to the Central Trigger Processor for each object type and for each bunch crossing. In the case of electron/γ, hadron/τ and jet triggers, this is the multiplicity of objects for each set of thresholds. For the energy-sum triggers, information is sent indicating which thresholds have been passed.

4.1.1.2 Muon Trigger

The muon trigger receives as input the pattern of hit strips (and wire groups in the case of the TGC detectors) in the muon trigger chambers. There are a total of more than 800k input signals to the muon trigger system. The timing resolution is sufficiently good so that the trigger can, with very high probability, identify the bunch crossing that contained the muon.

The trigger searches for patterns of hits consistent with high-p_T muons originating from the interaction region. The logic provides six independently-programmable p_T thresholds. The output sent to the CTP for each bunch crossing is the multiplicity of muons for each of the six p_T thresholds.

As it can be seen in Fig. 4.1, the muon trigger system is subdivided into a part specific to the RPC detectors, a part specific to the TGC detectors, and a part that combines information from the full system and prepares the input to the CTP.

4.1.1.3 Central Trigger Processor

The role of the CTP is to combine the information for the different object types and to make the overall LVL1 accept/reject decision. *Trigger menus* can be programmed with up to 96 items, each item being a combination of requirements on the input *trigger objects* (e.g. a high-p_T muon, an isolated lepton,...). In section 4.2 the trigger menus will be discussed in detail. These requirements on the trigger objects can be very simple, demanding for example at least one muon for a given p_T threshold, or more complicated, for example requiring at least one electron above a specified p_T threshold, E_{Tmiss} above another specified threshold and no high-p_T muons. The CTP can also combine the information on jet multiplicity versus threshold to estimate the jet-E_T sum, to which it can apply a threshold.

The overall LVL1 decision will be to accept an event if any of the 96 menu items is

satisfied. This decision is distributed via Timing, Trigger and Control system (TTC) to the front-end electronics of the detector systems, which initiates the readout.

4.1.1.4 From LVL1 to LVL2

The LVL2 trigger is seeded by the Regions of Interest (RoIs) provided by the LVL1 trigger. An example of LVL1 RoI can be seen in Fig. 4.2. Every RoI includes information on the position (η and ϕ) and p_T range of candidate objects (high-p_T muons, electrons/photons, hadrons/taus, jets) and energy sums (E_{Tmiss} vector and scalar-E_T value). There are two types of RoI:

- Primary or 'trigger' RoIs are any objects found at LVL1 that have been used in accepting the event.
- Secondary or 'non-trigger' RoIs are objects from LVL1 with transverse energies too low to contribute to the trigger. They are passed to LVL2 purely as additional information about the event, and they do not contribute to the LVL1 accept/reject decision.

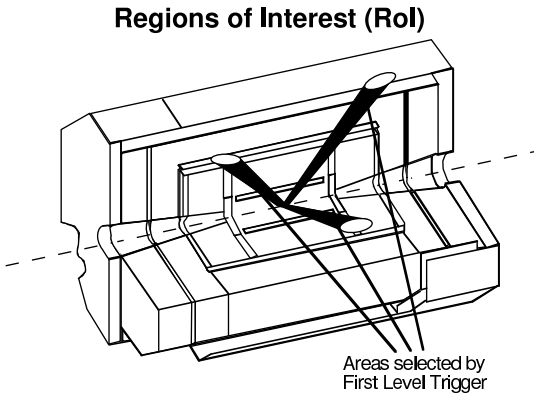

Figure 4.2: Region of Interest (RoI).

The various LVL1 fragments that constitute a RoI arrive at the RoI Builder (RoIB) within one millisecond of each other. The RoIB decides which data from each subdetector is associated with each of the RoIs. In the RoIB this event data is assembled and sent to a supervisor processor which then initializes the LVL2 processing.

4.1.2 Level 2 trigger

The LVL2 trigger provides the next stage of event selection after the hardware-based LVL1 trigger. It uses RoI guidance received from LVL1 to seed the validation and enhancement of the LVL1 trigger using selected full granularity event data.

It is assumed that the LVL2 can reduce the trigger rate by a factor of about 100 in order to reach a final acceptance of $\sim$2 KHz. This is achieved by sharpening the thresholds for inclusive triggers and performing more complex processing that is possible at LVL1. In particular, LVL2 is the first place where data from the tracking detectors are available.

Event processing at the LVL2 trigger can be decomposed into a number of broad steps:

- **Feature extraction** (FEX). It provides physics parameters for each RoI of the individual subdetectors (data collection and data preprocessing). For example, for the calorimeter, this process would take cell information and produce cluster parameters; for a tracker, the basic hit information would be converted to track or track-segment parameters.
- **Object building**. During the object building, the features for one RoI from all relevant detectors are taken and the particle parameters and possibly the particle type are returned. If the data are consistent with more than one particle type, subsequent processing performs tests with each of the possible object types.
- **Trigger type selection**. In this phase, all the objects found in the event are combined and compared with the topologies (particle types, momenta, inclusive/missing mass, etc.) expected for a menu of physics selections. Flags are set for each menu item for which a match is found.

The architecture of the LVL2 trigger system can be described in terms of four main functional blocks [59]: the Region of Interest Builder (RoIB), the LVL2 Supervisor (L2SV), the LVL2 Processing Unit (L2PU) and the LVL2 Network (L2N).

- **Region of Interest Builder (RoIB).** As it was already pointed out in section 4.1.1.4, the RoIB is the component which determines which fragments have to be analysed by LVL2 for a particular event, based on the information received from the LVL1 trigger. This component takes input from the LVL1 RODs and provide

RoI information to the LVL2 supervisors (see below). The RoIB will run at the rate of the LVL1 trigger.

- **LVL2 Supervisor (L2SV).** This is the component which, for a given event accepted by LVL1, receives the information produced by the RoIB, assigns a L2PU to process the event and sends the L2PU the information provided by the RoIB (that is, the list of ROL[1] fragments constituting the complete RoI computed by LVL1). It receives, from the L2PU, the accept/reject decision for the event. If an event is rejected, the decision is passed to the ROS[2] so that the event can be removed. If an event is accepted, the decision is forwarded to the DataFlow Manager (DFM) in order for it to supervise the transfer of the corresponding event to the Event Filter.

- **LVL2 Processing Unit (L2PU).** This component, using the information provided by the L2SV, requests event fragments from the ROS and processes the RoIs, i.e., it runs trigger algorithms in the event data belonging to the RoI, and produces an accept/reject decision for the event. The decision is passed back to the L2SV.

- **LVL2 Network (L2N).** This is the networking system used to connect all the ROSses, LVL2 processors and supervisors for the purpose of moving RoI data and LVL2 decisions between the Trigger-DAQ buffers, LVL2 processors and supervisory components. Data transport and its control share the same network.

4.1.3 Event Filter

The Event Filter (EF) is the third and last step of the online selection chain. It makes use of the full event information and it will use the offline framework ATHENA (see section 5.1 for a detailed description) to execute filtering algorithms which will be taken from the offline suite. The functionality of the EF has been logically distributed between two main entities:

- **Event Handler (EH)**. It is in charge of performing the activities related to the event selection. This includes the dataflow between the main DAQ system and the

[1]The ROLs (ReadOut Links) are the communication links from the detector buffers (RODs) to the Trigger-DAQ buffers (ROBs) as it was shown in Fig. 3.11. Each ROD may have one or more ROLs; each ROL corresponds to one event fragment.

[2]The ROS (ReadOut System) is the component for serving, out of the ROB buffers, data to the LVL2 and event builder.

EF as well as between the different steps of the selection itself. It also includes the framework to run the Processing Tasks (PT).

- **EF Supervisor**. The EF Supervisor is in charge of the control operations, in coordination with the overall Trigger-DAQ control system. Its responsibilities include the monitoring of the EF functionality.

The baseline Event Filter architecture is made of PCs linked by Ethernet networks. A detailed description of the architecture can be found in [68]. The EF farm is organized in independent sub-farms, each one connected to a different Sub-Farm Input (SFI). Several Sub-Farms Outputs (SFOs) can be connected to a given sub-farm. A given SFO may also be accessed by different sub-farms. Backend switches are Gigabit Ethernet, while the sub-farm switch are Fast Ethernet.

The processing of events is decomposed into steps which can be configured dynamically. Each step provides a basic function: event input or output, event sorting, event duplication, internal processing (e.q. for monitoring purposes), external processing, etc. The different stages of the processing chain are implemented by *tasks*. Examples are tasks providing the interface with the DAQ dataflow, tasks to perform internal monitoring activity, tasks to sort events towards different data paths according to internal flags (e.g. the result of the reconstruction and selection process), etc. An example of the Event Filter Dataflow (EFD) implementation is given in Fig. 4.3. There, an *Input Task* makes the interface with the main dataflow system. Events are counted in an *Internal Monitoring Task*. The *External PT Task* provides the interface for synchronization and communication with PTs in charge of performing the selection. Events which have not been marked as rejected by the PT are then duplicated. In one path, events are counted and passed to *Output Tasks* to be sent to permanent storage. In the other path, events are made available to different monitoring tasks according to the tag they received during the selection in the PT.

4.2 ATLAS trigger menus

The Trigger Performance and the Physics working groups of the ATLAS Collaboration wrote a very simple set of menus that covers the vast majority of main stream 'discovery'

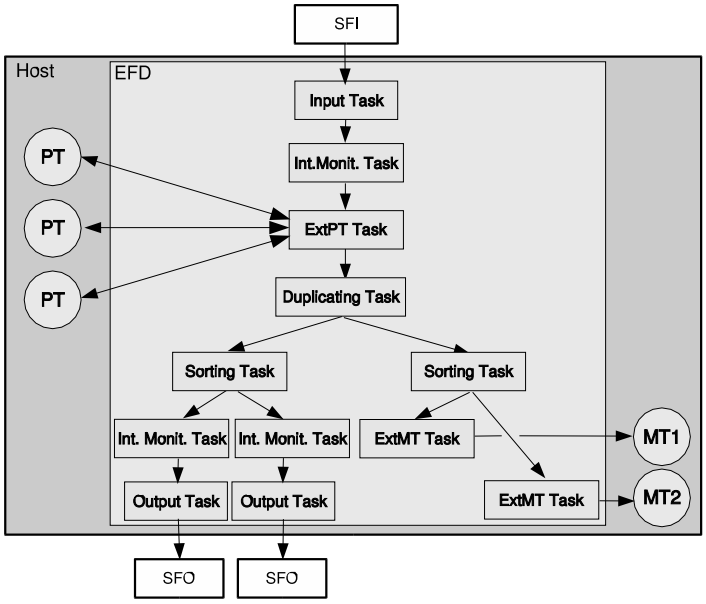

Figure 4.3: An example of an Event Filter Dataflow implementation. Taken from [59].

physics [59, 69]. These physics-oriented trigger menus are determined by the best compromise between efficiency for physics channels and tolerable trigger rates. Nevertheless, it is clear that trigger menus will continue to evolve up to and during the experiment.

4.2.1 Trigger objects

At LVL2 trigger, each RoI is examined in the detector system from which it is originated, i.e. in the muon or calorimeter system, to see if it is confirmed as a valid object. In parallel or after the confirmation of the LVL1 RoI, additional features may be searched for in other detectors, such as the SCT/Pixel and TRT. The information from all systems is then combined to form more precise global trigger objects, which become candidates for muons, electrons, photons, taus and jets, as well as generalized missing-E_T and B-physics objects.

4.2.1.1 LVL1 objects

LVL1 objects are inclusive, with a small number of attributes and a set of discrete threshold values. They are listed in Table 4.1 with the corresponding η coverage.

Object	Isolation	η range	Description
MU	no	2.4	muon
EM	yes	2.5	e.m. cluster
T	yes	2.5	$\tau \rightarrow$ hadrons or single hadron
J	no	3.2	jet
XE	-	4.9	missing-E_T
SE	-	4.9	total scalar E_T

Table 4.1: LVL1 trigger objects and their attributes in addition to E_T.

The LVL1 trigger ensures that trigger objects of the same type are not double counted. However, overlaps between different trigger categories are not resolved at LVL1. For example, an energetic electron may pass simultaneously as an e.m. cluster, a tau and a jet trigger. These overlaps will be taken into account in the global decision at LVL2.

4.2.1.2 LVL2 objects

In Table 4.2 the LVL2 trigger objects are listed. They have threshold and isolation attributes as in LVL1 but the complete list of characteristics attached to each trigger object is much richer than at LVL1. For example, the e.m. cluster is described by its transverse energy in several windows, by its lateral and longitudinal shape and by several parameters than characterize the fine-grained information in the e.m. pre-shower compartment.

The local objects are combined to form global objects, e.g. the calorimeter information is combined with the information from the inner detector and the quantities that characterize the quality of matching between track and cluster.

Object	Attribute	η range	Candidate for
μ	isolation	2.4	muon
e	isolation	2.5	electron
γ	isolation	2.5	photon
τ	isolation	2.5	$\tau \rightarrow$ hadrons
h	isolation	2.5	single hadron
j	b-tag ($\|\eta\|$ <2.5)	3.2	jet
xE	-	4.9	missing-E_T

Table 4.2: LVL2 trigger objects.

4.2.2 Trigger menus

Trigger menus have been derived from the ATLAS physics requirements. They classify the physics signatures such that a combination of trigger objects is sufficient to select events. Thresholds and attributes for the trigger objects are optimized to meet the requirement of high efficiencies and acceptable rates. These menus will evolve during the lifetime of the experiment, with improved understanding of the detector, development of technology and shifting physics interests.

The notation used in the menus is summarized in Fig. 4.4. LVL1 trigger objects are shown in capital letters. The E_T threshold and the requirement of isolation are indicated after the object code. The thresholds are generally given at the point where the LVL1 (LVL2) algorithms are 95% (90%) efficient. Exceptions include the E_{Tmiss} trigger, where the actual cut is given, and the muon triggers which are given at ~90% efficiency for LVL1. Besides, the isolation thresholds will change with the p_T of the trigger object, becoming more loose for higher p_T candidates and being completely removed at very high p_T.

4.2.2.1 LVL1 menus

The LVL1 trigger menus at low luminosity and high luminosity are summarized in Table 4.3. The first (second) column show the expected trigger rates in kHz at low luminosity operation, $\mathcal{L} = 1 \cdot 10^{33}\text{cm}^{-2}\text{s}^{-1}$ ($\mathcal{L} = 2 \cdot 10^{33}\text{cm}^{-2}\text{s}^{-1}$), whereas the last column give the

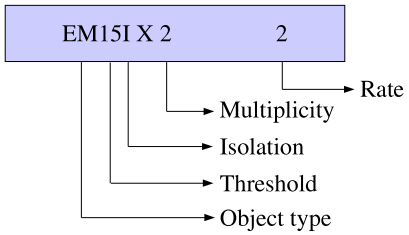

Figure 4.4: Notation used in the menus.

expected trigger rates at high luminosity ($\mathcal{L} = 1 \cdot 10^{34}\text{cm}^{-2}\text{s}^{-1}$).

Selection	**Rate (kHz) at** $\mathbf{1 \cdot 10^{33} cm^{-2} s^{-1}}$	**Rate (kHz) at** $\mathbf{2 \cdot 10^{33} cm^{-2} s^{-1}}$	**Rate (kHz) at** $\mathbf{10^{34} cm^{-2} s^{-1}}$
MU6 (8/20)	23.0	19.0	4.0
2MU6		0.2	1.0
EM20I (25/30)	11.0	12.0	22.0
2EM15I (15/20)	2.0	4.0	5.0
J180 (200/290)	0.2	0.2	0.2
3J75 (90/130)	0.2	0.2	0.2
4J55 (65/90)	0.2	0.2	0.2
J50+xE50 (60+60/100+100)	0.4	0.4	0.5
TAU20+xE30 (25+30/60+60)	2.0	2.0	1.0
MU10+EM15I		0.1	0.4
Others	5.0	5.0	5.0
Total	**∼44**	**∼43**	**∼40**

Table 4.3: LVL1 trigger menus. First column, thresholds in GeV at $\mathcal{L} = 1{\cdot}10^{33}\text{cm}^{-2}\text{s}^{-1}$ and in parenthesis, thresholds at $\mathcal{L} = 2 \cdot 10^{33}\text{cm}^{-2}\text{s}^{-1}$ and $\mathcal{L} = 10^{34}\text{cm}^{-2}\text{s}^{-1}$ respectively. In second, third and fourth columns, the trigger rates in kHz are given for each luminosity. Data taken from [70].

The MU6 trigger selects events for B-physics studies, however, higher p_T muons relevant for other physics studies are also included in this. The threshold for the two EM object trigger (2EM15I) is set as low as possible to maximize for $H \to \gamma\gamma$ and $Z \to ee$ decays. The thresholds of the multijet triggers are chosen to give acceptable rates for LVL2 and to make more room for other triggers. On the other hand, the J50+xE50 and

the TAU20+xE30 triggers are intended to provide efficient inclusive triggers for SUSY production (such as charged Higgs, $H^{\pm} \to \tau\nu$, studied in this thesis) and also for calibration via $W^{\pm} \to \tau\nu$ and $Z \to \tau\tau$. The table entry 'others' indicates the rate budget which is reserved for specialized, monitoring and calibration triggers.

As it can be seen in Table 4.3, the two LVL1 dominating triggers are the MU6 and the EM20I. The first one has such a low threshold in order to trigger on low energy μ produced in B hadron decays. The EM20I trigger has also a considerable rate due to the fake electrons from misidentified jets. This rate is substantially reduced when asking from two isolated electromagnetic clusters instead of one, 2EM15I.

The high luminosity menu contains mostly the same objects as the low luminosity menu but with higher thresholds. An additional trigger at high luminosity is MU10+EM15I to select, for example $H \to 4l$ events.

4.2.2.2 High Level Trigger menus

The High Level Trigger (HLT) menus, that is, LVL2+EF, have been chosen in order to optimize the physics performance (signal efficiency and background rejection) and the system performance (CPU execution time and data volume). The HLT menus are given in Table 4.4. The second column gives the thresholds at $\mathcal{L} = 2 \cdot 10^{33}\text{cm}^{-2}\text{s}^{-1}$ while the third column gives the thresholds at high luminosity operation. Compared to low luminosity, high luminosity thresholds have generally been raised and the requirement of isolation has been added to the muon trigger.

In Table 4.5, the same HLT menus are given with its expected rate to storage at $\mathcal{L} = 2 \cdot 10^{33}\text{cm}^{-2}\text{s}^{-1}$. It is worth noticing here that there is no 'safety factor' since the total trigger rate at this luminosity is about 200 Hz, which is approximately the maximum acceptance rate after the EF selection.

4.3 The tau trigger

The tau trigger is of capital importance for the selection of Standard Model processes such as $pp \to W^{\pm} \to \tau\nu$ ($\sigma \sim 19$ nb) and $pp \to Z \to \tau\tau$ ($\sigma \sim 3$ nb). The overall tau production rate from these sources is of the order of 10 Hz at low luminosity. Moreover,

Selection	$2 \cdot 10^{33} cm^{-2} s^{-1}$	$10^{34} cm^{-2} s^{-1}$
Electron	e25i, 2e15i	e30i, 2e20i
Photon	γ60i, 2γ20i	γ60i, 2γ20i
Muon	μ20, 2μ10	μ20i, 2μ10
Jets	j400, 3j165, 4j110	j590, 3j260, 4j150
Jet & E_{Tmiss}	j70xe70	j100xe100
Tau & E_{Tmiss}	t35xe45	t60xe60
Muon & Electron	μ10e15i	μ10e15i
B-physics	2μ6 with $m_B/m_{J/\Psi}$	2μ6 with m_B

Table 4.4: HLT menus. The second column contains the thresholds in GeV at $\mathcal{L} = 2 \cdot 10^{33}$cm^{-2}s^{-1}, and the third one, the thresholds at high luminosity operation. Data taken from [70].

Selection	Rate (Hz) to storage at $2 \cdot 10^{33} cm^{-2} s^{-1}$	Physics motivations (examples)
e25i, 2e15i μ20i, 2μ10	$\sim$40 (55% $W/b/c \rightarrow eX$) $\sim$40 (85% $W/b/c \rightarrow \mu X$)	Low-mass Higgs (ttH, $H \rightarrow 4l$, $qq\tau\tau$) W, Z, top, New Physics?
γ60i, 2γ20i	$\sim$40 (57% prompt γ)	$H \rightarrow \gamma\gamma$, New Physics (e.g. $X \rightarrow \gamma yy$ with $m_X \sim 500$ GeV)?
j400, 3j165, 4j110	$\sim$25	Overlap with Tevatron for new $X \rightarrow jj$ in danger...
j70xe70	$\sim$20	SUSY: $\sim$ 400 GeV squarks/gluinos MSSM $H^{\pm}$ (e.g. $H^{\pm} \rightarrow \tau\nu$)
t35xe45	$\sim$5	MSSM Higgs (e.g. $H^{\pm} \rightarrow \tau\nu$), New Physics (3rd family!), more difficult at high $\mathcal{L}$
2μ6+(m_B)	$\sim$10	Rare decays $B \rightarrow \mu\mu X$
Others	$\sim$20	Only 10% of total
Total	**$\sim$200**	**No safety factor included.** **"Signal" (W, γ, etc): $\sim$ 100 Hz**

Table 4.5: HLT output to storage at $\mathcal{L} = 2 \cdot 10^{33}$cm^{-2}s^{-1}. Data taken from [71].

the tau lepton will also play a key role in the search for new physics. For example, in the MSSM, the heavy scalar H and the pseudoescalar A Higgs bosons decays into tau lepton pairs are enhanced with respect to the Standard Model Higgs boson as it was pointed out in section 2.2.4. In addition, the $H^{\pm} \rightarrow \tau\nu$ is also a key decay channel for the charged Higgs boson.

The identification of the hadronic tau lepton decays is based on the selection of narrow isolated jets with low multiplicity in the tracking system. The shower isolation and shape are calculated for both the EM and hadronic calorimeters separately. The fraction of energy deposited by the tau jet in the EM calorimeter has a mean value around 60%. The hadronic shower is broader in the hadronic calorimeter than in the EM one. Therefore, the jet information obtained from the EM calorimeter is more selective than that from the hadronic calorimeter.

4.3.1 LVL1 tau trigger

There are three main reasons which motivate a LVL1 tau calorimeter trigger [59]:

- A LVL1 tau trigger could improve the efficiency for triggering on $Z \rightarrow \tau\tau$ or on low mass $A/H \rightarrow \tau\tau$ decays, in coincidence with an electron or muon trigger.
- It could provide a trigger on $A/H \rightarrow \tau\tau$, Z $\rightarrow \tau\tau$, $W^{\pm} \rightarrow \tau\nu$ and $H^{\pm} \rightarrow \tau\nu$ processes in coincidence with missing transverse energy E_{Tmiss}.
- Using the measured momentum from the tracking system, it could be used to select high-E_T hadronic tau decays for calibration of the hadron calorimeter.

Moreover, for the first two points, narrow tau jets containing 1 or 3 associated tracks in the Inner Detector give rise to narrow isolated energy depositions in the calorimetry.

The LVL1 tau/hadron calorimeter trigger is based on a 4×4 array of *trigger towers* in the electromagnetic and hadronic calorimetry (within the region $|\eta| < 2.5$) where the granularity of each trigger tower in $\Delta\eta \times \Delta\phi$ is 0.1×0.1. A core E_T is defined in the trigger algorithms as the sum of the electromagnetic and hadronic E_T in a 2×2 trigger tower [69, 72] as shown schematically in Fig. 4.5. The trigger algorithm is based on four

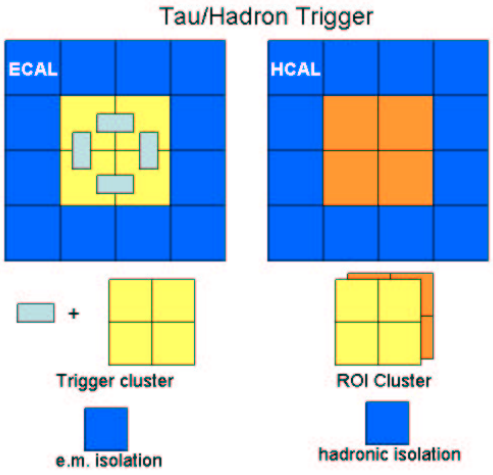

Figure 4.5: A schematic view of the tau/hadron LVL1 trigger algorithms. Taken from [59].

elements: the trigger cluster(s), an EM isolation region[3], a hadronic isolation[4] region and a RoI cluster. The requirements for a window to be accepted as containing a valid trigger object are:

- At least one of the four $(1 \times 2$ / $2 \times 1)$ trigger clusters passes a certain EM cluster threshold.
- The trigger cluster formed from 2×2 hadronic towers pass a certain hadronic cluster threshold.
- The 2×2 RoI cluster is a local E_T maximum, i.e. more energetic than the 8 neighbouring clusters of the same type contained in the 4×4 trigger window.

The signal selection is tuned using $Z \rightarrow \tau\tau$ events whereas the background selection is performed using fully simulated dijet events.

[3]The total E_T in the EM isolation region is less than the 12-tower EM "ring" isolation threshold.

[4]The total E_T in the hadronic isolation region is less than the 12-tower hadronic "ring" isolation threshold.

4.3.2 HLT tau

The LVL2 tau trigger involves the verification of the LVL1 decision and tau identification using parameters that describe the shower shape and the isolation of the narrow jet. Additional rejection of background jets can be achieved by using the information from tracks associated to the tau RoI.

The LVL2 algorithm is applied to LVL1 tau RoIs. The first part of the LVL2 algorithm is the confirmation of the LVL1 decision. In order to do this, the before described LVL1 algorithm is executed except that fine grained cell information is used and no threshold is applied to the trigger towers.

The next step in the LVL2 is to look at core energy and isolation. Isolation windows and thresholds are defined separately for the EM and the hadronic parts.

Afterwards, the LVL2 algorithm selects tracks within a window of $\Delta\eta \times \Delta\phi = 0.4 \times 0.4$ centered at the tau cluster. Only tracks above a certain p_T threshold are used. Exactly one track or one to three tracks within the window are required.

At the Event Filter stage, one has access to the complete and calibrated event for the first time. Thus, it is possible to refine the LVL2 decision. The EF decision will be based on the existing offline studies of tau/hadron identification and jet rejection. One of this studies was already presented in section 3.3.5 where the results presented in [64] and [65] were summarized.

A method of improving the signal acceptance for final states involving taus as well as retaining an acceptable trigger rate is combining a tau trigger with an E_{Tmiss} trigger. The combined tau/hadr+E_{Tmiss} trigger is going to be described in the next section.

4.4 Jet+E_{Tmiss} and tau/hadr+E_{Tmiss} triggers

The jet+E_{Tmiss} and tau/hadr+E_{Tmiss} menus are appropriate to select the MSSM charged Higgs boson studied in this thesis[5]. The production and decay modes exploited in this analysis are shown in Fig. 4.6. The topology of the event include a τ jet, two b jets, two light jets from W decay and large E_{Tmiss}.

In the next sections, the performance studies on these triggers are briefly presented.

[5] More details about this signature are going to be extensively explained in the forthcoming chapters.

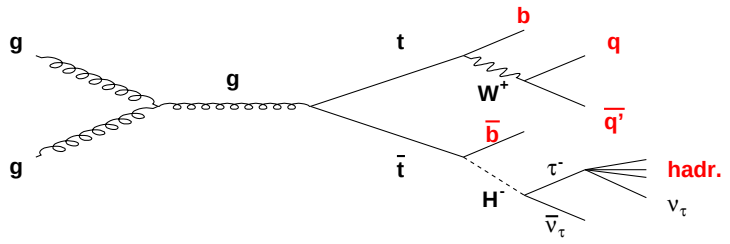

Figure 4.6: Feynman diagram of the MSSM $H^{\pm}$ ($m_{H^{\pm}} < m_{top}$) production and decay studied in this thesis.

4.4.1 Jet+E_{Tmiss} trigger

This trigger is an example of a trigger based on the combination of a global variable (E_{Tmiss}) and localized RoIs in the detector. The bulk of the trigger rate will result from fluctuations in the energy measurements of QCD jets, partly as a result of the presence of large amounts of material in front of the calorimeters at the interface regions between different elements of the calorimetry. The main instrumental effects arise from the difference in response between the various calorimeter technologies used, from the fact that the electromagnetic calorimeter is highly non-compensating and from the electronic noise and the minimum bias events.

The EF will reduce the LVL1 E_{Tmiss} trigger rate due to three reasons:

- Accurate calorimeter calibration and inter-calibration.
- Use of different calibration for low-energy calorimeter cells and for cells outside clusters.
- Accurate tunning of the cell E_T cutoff applied to suppress the noise contribution.

In the study presented in [73], a first estimate of the jet+E_{Tmiss} trigger rates was done at the Event Filter level for the low luminosity operation. In order to do so, QCD dijet events were generated with Pythia 5.7 [74]. In such events, the whole missing transverse energy is due to instrumental effects (except a negligible contribution due to neutrinos produced in b, c or μ decay). A comparison between the results obtained with a modified version of ATLFAST[6] (this modified version included a parametrisation of the calorimeter

[6]The ATLFAST simulation program is going to be described in section 5.3.

response and resolution functions determined with the full ATLAS GEANT simulation [76]) and the results obtained with GEANT full simulation showed a good agreement in the $|\eta| < 3$ region. Therefore, that modified version of ATLFAST was used to construct the tables of expected rates at the EF level for different *software* thresholds on the jet p_T and on the E_{Tmiss} (the thresholds computed with the ATLFAST program were referred as software thresholds). In Table 4.6, the rates at the three trigger levels are shown for four values of the software E_{Tmiss} threshold and two different software jet thresholds. For a p_T jet threshold of 60 GeV and a threshold on E_{Tmiss} of 60 GeV, the EF rate was $\sim$ 40 Hz with a reduction of approximately a factor of ten with respect to the LVL1 trigger with matching thresholds.

E_{Tmiss}	50 GeV jet p_T threshold			60 GeV jet p_T threshold		
(GeV)	LVL1	LVL2	EF	LVL1	LVL2	EF
40	40400	6450	400	21000	4000	260
50	4190	1450	140	2550	1050	90
60	600	390	50	430	290	40
70	150	120	15	130	90	15

Table 4.6: Rates of a jet+E_{Tmiss} trigger in Hz for software jet E_T thresholds of 50 GeV and 60 GeV, showing the three trigger levels. For the low luminosity case shown, on average 2.3 minimum-bias events have been superimposed. Data taken from [73].

Finally, it was verified that such thresholds were adequate for the study of Supersymmetry in those channels with a jet+E_{Tmiss} signature.

4.4.2 Tau/hadr+E$_{Tmiss}$ trigger

The tau/hadr combined with the E_{Tmiss} trigger will be used to select several physics processes such as SUSY searches like $H^{\pm} \rightarrow \tau\nu$ decays. A first estimation of this global trigger rate at the EF level was presented in [77].

The proposed trigger menus at the time of writing the note in [77] were T20+XE30 at LVL1 and t20xe30 at the Event Filter for the low luminosity phase. Those triggers correspond to events with at least one reconstructed τ-jet which transverse momentum is greater than 20 GeV and with a measured E_{Tmiss} greater than 30 GeV.

Since both tau/hadr and E_{Tmiss} triggers will be dominated by QCD events, in the study presented in [77], dijet events generated with Pythia 6.122 [74] were used to evaluate the rate.

The EF efficiency was estimated with the physics channel $pp \rightarrow W+(\text{jet})+X$ followed by $W^{\pm} \rightarrow \tau^{\pm}\nu_{\tau}$ and $\tau^{\pm} \rightarrow h^{\pm}\nu_{\tau}$ (with $h^{\pm}$ either a $\pi^{\pm}$ or a $K^{\pm}$). The $\tau^{\pm}$ decay was performed with the TAUOLA 2.6 package [78].

The detector response was simulated with ATLFAST 2.20. Calorimetric clusters were reconstructed with the fixed cone algorithm (radius $R = 0.4$) and resulting jets were defined if their transverse momentum was above 15 GeV in the $|\eta| < 5$ range. Besides, the E_{Tmiss} was computed on the basis of the visible energy, without any threshold on the cells transverse energy. This calculation did not take into account detector effects (as energy loss in cracks), but the resolution effects were included via gaussian smearing.

In ATLFAST, jets are labeled as τ-jets if their hadronic decays ($\tau - hadr$) satisfy the criteria: $p_T(\tau - hadr) > 10$ GeV; $\eta(\tau - hadr) < 2.5$; $p_T(\tau - hadr)/p_T(jet) > 90\%$ and $\Delta R(\tau - hadr, jet)$ <0.3. Afterwards, the miss-identification τ-jet efficiencies were parametrised with ATLFAST-B [75] (the ATLFAST-B program is going to be described in the next chapter) following the results obtained in [64], for the $A \rightarrow \tau\tau$ channel study.

The results of this study are shown in Fig. 4.7 for 50% τ-tagging efficiency. Each point in the plot represents a couple of thresholds ($p_{T\tau jet}$[7], E_{Tmiss}) in GeV. For example, for the couple of thresholds (20, 30), and a τ-jet efficiency of 50%, the resulting trigger rate is 44.9 Hz, with a signal efficiency of 4.12%. Whatever the point considered, the rate is clearly dominated by QCD events.

According to the segment slopes, the rise in the E_{Tmiss} threshold is very useful to decrease the QCD rate (for any value of the τ jet transverse momentum). On the contrary, when rising the τ jet p_T threshold a poor diminution of the QCD rate is obtained, and in addition, a substantial decrease of the signal efficiency is produced. Therefore, if the thresholds have to be increased, the most effective way is to increase the E_{Tmiss} one.

[7] At least one τ-jet above this threshold is required.

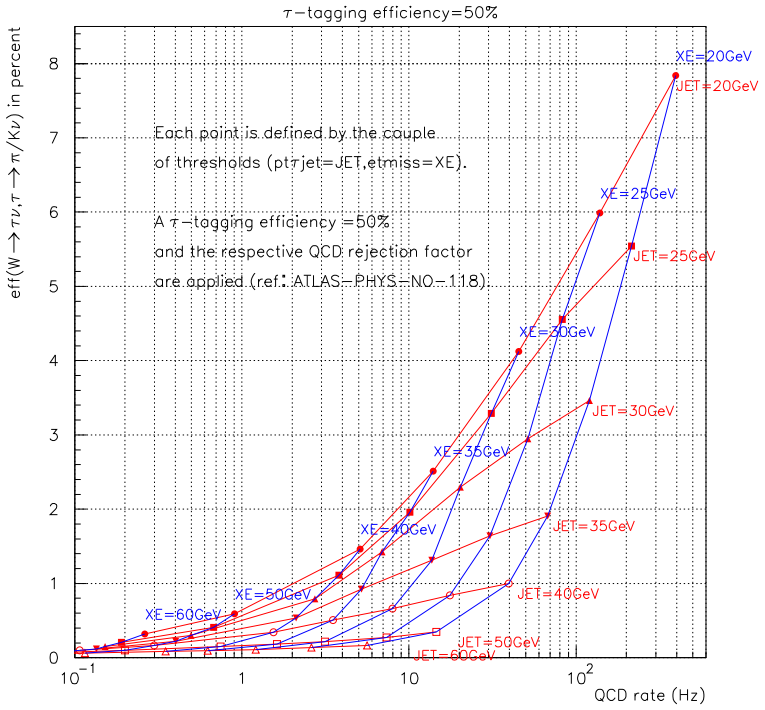

Figure 4.7: $W^{\pm} \to \tau^{\pm}\nu_{\tau}$ selection efficiency as a function of the QCD rate. Each point is defined by the couple of thresholds ($p_{T\tau jet}$, E_{Tmiss}). Each threshold value is written at the end of each line. The τ-tagging efficiency value is 50%. Taken from [77].

4.4.3 Combined performance for $H^{\pm} \to \tau\nu$

For the present thesis, the combined performance of both jet+E_{Tmiss} and tau/hadr + E_{Tmiss} triggers was studied. The multijet triggers (listed also in Table 4.4) were not suitable for our signature since they required too high thresholds for at least 3 or 4 jets.

A 600 k sample of $t\bar{t}$ signal events (for the process shown in Fig. 4.6) were generated with Pythia 6.161 and Parton Distribution Function (PDF) CTEQ5L [79]. The τ lepton decay was performed with TAUOLA 2.6 with the τ polarization switched on. The detector response was simulated with ATLFAST and the τ miss-identification was parametrised with ATLFAST-B. Moreover, a jet energy threshold of 15 GeV with a fixed cone of ΔR=0.4 was used and b-tagging efficiency was settled to 60% (c jet rejection=6.7, light-τ jet rejection=93).

In Fig. 4.8 upper plot the combined (τ+xe .OR. j60xe60) signal trigger efficiency for a MSSM $H^{\pm}$ of mass $M_{H^{\pm}}$=127.0 GeV and tan β=30 versus the τ jet energy threshold using different E_{Tmiss} thresholds is given for a τ-tagging efficiency of 30% [8] (see corresponding rejection factor in Fig. 3.15). In the lower plot, the standalone τ+xe signal trigger efficiency versus the τ jet energy threshold using different E_{Tmiss} thresholds for the same $H^{\pm}$ is represented. For the combined (τ+xe).OR.(j60xe60) trigger, the efficiency for the signal is only reduced by 1-2% when increasing the τ jet energy threshold from 20 to 40 GeV and it decreases by $\sim$1% every E_{Tmiss} threshold increase of 5 GeV. In addition, although the τ+xe trigger depends critically on the τ jet energy threshold (Fig. 4.8, lower plot), the $H^{\pm}$ signal considered here has no significant dependency on such trigger as it can be derived form Fig. 4.8, upper plot: using the j60xe60 trigger standalone a 48.8% efficiency for the signal can be achieved and when combining that trigger with the τ+xe one, the efficiency for the signal is only increased by less than 7%[9] (e.g. using t20xe30) depending on the E_{Tmiss} threshold.

Moreover, the trigger efficiency for the signal and the number of expected signal events for one year of running at low luminosity was computed for different $M_{H^{\pm}}$ for a τ-tagging efficiency of 50%. Results are shown in Fig. 4.9. In the upper plot the signal efficiency versus the Higgs mass is represented. One can see there that the efficiency for the signal increases with $M_{H^{\pm}}$ since the τ jets become harder. Besides, when combining both triggers (t20xe30 .OR. j60xe60), the performance is improved in a moderate way (namely a $\sim$18% increase is obtained for a $H^{\pm}$ mass of 127 GeV) since most of the τ jets produced in $H^{\pm}$ decays are quite hard due to polarization effects (the τ polarization effects will be extensively explained in section 6.3.1). Hence, those τ jets will also fulfil the j60xe60 trigger. This effect is illustrated by Fig. 4.10 which represents the E_{Tmiss} after the (t20xe30).OR.(j60xe60) trigger cut of a MSSM $H^{\pm}$ signal of mass 127 GeV and tan β =30. The greater part of the events ($E_{Tmiss} > 60$ GeV) fulfiled the (j60xe60) trigger condition (and some of these events are of the form: 1 τ jet with $p_T^{\tau\ jet}$ >60 GeV and E_{Tmiss}). The events with $E_{Tmiss} < 60$ GeV fulfiled the (t20xe30) one.

It's worth commenting here why these combined performance studies were done for the j60xe60 and t20xe30 trigger thresholds instead of the j70xe70 and t35xe45 thresholds that appear on Tables 4.4 and 4.5: when the studies for the present thesis were being

[8] The τ-tagging efficiency was set to such a low value in order to choose a difficult scenario for τ identification.

[9] However, after all selection cuts, this relative gain is much bigger.

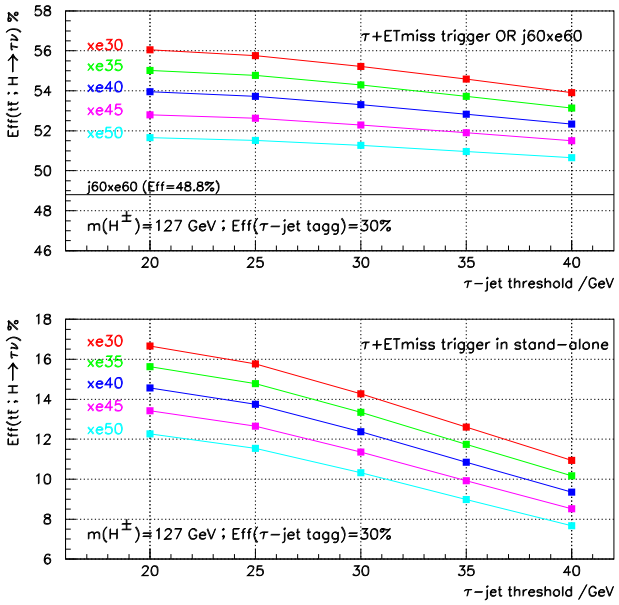

Figure 4.8: Upper plot: combined (τ+xe .OR. j60xe60) signal trigger efficiency for a MSSM $H^{\pm}$ of mass $M_{H^{\pm}}$=127.0 GeV and tan β=30 versus the τ jet energy threshold using different E_{Tmiss} thresholds. Lower plot: standalone τ+xe signal trigger efficiency versus the τ jet energy threshold using different E_{Tmiss} thresholds for the same MSSM $H^{\pm}$.

carried out, these new trigger thresholds were still not published.

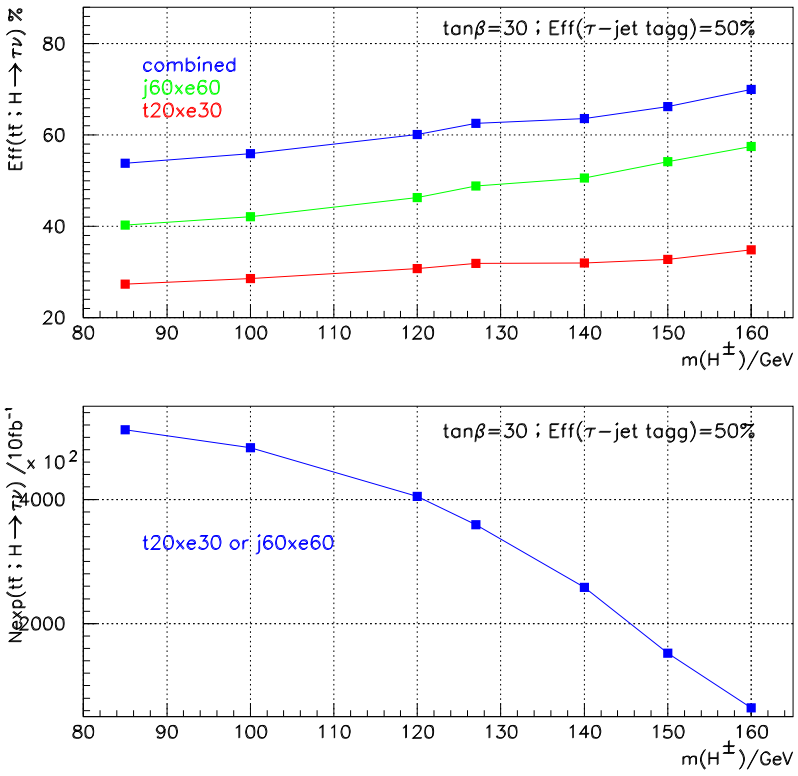

Figure 4.9: Upper plot: combined (τ+xe .OR. j60xe60) and standalone signal trigger efficiency versus $M_{H^\pm}$. Lower plot: Number of expected signal events for one year running at low luminosity ($\mathcal{L} = 1 \cdot 10^{33}\text{cm}^{-2}\text{s}^{-1}$) as a function of $M_{H^\pm}$ for the combined (τ+xe .OR. j60xe60) trigger.

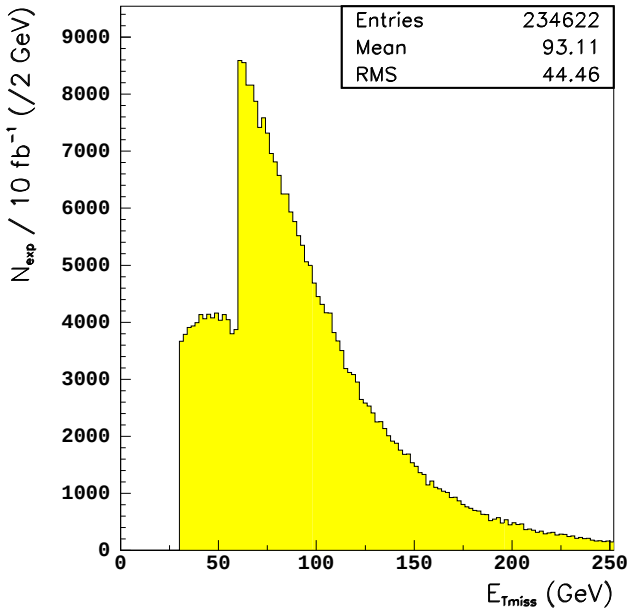

Figure 4.10: Missing transverse energy for a MSSM charged Higgs signal of mass 127 GeV and tan β =30 after (t20xe30).OR.(j60xe60) trigger condition for one year of running at low luminosity.

Chapter 5

Event simulation and reconstruction

Monte Carlo (MC) simulation techniques are widely used in High Energy Physics (HEP) in order to compare the theoretical models to the experimental results and to make studies of the potential of a physics experiment. Such simulations are used for generating the physics processes according to a certain theoretical framework and also for parametrising the detector response.

In this chapter, the tools used for generating the Monte Carlo event samples for the analysis presented in this thesis are reviewed. The ATLAS offline software is exposed in section 5.1. Then, in section 5.2, the Monte Carlo event generation with the Pythia and TAUOLA packages is presented. In section 5.3, the ATHENA-Atlfast fast simulation program is described together with the AtlfastB Algorithm for jet calibration and mis-tagging. Finally, in section 5.4, the AtlfastAnalysis package is briefly summarized.

5.1 ATLAS offline software

The ATLAS offline software is composed by a set of Monte Carlo programs for event simulation and reconstruction written in C++ within the so-called ATHENA framework [80]. Here below the ATHENA framework is described. Afterwards, a summary of the ATLAS offline software organization is given.

5.1.1 ATHENA framework

In Object Oriented programming, a **framework** is an *architectural pattern* made of a set of cooperating classes that make up a reusable design for a specific class of software [81]. That is, a skeleton of an application into which developers plug in their code and provides most of the common functionality. In HEP experiments, a framework can be used to develop all kinds of event data processing applications running in the various processing environments. Examples include the high level triggers that acquire their data directly from the online system, the event simulation software that runs over offline data in a batch environment and the event visualization software which is used interactively.

In that sense, ATHENA is a framework written in C++ that is the specific implementation for ATLAS of an underlying architecture, the GAUDI architecture [82] originally developed by the LHCb experiment. The GAUDI project is today an open project for providing the necessary interfaces and services for building HEP experiment frameworks in the domain of event data processing applications.

In Fig. 5.1, the ATHENA-GAUDI object diagram is shown. The most important ATHENA components are:

- **Algorithm**: building block of user applications, visible and controlled by the framework. Inherits from the framework Algorithm abstract class and implements three methods for invocation by the framework: `initialize()`, `execute()` and `finalize()`. The `execute()` method is called once per physics event.
- **Data Object**: they are produced/accessed by Algorithms, acting as their input and output. E.g. a Collection containing Cluster objects is a Data Object.
- **Transient Data Store**(s) (TDS): central service and repository for data objects. Thus, an Algorithm will locate input information from a TDS, and write out newly generated information derived from its processing into the TDS again, where it can be later retrieved by downstream Algorithms. Examples of TDS are: Event Data Store, Detector Data Store, Histogram Data Store and Ntuple Data Store.
- **Services**: globally available software components providing specific framework capabilities, e.g. Histogram Service, Persistency Service, jobOptions Service. The different persistency services provide the functionality needed to populate the Transient Data Stores from persistent data and vice versa.

- **Data Converter**: it provides explicit/implicit conversion from/to persistent data format to/from transient data. A Converter, with a common interface, is called whenever an object needs to be created in another representation.

- **Properties**: control and data parameters for Algorithms and Services. They allow for run-time configuration and they are specified via a startup text file, *jobOptions* file, or Python script.

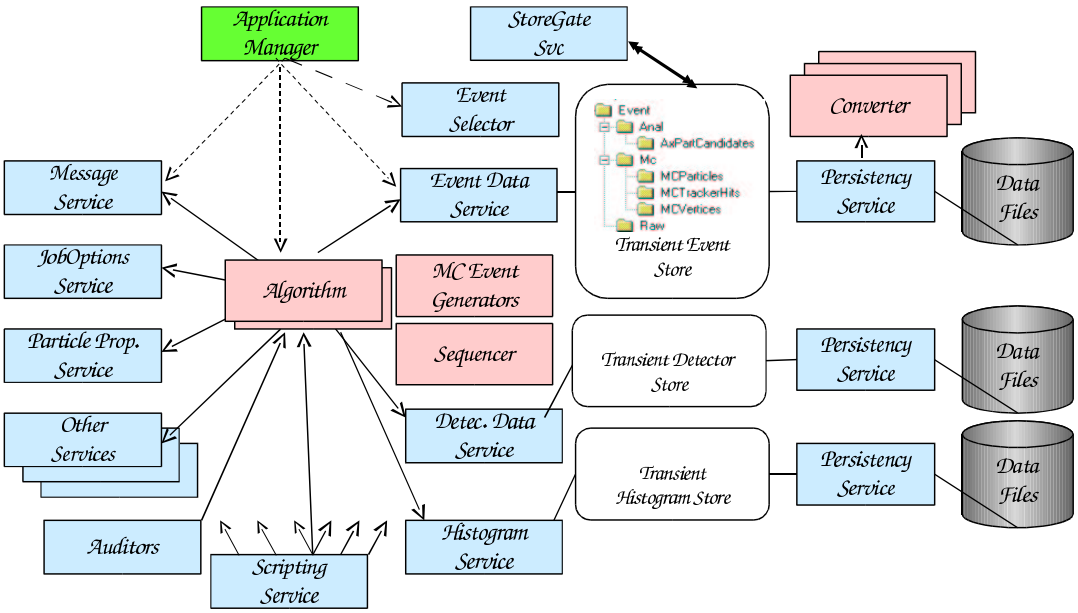

Figure 5.1: ATHENA-GAUDI object diagram.Taken from [83].

Last but not least, the ATLAS High Level Trigger will base its event selection software on the offline reconstruction framework ATHENA. In [84], a first evaluation of the suitability of ATHENA in the Event Filter is presented.

5.1.2 ATLAS offline software organization

The ATLAS offline software is grouped into different packages. A package is a set of Algorithms and classes that carry out a common application: for example, the GeneratorModules package is composed by the Algorithms that interface the different Monte Carlo event generators like Pythia, Tauola and Herwig. All these packages are embedded

within the ATHENA framework that provides the needed services and utilities in order to run each application. In each package, the Data Objects are distinguished from the Algorithm Objects. For example, *hits* and *tracks* may be considered as Data Objects, and the Algorithms to manipulate these Data Objects will be encapsulated in different objects such as *TrackFinder*. The methods in the Data Objects will be limited to manipulations of internal data members. The Algorithms will, in general, process Data Objects of some type and produce new Data Objects of another type. For example, the *TrackFinder* Algorithm will produce *track* Data Objects from *hit* Data Objects.

The ATLAS offline software is organized in releases, that is, when substantial modifications are done to the packages, a new release is constituted. All releases are kept in the ATLAS CVS (Concurrent Versions System) [85] repository.

Moreover, a Configuration Management Tool (CMT) [86] is used to build (compile and link) and run the software.

For the analysis presented in this thesis, several packages were employed, within the **ATLAS release 3.1.0**. First of all, the GeneratorModules package contains the C++ code that interfaces with the different MC generators. PythiaModule and TauolaModule were used, the later specifically developed for this thesis. They are ATHENA Algorithms that interface to the Fortran Pythia [74] and TAUOLA [78] MC generators. They will be described in more detail in the next section.

On the other hand, the ATHENA-Atlfast [87] simulation package was used for fast event simulation and is going to be reviewed in section 5.3.

5.2 Monte Carlo event generators

Event generators simulate the scattering processes in high energy physics. Such processes can be complex and large programs are needed to simulate the large variety of interactions. In the following subsections, the Pythia and TAUOLA MC generators used for the analysis presented in this thesis are summarized.

5.2.1 Pythia

Pythia, written in Fortran, is one of the most general event generators, since it includes a large number of scattering processes. The program can simulate the collisions of ee, pp, $p\bar{p}$ and ep. From the version 6.1 on, the original Pythia and Jetset programs have merged and a supersymmetric extension [88] has been included. For this thesis, **Pythia version 6.161** was used. Together they contain theory and models for a number of physics aspects, including hard and soft interactions, parton distributions, initial and final state parton showers, multiple interactions, fragmentation and decay.

5.2.1.1 PythiaModule

In order to run Pythia within the ATHENA framework, one makes use of the PythiaModule Algorithm of the GeneratorModules package (version **GeneratorModules-01-02-08** was used). PythiaModule is an interface to the Fortran Pythia code. The PythiaModule Algorithm runs Pythia from within ATHENA and puts the generated events in the Transient Data Store so they can be used later by other Algorithms like TauolaModule or Atlfast. The Pythia parameters are set from the jobOptions Service via a text jobOptions.txt file.

5.2.1.2 MSSM in Pythia

Pythia simulates the Minimal Supersymmetric Standard Model based on an effective Lagrangian of softly-broken SUSY with parameters defined at the weak scale, which is typically between m_Z and 1 TeV. The MSSM particle spectrum is minimal in the sense that it includes only the partners of all Standard Model particles (presently without massive neutrinos), two Higgs doublets with partners and the gravitino.

For this thesis, the MSSM in the Maximal Mixing Scenario was used. The parameters were given in Table 2.4.

Once the parameters of the softly broken SUSY Lagrangian are specified[1], the interactions are fixed, and the sparticle masses can be calculated. After Supersymmetry breaking (section 2.2.2), the masses of the scalar partners of fermions, sfermions, depend on soft

[1] $\tan\beta$ and m_A are also inputs in the MSSM. For the analysis presented here, several (m_A,$\tan\beta$) points in the MSSM space were considered, as it is going to be explained in the next chapter.

scalar masses, trilinear couplings, the higgsino mass μ and the ratio of the Higgs vacuum expectation values $\tan\beta$. The masses of the fermion partners of the gauge and Higgs bosons, the neutralinos and charginos, depend on soft gaugino masses, μ and $\tan\beta$. Finally, the properties of the Higgs scalar sector are calculated from the input pseudoscalar Higgs boson mass m_A, $\tan\beta$, μ, trilinear couplings and the sparticle properties in an effective potential approach. Of course, these calculation also depend on SM parameters (m_t, m_Z, α_S, etc).

5.2.2 TAUOLA

TAUOLA is a library of Monte Carlo Fortran programs for leptonic and semileptonic decays of the τ lepton. It provides final state with full topology including neutrinos, resonant distributions for intermediate particles and complete spin structure throughout the decay.

Although Pythia makes τ leptons decay, no spin polarization effects are included, i.e., the τ is always assumed to decay isotropically. Usually this is not correct, since a τ is produced polarized in Z, $W^{\pm}$ and $H^{\pm}$ decays. The τ leptons coming from a $W^{\pm}$ and $H^{\pm}$ decays have different polarization states [89]. The tau polarization effects are going to be extensively discussed in section 6.3.1.

In order to perform the whole physics analysis within the ATHENA framework, it was necessary to program a C++ interface to Fortran TAUOLA version 2.6. This interface is the TauolaModule Algorithm. TauolaModule reads the events generated by PythiaModule from the Transient Data Store. Those events are fed in TAUOLA in a common block. Afterwards, TAUOLA searches for τ's and makes them decay. The events together with the τ decay products are written back to the Transient Data Store.

The TauolaModule input parameters are also set via a text jobOptions.txt file like it was done with PythiaModule.

5.3 Simulation of the detector response with ATHENA-Atlfast

ATHENA-Atlfast is a particle-level simulation program which allows for fast analysis of the fully generated event in the pp collision including parametrisation of the most crucial detector aspects, namely: jet reconstruction in the calorimeters, momentum/energy smearing for leptons and photons, magnetic field effects and missing transverse energy. It provides, starting from the list of particles in the event, a list of reconstructed jets, isolated leptons and photons, the expected missing transverse energy, and reconstructed charged tracks. Values for the rejections against non b-jets and non τ-jets are also provided as a function of the efficiencies for identifying b-jets and τ-jets.

Fast particle-level simulation and reconstruction is an intermediate step between simple parton-level analysis of the event topology, which in general yields too much optimistic results for physics processes at hadron colliders, and very sophisticated and CPU-consuming full detector simulation and reconstruction. In full simulation, the detector response is modeled in a very accurate way making use of the GEANT [76] package. In Atlfast, the detector-dependent parameters are tuned to what is expected for the performance of the ATLAS detector from full simulation and reconstruction.

However, fast simulation is never meant to replace the full simulation of the detector response. On the other hand, this kind of simulations are necessary for quick and approximate estimates of signal and background rates for specific channels. In addition, fast simulation is the only practical tool for high-statistics studies of complex background processes at the LHC.

Detailed comparisons between fast and full simulation were done for the WH, $H \to b\bar{b}$ and $A \to \tau\tau$ channels [90], in terms of the calculated acceptances for the selection cuts, the jet reconstruction efficiencies and mass resolutions. A very good agreement between fast and full simulation was found.

The main goal of the Atlfast package is to reproduce as well as possible the expected detector performance in terms of the resolution and particle-identification for important physics signals. A reasonably accurate parametrisation of photon, electron and muon momentum resolution is included, as well as a parametrisation of the hadronic calorimeter energy resolution and the effect of the ATLAS magnetic field on jet reconstruction.

The reconstruction of helix track parameters in the Inner Detector is also provided with separate parametrisations of the resolutions for muon, electron and pion tracks.

Not all the detector effects can be readily parametrised in fast simulation and only the basic information of the detector geometry is used in the package. This basic information is for example: the η-coverage for precision physics and for the calorimetry, the size of the barrel/end-cap transition region for the electromagnetic calorimeter, and the granularity of the hadronic calorimeters. No effects related to the detailed shapes of particle showers in the calorimeters, the charged track multiplicity in jets, etc., are taken into account.

5.3.1 ATHENA-Atlfast organization

The ATHENA-Atlfast package is organized in several subpackages. The most important ones are AtlfastAlgs and AtlfastEvent. Specifically, **AtlfastAlgs-00-00-09** and **AtlfastEvent-00-00-09** versions were used. AtlfastAlgs contains the ATHENA-Algorithms that are responsible for the reconstruction of tracks, jets, isolated leptons and missing transverse energy. AtlfastEvent is a subpackage that holds the Data Objects produced by AtlfastAlgs algorithms, namely reconstructed particles, cells, clusters, jets and tracks. All these Data Objects are *contained* in Data Collection objects, such as JetCollection, and they are kept in the Transient Data Store. The StandardNtupleMaker Algorithm is in charge to convert this Data Objects into persistency, by putting all their information in a HBOOK ntuple.

The sequence of execution of the different Algorithms in AtlfastAlgs can be seen in Fig. 5.2.

5.3.2 Jet Reconstruction in Atlfast

The transverse energies of all particles that did not decay (except for neutrinos, muons and the SUSY LSP) are summed up in calorimeter *cells* of a given granularity in $\eta \times \phi$ coordinates (default: 0.1×0.1 for $|\eta| < 3.2$ and 0.2×0.2 for $|\eta| > 3.2$) over the full calorimeter coverage (default: $|\eta| < 5$).

The effect of the solenoidal 2T magnetic field on the ϕ-position of charged particles with p_T above 0.5 GeV threshold is parametrised. It has been checked that the contribution from charged particles with p_T below this threshold can be neglected.

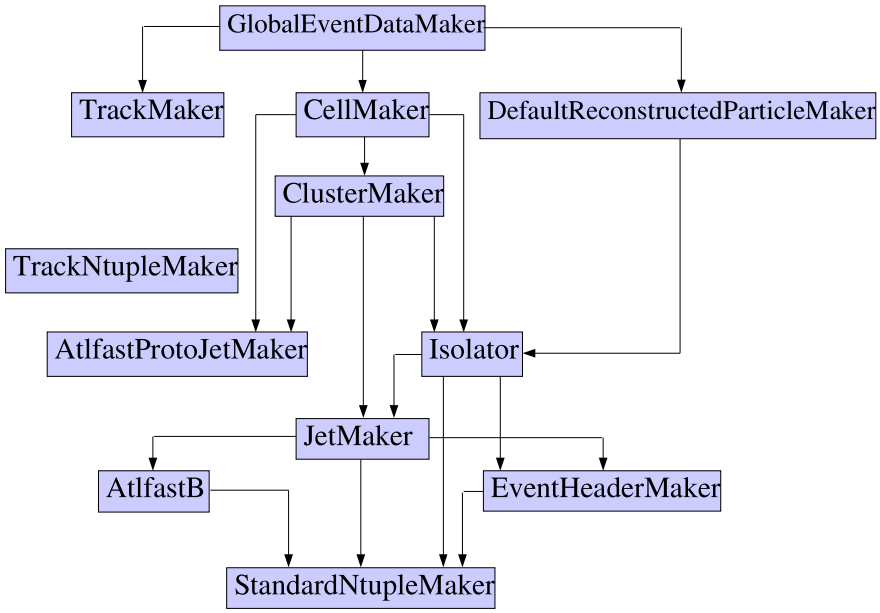

Figure 5.2: Execution order of Algorithms in AtlfastAlgs.

All calorimeter cells with transverse energy greater than a given threshold (default: $E_T > 1.5$ GeV) are taken as possible initiators of *clusters*. These are scanned in order of decreasing E_T to verify whether the total E_T summed over all cells in a cone $\Delta R = \sqrt{\Delta\eta^2 + \Delta\phi^2}$ exceeds the minimum required threshold for a reconstructed cluster. The reconstruction cone is defined separately for the barrel/endcap ($|\eta| < 3.2$) and forward ($|\eta| > 3.2$) part (default for barrel/endcap and forward: $\Delta R = 0.4$). As coordinates (η^{clu}, ϕ^{clu}) of the reconstructed clusters are taken the coordinates of the barycenters of the cones weighted by the cell E_T for all cells inside the cone around the initiator cell. No energy smearing is applied yet to these clusters, since some of them represent photon clusters or electron clusters. Appropriate energy smearing will be applied only after cluster identification. In the ATHENA-Atlfast version, cell energy sharing of cells belonging to overlapping jets is not taken into account (while it is done in the Fortran version).

Clustered cells are possible jet candidates. The energies of those clusters that have not been selected as associated with isolated electrons or photons (see section below), are smeared with the energy resolution parametrised according to the results obtained in the full simulation of the hadron calorimeters. When the high luminosity option is chosen, pile-up events are included in the parametrisation of the resolution. The measured mo-

menta from non-isolated muons which fall inside the cluster cone and are within $|\eta|$ <2.5 are added to the smeared cluster energy. Finally, the resulting jets with E_T above a given threshold (in the present work E_T >10 GeV was used) as labeled as reconstructed jets.

Jets are identified as b-jets if a b-quark of $p_T > 5$ GeV (after FSR) is found in a cone of $\Delta R = 0.2$ around the reconstructed jet for jets with $|\eta| < 2.5$. And jets are labeled as c-jets if similar criteria are satisfied.

Concerning τ-jets, they can be identified in case of hadronic τ-decays. The hadronic τ-decay products are required to have $p_T^{\tau-had} > 10$ GeV inside the tracking range $|\eta| < 2.5$ and also $p_T^{\tau-had}/p_T^{jet} > 0.9$.

The efficiencies for b-jet identification and the corresponding rejection factors for c-jet and other jets (τ-jets, light-jets) have been parametrised as p_T dependent functions in AtlfastB algorithm as well as the τ-jet efficiencies for τ-jet identification and the corresponding non τ-jet rejection factors, see section 5.3.5 for more details.

5.3.3 Isolated electrons, photons and muons

Those photon and electron candidates that are isolated from any hadronic activity are searched for in the particle list. The photon and electron four momenta are smeared with a parametrisation that was derived from full simulation studies. Isolation criteria in terms of distance from other clusters and of maximum transverse energy deposition in a cone around the photon/electron candidate, as well as the geometrical acceptance, are verified.

Isolated muons are also searched for in the particle list. Their momentum is smeared according to a resolution parametrised as a function of the muon p_T, $|\eta|$ and ϕ. Three options depending on which subdetectors are assumed to be used for the muon measurement can be invoked: Muon System standalone, Inner Detector standalone and combined Inner Detector plus Muon System. Isolation criteria in terms of distance from other clusters and of maximum transverse energy deposition in a cone around the muon candidate, as well as the fiducial geometrical acceptance, are applied.

However, Atlfast does not correct for efficiencies in the reconstruction/identification of muons, electrons nor photons, so the estimated efficiencies (from full simulation studies) should be included by the user in the event analysis.

5.3.4 Missing transverse energy

The missing transverse energy (E_{Tmiss}) is calculated by summing up the transverse momenta of identified isolated photons, electrons and muons, jets, and non-isolated muons not added to any jet cluster. Those transverse energies deposited in cells that were not used for cluster reconstruction are also included in the total sum and they are smeared according to the same energy resolution function that was applied in the case of jets. In the case of high luminosity, pile-up is included in the smearing parametrisation for energy deposited in unused cells. From this total transverse energy sum, E_{Tobs} the missing transverse energy is obtained, $E_{Tmiss} = E_{Tobs}$, as well as its components $p_{xmiss} = -p_{xobs}$, $p_{ymiss} = -p_{yobs}$.

5.3.5 AtlfastB Algorithm for jet energy calibration and mis-tagging

In order to have a complete treatment of jets in Atlfast-ATHENA, it was necessary to program the AtlfastB Algorithm. This Algorithm is the "translation" into ATHENA-C++ of the ATLFAST-B program in the old ATLFAST-Fortran package. AtlfastB is in charge of:

- performing jet energy calibration and
- computing efficiencies for τ, b and c jet tagging and rejection

5.3.5.1 Jet energy calibration

Concerning the jet energy calibration, the possibility to recalibrate the peak position for the dijet mass was studied for samples of u-jets, gluon-jets and b-jets obtained from WH production with respectively $H \to u\bar{u}$, $H \to gg$ and $H \to b\bar{b}$ decays. In [91], the parton-level simulation was compared to the particle-level simulation (called there jet-level simulation), and large differences were observed for the reconstruction of b-jets and of invariant $b\bar{b}$ masses. For example, due to final state radiation and hadronization effects, a large shift in the peak position of the reconstructed mass $m_{b\bar{b}}$ of two b-jets was observed.

As a result of this studies, the effect of the energy loss outside the jet reconstruction cone is parametrised in AtlfastB using a p_T^{jet} dependent calibration factor, namely $K_{jet} = p_T^{parton}/p_T^{jet}$, were p_T^{parton} denotes the transverse momentum of the parton which initiated

the jet (before FSR). Fig. 5.3 shows these calibration factors as a function of p_T^{jet} for the three jet flavour initiators, b-jets, gluon-jets and light-quark jets. One can see there that, for p_T^{jet} >50 GeV, the distributions become asymptotically flat at a value $K_{jet} \sim$ 1.2 independent of the jet flavour.

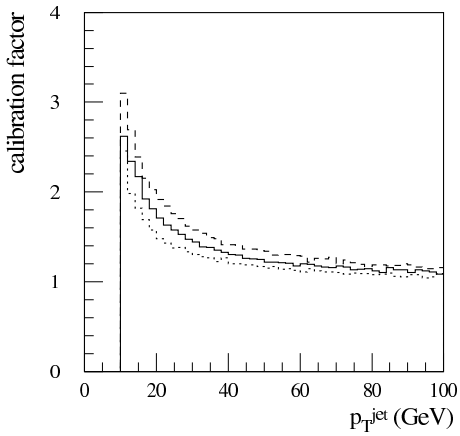

Figure 5.3: Calibration factor, $K_{jet} = p_T^{parton}/p_T^{jet}$, as a function of the reconstructed jet transverse momentum, p_T^{jet}, for b-jets (solid line), gluon-jets (dashed line) and light-quark jets (dots). Taken from [75].

5.3.5.2 b-jet and τ-jet tagging

The b-jets can be identified using different b-tagging techniques: vertex or soft-lepton tags, see [51]. In the first technique, a vertexing algorithm reconstructs the displaced vertices from b-hadron decay ($c\tau \sim 470$ μm). In the second one, the soft leptons (electrons and muons) from semi-leptonic b-quark decay are used to tag the b-jets.

As it was already mentioned above, Atlfast (without AtlfastB) labels jets as b-jets and c-jets on the criteria that in the distance of $\Delta R_{cone} = 0.2$ from the jet axis the heavy flavour quark after FSR with $p_T > 5$ GeV is found. Obviously this does not parametrise the reality in an accurate way. Thus, AtlfastB implements a realistic parametrisation of the b-tagging performance following the results presented in [52] for WH, $H \rightarrow b\bar{b}$ associated production. In this study, with the vertexing algorithm method, it was shown that for low-p_T jets (for example, as produced by Higgs decays with $m_H = 100$ GeV), the u-jet rejection R_u was limited by a decrease of the charged particle multiplicity in jets and the worse impact parameter resolution arising from an increase of the multiple

scattering of tracks. On the other hand, for high-p_T jets (m_H = 400 GeV), the rejection was limited by an increase of the multiplicity of charged particles from the primary interaction vertex (due to the increase of the fragmentation component of the jet, the discrimination between b-jets and u-jets is reduced), and also by an increase in the fraction of reconstructed secondaries contained in the jet, owing to the higher momentum of the interacting particles. Thus, due to this dense environment at larger p_T jet values, large tails in the impact parameter distributions arise making more difficult the b-tagging by means of the vertexing method.

The rejection of gluon jets R_g was limited by the heavy quark content of the jets; while the rejection of c-jets, was limited by the lifetime of the c-hadrons. Table 5.1 show the rejections for u, d, s and gluon jets (not containing c-quarks nor b-quarks in the final parton shower process) averaged over η and p_T as a function of the b-tagging efficiency. The other columns show the correction factors applied to these values to account for the p_T dependence of the jet rejection.

b-tagging efficiency	Global rejection	Correction: 15< p_T <30	Correction: 30< p_T <45	Correction: 45< p_T <60	Correction: 60< p_T <100	Correction: p_T >100
$\varepsilon_b = 33\%$	1400 ± 400	0.11	0.35	1.80	1.80	1.80
$\varepsilon_b = 43\%$	220 ± 30	0.28	0.49	2.16	2.16	1.58
$\varepsilon_b = 53\%$	91 ± 7	0.24	0.51	1.75	2.10	1.95
$\varepsilon_b = 64\%$	32 ± 2	0.18	0.59	1.50	2.11	1.94

Table 5.1: Rejections achieved by vertexing alone as a function of the jet p_T (in GeV) and of the chosen b-tagging efficiency for calibrated jets from SM Higgs decay with m_H=100 GeV not containing any heavy flavour component from charm or bottom. Taken from [52].

On the other hand, the expected detector performance for identifying hadronic τ-jets was studied extensively with full simulation in [64]. In this work, the p_T and η jet rejections for required efficiency for τ-jet identification at low luminosity were studied using full simulated $A \to \tau\tau$ events. Those results were implemented in AtlfastB. The parametrisation is given for three ranges of pseudorapidity: $|\eta|$ <0.7, 0.7< $|\eta|$ <1.5 and $|\eta|$ <1.5 and for 15< p_T^{jet} <150 GeV. The parametrisation for non-τ jet rejection for a fixed value of the τ-tagging efficiency is shown in Fig. 5.4 for 15< p_T^{jet} <150 GeV. For higher transverse momentum of the jets, a rejection of 2500 was assumed.

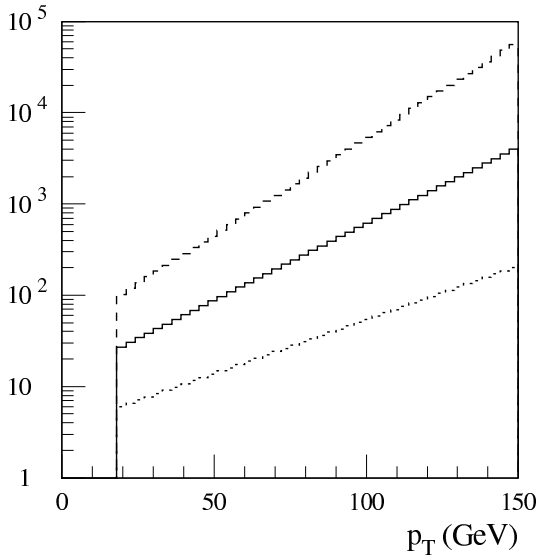

Figure 5.4: Parametrisation for non-τ jet rejection for fixed value of τ-tagging efficiency (from top to bottom) 30%, 50%, 70% and central rapidity range $|\eta|$ <0.7. Taken from [75].

5.3.5.3 Validation of AtlfastB Algorithm in ATHENA

In order to validate the newly programmed AtlfastB Algorithm within the AtlfastAlgs package in ATHENA, several tests were performed. Two samples of 50000 events of the type: $pp \to t\bar{t}$; $t \to H^+b$, $H^+ \to \tau^+\nu_\tau$; $\bar{t} \to W^-\bar{b}$, $W^- \to q\bar{q}$ were generated. One sample was completely simulated with Fortran tools, namely: Pythia 6.161+TAUOLA 2.6 generators and ATLFAST + ATLFAST-B simulation programs. On the other hand, the second sample was fully generated within ATHENA: PythiaModule and TauolaModule Algorithms interfaced Pythia 6.161 and TAUOLA 2.6 generators. Afterwards, ATHENA-Atlfast (together with AtlfastB Algorithm) performed detector simulation, energy calibration and mis-tagging of jets. Logically, the same parameters were used when generating both samples (see Table 5.2 next section).

Fig. 5.5 upper plot shows the p_T of the b jet after jet mis-tagging and energy calibration is applied by AtlfastB, for the Fortran and the ATHENA cases. Fig. 5.5 lower plot shows the energy of the b jet also after AtlfastB. A b jet tagging efficiency of 50% was used. The rejection for c jets and τ jets was 10.9 and 231 respectively. It can be seen, though, that Fortran and ATHENA results are in very good agreement.

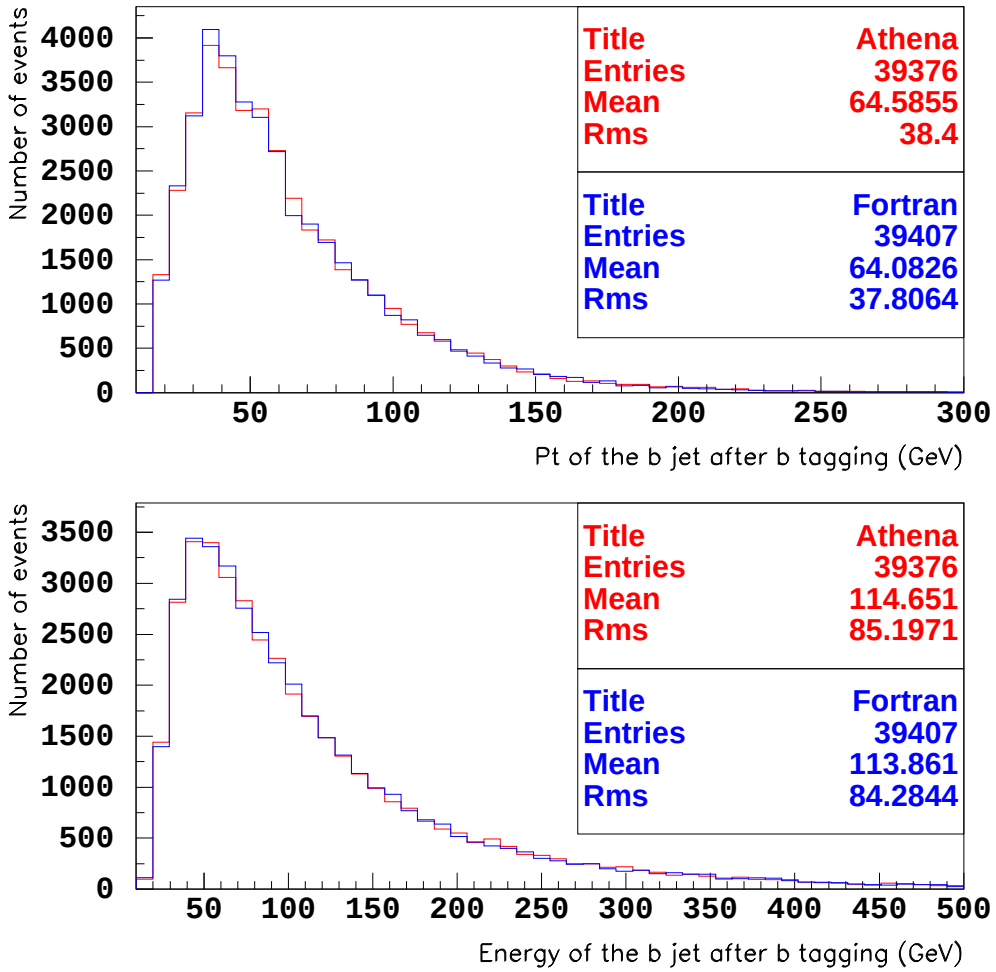

Figure 5.5: Upper plot: p_T of the b jet after jet mis-tagging and energy calibration applied by AtlfastB for the Fortran and the ATHENA simulation codes. Lower plot: Energy of the b jet after AtlfastB. A b jet tagging efficiency of 50% was used and the rejection for c jets and τ jets was 10.9 and 231 respectively.

Moreover, Fig. 5.6 shows the p_T of the τ jet after tau mis-tagging is applied by AtlfastB for both Fortran and ATHENA programs. A τ jet tagging efficiency of 50% was used.

After this validation, it was clear that either of them could be used for the analysis. Therefore, for the discovery potential of the MSSM $H^{\pm}$ studies exposed in chapter 6, the Fortran code was used and for the mass reconstruction studies presented in chapter 7, the

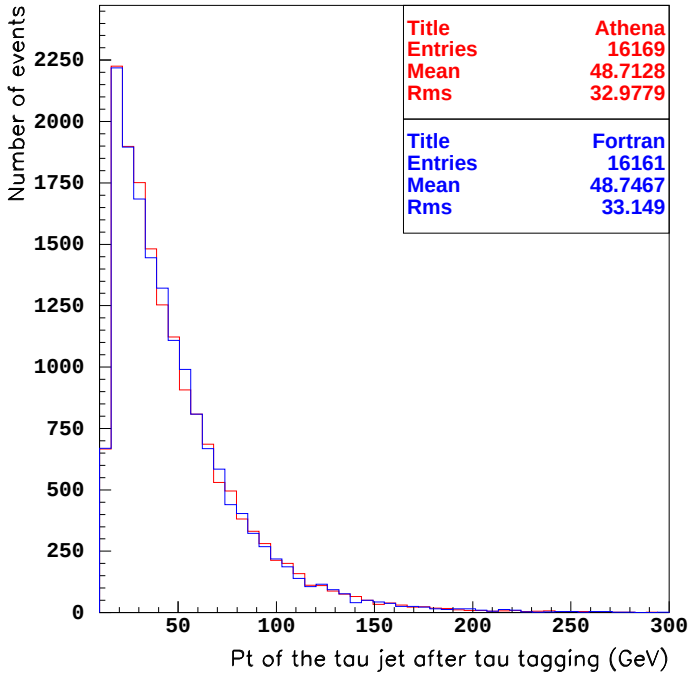

Figure 5.6: p_T of the τ jet after tau jet mis-tagging is applied by AtlfastB for both Fortran and ATHENA programs. A τ jet tagging efficiency of 50% was used.

ATHENA code was taken.

5.3.6 Atlfast parameters

For the present thesis, the standard set of Atlfast parameters shown in Table 5.2 were used.

5.4 Analysis tools

In this work, the AtlfastAnalysis package [92] version **AtlfastAnalysis-01-03-09** was used. This package is made of a set of ATHENA Algorithms and classes which perform the repetitive tasks which comprise an analysis, such as searching for topological signatures, cutting on quantities and histogramming of certain quantities.

Making use of the StandardNtupleReader Algorithm, HBOOK ntuples produced by

Parameter	Value
electron p_T^{min}	5.0 GeV
muon p_T^{min}	6.0 GeV
photon p_T^{min}	5.0 GeV
cluster threshold E_T^{min}	5.0 GeV
jet threshold p_T^{min}	10.0 GeV
ΔR_{jet}^{cone}	0.4
b-tagging efficiency	60%
Rejection on c jets [2]	10
Rejection on light jets [2]	100
tau-tagging efficiency [3]	50%
luminosity	$1 \cdot 10^{33} \mathrm{cm}^{-2}\mathrm{s}^{-1}$
magnetic field	2 T

Table 5.2: Atlfast parameters used in this thesis.

Atlfast are fed into the program and saved into the Transient Data Store. Afterwards, the OOAnalyser Algorithm reads the event from the TDS, it aggregates all the manager classes responsible for making the Signature object, monitoring variables, applying cuts and plotting histograms.

It's worth commenting here, that it was quite difficult to get used to the AtlfastAnalysis package. For example, something as easy as implement some basic cuts was not straightforward for the new user and lots of troubles were found when trying to introduce some modifications due to an "excessive" encapsulation of the C++ code. At present, the AtlfastAnalysis package is not included in the ATLAS offline software release anymore.

[2] The matching between the b-tagging efficiency and c jet and light jet rejections were implemented in AtlfastB (see Table 5.1) following the results obtained in [52].

[3] The corresponding jet rejections for a τ-tagging efficiency of 50% can be derived from plot in Fig. 5.4.

Chapter 6

Discovery potential of a MSSM $H^{\pm}$ produced in top decays with the ATLAS detector

Whereas the neutral MSSM Higgs bosons may be hard to distinguish from the Standard Model Higgs, the charged Higgs carries a unique signature of the SUSY Higgs sector. Therefore, the detection of the $H^{\pm}$ and the measurement of its mass and couplings are expected to play a very important role in the discovery of new physics.

In this chapter, the possibility to observe a light MSSM $H^{\pm}$ in ATLAS[1] is reviewed. In section 6.1, the main motivations that inspired this analysis are exposed. In section 6.2 the statistical significance is introduced. In section 6.3 the signal and background processes are presented together with the statistics of Monte Carlo samples that have been used. Next, in section 6.4, the selection cuts applied on the signal and background event samples are listed. Finally, in sections 6.5 and 6.6, the systematic errors are exposed and the final significance for a light MSSM charged Higgs signal is given as well as the 5σ discovery curve in the $(m_A, \tan\beta)$ space.

[1] In this thesis, light charged Higgs refers to $H^{\pm}$ with $m_{H^{\pm}} < m_{top}$.

6.1 Motivations

The NLO prediction of the $t\bar{t}$ cross section is 833 pb [93], this implies a production of over 8 million $t\bar{t}$ pairs in one year at low luminosity at the LHC. Thus, for $m_{H^{\pm}} < m_t - m_b$, $H^{\pm}$ can be copiously produced in top decays as it will be shown here below. Moreover, at certain points in the (m_A,tan β) space, it exceeds the $W^{\pm}$ production rate.

At the LHC, the gluon-gluon fusion process, $gg \to t\bar{t}$ accounts for about 90% of the total $t\bar{t}$ production, with $q\bar{q}^{'} \to t\bar{t}$ accounting for the rest[2]. Thus, in most of the cases the charged Higgs is produced through the $gg \to t\bar{t}$ process, followed by $t \to H^+b$ decay for $m_{H^+} < m_t$. The decay $t \to H^+b$, if kinematically allowed, can compete with the $t \to W^+b$ decay (the branching ratio of $t \to W^+b$ in the SM is almost 1 [94]). The MSSM $H^{\pm}$ signature considered in this thesis (shown in Fig. 4.6) is:

$$
\begin{array}{llll}
pp \to & t\bar{t} & X & \\
 & t \to & W^+b & \\
 & & W^+ \to & q\bar{q}\prime \\
 & \bar{t} \to & H^-\bar{b} & \\
 & & H^- \to & \tau^-\bar{\nu_\tau} \\
 & & & \tau^- \to hadrons\ \nu_\tau
\end{array}
$$

with charged conjugate channels ($t \to H^+b$ and $\bar{t} \to W^-\bar{b}$) also considered.

This channel (often called *the hadronic channel* due to the $W^{\pm} \to q\bar{q}\prime$ decay) was not investigated at the LHC before. Moreover, it complements the studies done on the light MSSM $H^{\pm}$ with the $W^{\pm}$ boson decaying leptonically [44].

In the next subsection the light charged Higgs couplings and decay branching ratios, namely, $BR(t \to H^+b)$ and $BR(H^+ \to \tau^+\nu_\tau)$ will be presented to show that $H^{\pm}$ can be produced with an acceptable rate in the MSSM. Furthermore, the previous analysis on the light charged Higgs using the $W^{\pm}$ leptonic channel is summarized.

[2]These fractions are approximately reversed in the case of $p\bar{p} \to t\bar{t}$ in Tevatron, where $q\bar{q}^{'}$ annihilation dominates.

6.1.1 MSSM $H^{\pm}$ couplings and branching ratios

In the diagonal Kobayashi-Maskawa (KM) matrix approximation, the MSSM charged Higgs boson couplings to the fermions are given by [89]:

$$\mathcal{L} = \frac{g}{\sqrt{2}m_W} H^+ \{\cot\beta m_{u_i} \bar{u}_i d_{iL} + \tan\beta m_{d_i} \bar{u}_i d_{iR} + \tan\beta m_{l_i} \bar{\nu}_i l_{iR}\} + h.c. \tag{6.1}$$

where the subscript i denotes quark and lepton generation. The leading log QCD correction is taken into account by substituting the quark mass parameters by their running masses evaluated at the $H^{\pm}$ mass scale [95]. The resulting decay widths are given by [89]:

$$\begin{aligned}
\Gamma_{t\to bW^+} =& \frac{g^2}{64\pi m_W^2 m_t} \lambda^{1/2}\left(1, \frac{m_b^2}{m_t^2}, \frac{m_W^2}{m_t^2}\right) \\
& \left[m_W^2(m_t^2 + m_b^2) + (m_t^2 - m_b^2)^2 - 2m_W^4\right] \qquad (6.2) \\
\Gamma_{t\to bH^+} =& \frac{g^2}{64\pi m_W^2 m_t} \lambda^{1/2}\left(1, \frac{m_b^2}{m_t^2}, \frac{m_{H^+}^2}{m_t^2}\right) \\
& \left[(m_t^2\cot^2\beta + m_b^2\tan^2\beta)(m_t^2 + m_b^2 - m_{H^+}^2) - 4m_t^2 m_b^2\right] \qquad (6.3) \\
\Gamma_{H^\pm\to\tau\nu} =& \frac{g^2 m_{H^\pm}}{32\pi m_W^2} m_\tau^2 \tan^2\beta \qquad (6.4) \\
\Gamma_{H^\pm\to cs} =& \frac{3g^2 m_{H^\pm}}{32\pi m_W^2}(m_c^2\cot^2\beta + m_s^2\tan^2\beta) \qquad (6.5)
\end{aligned}$$

where

$$\lambda^{1/2}(1, x^2, y^2) \equiv \sqrt{[1-(x+y)^2][1-(x-y)^2]} \tag{6.6}$$

is known as Källen's function and comes from phase space integration.

From these expressions one can construct the relevant branching ratios:

$$BR(t \to bH^+) = \frac{\Gamma_{t\to bH^+}}{\Gamma_{t\to bH^+} + \Gamma_{t\to bW^+}} \tag{6.7}$$

$$BR(H^\pm \to \tau\nu) = \frac{\Gamma_{H^\pm\to\tau\nu}}{\Gamma_{H^\pm\to\tau\nu} + \Gamma_{H^\pm\to cs}} \tag{6.8}$$

Here one assumes $BR(t \to bH^+) + BR(t \to bW^+) \approxeq 1$ and $BR(H^\pm \to \tau\nu) + BR(H^\pm \to cs) \approxeq 1$.

Eq. (6.2)-(6.5) result in a large branching ratio for $t \to bH^+$ decay at $\tan\beta \lessapprox 1$[3] and $\tan\beta \gtrapprox m_t/m_b$, while the branching ratio for $H^{\pm} \to \tau\nu$ decay is ~ 1 for $\tan\beta \gg 1$ (whereas $BR(W^{\pm} \to \tau\nu)$ ~10 %). In addition, the $t \to bH^+$ has a pronounced dip at $\tan\beta = \sqrt{m_t/m_b} \sim 7.5$ where $\Gamma_{t\to bH^+}$ has a minimum. However, this is partly compensated by the large value of the $H^{\pm} \to \tau\nu$ branching ratio, which is ≈ 1 for $\tan\beta > 2$.

Thus, one expects a large charged Higgs boson signal in top quark decay into the τ channel in the large $\tan\beta$ region ($\tan\beta \gtrapprox m_t/m_b$).

The branching ratios for the processes $t \to H^+b$ and $H^+ \to \tau^+\nu_\tau$ were computed with PythiaModule (which interfaces Pythia version 6.161) and Parton Distribution Function (PDF) CTEQ5L. MSSM Maximal Mixing scenario was used (see 2.3.2).

The branching ratio of $t \to H^+b$ versus $\tan\beta$ is shown in Fig. 6.1 for different m_{H^+} values. This branching ratio has the mentioned minimum around $\tan\beta = \sqrt{m_t/m_b}$ ~7.5, due to the term proportional to $(m_t^2 \cot^2\beta + m_b^2 \tan^2\beta)$ in the branching ratio expression. As m_{H^+} approaches m_t, the importance of this term decreases as $(m_t^2 - m_{H^+}^2)$ (see Eq. (6.3)) and the $t \to H^+b$ branching ratio becomes asymptotically independent of $\tan\beta$ for $m_{H^+} \sim m_t$. The decays of the charged Higgs boson are controlled by its Yukawa couplings as it can be derived from Eq. (6.1). Fig. 6.2 represents the branching ratio of $H^+ \to \tau^+\nu_\tau$ for different values of $\tan\beta$. This plot should be complemented with the one in Fig. 2.3, where the branching ratio of the charged Higgs for all its decay channels is given as a function of $m_{H^{\pm}}$ for $\tan\beta = 1.5$ and $\tan\beta = 30$. By having a look at both plots, it can be seen that in the mass region $m_t < m_{H^{\pm}}$, $H^{\pm} \to \tau\nu$ is the dominant decay channel independently of $\tan\beta$ (with $BR(H^{\pm} \to \tau\nu)$ >99 %).

It's worth commenting here, what would happen if instead of a type II 2HDM like the MSSM, a type I 2HDM was considered. The pattern of enhanced and suppressed couplings of a 2HDM of type I is quite different from that of a type II 2HDM (see sections 2.2.3 and 2.2.4) [40]: in type I 2HDM the couplings of the pseudoescalar and charged Higgs bosons to all fermion types are uniformly suppressed (enhanced) if $\tan\beta > 1 (\tan\beta < 1)$.

Taking Eq.(6.2) and Eq.(6.3), one finds:

$$\frac{BR(t \to bH^+)}{BR(t \to bW^+)} \propto \frac{(m_t^2 \cot^2\beta + m_b^2 \tan^2\beta)(m_t^2 + m_b^2 - m_{H^+}^2) - 4m_t^2 m_b^2}{m_W^2(m_t^2 + m_b^2) + (m_t^2 - m_b^2)^2 - 2m_W^4} \tag{6.9}$$

[3] But the region $0.5 < \tan\beta < 2.4$ was already excluded by LEP [96].

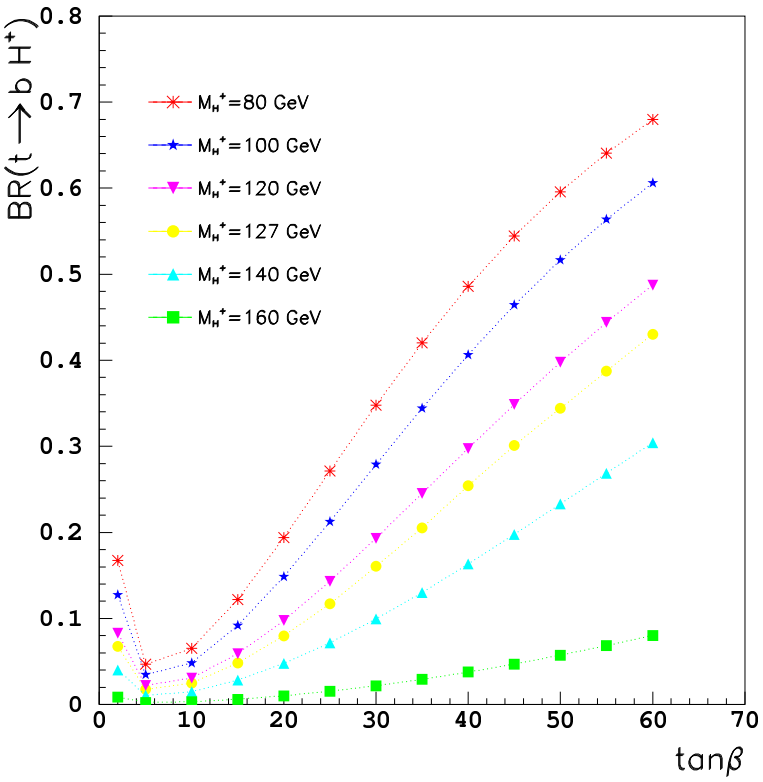

Figure 6.1: Branching ratio of $t \to H^+b$ as a function of $\tan\beta$ for different m_{H^+} values in the MSSM Maximal Mixing scenario. Results obtained with Pythia 6.161 and PDF CTEQ5L.

For a type I 2HDM one should change in Eq.(6.9) $\tan\beta \to -\cot\beta$ keeping $\cot\beta$ unchanged. Thus, For $\tan\beta < 2$ values, the $(BR(t \to bH^+))/(BR(t \to bW^+))$ ratio remains the same for type I and type II 2HDM, but for $\tan\beta > 10$, such ratio is substantially greater in type II 2HDM than in type I, in the later, $BR(t \to W^+b) \gg BR(t \to H^+b)$ being the $t \to H^+b$ decay almost suppressed. Therefore, for a given charged Higgs mass and $\tan\beta$, the branching ratio gives information of the theoretical model to which the charged Higgs may belong.

On the other hand, for a type I 2HDM, $BR(H^+ \to \tau^+\nu)$ ~30% independently of $\tan\beta$.

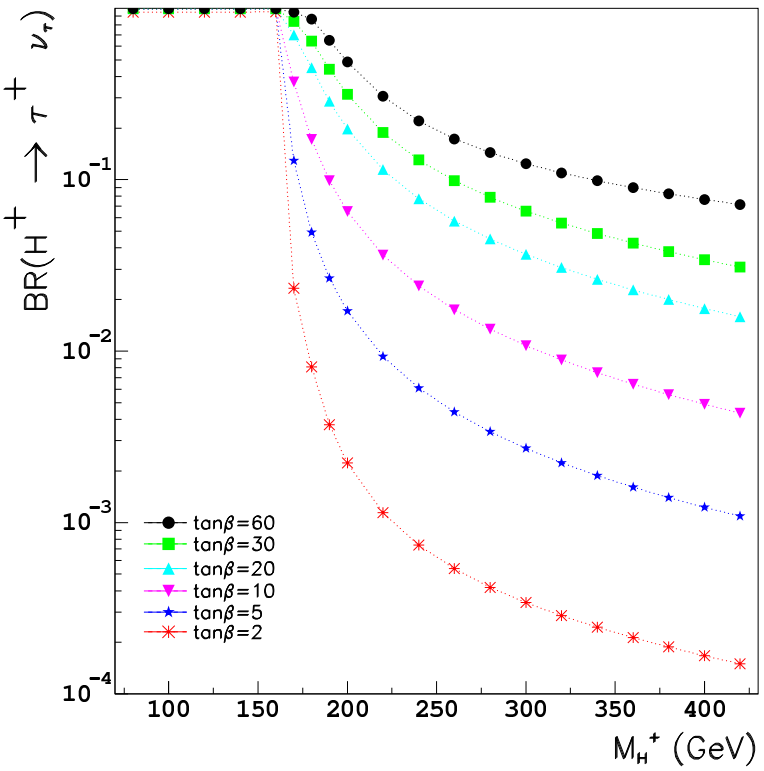

Figure 6.2: Branching ratio of $H^+ \to \tau^+\nu_\tau$ as a function of m_{H^+} for different $\tan\beta$ values in the MSSM Maximal Mixing scenario. Results obtained with Pythia 6.161 and PDF CTEQ5L.

6.1.2 Leptonic channel

As it was already pointed out in 2.3.5, the leptonic channel was studied in detail in [44]. This study concentrated on the search in $t\bar{t}$ events for an excess of τ leptons from $H^{\pm} \to \tau\nu$ decay with respect to the expected τ leptons rate from $W^{\pm} \to \tau\nu$ decay. At that moment, the τ trigger was not yet considered, thus the leptonic channel was taken in order to trigger on the e or μ from the W boson decay or from the second charged Higgs semileptonic decay, i.e. $H^{\pm} \to \tau\nu$ and $\tau \to l\nu_l$ ($l = e, \mu$). However, in this channel the charged Higgs boson mass cannot be directly reconstructed because several neutrinos split in different hemispheres of the event (i.e., the missing transverse energy E_{Tmiss} is not equivalent to the transverse energy of the neutrinos in the final state) are produced in the final states of interest:

$$
\begin{array}{llll}
pp \rightarrow & t\bar{t} & X & \\
 & t \rightarrow & H^+ b & \\
 & & H^+ \rightarrow & \tau^+ \nu_\tau \\
 & & & \tau^+ \rightarrow hadrons\ \bar{\nu_\tau}
\end{array}
$$

with three different possibilities for the $\bar{t}$ decay:

$$
\begin{array}{lll}
\bar{t} \rightarrow W^- \bar{b} & W^- \rightarrow l\nu_l & (l = e, \mu) \\
\bar{t} \rightarrow W^- \bar{b} & W^- \rightarrow \tau\nu_\tau & \tau \rightarrow l\nu_\tau\nu_l \\
\bar{t} \rightarrow H^- \bar{b} & H^- \rightarrow \tau\nu_\tau; & \tau \rightarrow l\nu_\tau\nu_l
\end{array}
$$

In Fig. 2.7, the expected 5σ discovery contour curves for this channel in the $(m_A, \tan\beta)$ plane for an integrated luminosity of 30 fb^{-1} were shown. A signal from charged Higgs boson production in $t\bar{t}$ decays would be observed for all values of $m_{H^\pm}$ below the kinematical limit of $\sim m_t$-20 GeV over most of the $\tan\beta$ range. For moderate values of $\tan\beta$, for which the expected signal rates are lowest, the accessible values of $m_{H^\pm}$ are lower than this kinematical limit by ~20 GeV.

One of the goals of this thesis is to complement the significance studies done for the leptonic channel and achieve a significance greater than 5σ for those $m_{H^\pm}$ values that were not observable in that study. Furthermore, the charged Higgs mass can be reconstructed by making use of the transverse mass distribution, since the neutrinos in the final state (from $H^\pm \rightarrow \tau\nu$; $\tau \rightarrow \nu_\tau + hadr$) are produced in the same hemisphere of the event, that is, the E_{Tmiss} of the event reconstructs quite accurately the final state neutrinos' transverse energy as it can be seen in Fig. 6.3. The charged Higgs mass extraction is going to be extensively described in the next chapter. Last but not least, the full reconstruction of the top mass using the two light jets and a b jet on the W side turns to be very useful against QCD as it will be shown in section 6.4.

6.2 Definition of statistical significance

In order to assess the sensitivity of ATLAS to the discovery of a light charged Higgs a counting experiment is considered. The number of events after cuts is compared with the null (i.e., background only) hypothesis. In that way, the excess of events is given by:

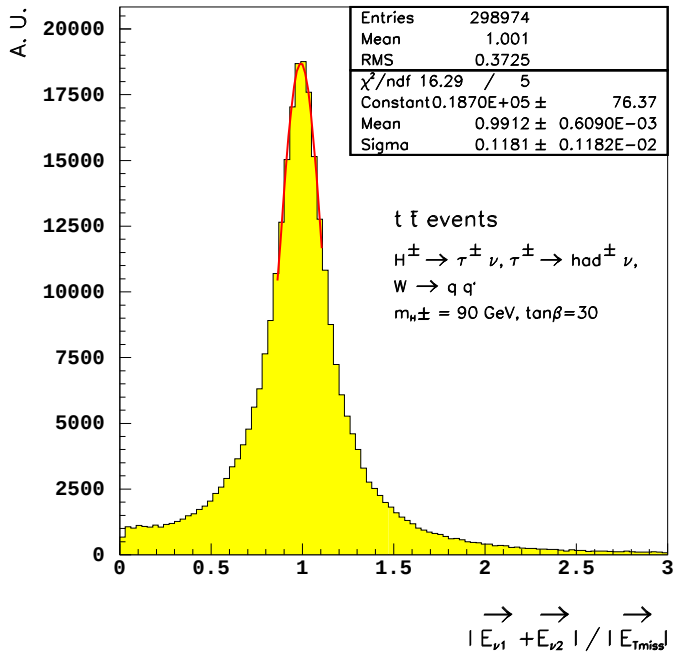

Figure 6.3: Ratio between the modulus of the vectorial sum of the transverse energy of the two neutrinos produced in the final state and the missing transverse energy for a MSSM charged Higgs of mass 90 GeV and tan β=30.

$$N_{EXCESS} = N_{OBS} - N_{BKG} \tag{6.10}$$

where $N_{OBS}(N_{BKG})$ is the number of observed(background) events. Thus, in case of signal+background present in the final sample, this will reduce to:

$$N_{EXCESS} = (S + B) - B = S \tag{6.11}$$

where S accounts for the MSSM charged Higgs signal and B for the background processes.

Since one wants to compare with the background only hypothesis, the expected error

on the number of events will be (on the basis of gaussian statistics [4]):

$$\sigma = \sqrt{B} \tag{6.12}$$

And the observed statistical significance will be given by:

$$S_{STAT} = \frac{N_{EXCESS}}{\sigma} = \frac{S}{\sqrt{B}} \tag{6.13}$$

In addition, the statistical significance given by Eq. (6.13) can be addressed from two different perspectives:

- One wants to show an excess compared to the SM hypothesis. In that case, the 'B' in Eq. (6.13) will be made of only SM backgrounds processes (SM $t\bar{t}$ and other SM backgrounds).
- One wants to show an excess of events within the MSSM itself. This applies when an excess was already observed in the SM hypothesis so that one would like to know if the signal can be extracted from the MSSM background and measure its properties like the mass or the couplings. Here, the 'B' will be represented by all backgrounds existing within the MSSM, that is, MSSM $t\bar{t}$, SM and SUSY background processes.

All the considered background processes are going to be described in detail in the next section.

6.3 Signal and Background processes

The signal process was already presented in section 6.1, and its Feynman diagram was given in Fig. 4.6. Therefore, the signal final state is made of **2 b jets**, **2 light jets** (from W decay), **1 τ jet** (from hadronic τ decay) and **high E_{Tmiss}**. Moreover, the $t\bar{t}$ events with two charged Higgs in the final state:

$$\begin{aligned} pp \rightarrow \quad & t\bar{t} \quad X \\ & t \rightarrow \quad H^+ b \\ & \bar{t} \rightarrow \quad H^- \bar{b} \end{aligned}$$

[4] This approximation is only true if at the end of the selection cuts a considerable amount of background events still remain, approximately $B \gtrsim 20$ events.

were also considered as signal for the discovery potential studies when looking for an excess of events compared to the SM hypothesis (see section 6.2). On the contrary, those events were considered as background for the mass studies, since the charged Higgs mass cannot be reconstructed in this case due to the fact that the final state neutrinos are split in two different hemispheres (i.e., $|\vec{E}_{Tmiss}| \neq |\sum_i \vec{E}_{\nu_i}|$).

On the background side, three types of processes can be distinguished:

1. $t\bar{t}$ background:

   - $t\bar{t}$ background with no $H^{\pm}$ in the final state:

     $$\begin{array}{llll} pp \rightarrow & t\bar{t} & X & \\ & t \rightarrow & W^+b & \\ & \bar{t} \rightarrow & W^-\bar{b} & \end{array}$$

     Among this processes, the main expected backgrounds come from $W^{\pm} \rightarrow q\bar{q}'$ and $W^{\mp} \rightarrow \tau\nu$; $\tau \rightarrow hadrons\ \nu_\tau$ which can fake the one charged Higgs signal final state. However, the τ polarization effects (see next section) and the reconstructed charged Higgs transverse mass (see section 6.4.2) will be very useful to distinguish them from the signal.

   - $t\bar{t}$ background with $H^{\pm} \rightarrow \tau\nu$ in the final state and τ decaying leptonically:

     $$\begin{array}{llll} pp \rightarrow & t\bar{t} & X & \\ & t \rightarrow & W^+b & (or\ \ H^+b) \\ & & W^+ \rightarrow & all \\ & \bar{t} \rightarrow & H^-\bar{b} & (or\ \ W^-\bar{b}) \\ & & H^- \rightarrow & \tau^-\bar{\nu}_\tau \\ & & & \tau^- \rightarrow l^-\nu_l\nu_\tau\ \ (l = e,\ \mu\ \tau) \end{array}$$

   - $t\bar{t}$ background with $H^{\pm} \rightarrow cs$ in the final state:

     $$\begin{array}{llll} pp \rightarrow & t\bar{t} & X & \\ & t \rightarrow & W^+b & (or\ \ H^+b) \\ & & W^+ \rightarrow & all \\ & \bar{t} \rightarrow & H^-\bar{b} & (or\ \ W^-\bar{b}) \\ & & H^- \rightarrow & \bar{c}s \end{array}$$

The branching ratio of this charged Higgs decay channel is very low in the $m_{H^\pm} < m_{top}$ mass region as it was shown in Fig. 2.3. However, it is also taken into account to have a more complete analysis.

- $t\bar{t}$ background with $H^\pm$ in the final state and W decaying leptonically:

$$\begin{array}{lllll} pp \to & t\bar{t} & X & & \\ & t \to & W^+ b & (or\ \ H^+ b) & \\ & & W^+ \to & l^+ \bar{\nu}_l & (l = e,\ \mu,\ \tau) \\ & \bar{t} \to & H^- \bar{b} & (or\ \ W^- \bar{b}) & \\ & & H^- \to & \tau^- \bar{\nu_\tau} & \\ & & & \tau^- \to hadrons\ \nu_\tau & \end{array}$$

2. Other SM background processes:

   - QCD background:

$$pp \to qqX$$

   Even if the signature in this case is very different, QCD events have a very high cross section as it will be shown at the end of this section and some events can really fake the signal (see section 6.4).

   - Z/γ^* and W backgrounds:

$$\begin{array}{lll} pp \to & (Z/\gamma^*) + jet & \\ pp \to & W + jet & \\ pp \to & (Z/\gamma^*)(Z/\gamma^*);\ (Z/\gamma^*)W;\ WW & \end{array}$$

   Those events have also quite high cross sections. In addition, W and Z bosons can produce true τ jets.

3. SUSY background processes:

$$\begin{array}{lll} pp \to & \tilde{t}\tilde{t};\ \chi_1^\pm \chi_1^\pm, ... & \\ pp \to & Z\phi;\ W^\pm \phi;\ ff\phi & (\phi = h, H) \\ pp \to & t\bar{t}\phi;\ b\bar{b}\phi & (\phi = h, H, A) \end{array}$$

The $\tilde{t}$ production was considered since the stop can decay in t which can fake the signal. Besides, the chargino production was also considered since it is one of the SUSY processes with higher cross section in the MSSM as it will be shown in a table below.

The cross sections ($\sigma \times BR$) for the different processes are listed in Table 6.1. They were computed with Pythia 6.161 and parton distribution function CTEQ5L at $\sqrt{s} = 14$ TeV assuming MSSM Maximal Mixing scenario. However, large uncertainties in the signal and background cross sections production still remain, due to the uncertainties in the knowledge of the parton distribution functions (i.e., $f_{A/a}(\mu, x)$: a parton distribution function inside the hadron A, with x the fraction of momentum carried by the parton a and μ the momentum scale involved in the process) and to higher-order corrections.

Process		$\sigma \times BR$ **(pb)**
MSSM $t\bar{t}$	$t\bar{t}$ signal, one $H^{\pm}$ prod.	57.2
	$t\bar{t} \to H^{+}bH^{-}\bar{b}$	12.6
	rest of $t\bar{t}$ decays to SM particles	422.2
SM $t\bar{t}$		492.2
SM backgrounds	QCD ($\hat{p_T}$ >10 GeV)	55.22×10^{9}
	W+jet	15.9×10^{4}
	Z/γ^{*}+jet	48.2×10^{3}
	WW; $W(Z/\gamma^{*})$; $(Z/\gamma^{*})(Z/\gamma^{*})$	24.4×10^{3}
SUSY backgrounds	$\tilde{t}\tilde{t}$; $\chi_1^{\pm}\chi_1^{\pm}$...	$\sim$1
	$Z\phi$; $W^{\pm}\phi$; $ff\phi$ ($\phi = h, H$)	<1
	$t\bar{t}\phi$ ($\phi = h, H, A$)	<1
	$b\bar{b}\phi$ ($\phi = h, H, A$)	$< 1 \times 10^{-3}$

Table 6.1: Cross section times branching ratio values for the different processes computed with Pythia and PDF CTEQ5L. MSSM Maximal Mixing scenario and ($m_A = 95$ GeV, $\tan\beta = 30$) point in the MSSM ($m_A, \tan\beta$) plane were assumed.

In Fig. 6.4, the gluon distribution in a proton is shown according to the parton distribution sets CTEQ3M [97] and CTEQ5L [79] for a momentum scale of 100 GeV.

Thus, whereas the $t\bar{t}$ cross section computed with Pythia 6.161 and CTEQ5L turned to be $\sigma(t\bar{t})$ =492 pb, the computed value when using CTEQ3M was $\sigma(t\bar{t})$ =626 pb.

In addition, despite the existence of many higher-order QCD correction calculations which correct the tree level cross section calculations making use of the so called K-factors, not all processes of interest at the LHC have benefited from this theoretical effort. Therefore, the present thesis has consistently and conservatively avoided the use

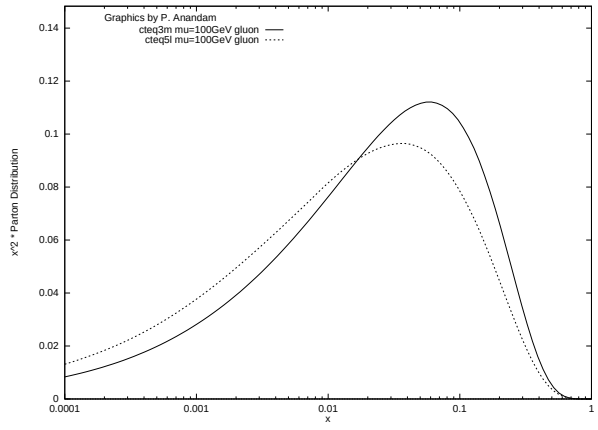

Figure 6.4: Gluon distributions in the proton according to the CTEQ3M and CTEQ5L parton distribution sets for a momentum scale of μ =100 GeV. Taken from [98].

of K-factors, resorting to lowest-order predictions for both signal and backgrounds.

Pythia computes $\sigma(t\bar{t})$ at the Leading Order approximation. On the contrary, the theoretical calculation given in [93] computes such cross section at the Next to Leading Logarithmic level. Thus, whereas the $t\bar{t}$ cross section computed by Pythia and CTEQ5L was 492 pb, the theoretical calculated value that was given at the beginning of the present chapter is $\sigma(t\bar{t}) = 831$ pb. Therefore, using Pythia, a conservative estimation of the number of expected $t\bar{t}$ events is obtained for the analysis presented here. That is, when using the theoretical calculated value, one would need $\sim$ seven months instead of twelve to get the same number of expected $t\bar{t}$ events.

6.3.1 Tau polarization effects

The background that can best fake a light charged Higgs signature is $pp \rightarrow t\bar{t} \rightarrow W^+bW^-\bar{b}$, with one W boson decaying leptonically into $\tau\nu$ and the other one decaying hadronically in two light jets. However, in one-prong τ hadronic decays, τ-jets from $H^\pm$ decay are harder than the ones produced in $W^\pm$ decay as it will be shown here below.

Due to the nature of the Weak interaction, the W^- boson will only couple to left handed taus. On the other hand, the H^- boson, with spin 0, can only couple to right handed taus. An scheme of the polarization of taus produced in W^- and H^- decays is given in Fig. 6.5.

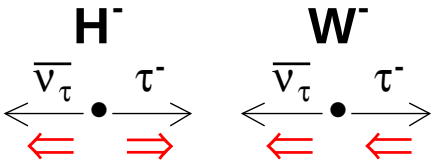

Figure 6.5: Polarization states of τ^- leptons from H^- and W^- boson decays.

The τ polarization is defined as:

$$P_{\tau^{\pm}} = \frac{\sigma(\tau_R^{\pm}) - \sigma(\tau_L^{\pm})}{\sigma(\tau_R^{\pm}) + \sigma(\tau_L^{\pm})} \tag{6.14}$$

where $P_\tau \equiv P_{\tau^-} = -P_{\tau^+}$ and $\sigma(\tau_{R,L}^{\pm})$ are the cross sections for producing $\tau^{\pm}$'s with right- and left-handed helicities respectively. Thus, tau leptons produced in W^- and H^- decays correspond to exactly opposite states of τ polarization: i.e.,

$$P_{\tau^-}^{H^-} = +1; \quad P_{\tau^-}^{W^-} = -1$$

One should concentrate on the one-prong hadronic decay channel of the tau lepton, which is the best one for τ identification. This decay channel accounts for 80% of hadronic τ decays and 50% of overall τ decays. The main contributions to the one-prong hadronic τ decay are:

$$\begin{aligned}
\tau^{\pm} &\to \pi^{\pm}\nu_\tau & (12.5\%)\\
\tau^{\pm} &\to \rho^{\pm}\nu_\tau \to \pi^{\pm}\pi^0\nu_\tau & (24\%)\\
\tau^{\pm} &\to a_1^{\pm}\nu_\tau \to \pi^{\pm}\pi^0\pi^0\nu_\tau & (7.5\%)
\end{aligned}$$

A detailed discussion on the formalism relating the τ polarization to the momentum distribution of its decay particles can be found in [99]. For τ's decaying into π's or a vector meson v (ρ, a_1), the angular distribution of these decay products in the τ rest

frame is given by:

$$\frac{1}{\Gamma_\pi}\frac{d\Gamma_\pi}{d\cos\theta} = \frac{1}{2}(1 + P_\tau \cos\theta)$$

$$\frac{1}{\Gamma_v}\frac{d\Gamma_{v_L}}{d\cos\theta} = \frac{1}{2}\frac{m_\tau^2}{m_\tau^2+2m_v^2}(1 + P_\tau \cos\theta) \tag{6.15}$$

$$\frac{1}{\Gamma_v}\frac{d\Gamma_{v_R}}{d\cos\theta} = \frac{m_v^2}{m_\tau^2+2m_v^2}(1 - P_\tau \cos\theta)$$

where L, T denote the longitudinal and transverse polarization states of the vector boson v. The angle θ measures the direction of the meson in the τ rest frame relative to the τ line of flight, which defines its polarization axis.

The angular distributions given in 6.15 can be understood in terms of angular momentum conservation. For $\tau^-_{R(L)} \to \nu_L \pi^- /\ v^-_{\lambda=0}$ it favours forward (backward) emission of π or longitudinal vector boson, while it is the other way round for transverse vector meson emission, $\tau^-_{R(L)} \to \nu_L \pi^- /\ v^-_{\lambda=-1}$ where λ is the vector meson polarization state.

As a result, the τ polarization effect given by Eqs. (6.15) is reflected in a significantly harder $\pi^\pm$ momentum distribution for the charged Higgs signal compared to the W boson background. This effect can still be observed when adding the detector effects, that is, when looking at the transverse momentum of the produced τ jet. Fig. 6.6 gives the transverse momentum of the τ jet for a charged Higgs of mass 93.3 GeV and for the W boson. When 'switching on' the τ polarization, those tau jets produced in $H^\pm$ decays acquire a higher momentum. On the contrary, the momentum of those tau jets produced in $W^\pm$ decays diminishes when taking into account the τ polarization effects.

The same is true for the longitudinal vector mesons; but the presence of the transverse component dilutes somewhat this effect.

6.3.2 Statistics of Monte Carlo samples

Events were generated with Pythia 6.161 PDF CTEQ5L and TAUOLA 2.6 for τ lepton decay at $\sqrt{s} = 14$ TeV with the detector resolutions and efficiencies parametrised by ATLFAST and ATLFAST-B. Concerning the MSSM events, Maximal Mixing scenario was used and several points in the $(m_{H^\pm}/m_A, \tan\beta)$ plane were generated as shown in Fig. 6.7. The shaded area was excluded by LEP2 [96] ($m_h > 91.0$ GeV, $m_A > 91.9$ GeV).

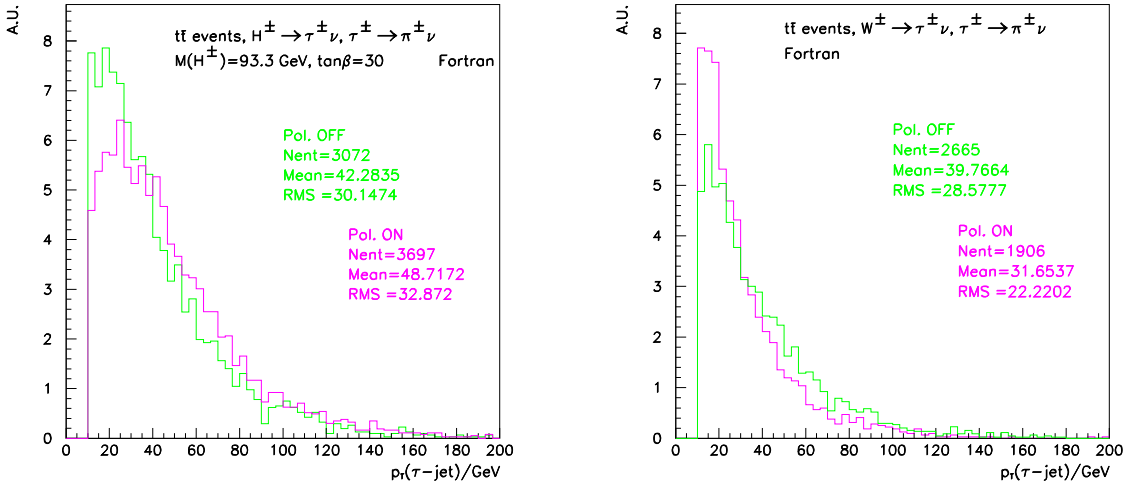

(a) $H^{\pm} \to \tau\nu$ (b) $W^{\pm} \to \tau\nu$

Figure 6.6: p_T of the τ jet produced in $H^{\pm}$ and $W^{\pm}$ decays, $m_{H^{\pm}} = 93.3$ GeV and $\tan\beta$ =30. The effect of the polarization produces an increase (decrease) of the transverse momentum of those τ jets produced in $H^{\pm}$ ($W^{\pm}$) decays.

The statistics of each generated process is given in Tables 6.2 and 6.3. First of all, a sample of $t\bar{t}$ SM processes was generated. In addition, another sample of $t\bar{t}$ processes, now in the MSSM scenario, was produced as shown in Fig. 6.7.

Process		Events
$t\bar{t}$	MSSM	1600 k/point
	SM	3900 k
QCD (21 $\hat{p_T}$ bins)		1500 k/bin
Z/γ^*+jet (3 m_Z bins)		1200 k/bin
W+jet		1200 k
WW; $W(Z/\gamma^*)$; $(Z/\gamma^*)(Z/\gamma^*)$		1200 k

Table 6.2: Statistics of the Monte Carlo generated samples. Only SM backgrounds exposed. QCD and Z/γ^*+jet events were split in 21 $\hat{p_T}$ and 3 m_Z bins respectively.

For the QCD background, several samples were generated in 21 different $\hat{p_T}$ bins[5], since

[5] $\hat{p_T}$ is the transverse momentum at parton level.

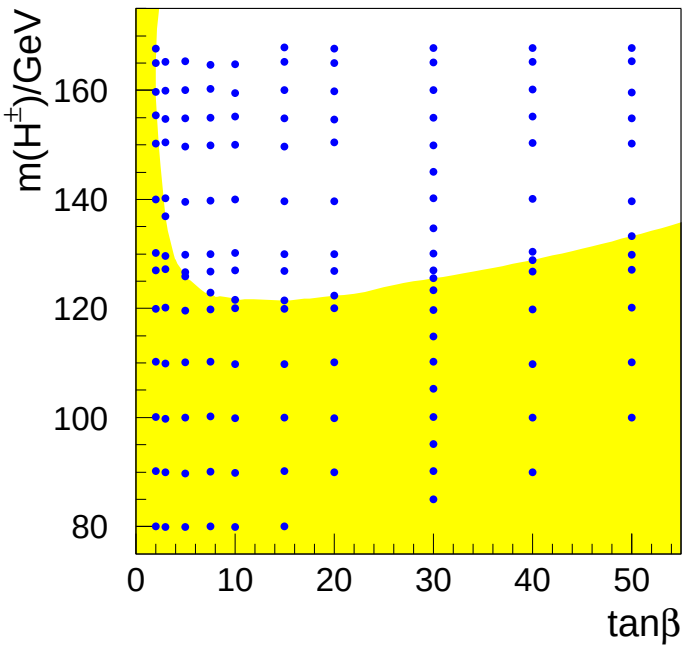

Figure 6.7: Points generated in the $(m_{H^\pm}, \tan\beta)$ plane. The shaded area was excluded by LEP2.

Process	**Events**
$gg,\ q_i\bar{q}_i \to \tilde{t}\tilde{t};\ \chi_1^\pm\chi_1^\pm ...$	1600 k
$gg,\ q_i\bar{q}_i \to b\bar{b}\phi\ (\phi = h, H, A)$	400
$gg,\ q_i\bar{q}_i \to t\bar{t}\phi\ (\phi = h, H, A)$	40 k
$f\bar{f}_i \to W^\pm\phi\ (\phi = h, H)$	40 k
$f_i f_j \to f_i f_j \phi + f_k f_k \phi\ (\phi = h, H)$	40 k
$f_i\bar{f}_i \to Z\phi\ (\phi = h, H)$	40 k

Table 6.3: Statistics of the SUSY background Monte Carlo generated samples.

the QCD cross section is decreasing exponentially with p_T. The first sample contained QCD events with 10 GeV $< \hat{p_T} <$ 20 GeV. The last bin was made of the events with $\hat{p_T} >$ 400 GeV. The statistical weight of each QCD Monte Carlo event is given in Table 6.4.

For the W+jet and diboson ($(Z/\gamma^*)(Z/\gamma^*)$, $(Z/\gamma^*)W$, WW) backgrounds, a sample of 1200 k Monte Carlo events each was generated.

$\hat{p_T}$ bin (GeV)	Statistical weight
10< $\hat{p_T}$ <20	7.23 $\cdot 10^7$
20< $\hat{p_T}$ <40	6.32 $\cdot 10^6$
40< $\hat{p_T}$ <60	3.96 $\cdot 10^5$
60< $\hat{p_T}$ <80	6.76 $\cdot 10^4$
80< $\hat{p_T}$ <100	1.82 $\cdot 10^4$
100< $\hat{p_T}$ <120	6.32 $\cdot 10^3$
120< $\hat{p_T}$ <140	2.59 $\cdot 10^3$
140< $\hat{p_T}$ <160	1.20 $\cdot 10^3$
160< $\hat{p_T}$ <180	6.08 $\cdot 10^2$
180< $\hat{p_T}$ <200	3.30 $\cdot 10^2$
200< $\hat{p_T}$ <220	1.89 $\cdot 10^2$
220< $\hat{p_T}$ <240	1.14 $\cdot 10^2$
240< $\hat{p_T}$ <260	71.4
260< $\hat{p_T}$ <280	46.0
280< $\hat{p_T}$ <300	30.6
300< $\hat{p_T}$ <320	20.9
320< $\hat{p_T}$ <340	14.5
340< $\hat{p_T}$ <360	10.3
360< $\hat{p_T}$ <380	7.4
380< $\hat{p_T}$ <400	5.4
$\hat{p_T}$ >400	18.0

Table 6.4: Statistical weight of each Monte Carlo generated QCD event for each $\hat{p_T}$ bin.

The (Z/γ^*)+jet background generation was split in tree different mass bins, namely: 2 GeV< m_Z <60 GeV (photon peak), 60 GeV< m_Z <130 GeV (contains the Z boson peak) and m_Z >130 GeV.

Finally, the SUSY background generation was split in six different samples as shown in Table 6.3. For those backgrounds with one neutral Higgs boson production a scan in the MSSM plane was done searching for that $(m_A, \tan\beta)$ point with the maximum cross section. Afterwards, a sample of 1600k Monte Carlo events for each single process

containing neutral Higgs was generated at that maximum cross section $(m_A, \tan\beta)$ point.

6.4 Selection cuts

As it was pointed out before, the light charged Higgs signal final state considered in this thesis consists of 2 b jets, 2 light jets (from hadronic W decay), 1 τ jet and large E_{Tmiss} from $H^{\pm} \to \tau\nu$ decay. The cuts presented below are optimized for a signal of only one charged Higgs production. Those signal events with two charged Higgs in the final state have a $(\sigma \times BR)$ almost 5 times lower, thus their contribution is rather small, although they were also taken into account for the discovery studies. From now on, charged Higgs signal will refer to the signal with the production of only one charged Higgs.

The selection cuts applied to the signal and background processes were specially designed to achieve a high statistical significance (given by Eq. (6.13)) throughout the whole $(m_A, \tan\beta)$ space. First of all, an event selection was applied to extract the charged Higgs signal event topology and to filter as much as possible the QCD background contribution (with a cross section 9 orders of magnitude larger than the signal). Furthermore, an event selection based on cuts on the p_T of the τ jet and the transverse mass (M_T) was applied. Such cuts were decisive to suppress the SM $t\bar{t}$ background contribution such that a notable improvement on the significance for every one of the $(m_A,\ \tan\beta)$ considered points was achieved.

6.4.1 Event selection (QCD filter)

To start with, a set of standard cuts were applied to both signal and background samples (given in Table 6.2) in order to eliminate the large amount of QCD background events that could fake the signal topology.

The events were selected as follows:

1. Trigger selection.
   The τ + E_{Tmiss} and the jet+E_{Tmiss} triggers are specially suitable for the light charged Higgs signature presented in this thesis (see Section 4.4). Specifically the (t20xe30) OR (j60xe60) trigger condition was applied, that is:

- at least one tau jet of $p_T > 20$ GeV and $E_{Tmiss} > 30$ GeV
  or
- at least one jet of $p_T > 60$ GeV and $E_{Tmiss} > 60$ GeV

As it was already pointed out at the end of section 4.4.3, at the moment of writing this thesis, the thresholds for the $\tau + E_{Tmiss}$ and jet+E_{Tmiss} triggers were changed, namely, (t20xe30)→(t35xe45) and (j60xe60)→(j70xe70) (those new thresholds were already listed in Table 4.4). In spite of this, the discovery potential results did not experiment any dramatic changes as it will be shown in appendix A.

2. *3-tag* cut and no isolated lepton.
   Search for:

   - exactly 2 b-tagged jets (ε_b =60%, $R_c = 10$, $R_{light} = 100$, see section 5.3.5.2),
   - exactly 1 τ-tagged jet (ε_τ =50%, jet rejection given by Fig. 5.4),
   - at least 2 light jets
     and
   - no isolated leptons

   When requiring no isolated lepton, one cuts very hard on the signal and background samples (especially on the W+jet, (Z/γ^*)+jet and WW, $W(Z/\gamma^*)$ and $(Z/\gamma^*)(Z/\gamma^*)$ backgrounds), but a cleaner sample is obtained. The total number of jets as well as the number of τ and b jets and the number of isolated leptons are shown in Fig. 6.8 for a charged Higgs signal of $m_{H^\pm} = 127.0$ GeV and $\tan\beta = 30$ for one year running at low luminosity and a jet threshold of 10 GeV. As it can be seen, the mean value of the total number of jets is not 5 as one would expect. This is due to ISR/FSR gluons that can fake an additional jet.

3. p_T and E_{Tmiss} cuts.
   Since the signal is characterized by a high p_T τ jet and a large E_{Tmiss} due to the neutrinos on the $H^\pm$ side, one requires:

   - $E_{Tmiss} > 45$ GeV
   - $p_T^{\tau jet} > 25$ GeV
   - $p_T^{b\,jet1} > 35$ GeV; $p_T^{b\,jet2} > 20$ GeV

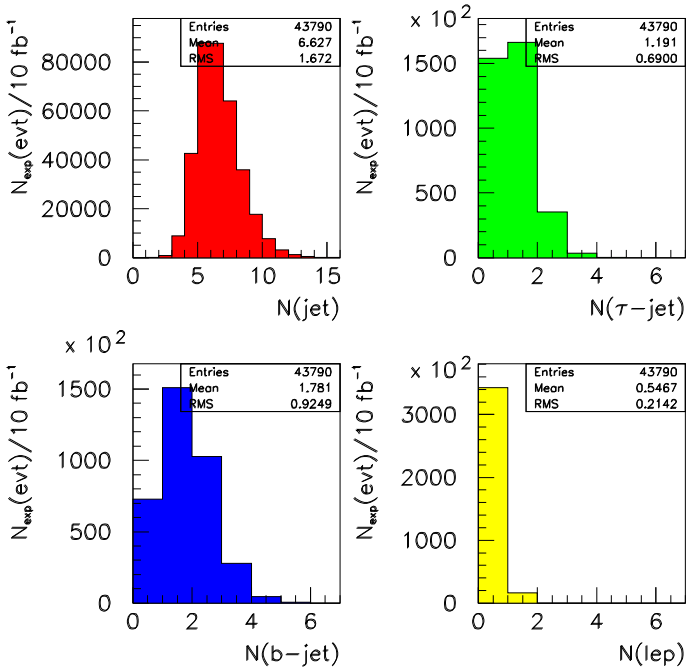

Figure 6.8: Total number of jets, number of τ and b jets and number of isolated leptons for a charged Higgs signal of $m_{H^\pm}$ =127 GeV and $\tan\beta = 30$ for one year running at low luminosity. The jet threshold was set to 10 GeV.

Concerning the p_T cut on the b jets, one keeps two thresholds, the lower one for the b jet on the $H^\pm$ side: since $m_{W^\pm} < m_{H^\pm}$, the b jet accompanying the $W^\pm$ will be harder than the other one.

The E_{Tmiss} cut is very effective against QCD background as shown in Fig. 6.9. In addition, the QCD rejection obtained with the E_{Tmiss} cut is not dependent on the E_{Tmiss} resolution, since the 45 GeV threshold is well above the expected ATLAS resolution on E_{Tmiss}, which is 5-10 GeV depending on the total event transverse energy (see section 3.3.2).

The p_T of the τ jet is shown in Fig. 6.10 for the same charged Higgs signal, for $t\bar{t}$ SM events and for QCD background.

The $p_T^{\tau jet}$ and the E_{Tmiss} cuts are also very effective against SM $t\bar{t}$ events while keeping a good efficiency for a charged Higgs signal of rather low mass. In Fig. 6.11, the E_{Tmiss} for SM $t\bar{t}$ events is shown together with the E_{Tmiss} for a charged Higgs

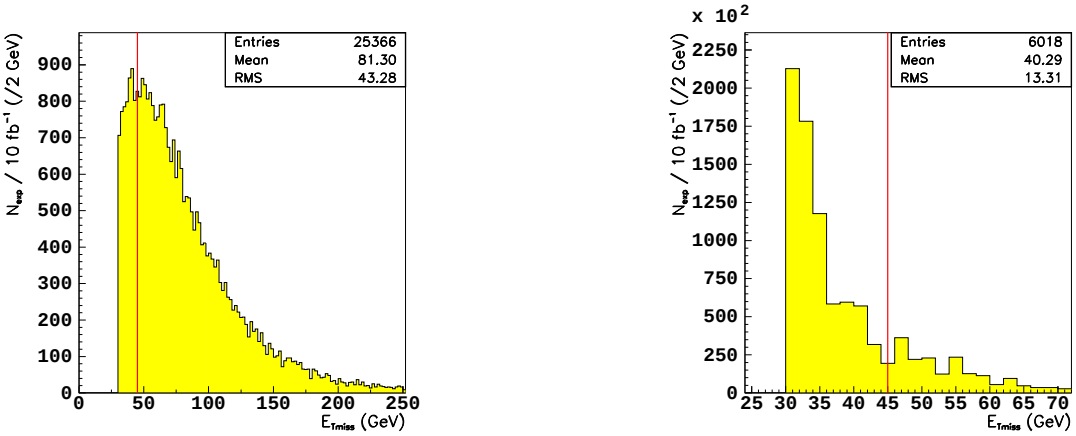

(a) $H^{\pm}$ signal

(b) QCD background

Figure 6.9: Missing transverse energy for a $H^{\pm}$ signal with $m_{H^{\pm}} = 127$ GeV and $\tan\beta = 30$ and for the QCD background events after the second group of selection cuts[7].

signal of $m_{H^{\pm}}$=90 GeV and $\tan\beta = 30$ for one year of running at low luminosity. In Fig. 6.12 the $p_T^{\tau jet}$ is shown for the same kind of events. One can see there that the τ polarization effects described in section 6.3.1 can still be observed in the $p_T^{\tau jet}$ distribution of a charged Higgs signal of such low mass, i.e. the τ jets from $H^+ \to \tau^+\nu_\tau$ produced in one prong τ decays are harder than the ones produced through $W^+ \to \tau^+\nu_\tau$.

4. Top mass reconstruction in the W side ($t \to W^+b$; $W \to q\bar{q}\prime$).
   The W mass is reconstructed with the two light jets, m_{jj}. In case than more than two light jets exist (a gluon jet with high energy may be assigned as a light jet), the combination with the mass closest to the W mass, $m_{W^{\pm}} = 80.33$ GeV[8] is selected. Afterwards, two top masses can be reconstructed taking the two light jets and each one of the b jets (m_{jjb}). The m_{jjb} which is closest to the top mass, $m_t = 175.0$

[7] In this section, the distributions of the cuts will be given for those events that passed the previous group of selection cuts, for example, the E_{Tmiss} distributions in Fig. 6.9 are given for signal and QCD background events after the second group of selection cuts (i.e., $N_{b\text{ jet}} = 2$, $N_{\tau\text{ jet}} = 1$, $N_{\text{light jet}} \geqq 2$ and no isolated lepton).

[8] Quoted value in Pythia.

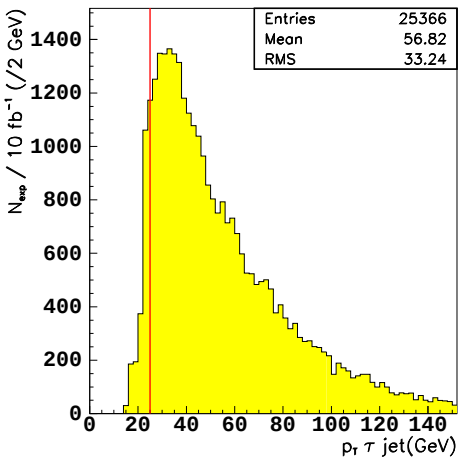

(a) $H^{\pm}$ signal

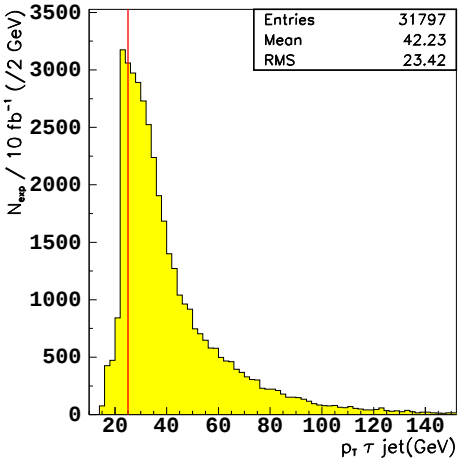

(b) $t\bar{t}$ SM

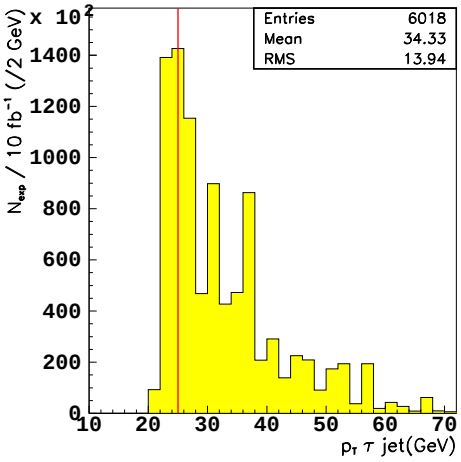

(c) QCD background

Figure 6.10: p_T of the τ jet after the second group of selection cuts (3-tag and no isolated lepton) for a $H^{\pm}$ signal with $m_{H^{\pm}} = 127$ GeV and $\tan\beta = 30$, for SM $t\bar{t}$ events and for QCD background.

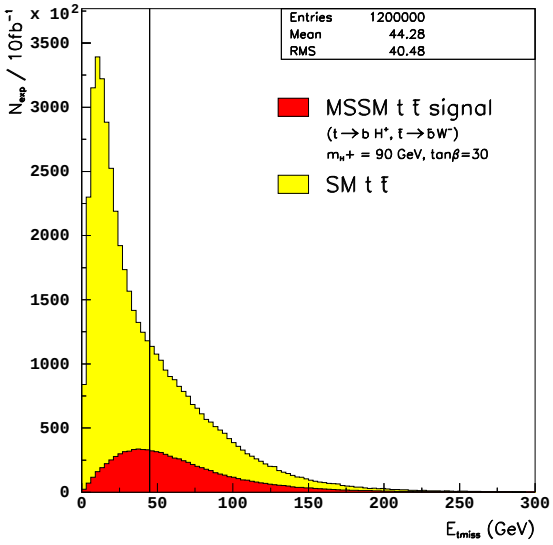

Figure 6.11: Missing transverse energy for a MSSM charged Higgs signal of $m_{H^{\pm}} = 90$ GeV and $\tan\beta = 30$ and for SM $t\bar{t}$ events for one year of running at low luminosity. No cuts were applied.

GeV[8]is taken. In addition, a p_T cut on the light jets is also performed. The applied cuts are:

- $|m_{jj} - m_W| < 20$ GeV with $m_W = 80.33$ GeV
- $p_T^{light\ jet1} > 30$ GeV; $p_T^{light\ jet2} > 20$ GeV
- $|m_{jjb} - m_t| < 40$ GeV with $m_t = 175$ GeV

The reconstructed $W^{\pm}$ and top masses for a charged Higgs signal with $m_{H^{\pm}} = 127.0$ GeV and $\tan\beta = 30$ after the third set of cuts are shown in Fig. 6.13. Due to FSR, the mjj and $mjjb$ distributions become relatively broad: FSR could reduce a reconstructed mass if energy is radiated outside the reconstruction cone. On the other hand, FSR from other partons could also fall within a cone, increasing the reconstructed mass.

5. Back-to-back topology.
   Some further reduction of the QCD background is possible by requiring a $t\bar{t}$ back-to-back topology, since the signal events are split in two differentiated hemispheres, namely, the $W^{\pm}$ side and the $H^{\pm}$ side. The following cuts are applied:

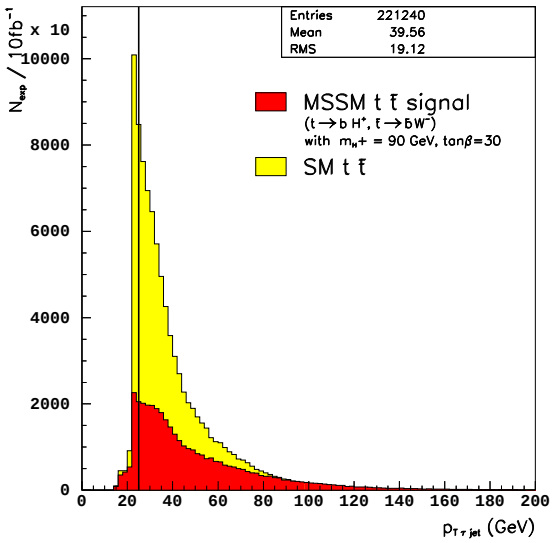

Figure 6.12: Transverse momentum of the τ jet for a MSSM charged Higgs signal of $m_{H^\pm} = 90$ GeV and $\tan\beta = 30$ and for SM $t\bar{t}$ events for one year of running at low luminosity. No cuts were applied.

- $\Delta\phi(\vec{p}_T^{\,top1}, \vec{p}_T^{\,top2}) > 2.5$ rad with $\vec{p}_T^{\,top2} = \vec{p}_T^{\,b\ jet} + \vec{p}_T^{\,\tau\ jet} + \vec{E}_{Tmiss}$ for the top quark on the $H^\pm$ side [9].
- $p_T^{top\ 1}/p_T^{top\ 2} < 2$ (balanced momentum between 2 tops with $p_T^{top\ 1}(p_T^{top\ 2})$ the p_T of the hardest(softest) top.)
- $\Delta R(b\ jet1, b\ jet2) > 1.0$ with

$$\Delta R(b\ jet1, b\ jet2) \equiv \sqrt{\Delta\eta^2(b\ jet1, b\ jet2) + \Delta\phi^2(b\ jet1, b\ jet2)}$$

- $\Delta\phi(\vec{E}_{Tmiss}, \vec{p}_T^{\,b\ jet_W}) > 0.5$ with $b\ jet_W$ the b jet on the W side.

The $\Delta\phi$ between the two reconstructed tops is seen in Fig. 6.14 for a $H^\pm$ signal of $m_{H^\pm}$ =127 GeV and for QCD after the fourth set of cuts. Most of the signal events are really back to back, i.e. $\Delta\phi(\vec{p}_T^{\,top1}, \vec{p}_T^{\,top2})$ >2.5. The ratio between the transverse momentum of the two reconstructed tops is shown in Fig. 6.15 for the also for a $H^\pm$ signal of $m_{H^\pm} = 127.0$ GeV and for the QCD background after the fourth group of selection cuts.

[9] Only the transverse component could be used since for the reconstructed top on the $H^\pm$ side one has no information on the z component of the momentum.

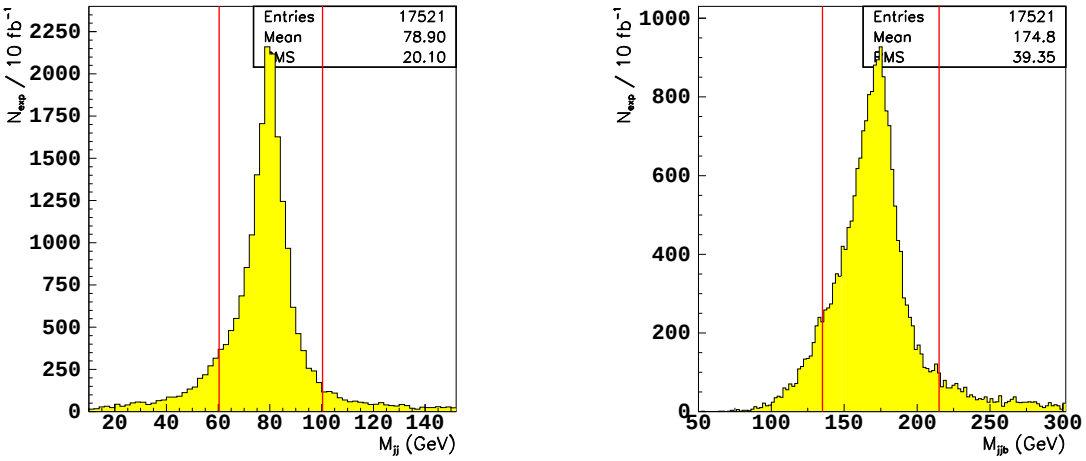

(a) m_{jj}: reconstructed $W^{\pm}$ mass

(b) m_{jjb}: reconstructed top mass

Figure 6.13: Reconstructed $W^{\pm}$ and top masses for charged Higgs signal events with $m_{H^{\pm}} = 127.0$ GeV and $\tan\beta = 30$ after the third group of selection cuts.

In addition, ΔR between the two b jets and $\Delta\phi$ between the b jet on the W side and the E_{Tmiss} distributions can be seen in Figs. 6.16 and 6.17 respectively for the same kind of events after the fourth set of cuts. As in can be seen in Fig. 6.17, the $\Delta\phi(\vec{E}_{Tmiss}, \vec{p}_T^{\,b\ jet_W})$ cut is very effective against QCD events.

6. Cuts on the charged Higgs side ($\bar{t} \to H^- \bar{b};\ H^- \to \tau^- \bar{\nu}_\tau$).
   On this side one has a reconstructed b jet and a τ jet. This structure can be faked by a quark+FSR as shown schematically in Fig. 6.18. In order to eliminate these QCD events the following cuts are applied:

   - $P_{REL}(\tau\ jet, b\ jet) \equiv \frac{|\vec{p}_{\tau\ jet}| \sin\theta_{\tau\ b}}{|\vec{p}_{\tau\ jet} + \vec{p}_{b\ jet}|} > 0.2$
   - $p_T^{\tau\ jet}/p_T^{b\ jet} > 0.8$

   The P_{REL} variable is quite powerful against QCD as it can be seen in Fig. 6.19 for a charged Higgs signal with $m_{H^{\pm}} = 127.0$ GeV and $\tan\beta = 30$ and for QCD events after the fifth group of selection cuts. For the charged Higgs signal, those events with $P_{REL} \sim 1$ are the ones with $\theta_{\tau\ b} \approx 90^o$ and with $|\vec{p}_{\tau\ jet}| \gg |\vec{p}_{b\ jet}|$. In addition,

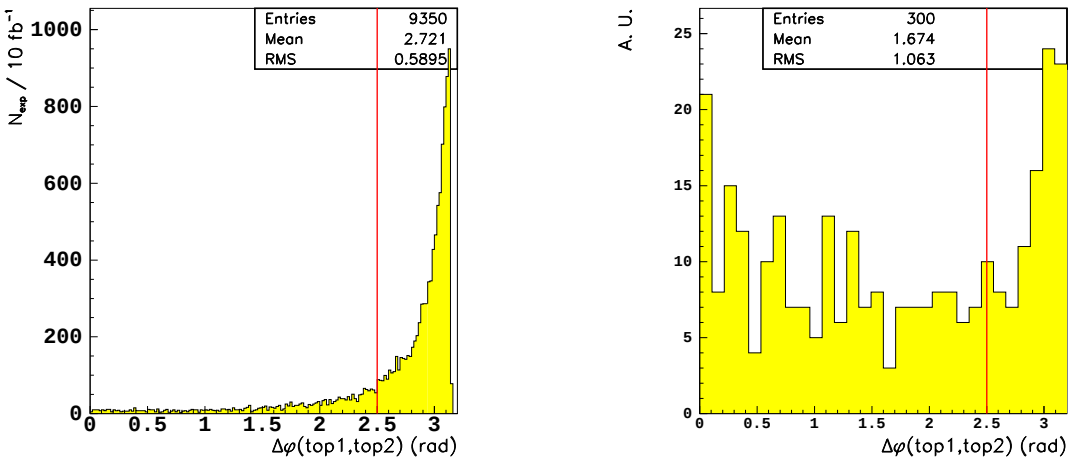

(a) $H^{\pm}$ signal

(b) QCD background

Figure 6.14: $\Delta\phi(\vec{p}_T^{\,top1}, \vec{p}_T^{\,top2})$ between the two tops for a charged Higgs signal with $m_{H^{\pm}} = 127.0$ GeV and $\tan\beta = 30$ and for QCD events after the fourth group of selection cuts. $H^{\pm}$ signal events distribution is done for one year of running at low luminosity, on the contrary, QCD events distribution contains unweighted Monte Carlo events for a better graphical understanding.

in the $0.9 \lesssim P_{REL} \lesssim 1$ region, the contribution of the signal events with $\theta_{\tau\, b} \gtrsim 90^o$ and $\theta_{\tau\, b} \lesssim 90^o$ is summed up.

The $p_T^{\tau\, jet}/p_T^{b\, jet}$ distribution is shown in Fig. 6.20 for two charged Higgs samples of mass $m_{H^{\pm}} = 127.0$ GeV and $m_{H^{\pm}} = 145.0$ GeV, $\tan\beta = 30$, for $t\bar{t}$ SM events and for QCD events after the fifth group of selection cuts. As it can be seen, this cut depends critically on the charged Higgs mass: the hardness of the τ jet increases with the charged Higgs mass and this translates in an increase of the $p_T^{\tau\, jet}/p_T^{b\, jet}$ ratio. Moreover, those τ jets produced in $W^{\pm}$ decay from $t\bar{t}$ SM are not as hard as the ones produced in $H^{\pm}$ decay. Thus, the $p_T^{\tau\, jet}/p_T^{b\, jet}$ ratio is a good discriminating variable against SM $t\bar{t}$ background.

Using this set of cuts, all the SM backgrounds were swept away except the SM $t\bar{t}$ events and few QCD background events.

In order to be sure about the consistency of the results concerning the QCD back-

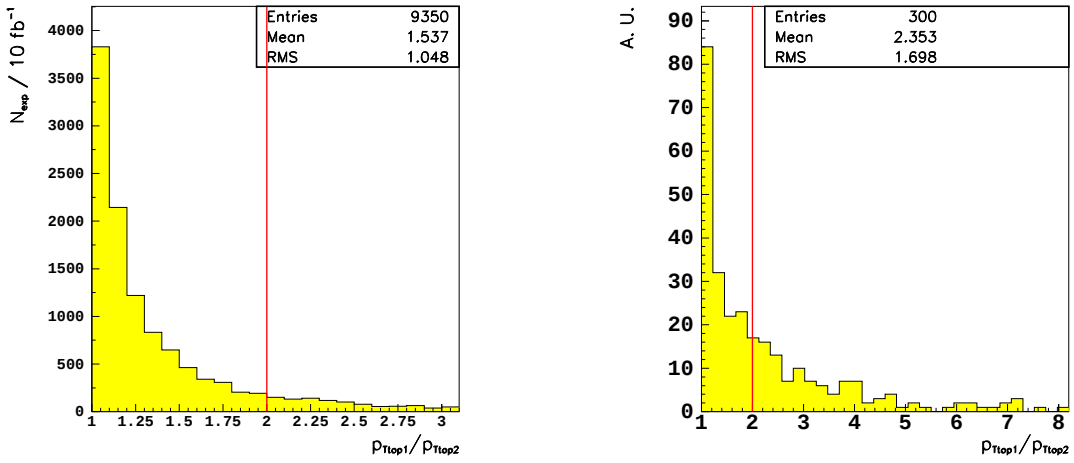

(a) $H^{\pm}$ signal

(b) QCD background

Figure 6.15: Ratio of the transverse momentum of the two reconstructed tops for a charged Higgs signal with $m_{H^{\pm}} = 127.0$ GeV and $\tan\beta = 30$ and for QCD events after the fourth group of selection cuts. The top with highest p_T comes in the nominator. Event distributions as in Fig. 6.14.

ground, five different random numbers where used in the analysis embedded in AtlfastB-Fortran. After passing all QCD $\hat{p_T}$ bin samples through the analysis 5 times, for each one of the 5 random number set only 0, 0, 19.7, 10.1, and 7.2 events were respectively left.

The number of expected events after trigger and the relative efficiency at each cut step is given in Table 6.5 for a MSSM charged Higgs signal at 6 different $m_{H^{\pm}}$ (and consequently, m_A) points keeping $\tan\beta$ constant to 30 for one year of running at low luminosity. In addition, the final number of expected events after all cuts is also given.

The number of expected events after 3-tag + no isolated lepton selection (cuts group number 2. at the beginning of this section) as well as the relative efficiency after each group of cuts is given in Table 6.6 for the SM backgrounds (For the QCD events, only the first random number set is shown) for the same luminosity conditions. As in the signal case, the number of expected events after all set of cuts is also given.

Table 6.7 shows the number of expected events after 3-tag + no isolated lepton selection and the relative efficiency after each group of cuts as it was given in Table 6.6 for

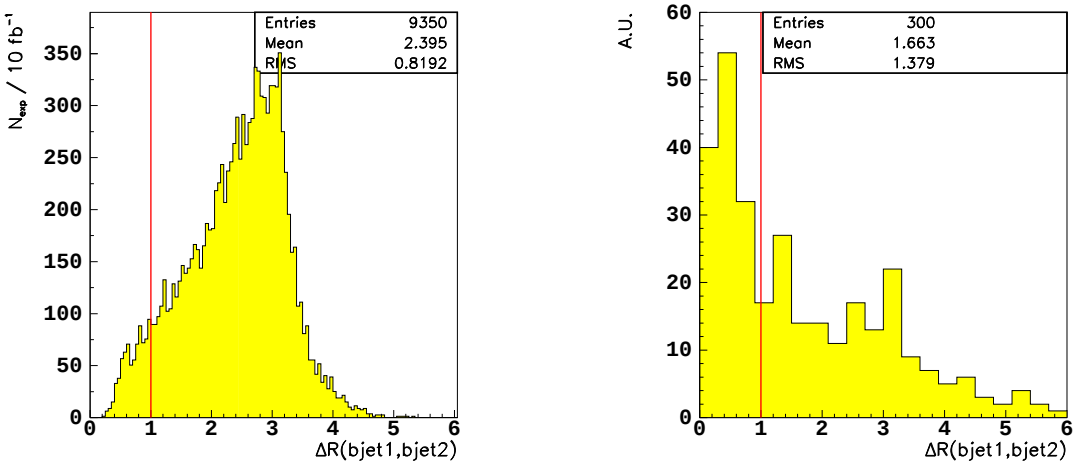

(a) $H^{\pm}$ signal

(b) QCD background

Figure 6.16: ΔR between the two b jets for a charged Higgs signal with $m_{H^{\pm}} = 127.0$ GeV and $\tan\beta = 30$ and for QCD events after the fourth group of selection cuts. Event distributions as in Fig. 6.14.

the SUSY backgrounds that were listed in Table 6.1. Only the data corresponding to the (m_A, $\tan\beta$) point with biggest $\sigma \times BR$ is shown. The same luminosity conditions were applied.

In Fig. 6.21, the relative efficiency for a single charged Higgs production signal as a function of the charged Higgs mass is shown for three different cases:

- Global[10] vs. 3-tag: relative efficiency between the complete set of selection cuts and the cuts at the 3-tag + no isolated lepton step.
- 3-tag vs. trigger: relative efficiency between the 3-tag + no isolated lepton cuts and the trigger cuts.
- Global vs. trigger: relative efficiency between the whole set of selection cuts and the trigger cuts.

[10]Here global refers to all selection cuts.

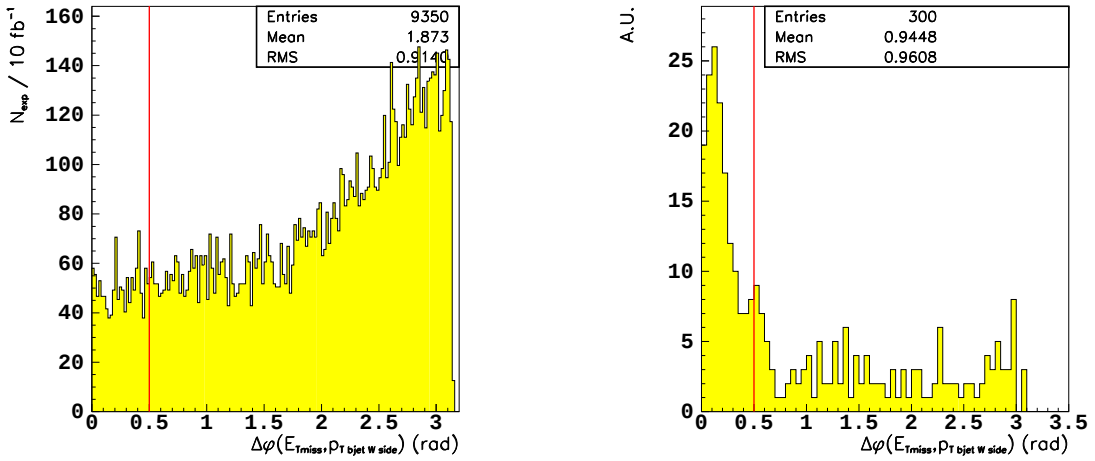

(a) $H^{\pm}$ signal

(b) QCD background

Figure 6.17: $\Delta\phi$ between the b jet on the W side and the E_{Tmiss} for a charged Higgs signal with $m_{H^{\pm}} = 127.0$ GeV and $\tan\beta = 30$ and for QCD events after the fourth group of selection cuts. Event distributions as in Fig. 6.14.

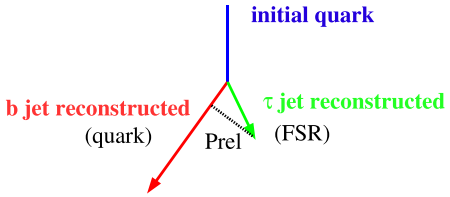

Figure 6.18: Scheme of a quark with FSR faking a τ jet and a b jet.

The 3-tag + no isolated lepton cuts have a low efficiency especially for high charged Higgs masses (3-tag vs. trigger curve), but these cuts were applied in order to obtain a clean signature. Therefore, one tries to enhance the efficiency for high charged Higgs masses by means of the cuts that come after the 3-tag + no isolated lepton step (global vs. 3-tag curve). At the end, almost a flat efficiency is obtained (global vs. trigger curve). Therefore, after the complete set of cuts, a constant efficiency is obtained throughout the whole charged Higgs mass spectrum.

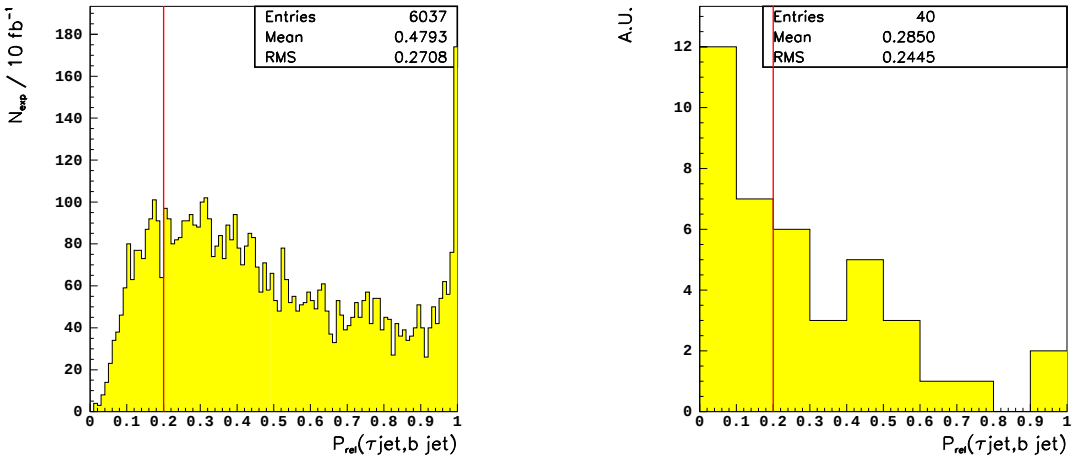

(a) $H^{\pm}$ signal

(b) QCD background

Figure 6.19: $P_{REL}(\tau\ jet, b\ jet)$ between the τ jet and the b jet on the $H^{\pm}$ side for a charged Higgs signal with $m_{H^{\pm}} = 127.0$ GeV and $\tan\beta = 30$ and for QCD events after the fifth group of selection cuts. Event distributions as in Fig. 6.14.

6.4.2 Further event selection

After the previous event selection, there were still some SM $t\bar{t}$ background events left as shown in Table 6.6 as well as a few SUSY events mainly from $b\bar{b}\phi$ ($\phi = h, H, A$) processes.

The MSSM $(m_A, \tan\beta)$ points with $m_{H^{\pm}}$ <113 GeV had a big enough $BR(t \to bH^{+})$ so that when computing the statistical significance given by Eq. (6.13) a value well above 5 was obtained. Therefore, no further cuts were applied to those events.

On the contrary, those events with $m_{H^{\pm}} \gtrapprox$113 GeV had a limited significance. Therefore, a harder cut on the p_T of the τ jet (taking profit of the τ polarization effect described in section 6.3.1) was applied, namely $p_T^{\tau\ jet} > 30$ GeV. Moreover, the transverse mass given by Eq. (6.16) turned to be a decisive variable to cut on, since its distribution for the MSSM $t\bar{t}$ and SM $t\bar{t}$ events is quite different as it can be seen in Fig. 6.22: the M_T distribution for the SM $t\bar{t}$ processes is kinematically constrained to be below $m_{W^{\pm}}$, but for the MSSM $t\bar{t}$ processes, this upper bound is given by $m_{H^{\pm}}$. Thus, a M_T >80 GeV

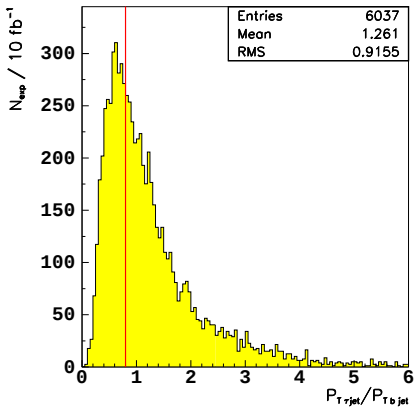

(a) $H^{\pm}$ signal, $m_{H^{\pm}} = 127.0$ GeV

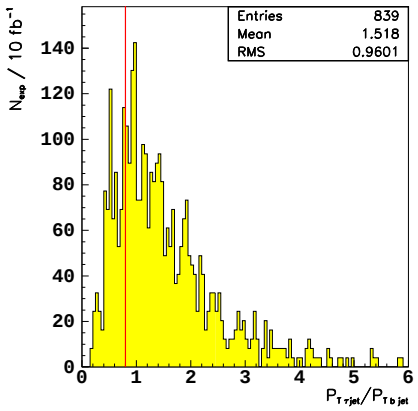

(b) $H^{\pm}$ signal, $m_{H^{\pm}} = 145.0$ GeV

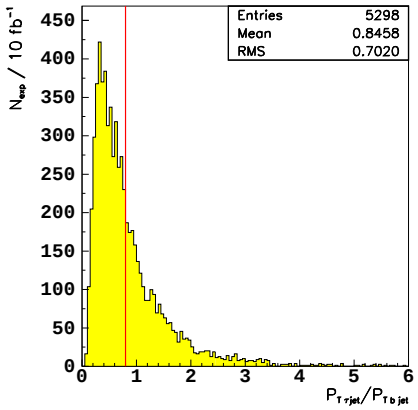

(c) $t\bar{t}$ SM

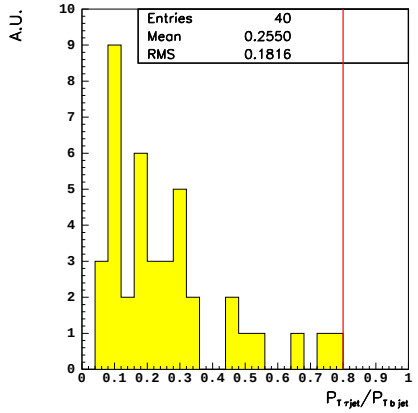

(d) QCD background

Figure 6.20: $p_T^{\tau\,jet}/p_T^{b\,jet}$ for two charged Higgs of mass $m_{H^{\pm}} = 127.0$ GeV and $m_{H^{\pm}} = 145.0$ GeV respectively and $\tan\beta$=30, for SM $t\bar{t}$ background and for QCD background events after the fifth group of selection cuts. $H^{\pm}$ signal and $t\bar{t}$ SM events distributions are done for one year of running at low luminosity, on the contrary, QCD events distribution contains Monte Carlo events.

cut was also applied.

$$M_T = \sqrt{2 \cdot |\vec{p}_T^{\,\tau jet}| \cdot |\vec{E}_{T miss}| \cdot \cos(\Delta\phi(\vec{p}_T^{\,\tau jet}, \vec{E}_{T miss}))} \tag{6.16}$$

Cuts $m_A \rightarrow$ / $\downarrow$ $m_{H^\pm} \rightarrow$	Signal					
	11.0 / **84.9**	**53.9** / **100.1**	**84.9** / **119.7**	**94.8** / **127.0**	**111.8** / **140.2**	**135.8** / **160.0**
(t20xe30)OR(j60xe60) N_{EXP}	$51.2{\cdot}10^4$	$48.4{\cdot}10^4$	$40.5{\cdot}10^4$	$35.3{\cdot}10^4$	$25.8{\cdot}10^4$	$6.4{\cdot}10^4$
(t20xe30)OR(j60xe60)	53.8	55.9	60.1	60.7	63.6	70.0
3-tag & no isol. lep	10.3	10.0	9.5	8.9	6.9	4.1
$E_{Tmiss} > 45$ GeV	75.9	77.3	79.7	79.8	83.3	90.0
p_T^{bjets} >35, 20 GeV	95.9	95.0	93.4	93.1	90.6	81.3
$p_T^{\tau\ jet} > 25$ GeV	87.8	88.3	90.8	91.1	93.1	93.4
$\lvert m_{jj} - m_W \rvert < 20$ GeV	80.5	80.9	80.2	79.9	78.9	73.6
$p_T^{lightjets}$ >30, 20 GeV	76.0	76.5	76.8	76.6	75.0	73.4
$\lvert m_{jjb} - m_t \rvert < 40$ GeV	87.0	87.8	88.4	88.3	87.5	85.2
$\Delta\phi(top1, top2)$ >2.5 rad	82.2	81.8	80.4	80.5	78.8	82.7
$p_T^{top\ 1}/p_T^{top\ 2}$ <2	92.5	92.2	92.6	92.1	92.6	91.0
$\Delta R(b\ jet1, b\ jet2)$ >1.0	92.5	94.1	93.9	95.0	94.5	96.0
$\Delta\phi(\vec{E}_{Tmiss}, \vec{p}_T^{\ b\ jet_W})$ >0.5	93.5	93.5	92.3	92.0	91.7	86.3
$P_{REL}(\tau\ jet, b\ jet)$ >0.2	76.1	77.5	83.0	81.0	85.0	93.6
$p_T^{\tau\ jet}/p_T^{b\ jet} > 0.8$	57.3	58.2	66.4	69.9	76.0	84.7
All cuts N_{EXP}	$5.1{\cdot}10^3$	$5.1{\cdot}10^3$	$5.0{\cdot}10^3$	$4.2{\cdot}10^3$	$2.9{\cdot}10^3$	$4.1{\cdot}10^2$

Table 6.5: Number of expected events for the signal after trigger and after all selection cuts and relative efficiency (in percent) after each cut selection at different $m_A/m_{H^\pm}$ points and $\tan\beta$ =30 for 10 fb^{-1}. m_A and $m_{H^\pm}$ given in GeV. The first three columns were already excluded by LEP as seen in Fig. 6.7 but they are listed here in order to show how the cut efficiencies and the final number of expected events change with the $H^\pm$ mass.

After the $p_T^{\tau\ jet}$ and the M_T cuts, the SM $t\bar{t}$ background was reduced by ~85% and the SUSY backgrounds were reduced by ~95%. The efficiency of the $p_T^{\tau\ jet} > 30$ GeV and the M_T >80 GeV cuts as well as the final number of expected events for 10 fb^{-1} of data are given in Table 6.8 for the SM $t\bar{t}$ and QCD backgrounds and for the $gg,\ q_i\bar{q}_i \rightarrow \tilde{t}\tilde{t};\ \chi_1^\pm\chi_1^\pm$..., $gg,\ q_i\bar{q}_i \rightarrow b\bar{b}\phi$ and $gg,\ q_i\bar{q}_i \rightarrow t\bar{t}\phi$ ($\phi = h, H, A$) SUSY backgrounds.

In Fig. 6.23, the relative efficiency between the $m_T > 80$ GeV and $p_T^{\tau\ jet}$ >30 GeV cuts and the event selection (QCD filter cuts given in section 6.4.1) is shown as a function of $m_{H^\pm}$ for the charged Higgs signal. As it was stated above, the $m_T > 80$ GeV and

Cuts	SM backgrounds				
	$t\bar{t}$	QCD	(Z/γ^*) +jet	W +jet	WW;$W(Z/\gamma^*)$; $(Z/\gamma^*)(Z/\gamma^*)$
3-tag & no isol. lep N_{EXP}	$4.0{\cdot}10^4$	$1.0{\cdot}10^6$	$1.7{\cdot}10^3$	$2.6{\cdot}10^3$	$0.6{\cdot}10^2$
3-tag & no isol. lep **(2)**	0.8	$18{\cdot}10^{-8}$	$29{\cdot}10^{-6}$	$16{\cdot}10^{-5}$	$25{\cdot}10^{-5}$
E_{Tmiss} and p_T^{jet} cuts **(3)**	55.6	14.0	2.3	50.0	0
Top and W mass rec **(4)**	48.0	14.4	38.9	0	0
Back to back topology **(5)**	62.4	12.6	71.4	0	0
Cuts on the $H^{\pm}$ side **(6)**	34.3	0.8	0	0	0
All cuts N_{EXP}	$2.3{\cdot}10^3$	20.0	0	0	0

Table 6.6: Number of expected events for the SM backgrounds after 3-tag and no isolated lepton cuts (cuts group number 2.) and relative efficiency (in percent) after each group of cut selection for 10 fb^{-1}.

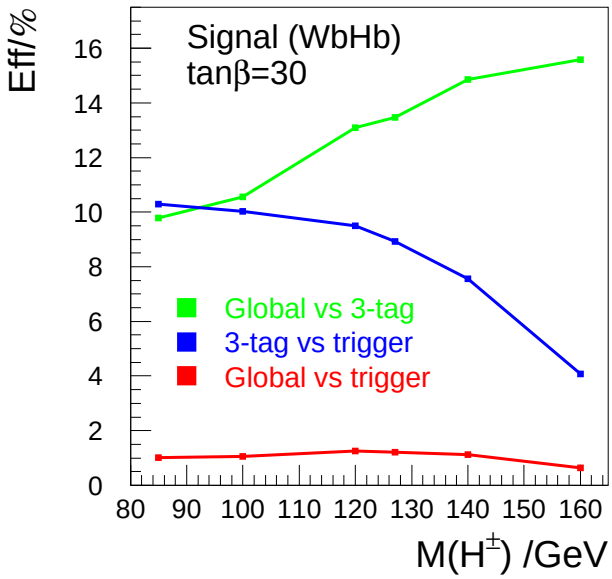

Figure 6.21: Relative efficiency for a single charged Higgs production signal as a function of the charged Higgs mass for three different cases: (i) global vs. 3-tag, relative efficiency between the complete set of selection cuts and the cuts at the 3-tag + no isolated lepton step; (ii) 3-tag vs. trigger, relative efficiency between the 3-tag + no isolated lepton cuts and the trigger cuts; (iii) global vs. trigger, relative efficiency between the whole set of selection cuts and the trigger cuts. In all cases, $\tan\beta$ =30 was used.

Cuts	**SUSY backgrounds:** $gg,\ q_i\bar{q}_i \to \tilde{t}\tilde{t};\ \chi_1^{\pm}\chi_1^{\pm}$		
	Value	m_A **(GeV)**	$\tan\beta$
3-tag & no isol. lep N_{EXP}	$2.6{\cdot}10^2$	91.8	20
3-tag & no isol. lep **(2)**	0.5	91.8	20
E_{Tmiss} and p_T^{jet} cuts **(3)**	76.7	91.8	20
Top and W mass rec **(4)**	36.7	94.8	30
Back to back topology **(5)**	13.7	112.8	3
Cuts on the $H^{\pm}$ side **(6)**	31.8	94.8	7.5
All cuts N_{EXP}	3.2	94.8	7.5

Cuts ↓	(m_A,$\tan\beta$) of $(\sigma \times BR)_{MAX} \to$	**Rest of SUSY backgrounds**				
		$gg,\ q_i\bar{q}_i \to b\bar{b}\phi$ **(112.8,3)**	$gg,\ q_i\bar{q}_i \to t\bar{t}\phi$ **(112.8,3)**	$f\bar{f}_i \to W^{\pm}\phi$ **(139.7,3)**	$f_i f_j \to f_i f_j \phi$ **(112.8,3)**	$f_i\bar{f}_i \to Z\phi$ **(92.8,50)**
3-tag & no isol. lep N_{EXP}		$3.8{\cdot}10^3$	$1.5{\cdot}10^2$	13.3	17.8	9.1
3-tag & no isol. lep **(2)**		$0.1{\cdot}10^{-1}$	2.0	$0.6{\cdot}10^{-1}$	$0.4{\cdot}10^{-1}$	$0.8{\cdot}10^{-1}$
E_{Tmiss} and p_T^{jet} cuts **(3)**		30.5	60.8	34.6	18.7	42.4
Top and W mass rec **(4)**		15.7	53.4	11.1	0	21.4
Back to back topology **(5)**		66.7	37.8	0	0	66.7
Cuts on the $H^{\pm}$ side **(6)**		50	39.1	0	0	50
All cuts N_{EXP}		62.0	7.2	0	0	0.3

Table 6.7: Number of expected events for the SUSY backgrounds after 3-tag and no isolated lepton selection and relative efficiency (in percent) after each group of cuts selection for 10 fb^{-1}. In the first Table, only the results of the (m_A,$\tan\beta$) point with maximum $\sigma \times BR$ (columns 3 and 4) are listed as well as in the second Table, where m_A and $\tan\beta$ of the maximum $\sigma \times BR$ point written at the header of each column.

$p_T^{\tau\ jet}$ >30 GeV cuts were only applied on those events with $m_{H^{\pm}}$ >113 GeV. For low charged Higgs masses (i.e., $m_{H^{\pm}} \to m_{W^{\pm}}$), the transverse mass cut is not very effective since it kills most of the signal. For higher charged Higgs masses it starts being quite effective since the upper bound on the M_T distribution is moved to a higher value. Moreover, when increasing the charged Higgs mass, the τ jet from $H^{\pm} \to \tau\nu$ decay becomes harder improving the efficiency of the combined m_T and $p_T^{\tau\ jet}$ cuts.

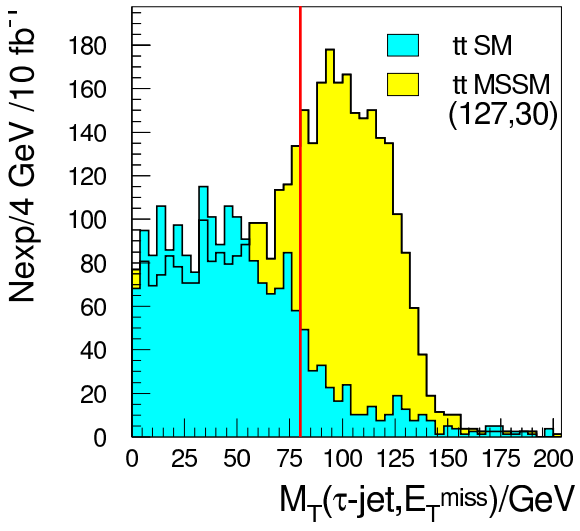

Figure 6.22: Transverse mass distribution after selection cuts (QCD filter) for MSSM $t\bar{t}$ events with $m_{H^{\pm}} = 127$ GeV and $\tan\beta$ =30 and for SM $t\bar{t}$ events for one year of running at low luminosity.

		$p_T^{\tau\,jet}$ >30 GeV & M_T > 80 GeV eff.	$p_T^{\tau\,jet}$ >30 GeV & M_T >80 GeV N_{EXP}
SM bkgs	$t\bar{t}$	15.0	$3.5{\cdot}10^2$
	QCD	0	0
SUSY bkgs	$gg,\ q_i\bar{q}_i \to \tilde{t}\tilde{t};\ \chi_1^{\pm}\chi_1^{\pm}$ $m_A = 94.8$ GeV, $\tan\beta = 30$	58.9	2
	$gg,\ q_i\bar{q}_i \to b\bar{b}\phi\ (\phi = h, H, A)$ $m_A = 112.8$ GeV, $\tan\beta = 3$	0	0
	$gg,\ q_i\bar{q}_i \to t\bar{t}\phi\ (\phi = h, H, A)$ $m_A = 112.8$ GeV, $\tan\beta = 3$	23.7	2

Table 6.8: Efficiency (in percent, second column) and number of expected events (third column) after the $p_T^{\tau\,jet}$ >30 GeV and M_T >80 GeV cuts for the SM $t\bar{t}$ and QCD backgrounds and for the most important SUSY backgrounds (numbers corresponding to the (m_A, $\tan\beta$) point with highest $\sigma \times BR$) for 10 fb^{-1} of data.

6.5 Systematic errors and other uncertainties

When computing the statistical significance (Eq. (6.13)), several sources of systematic uncertainties should be taken into account:

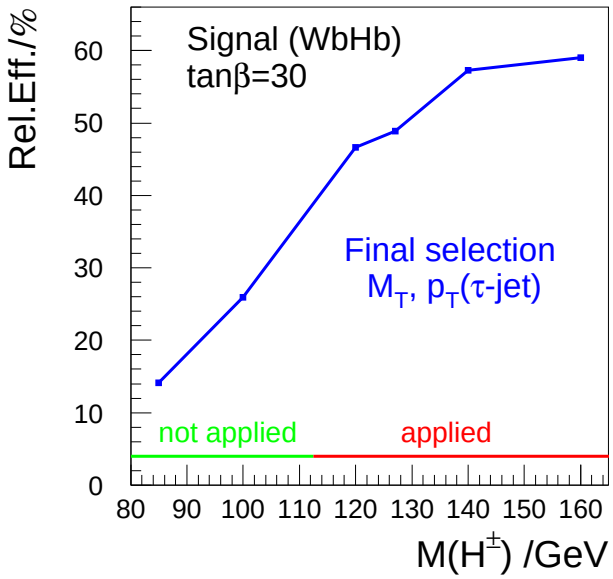

Figure 6.23: Relative efficiency between the $m_T > 80$ GeV and $p_T^{\tau\,jet}$ >30 GeV cuts and the event selection (QCD filter cuts given in section 6.4.1) as a function of $m_{H^\pm}$ for the charged Higgs signal. $\tan\beta$ was set to 30.

1. Systematics on the luminosity measurement.
   The luminosity is by definition a process-independent quantity which is completely determined by the properties of the colliding beams. Typically a 5-10% [42] precision for the luminosity determination is assumed for measurements in ATLAS, as obtained in previous and existing hadron-collider experiments. Here a ±10% effect is assumed in order to be conservative.

2. Systematics on the $t\bar{t}$ cross section.
   For the significance measurements, after the selection cuts given in the last section, almost all backgrounds are swept away except the $t\bar{t}$ SM one. Thus, the precision on the knowledge of $\sigma(t\bar{t})$ plays a very important role.

   Once the LHC will be running, $\sigma(t\bar{t})$ will be measured in ATLAS with a precision better than 10% [100]. So, the Pythia $\sigma_{LO\ pythia}(t\bar{t})$ was changed by ± 10% and the statistical significance was recalculated.

3. Systematics on the jet energy scale.
   The resolution on the absolute jet energy scale is subject to both physics (initial-

and final- state radiation, fragmentation, underlying event activity, jet algorithm, etc.) and detector (calorimeter response over a wide range of energies and over the full acceptance of the detector, non linearities at high energies, e/h ratio, etc.) effects.

The goal of the ATLAS experiment is to have a systematic uncertainty on the overall jet energy scale of ± 1 % as it was already pointed out in section 3.3.3. This can be possible by making use of several calibration methods. To start with, the ATLAS calorimeter modules are being calibrated in beams of electrons, muons and pions. After they will be installed into ATLAS, an inter-calibration between the different modules and calorimeters will be done by means of high p_T isolated charged pions from τ decays and QCD dijet events. Finally, once the LHC is running, light quark jets will be calibrated by making use of $W \rightarrow jj$ decays from top quark decay. Moreover, Z+jets events will be used not only to compare the calibration of the jet energy scale performed with $W \rightarrow jj$ but also to achieve a good accuracy on the b jet energy scale.

4. Systematics on the E_{Tmiss} scale.
   An accurate E_{Tmiss} measurement is crucial for the physics channel studied in this thesis. The most critical experimental issues for a reliable measurement of the event missing transverse energy are related to the performance of the calorimeters: good energy resolution, good response linearity and hermetic coverage are required.

   As it was pointed out in section 3.3.4, the overall E_{Tmiss} scale in ATLAS can be determined to ± 4 %.

5. Systematics on the τ-tagging efficiency.
   The uncertainty on τ-tagging efficiency arise mainly from the imperfect knowledge of the τ lepton efficiency from fake τ leptons present in the final sample. These effects were assumed to be $\pm 3\%$ from past experience [101].

6. Systematics due to different b-tagging efficiency/c and light jet rejections configurations.
   Concerning b-tagging, different "working points", that is, different b-tagging efficiency/jet rejection configurations were taken. The statistical significance was computed for two values of the light and c jet rejections maintaining the same b-tagging efficiency (used values in the Monte Carlo generation: $\epsilon_b = 60\%$, $R_c = 10$,

R_{light}=100). Thus, the c and light jet rejections were changed to R_c=9, R_{light}=90 and R_c=11, R_{light}=110 and then the statistical significance was recalculated.

7. Uncertainty on the $BR(t \to bH^+)/BR(t \to bW^+)$ values.
   Since these branching ratios are model dependent as it was pointed out in section 6.1.1, it was studied at which $BR(t \to H^+b)$ the statistical significance for a charged Higgs produced in top decays became equal to 5 for a given $\tan\beta$. These results will be given in the next section.

In addition, the systematic errors can be classified in three different categories:

- Systematic errors that affect only the background:
  for example the uncertainties on the luminosity and the $t\bar{t}$ cross section measurements[11]. To compute the effect of these systematics on the statistical significance, the number of expected events of the background is recalculated taking into account each systematic effect i. Thus, the significance due to the systematic effect i is calculated as:

$$S_{SYS_i} = \frac{N_{signal}}{\sqrt{N_{bkg_{SYS_i}}}} \tag{6.17}$$

  where N_{signal} is the number of signal events and $N_{bkg_{SYS_i}}$ is the number of background events applying the systematic error i. The variation that gives a bigger S_{SYS_i} is taken.

- Systematic errors that affect only the signal:
  the uncertainty on the $BR(t \to bH^+)/BR(t \to bW^+)$ would be one of those. But since nowadays there's no good estimate of this uncertainty, one presents it as a limit, i.e., for each $\tan\beta$, the minimum $BR(t \to bH^+)$ at which one gets a statistical significance equal to 5 is calculated.

- Systematic errors that affect both signal and background (correlated):
  the rest of systematic errors (jet energy scale, E_{Tmiss} scale, τ-tagging efficiency and

[11]Once ATLAS will be running, the number of expected signal events will be obtained from the experiment, and the number of expected background events will be taken from Monte Carlo generated samples, i.e., $N_{bkg} = (\sigma \times BR) \cdot \int \mathcal{L}dt \cdot \varepsilon_{CUTS}$

b-tagging efficiency/c and light jet rejections configurations) are of this type. The significance is recalculated as:

$$S_{SYS_i} = \frac{N_{signal_{SYS_i}}}{\sqrt{N_{bkg_{SYS_i}}}} \tag{6.18}$$

That is, both the signal and background expected number of events are computed taking into account the systematic error i. As before, the variation that increases the value of S_{SYS_i} is taken.

Each systematic error i will affect the statistical significance as:

$$\Delta S_{SYS_i} = \sqrt{S^2_{STAT} - S^2_{SYS_i}} \tag{6.19}$$

were S_{STAT} is given by Eq. (6.13). And if one assumes that the systematic errors are independent, the systematic errors global effect on the significance can be computed as:

$$\Delta S_{SYS_{total}} = \sqrt{\sum_i \Delta S^2_{SYS_i}} \tag{6.20}$$

To conclude, the final significance will be given by:

$$S_{FINAL} = \sqrt{S^2_{STAT} - \Delta S^2_{SYS_{total}}} \tag{6.21}$$

6.6 Statistical significance results

In section 6.2, the two different perspectives for computing the statistical significance were exposed. The results computed within the context of each one of the scenarios are given below.

6.6.1 SM hypothesis

In such scenario, an excess of events compared to the SM hypothesis should be demonstrated. To do so, the statistical significance is computed making use of Eqs. (6.13) and (6.19)-(6.21). The signal events considered in the SM hypothesis (S) are the MSSM $t\bar{t}$ events with one or two charged Higgs production as given at the beginning of section

6.3. The background processes (B) are strictly within the SM: $t\bar{t}$ SM and rest of SM backgrounds listed in Table 6.1.

The final significance results are given in Table 6.9 for 5 different points in the MSSM ($m_A/m_{H^\pm}$, $\tan\beta$) space for 1 year of running at low luminosity (10 fb^{-1}).

Sys. errors $m_A \rightarrow$ $\downarrow$ $m_{H^\pm} \rightarrow$	**11.0** **84.9**	**53.9** **100.1**	**84.9** **119.7**	**94.8** **127.0**	**111.8** **140.2**	**135.8** **160.0**
$\mathcal{L}$ measurement ($\pm$10%)	35.1	34.5	39.9	34.3	27.2	3.9
$\sigma(t\bar{t})$ precision ($\pm$10%)	35.0	34.2	39.5	34.0	27.0	3.8
Jet energy scale ($\pm$1%)	32.2	20.1	30.8	25.7	20.4	2.9
E_{Tmiss} scale ($\pm$4%)	32.8	25.9	53.1	35.8	30.4	3.6
τ-tagging eff. ($\pm$3%)	35.3	38.2	42.4	36.5	28.9	4.7
b-tagging (R_c, $R_{light}\pm$10%)	11.7	13.8	7.3	0	8.9	0
$\boldsymbol{\Delta S_{SYS_{total}}}$	77.1	71.3	93.7	74.9	61.0	8.5
$\boldsymbol{S_{STAT}}$	116.5	114.0	132.2	113.9	90.3	12.8
$\boldsymbol{S_{FINAL}}$	**87.3**	**88.9**	**93.2**	**85.8**	**66.6**	**9.6**

Table 6.9: Final significance results in the SM hypothesis at different (m_A,$m_{H^\pm}$, $\tan\beta$) points for 1 year of running at low luminosity (10 fb^{-1}). m_A and $m_{H^\pm}$ in GeV.

In addition, the number of expected signal events (with single charged Higgs production) can be seen in Fig. 6.24 for one year of running at low luminosity as a function of $\tan\beta$. Thus, already at the first year, a considerable yield of $t\bar{t} \rightarrow H^\pm bW^\mp\bar{b}$ events is foreseen in the MSSM. One can also observe the minimum around $\tan\beta \sim 7.5$ due to the $BR(t \rightarrow H^+b)$ dependence (see section 6.1.1). When $m_{H^\pm}$ approaches m_{top}, the number of expected events decreases dramatically, and the discovery in this mass region requires more statistics.

The final significance and the significance without taking into account systematic errors as a function of $\tan\beta$ are given in Fig. 6.25 for one year of running at low luminosity for different charged Higgs masses. The 5σ discovery limit is also drawn. As it was pointed out before, when $m_{H^\pm} \rightarrow m_{top}$ (e.g. $m_{H^\pm} = 155$ GeV) around the $\tan\beta$ minimum ($4 \lesssim \tan\beta \lesssim 10$) the charged Higgs cannot be discovered anymore, and for $m_{H^\pm} = 160$ GeV, the charged Higgs can only be discovered for $\tan\beta \gtrsim 20$ values. This situation improves a little bit when the significance is computed for 3 years of running at low

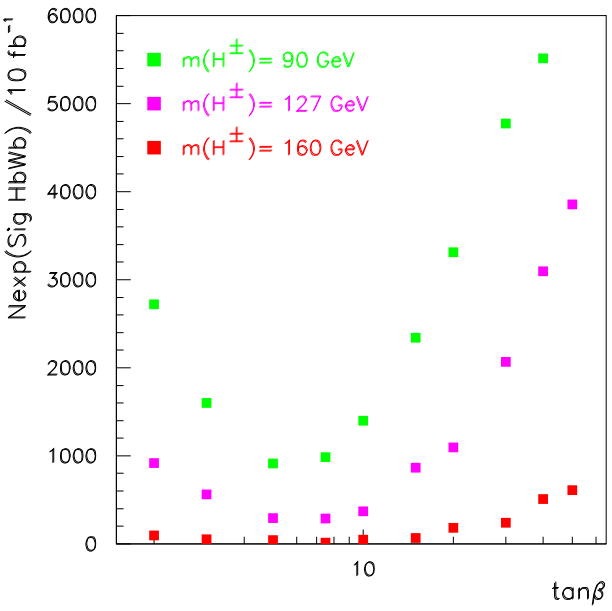

Figure 6.24: Number of expected signal events with single charged Higgs production as a function of $\tan\beta$ for one year running at low luminosity at three different $m_{H^{\pm}}$ values.

luminosity instead of one, i.e, $\int \mathcal{L}dt = 30$ fb^{-1}. On the other hand, a good significance is obtained for $m_{H^{\pm}} \lesssim 150$ GeV at any $\tan\beta$. As an example, for $m_{H^{\pm}} = 127$ GeV and $\tan\beta$ =30, and already at the first year, i.e., for 10 fb^{-1} of integrated luminosity, the final significance is 85 (and it gets reduced to 70 if the $p_T^{\tau\,jet} > 30$ GeV and M_T >80 GeV cuts are not applied).

In order to obtain the 5σ contour in the MSSM (m_A,$\tan\beta$) space, given a $\tan\beta$, the two closest m_A points (see Fig. 6.7) with S_{FINAL} >5 and S_{FINAL} <5 respectively were taken and a linear interpolation between them gave the m_A point at which S_{FINAL} =5. In Fig. 6.26, the 5σ discovery plot for a MSSM charged Higgs produced in top decays is shown in the (m_A, $\tan\beta$) space for the ATLAS detector. The results for the hadronic channel ($W \rightarrow qq\prime$) are represented for 10 and 30 fb^{-1} of integrated luminosity respectively. In addition, the 5σ line for the leptonic channel (that was already given in Fig. 2.7) for 30 fb^{-1} of data is superposed. Therefore, already at the first year of running at low luminosity ($\int \mathcal{L}dt = 10$ fb^{-1}), with the hadronic channel studied in this thesis, one is able to improve the discovery potential achieved with the leptonic one for 3 years of running at low luminosity. Moreover, with the hadronic channel for 3 years of running at low

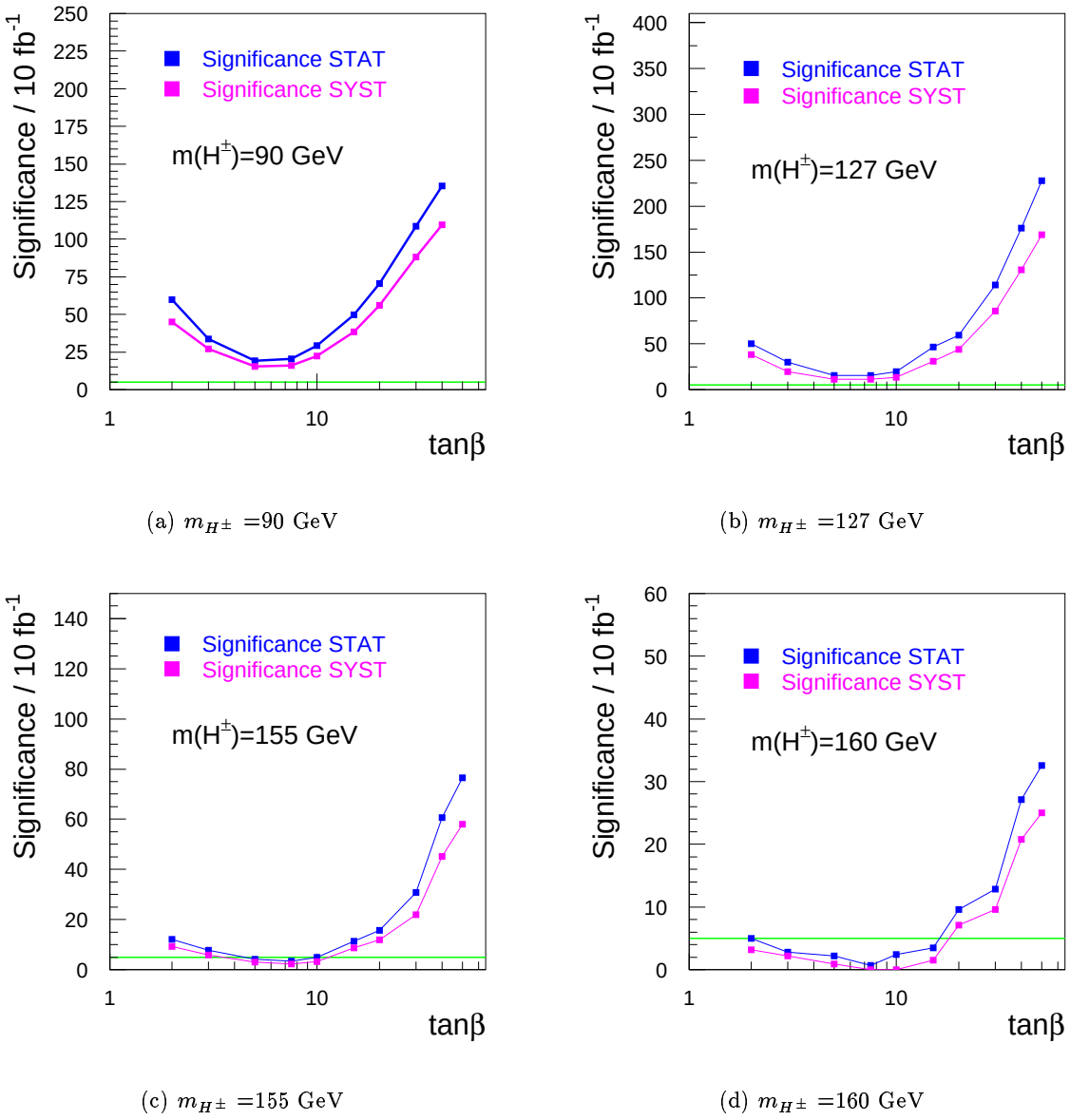

(a) $m_{H^\pm}$ =90 GeV

(b) $m_{H^\pm}$ =127 GeV

(c) $m_{H^\pm}$ =155 GeV

(d) $m_{H^\pm}$ =160 GeV

Figure 6.25: Final significance (Significance SYS) and significance without systematic errors effect (Significance STAT) as a function of $\tan\beta$ for one year of running at low luminosity and four different charged Higgs masses: 90, 127, 155 and 160 GeV. The 5σ line has also been drawn.

luminosity, the existing dip between $\tan\beta$ ~10 and $\tan\beta$ ~5 is now practically covered.

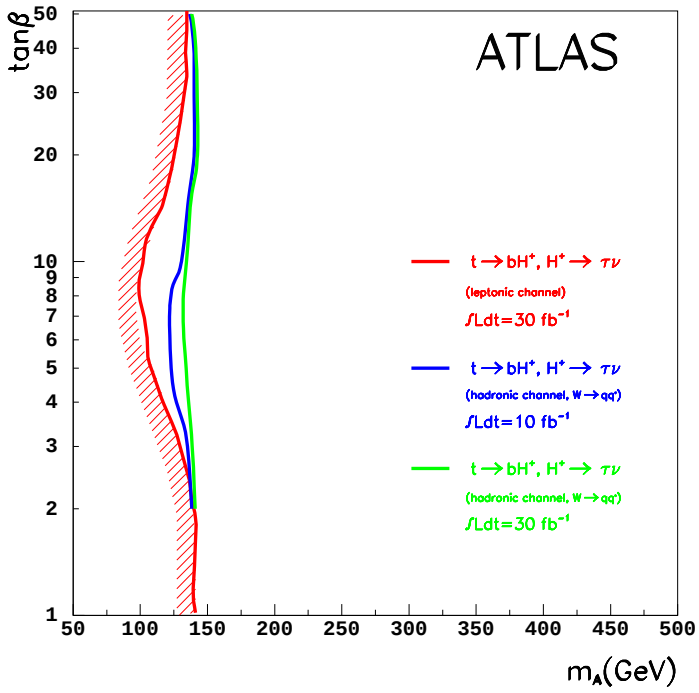

Figure 6.26: 5σ discovery plot for a MSSM charged Higgs produced in top decays for the ATLAS detector. The results for the hadronic channel ($W \to qq\prime$) are represented for 10 and 30 fb^{-1} of integrated luminosity respectively. In addition, the 5σ line for the leptonic channel for 30 fb^{-1} of integrated luminosity is also drawn. MSSM Maximal Mixing Scenario was used.

In Fig. 6.27(a), the 5σ discovery contour for a charged Higgs produced in top decays obtained in this work is superposed to Fig. 2.10 for one year of running at low luminosity. It can be seen that the before existing "hole" around $\tan\beta \sim$10 is now covered by this channel. To complement this plot, Fig. 6.27(b) shows the 5σ discovery contours for all MSSM Higgs for ATLAS and CMS combined and 30 fb^{-1} of integrated luminosity. The 5σ line for the channel studied in this thesis is superposed for 10 and 30 fb^{-1}: this channel contains the region around $\tan\beta \sim$6 that was before uncovered.

Hence, the 5σ survey in the MSSM (m_A, $\tan\beta$) space is now complete in ATLAS and CMS making use of the different MSSM Higgs (A, h, H, H^+, H^-) production and decay channels.

Finally, in Fig. 6.28, the $t \to H^+ b$ branching ratio at which one starts to be sensitive

(i.e. S_{FINAL} =5) to a charged Higgs produced in top decays is shown as a function of $\tan\beta$ for 10 fb^{-1} and for 30 fb^{-1} of integrated luminosity. The branching ratios were computed with Pythia 6.161 and a list of ($\tan\beta$, m_A, $BR(t \to H^+b)$) values was obtained. Then, given a $\tan\beta$, the m_A with S_{FINAL}=5 (i.e., from the 5σ line in Fig. 6.26) was taken and the corresponding branching ratio was linearly interpolated from the two nearest m_A values in the branching ratio list obtained with Pythia.

Already at the first year of running at low luminosity (10 fb^{-1}), one is sensitive to a MSSM $H^{\pm}$ signal produced with very low branching ratios, namely $BR(t \to H^+b)$ ~1.5% as it can be seen in Fig. 6.28.

6.6.2 MSSM hypothesis

Once it was shown that a good statistical significance can be obtained within the SM hypothesis, one wants to check if the charged Higgs signature can be extracted from the backgrounds within the MSSM frame (MSSM $t\bar{t}$, SM backgrounds and SUSY backgrounds listed in Table 6.1) as well, so that the charged Higgs properties like the mass and its couplings can be measured.

In this perspective, the signal S will be made of those processes with only one charged Higgs production (since the events with two charged Higgs cannot be used for the mass reconstruction as it was pointed out in section 6.3) as listed at the beginning of section 6.1. The background processes B will be represented by the before mentioned backgrounds existing in the MSSM scenario.

Since it was shown that almost all SUSY backgrounds were killed after selection and further selection cuts (see section 6.4), it can be stated than a good final significance can also be obtained in the MSSM hypothesis. Moreover, the MSSM $t\bar{t}$ background will also have a lower contribution than the SM $t\bar{t}$ background, since its branching ratio in the MSSM is always lower than 1. For example, for $m_{H^{\pm}}$ =127.0 GeV and $\tan\beta$ =30, the MSSM $t\bar{t}$ background branching ratio is 0.88. Therefore, the significance in the MSSM hypothesis was not recalculated since it was already demonstrated that the results would be similar to or even better than the ones obtained in the SM hypothesis.

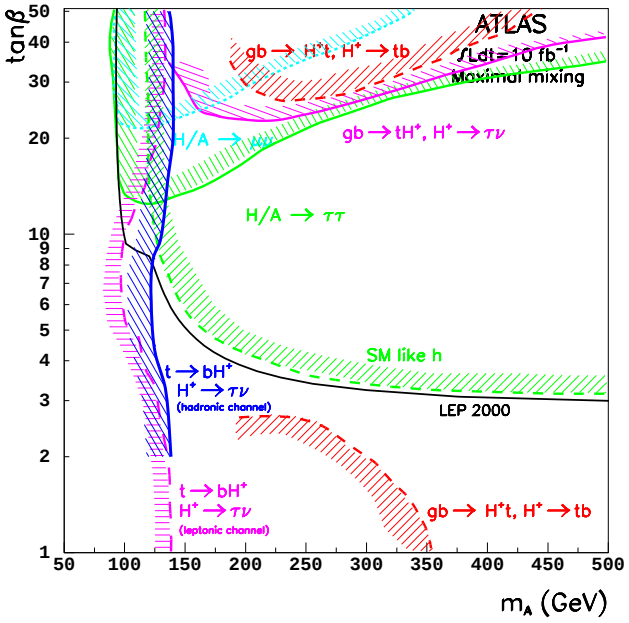

(a) ATLAS, $\int \mathcal{L}\mathrm{dt}$ =10 fb^{-1}.

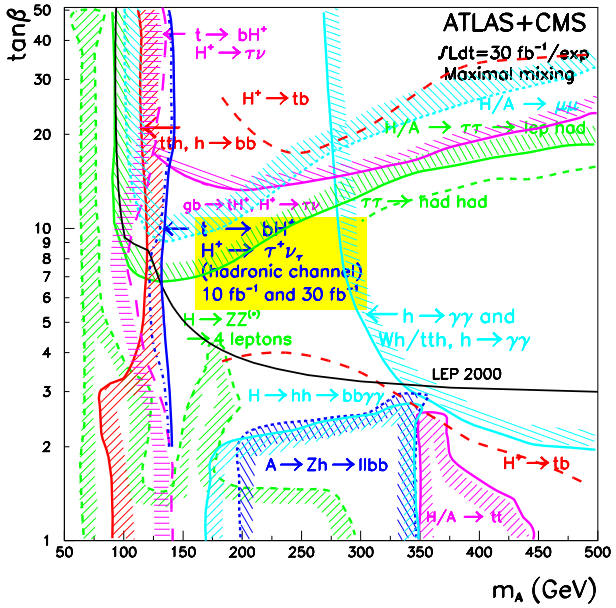

(b) ATLAS and CMS combined $\int \mathcal{L}\mathrm{dt}$ =30 fb^{-1}.

Figure 6.27: 5σ discovery contours for the MSSM Higgs bosons (h, H, A, H^+, H^-) obtained with different decay channels. The 5σ discovery contour for a charged Higgs produced in top decays obtained with the present work is also added (labeled as $t \to bH^+$, $H^+ \to \tau\nu$, hadronic channel). Maximal Mixing scenario was used. **Upper plot:** ATLAS, for 10 fb^{-1} of integrated luminosity. **Lower plot:** ATLAS and CMS combined, for 30 fb^{-1} of integrated luminosity.

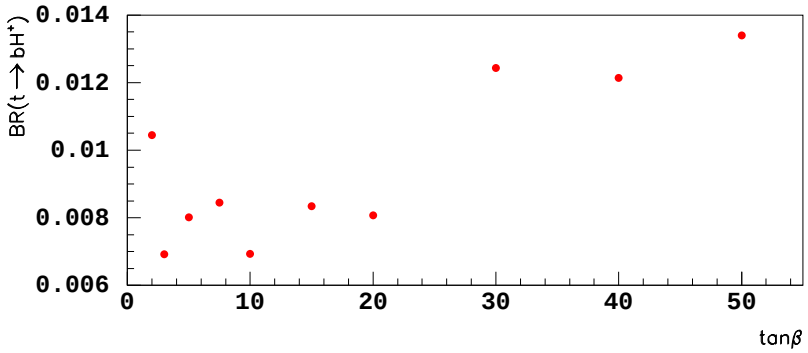

(a) $\int \mathcal{L}dt$=10 fb^{-1}

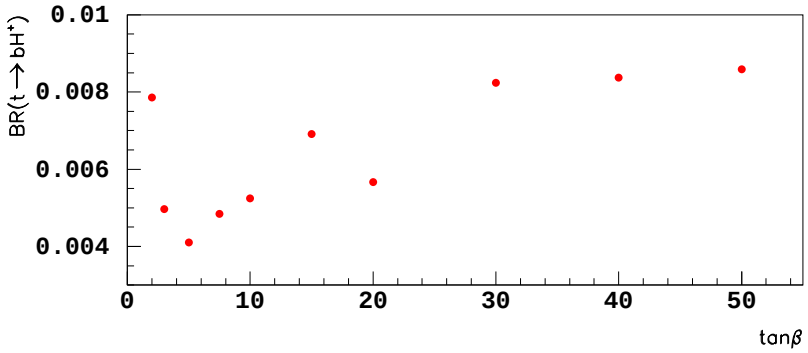

(b) $\int \mathcal{L}dt$=30 fb^{-1}

Figure 6.28: $BR(t \to H^+b)$ at which a final significance of 5σ for a MSSM charged Higgs produced in top decays is achieved. **Upper plot:** for 10 fb^{-1} of integrated luminosity. **Lower plot:** for 30 fb^{-1} of integrated luminosity.

Chapter 7

Mass extraction of a MSSM $H^{\pm}$ produced in top decays

In the previous chapter it was shown that within a SM as well as within a MSSM hypothesis, a good statistical significance could be obtained for a charged Higgs produced in top decays. Thus, it was demonstrated that in most of the ($m_A/m_{H^{\pm}}$, $\tan\beta$) space generated points, the charged Higgs signal could be extracted from the backgrounds that are present in the MSSM. Therefore, the charged Higgs boson parameters such as the mass, the decay width, the spin, the rates in the various decay channels and the couplings to SM and SUSY particles could in principle be measured. Furthermore, those measurements would be essential to determine the nature of the $H^{\pm}$ particle and to identify the actual scenario to which it belongs.

In this chapter, a method to reconstruct the charged Higgs mass is presented. Although the $H^{\pm} \to \tau^{\pm}\nu_{\tau}$ channel does not offer the possibility for the observation of a resonance peak above the background, the transverse charged Higgs boson mass given by Eq. (6.16) can be reconstructed because of the neutrinos in the final state. Therefore, the charged Higgs invariant mass is extracted from the transverse mass distribution by means of a maximum likelihood method.

In section 7.1, the signal and background Monte Carlo samples for the studies on the $H^{\pm}$ mass are listed. In section 7.2, the event selection cuts are exposed. Finally, in section 7.3, the light MSSM $H^{\pm}$ mass extraction procedure is described.

7.1 Signal and background Monte Carlo samples

The Monte Carlo event samples were generated with ATHENA PythiaModule with PDF CTEQ5L and TauolaModule[1] for polarized τ lepton decay within MSSM Maximal Mixing scenario at $\sqrt{s} = 14$ TeV. Besides, Atlfast package for fast detector simulation together with AtlfastB Algorithm for jet mis-tagging and energy calibration were used.

For the $t\bar{t}$ events generation, $\tan\beta = 30$ was taken and several charged Higgs masses were considered, namely:

$$\begin{aligned} m_H^{\pm}(\text{GeV}) = & 84.9, 90.2, 95.1, 100.1, 105.2, 110.2, 114.8, \\ & 119.7, 123.3, 127.0, 130.0, 134.7, 138.6, 145.0, \\ & 149.9, 155.8, 160.0, 165.1 \end{aligned} \tag{7.1}$$

Besides, the $t\bar{t}$ samples were split in three different groups (see Table 6.1):

- $t\bar{t}$ signal: signal process with one charged Higgs production as given at the beginning of section 6.1
- $t\bar{t} \to H^+ b H^- \bar{b}$ background: two charged Higgs in the final state
- Rest of $t\bar{t}$ background: rest of MSSM $t\bar{t}$ background processes

Moreover, the same SM backgrounds listed in Table 6.1 were also generated, namely:

- QCD: events generated in 22 different $\hat{p_T}$ bins
- (Z/γ^*)+jet: events generated in 3 different m_Z bins
- W+jet
- $(Z/\gamma^*)(Z/\gamma^*)$; $(Z/\gamma^*)W$; WW

SUSY background processes were not generated for the mass extraction studies since after the event selection cuts described in section 6.4, almost all of those events were

[1] As it was already pointed out in chapter 5, PythiaModule and TauolaModule interface respectively Fortran Pythia 6.161 and TAUOLA 2.6 versions.

rejected (see Table 6.7). Moreover, for the mass studies, only those events with transverse mass between 80 and 170 GeV were considered (as it will be show later on), and most of these SUSY background events had transverse masses lower than 80 GeV.

The statistics of the Monte Carlo samples for each process are listed in Table 7.1. Since the mass extraction studies started assuming a light charged Higgs of mass 127 GeV, the samples generated at this mass point have more statistics, in particular the MSSM $t\bar{t}$ Monte Carlo generated events at the $m_{H^\pm} = 127.0$ GeV and $\tan\beta = 30$ MSSM point have a statistical weight of $\lesssim 1$.

MSSM processes	**Events** ($\tan\beta = 30$)	
	$m_{H^\pm}$ **= 127 GeV**	**rest of** $m_{H^\pm}$
$t\bar{t}$ signal	597948	298974
$t\bar{t} \to H^+bH^-\bar{b}$	600 k	600 k
rest of $t\bar{t}$ bkg	4474300	797150

SM processes	**Events**
QCD (22 $\hat{p_T}$ bins)	1200 k/bin
Z/γ^*+jet (3 m_Z bins)	600 k/bin
W+jet	600 k
WW; WZ; ZZ	600 k

Table 7.1: Statistics of the Monte Carlo generated samples for mass extraction studies. MSSM $t\bar{t}$ events were generated at 18 different $m_{H^\pm}$ points with $\tan\beta = 30$. QCD and Z/γ^*+jet events were split in 22 $\hat{p_T}$ and 3 m_Z bins respectively.

7.2 Selection cuts

In order to extract the mass, the selection cuts given in section 6.4.1 were applied to both signal and background event samples. The number of expected events after trigger and after all selection cuts and the relative efficiency at each cut step are given in Table 7.2 for a MSSM $t\bar{t}$ signal with $m_{H^\pm}$=127.0, 138.6 and 145.0 GeV for one year of running at low luminosity (10 fb^{-1}). Note that this Table is not the same one as Table 6.5 obtained for the discovery studies: in the mass studies, the $t\bar{t} \to H^\pm bH^\mp\bar{b}$ events were considered

as background whereas in the discovery potential studies, they were considered as signal. In addition, the event generated samples are different as it was already pointed out in section 5.3.5.3: for the discovery potential studies, the Fortran code was used, and for the mass extraction studies, the ATHENA code was taken.

	Signal		
Cuts $m_A \rightarrow$	**94.8**	**109.8**	**117.8**
$\downarrow$ $m_{H^{\pm}} \rightarrow$	**127.0**	**138.6**	**145.0**
(t20xe30)OR(j60xe60) N_{EXP}	$36.4{\cdot}10^4$	$26.8{\cdot}10^4$	$20.5{\cdot}10^4$
(t20xe30)OR(j60xe60)	63.5	66.3	67.5
3-tag & no isol. lep	9.0	8.0	7.3
$E_{Tmiss} > 45$ GeV	81.2	83.6	84.0
p_T^{bjets} >35, 20 GeV	92.3	90.8	88.7
$p_T^{\tau\ jet} > 25$ GeV	90.2	91.1	91.0
$\lvert m_{jj} - m_W \rvert < 20$ GeV	84.5	83.5	83.4
$p_T^{lightjets}$ >30, 20 GeV	67.3	66.1	67.0
$\lvert m_{jjb} - m_t \rvert < 40$ GeV	87.6	87.3	86.6
$\Delta\phi(top1, top2)$ >2.5 rad	78.4	78.3	78.5
$p_T^{top\ 1}/p_T^{top\ 2}$ <2	91.5	90.8	90.6
$\Delta R(b\ jet1, b\ jet2)$ >1.0	95.0	95.0	95.0
$\Delta\phi(\vec{E}_{Tmiss}, \vec{p}_T^{\ b\ jet_W})$ >0.5	91.5	91.0	91.3
$P_{REL}(\tau\ jet, b\ jet)$ >0.2	82.9	86.1	86.6
$p_T^{\tau\ jet}/p_T^{b\ jet} > 0.8$	67.4	76.4	81.7
All cuts N_{EXP}	$3.8{\cdot}10^3$	$2.9{\cdot}10^3$	$1.8{\cdot}10^3$

Table 7.2: Number of expected events for the signal after trigger and after all selection cuts and relative efficiency (in percent) after each cut selection at the 3 different $m_A/m_{H^{\pm}}$ considered points and $\tan\beta$ =30 for 10 fb^{-1}. m_A and $m_{H^{\pm}}$ given in GeV.

In addition, in Tables 7.3 and 7.4, the number of expected events after 3-tag and no isolated lepton selection as well as the relative efficiency after each group of cuts (as they were numbered in section 6.4.1) are given for the MSSM $t\bar{t}$ backgrounds and SM backgrounds respectively. After the selection cuts, all the SM backgrounds are rejected except QCD, with only one MC event left in the last $\hat{p_T}$ bin ($\hat{p_T} > 400$ GeV) with statistical

weight 18. The results shown in Table 7.4 for the SM backgrounds are compatible with the ones shown in Table 6.6 for the discovery studies. There are slight variations due to the different nature of the Monte Carlo samples, fully generated in Fortran for the discovery analysis and generated within Athena for the mass studies.

	MSSM $t\bar{t} \to H^+bH^-\bar{b}$			rest of MSSM $t\bar{t}$ bkg		
Cuts $m_A \to$	**94.8**	**109.8**	**117.8**	**94.8**	**109.8**	**117.8**
$\downarrow$ $m_{H^\pm} \to$	**127.0**	**138.6**	**145.0**	**127.0**	**138.6**	**145.0**
3-tag & no isol. lep N_{EXP}	$3.2{\cdot}10^3$	$1.1{\cdot}10^3$	$5.1{\cdot}10^2$	$3.5{\cdot}10^4$	$4.4{\cdot}10^4$	$3.5{\cdot}10^4$
3-tag & no isol. lep **(2)**	4.6	3.8	3.1	2.5	2.7	2.4
E_{Tmiss} and p_T^{jet} cuts **(3)**	67.0	62.8	58.4	54.0	56.9	54.8
Top and W mass rec **(4)**	17.9	17.1	17.4	40.8	35.6	40.3
Back to back topology **(5)**	47.9	41.5	41.0	58.7	56.5	59.0
Cuts on the $H^\pm$ side **(6)**	65.0	73.3	76.4	34.2	35.5	33.9
All cuts N_{EXP}	$1.2{\cdot}10^2$	37	16	$1.6{\cdot}10^3$	$1.8{\cdot}10^3$	$1.6{\cdot}10^3$

Table 7.3: Number of expected events after 3-tag and no isolated lepton cuts (cuts group number 2.) and relative efficiency (in percent) after each group of selection cuts for MSSM $t\bar{t}$ backgrounds at the 3 different $m_A/m_{H^\pm}$ considered points and $\tan\beta = 30$ for one year of running at low luminosity (10fb^{-1}).

7.3 Mass extraction

Once the set of cuts were applied to both signal and background events, the transverse mass given by Eq. (6.16) was obtained from the τ jet and the missing transverse energy, since in the $H^\pm \to \tau\nu$ channel the full invariant mass cannot be reconstructed (because the z component of the missing energy is not known). In Fig. 7.1 the total transverse mass distributions of a MSSM charged Higgs of mass $m_{H^\pm}$ = 127.0, 138.6 and 145 GeV and $\tan\beta$ =30 are shown for 10 fb^{-1}. Because the $BR(t \to H^+b)$ decreases when m_{H^+} approaches m_{top} (see Fig. 6.1), the number of expected $t\bar{t}$ signal events diminishes when going from Fig. 7.1(a) to 7.1(c). This is also due to the fact that the applied selection cuts (those given in section 6.4.1) were not optimized for high charged Higgs masses, that is for $m_{H^+} \lesssim m_{top}$. For the $t\bar{t}$ backgrounds with a $W^\pm$ boson, the transverse mass is kinematically constrained to be smaller than $m_{W^\pm}$, but for the signal, the transverse

Cuts	SM backgrounds			
	QCD	(Z/γ^*) +jet	W +jet	WW;$W(Z/\gamma^*)$; $(Z/\gamma^*)(Z/\gamma^*)$
3-tag & no isol. lep N_{EXP}	$3.8{\cdot}10^6$	$4.1{\cdot}10^3$	$2.6{\cdot}10^3$	$1.2{\cdot}10^2$
3-tag & no isol. lep **(2)**	0.08	0.08	0.01	0.07
E_{Tmiss} and p_T^{jet} cuts **(3)**	8.4	0.65	0	53.5
Top and W mass rec **(4)**	10.6	33.3	0	0
Back to back topology **(5)**	9.8	0	0	0
Cuts on the $H^{\pm}$ side **(6)**	0.54	0	0	0
All cuts N_{EXP}	18	0	0	0

Table 7.4: Number of expected events after 3-tag and no isolated lepton cuts (cuts group number 2.) and relative efficiency (in percent) after each group of selection cut for each SM background process for one year of running at low luminosity (10 fb^{-1}).

mass is bound to be below $m_{H^{\pm}}$. Thus, the M_T >80 GeV region is almost background free, except for the $t\bar{t}$ background tails contribution.

In the following section, the maximum likelihood method used for extracting the MSSM charged Higgs mass out of the transverse mass distributions is described in detail.

7.3.1 Maximum likelihood method

The transverse mass distributions for each one of the generated charged Higgs masses listed by expression (7.1) were obtained for 10 fb^{-1}. The binning of the distributions was set to 6 GeV/bin. Next, the bin contents of the M_T histograms were smoothed and normalized to unity, since in this maximum likelihood method only the shape of the M_T distribution is considered. There exists also an 'extended likelihood method' [102] which takes into account the signal rate itself to get a better mass resolution. However, in this extended method, the expected signal rates must be known with a very good level of precision.

After smoothing and normalizing the M_T distributions (in order to get the M_T probability distribution), only those events with transverse masses between 80 GeV and 170 GeV (M_T kinematical bounds from $m_{W^{\pm}}$ to m_{top}) were kept. Next, a polynomial fit was

performed such that the probability density functions of the transverse mass distributions were obtained. Polynomial functions of the 7th degree provided the best fit. In Fig. 7.2 these transverse mass probability density functions are shown. When increasing the charged Higgs mass, the probability density functions grow on the right side since the upper bound of the M_T distributions is given by $m_{H^\pm}$. In some cases, for example for $m_{H^\pm} = 145$ GeV, two bumps can be distinguished: the left one resides where the $W^\pm$ boson transverse mass is and the right one, corresponds to the charged Higgs particle. In addition, the fits to those M_T probability density functions that have low statistics due to the top mass kinematical constraint (i.e. $m_{H^\pm}$=160.0, 165.1 GeV) gave less reliable results due to the large bin to bin fluctuations.

At that point, the existence of a charged Higgs boson of mass $m_{H^\pm}^{SEL}$ selected among the charged Higgs masses given by expression (7.1) with transverse mass probability density function $P_{SEL}(M_T)$ was assumed to be the experimental distribution[2]. The rest of the k generated masses had probability density functions $P_k(M_T)$ where $k = 1, ...17$.

Let's label the number of expected events of the transverse mass distribution for the selected charged Higgs mass N_{SEL}. The likelihood function at this $m_{H^\pm}^{SEL}$ point is given by:

$$\mathcal{L}_{SEL} = \prod_{i=1}^{N_{SEL}} P_{SEL}(M_{T_i}) \tag{7.2}$$

where M_{T_i} with $i = 1, ..., N_{SEL}$ is the transverse mass corresponding to the event number i. The likelihood functions of each one of the k masses are given by:

$$\mathcal{L}_k = \prod_{i=1}^{N_{SEL}} P_k(M_{T_i}) \tag{7.3}$$

that is, using the same set of M_{T_i} with $i = 1, ..., N_{SEL}$ transverse masses.

After taking the logarithm of Eq. (7.2) and (7.3), the delta log-likelihood function for each charged Higgs of mass k was computed:

$$\Delta \ln(\mathcal{L}_k) = \ln(\mathcal{L}_{SEL}) - \ln(\mathcal{L}_k) = \sum_{i=1}^{N_{SEL}} \Big[\ln(P_{SEL}(M_{T_i})) - \ln(P_k(M_{T_i})) \Big] \tag{7.4}$$

The delta log-likelihood function is an estimator of "how good the transverse mass probability density function k approaches the probability density function SEL".

[2]Once the LHC will be running, this selected sample will be the real data.

Next, the $\Delta \ln(\mathcal{L}_k)$ values were plot as a function of the k masses as it is shown in Fig. 7.3 below. Around the minimum of this delta-loglikelihood plot, which should be at the selected charged Higgs mass, a parabolic fit was performed. The minimum of this parabola determined the reconstructed charged Higgs mass.

This procedure was repeated many times in order to get N_{EXP} pseudo-experiments. To do so, for each pseudo-experiment a random gaussian fluctuation to the number of expected events N_{SEL} was computed, that is $N'_{SEL} = N_{SEL} + \delta N_{SEL}$. Afterwards, a random set of N'_{SEL}transverse masses was generated according to the probability density function $P_{SEL}(M_T)$ and the delta log-likelihood values were recalculated for each one of the k masses so that a new delta log-likelihood plot was obtained[3]. From this plot, a new reconstructed Higgs mass could be obtained as explained above.

Afterwards, the minimums of the parabolas of the delta log-likelihood fits were plotted in a distribution. This distribution has a gaussian shape if a reasonable number of pseudo-experiments are generated. Finally, a gaussian fit to the reconstructed this distribution was performed. The mean of such gaussian and the standard deviation gave the charged Higgs mass and the statistical error on it.

In Fig. 7.3, the delta log-likelihood values as a function of the k generated charged Higgs masses (given by expression (7.1)) are represented for $m^{SEL}_{H^{\pm}}$ =127, 138.6 and 145 GeV. A parabolic fit was performed around the minimum and the vertex of the parabola gave the reconstructed $H^{\pm}$ mass for that pseudo-experiment. The error bars are the standard deviations of the delta log-likelihood values for N_{EXP} =1000 pseudo-experiments. One can observe that for the three plots given in Fig. 7.3, the points with $m_{H^{\pm}} \lessapprox 110$ GeV have more or less the same behaviour. In this charged Higgs mass region, the contribution of the $t\bar{t}$ background (with two $W^{\pm}$ in the final state faking the $H^{\pm}$ signature) overlap with the $H^{\pm}$ signal contribution so that the sum of these two components give a similar M_T distribution. Hence, for a given $m^{SEL}_{H^{\pm}}$ the $\Delta \ln(\mathcal{L}_k)$ value is very similar for this $H^{\pm}$ m_k values and therefore, does not give any useful information. As a consequence this mass points were not used for the log-likelihood fit. In Fig. 7.4, the distribution of the reconstructed charged Higgs masses obtained with the delta log-likelihood fits is

[3]This procedure will also take place in the case of real data: from the M_T probability density function obtained for real events (with N_{EVT} the number of events in the transverse mass distribution), N_{EXP} pseudo-experiments can be generated each one with $N'_{EVT} = N_{EVT} + \delta N_{EVT}$ events, where δN_{EVT} is a gaussian fluctuation on the real number of events.

shown for 10000 pseudo-experiments and 3 different $m_{H^\pm}^{SEL}$, namely 127, 138.6 and 145 GeV. Such distributions are fitted with a gaussian and its mean value and standard deviation give the reconstructed charged Higgs mass and the statistical error on it. In Table 7.5, the reconstructed $H^\pm$ masses together with their statistical errors are listed for each generated $m_{H^\pm}^{SEL}$. One can see there that the generated $m_{H^\pm}$ does not lie in the reconstructed $m_{H^\pm}$ $\pm$ statistical error range since, as it will be shown in the next section, the systematic effects will contribute to increase this error.

Generated $m_{H^\pm}^{SEL}$ **(GeV)**	**Reconstructed** $m_{H^\pm}$ **(GeV)**	**Stat. Error (GeV)**
127.0	128.4	1.1
138.6	141.1	1.0
145.0	142.1	0.8

Table 7.5: Reconstructed charged Higgs masses and their statistical error as obtained with the maximum likelihood method.

7.3.2 Systematic errors

The statistical errors obtained with the maximum likelihood method are quite small. The main source of error for the charged Higgs signature under study is the systematic one. For the mass reconstruction, the systematic errors due to the uncertainty on the τ-tagging efficiency and the jet and E_{Tmiss} energy scales are considered as it was done for the charged Higgs discovery studies (see section 6.5).

On the contrary, the uncertainties on the $t\bar{t}$ cross section and on the luminosity measurement, that were important for the significance calculations, are not considered here, since they would only produce a global scale effect on the final M_T distribution. Such scale effect cancels out when normalizing in order to get the transverse mass probability density functions.

In the same way, the uncertainty on the b-tagging efficiency only produces a global scale effect on the final M_T distribution, since after the selection cuts, almost only those events that contain true b jets remain. In addition, the b jet quantities are not used when computing the transverse mass.

Moreover, other uncertainties intrinsically related to the mass reconstruction method were also considered:

1. Uncertainty due to different histogram binning.
   The maximum likelihood method for the mass reconstruction was applied to M_T distributions with a binning of 6 GeV/bin. The variation on the reconstructed charged Higgs mass when changing the M_T histograms binning to 4 GeV/bin and 5 GeV/bin was studied.

2. Uncertainty due to the change of polynomial degree in the M_T probability density function fits.
   Several other polynomial degrees where also tried for the mass reconstruction, specifically, polynomials of the 11th and 9th degree were used.

3. Error due to the lack of statistics of the Monte Carlo samples.
   The effect of the limited statistics was reflected on the bin by bin fluctuations of the M_T distributions. So that random poisson fluctuations on the M_T distributions were added for the Monte Carlo samples at the different m_k values. Next, the charged Higgs mass was reconstructed again with the maximum likelihood method.

These uncertainties produced a shift $\lessapprox$ 1GeV on the reconstructed charged Higgs mass peak. Thus, this error was added quadratically to the rest of systematic uncertainties.

In Table 7.6, the systematic errors computed for each selected charged Higgs mass are listed.

The E_{Tmiss} systematic error is the one that gives the largest contribution since the missing transverse energy enters directly in the transverse mass calculation (see Eq. (6.16)). Concerning the τ-tagging efficiency error, it is not negligible, and for a charged Higgs generated mass of 138.6 GeV this value is really high: 4.0 GeV. These fluctuations on the estimated systematic error between the different mass hypothesis are due to the statistical fluctuations in the transverse mass distributions, hence, the solution would be to increase the statistics of the Monte Carlo samples.

Systematic uncertainties	$H^{\pm}$ mass point (GeV)		
	127.0	**138.6**	**145.0**
Jet energy scale ($\pm 1\%$)	0.9	1.4	2.2
E_{Tmiss} scale ($\pm 4\%$)	3.0	2.8	2.2
τ-tagging eff. ($\pm 3\%$)	1.5	4.0	1.3
other uncertainties	1.0	1.0	1.0
Total sys. error	3.6	5.1	3.5

Table 7.6: Systematic errors given in GeV for the charged Higgs mass extraction. $\tan\beta = 30$ was used.

7.3.3 Results

The final reconstructed MSSM charged Higgs masses for each one of the Monte Carlo generated $m_{H^{\pm}}$; 127, 138.6 and 145.0 GeV; are listed in Table 7.7 together with the statistical and the systematic errors and the relative precision of the measurement. From these results it can be concluded that the precision on the charged Higgs mass is completely dominated by the systematic uncertainties. In addition, by making use of a maximum likelihood method, the light charged Higgs mass can be extracted from the transverse mass distribution with a precision of $\lesssim 5$ GeV.

Generated $H^{\pm}$ mass (GeV)	Reconstructed $H^{\pm}$ mass (GeV)	Statistical error (GeV)	Systematic error (GeV)	Rel. precision $\Delta M/M$ (%)
127.0	128.4	1.1	3.6	2.8
138.6	141.1	1.0	5.1	3.6
145.0	142.1	0.8	3.5	2.4

Table 7.7: Reconstructed MSSM charged Higgs mass values with the maximum likelihood method for the three generated charged Higgs masses.

At this point it's also worth commenting what would happen if other values of $\tan\beta$ were considered for the mass extraction studies. To have an idea of how things change when changing $\tan\beta$, one should take into account the $BR(t \to H^{+}b)$ plot in Fig. 6.1. For example, when increasing $\tan\beta$ (and for $\tan\beta > 10$), the number of $H^{\pm}$ increase for the same mass, so that more $t\bar{t}$ signal events are produced whereas the number of $t\bar{t}$ back-

ground events containing $W^{\pm}$ bosons diminish proportionally. So, if ones thinks about the M_T distribution (Fig. 7.1), this will translate not only into an increase of the number of expected events in the 80 GeV< M_T <170 GeV range but also the leading edge of the transverse mass distribution summing up all contributions will become more pronounced. On the other hand, when lowering $\tan\beta$ (and for $\tan\beta > 7.5$) the opposite effect would take place: the $BR(t \to H^+b)$ is decreasing whereas an increase of the $BR(t \to W^+b)$ is produced, and the number of expected events in the 80 GeV< M_T <170 GeV range would diminish giving a less pronounced edge on the transverse mass distribution. In the very unfavourable $\tan\beta \sim 7.5$ limit, it could happen that in the 80 GeV< M_T <170 GeV range, the signal would go below the $t\bar{t} \to W^{\pm}bW^{\mp}\bar{b}$ tail and the mass could not be extracted anymore. Hence, when dealing with real LHC data, one should perform the mass extraction studies for different $\tan\beta$ values, i.e., one should find the $\tan\beta$ which fits best the M_T distribution for a given charged Higgs mass. Besides, $\tan\beta$ can be directly measured in some decay channels: the production rates of $H/A \to \tau\tau$ and $H/A \to \mu\mu$ are sensitive to $\tan\beta$. In [103], an estimation of the precision on $\tan\beta$ is given. For example, in the $H/A \to \tau\tau$ channel, for m_A =150 GeV and an integrated luminosity of 300 fb^{-1}, $\tan\beta$ could be measured with an accuracy of $\pm$15% for $\tan\beta = 5$ and of $\pm$6% for $\tan\beta = 40$.

In Fig. 7.5, the reconstructed charged Higgs mass is plot as a function of the generated $m_{H^{\pm}}$ with the statistical and systematic errors drawn at each point. In addition, an ideal line (i.e. reconstructed $m_{H^{\pm}}$= generated $m_{H^{\pm}}$) is also drawn. Thus, the results, adding the statistical and the systematics effects, are compatible with the line of slope 1 for the ideal case.

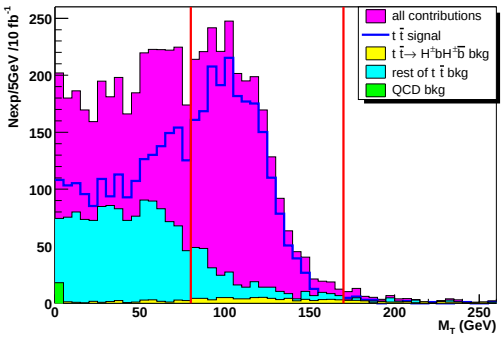

(a) $m_{H^\pm} = 127$ GeV, $\tan\beta = 30$

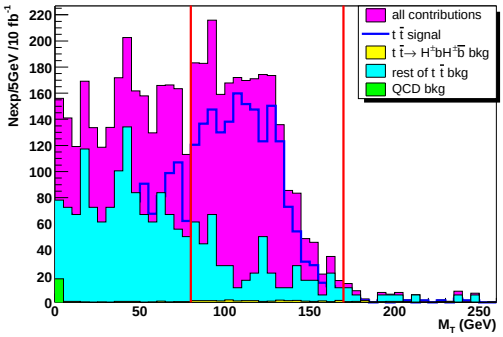

(b) $m_{H^\pm} = 138.6$ GeV, $\tan\beta = 30$

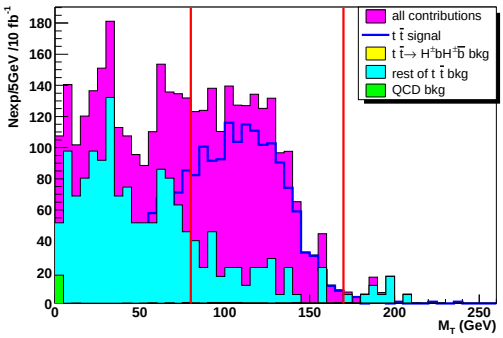

(c) $m_{H^\pm} = 145$ GeV, $\tan\beta = 30$

Figure 7.1: Transverse mass distributions of MSSM charged Higgs of masses 127.0 GeV, 138.6 GeV and 145 GeV for 10 fb^{-1}. For the signal, the leading edge shifts to higher transverse masses with increasing $H^\pm$ mass. Maximal Mixing scenario and $\tan\beta$ =30 were used. Only the region between the two vertical lines (80 GeV< M_T <170 GeV) was used for the mass extraction.

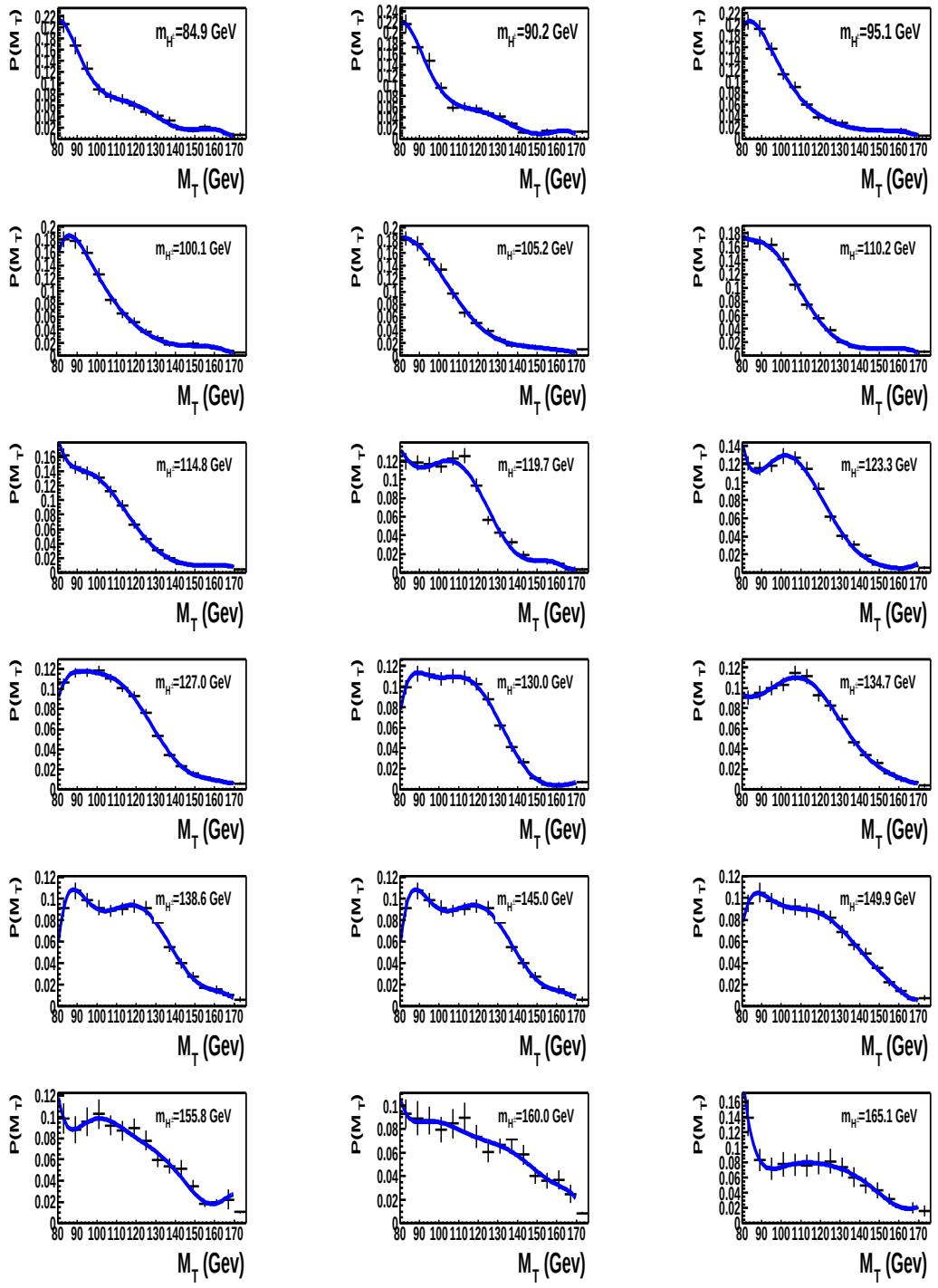

Figure 7.2: Transverse mass probability density functions obtained from a polynomial fit (of 7th degree) to the smoothed and normalized M_T distributions for different charged Higgs masses and $\tan\beta$=30.

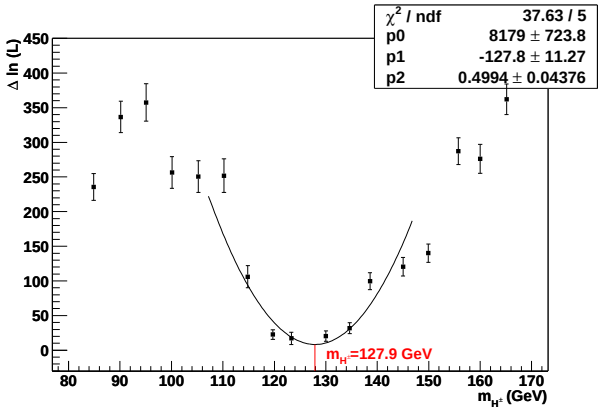

(a) $m_{H^\pm}^{SEL} = 127$ GeV. Fitting range: 107-147 GeV.

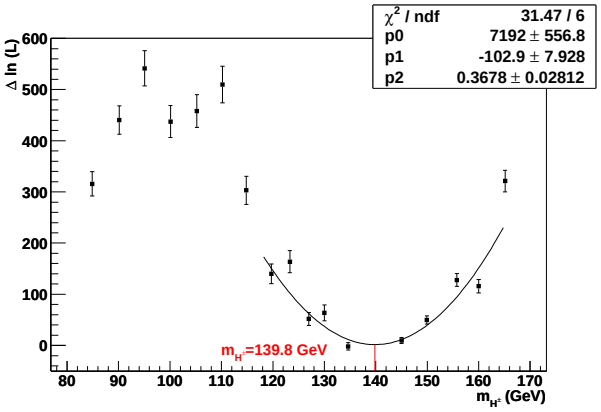

(b) $m_{H^\pm}^{SEL} = 138.6$ GeV. Fitting range: 118-165 GeV.

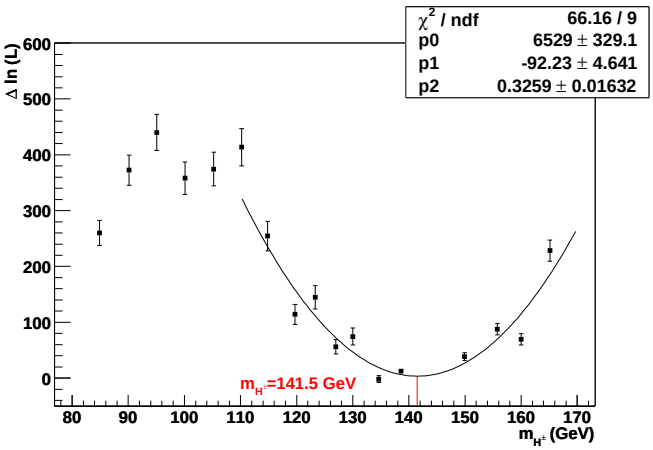

(c) $m_{H^\pm}^{SEL} = 145$ GeV. Fitting range: 125-170 GeV.

Figure 7.3: Parabolic fits to the delta log-likelihood functions versus $m_{H^\pm}$ for three different selected charged Higgs masses: 127.0, 138.6, 145 GeV and $\tan\beta = 30$. Inside each plot, the reconstructed charged Higgs mass is written.

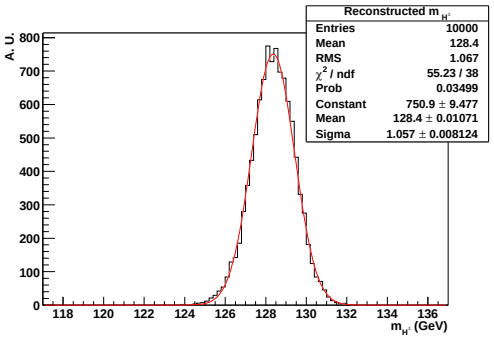

(a) $m_{H^{\pm}}^{SEL} = 127$ GeV, $\tan\beta = 30$

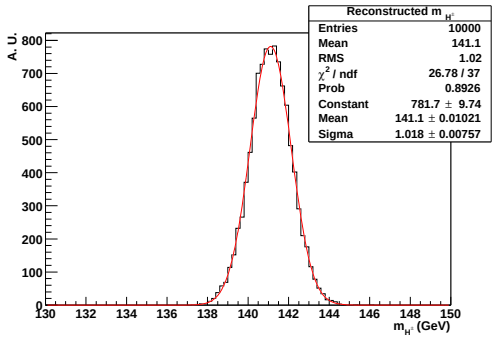

(b) $m_{H^{\pm}}^{SEL} = 138.6$ GeV, $\tan\beta = 30$

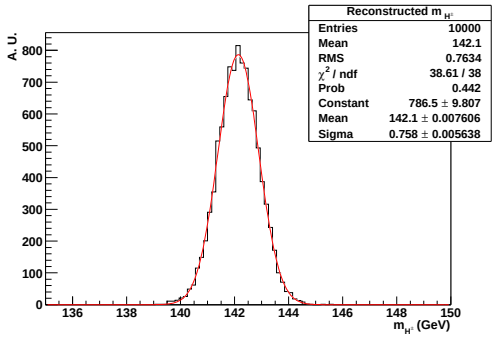

(c) $m_{H^{\pm}}^{SEL} = 145$ GeV, $\tan\beta = 30$

Figure 7.4: Distributions of the reconstructed $H^{\pm}$ masses for three different $m_{H^{\pm}}^{SEL}$: 127.0, 138.6, 145 GeV. A gaussian fit is performed and the mean and standard deviation give the reconstructed charged Higgs mass and its statistical error.

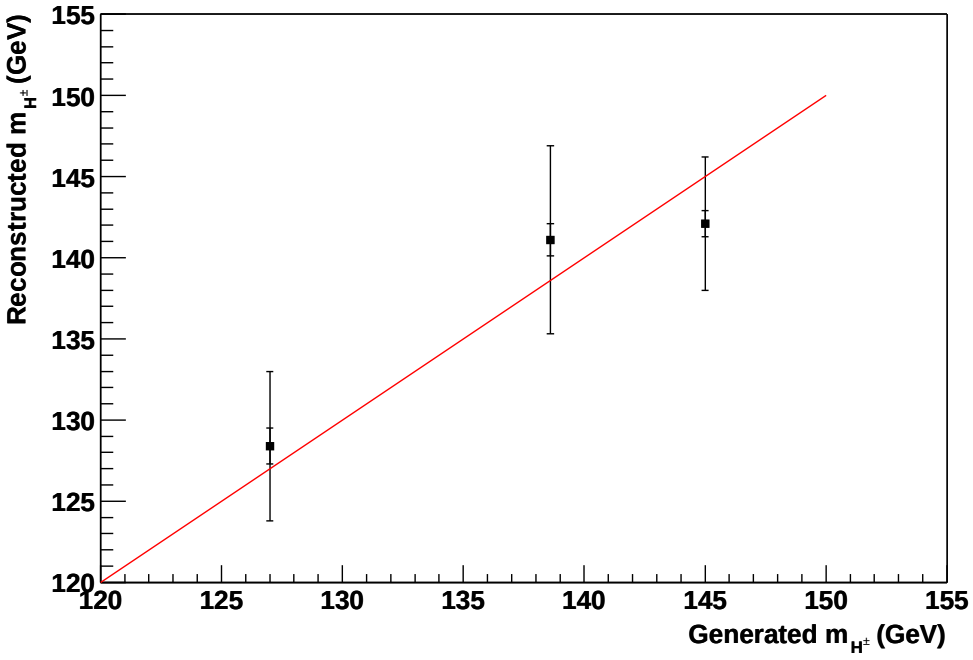

Figure 7.5: Reconstructed charged Higgs mass as a function of the generated $m_{H^\pm}$ for the three selected mass points with the statistical and systematic errors at each point. An ideal line with slope one is also drawn.

Chapter 8

Summary and Outlook

The sensitivity for the ATLAS detector to the discovery of a MSSM charged Higgs produced in top decays has been studied in detail in the channel $pp \to t\bar{t} \to H^{\pm}bW^{\mp}\bar{b}$ with $H^{\pm} \to \tau\nu$ and $W^{\mp} \to q\bar{q}\prime$.

After event selection (QCD filter), the most relevant remaining background is $t\bar{t} \to W^{\pm}bW^{\mp}\bar{b}$ with one W boson decaying leptonically into $\tau\nu$ and the other one decaying hadronically in two light jets. That background was further reduced by imposing a cut on the transverse mass and a harder cut on the τ jet transverse momentum: due to τ polarization effects [89], in one-prong τ hadronic decays, τ jets from $H^{\pm}$ decay are harder than the ones produced in $W^{\pm}$ decay.

The discovery potential of the ATLAS detector for a charged Higgs produced in top decays was already studied in [44] in the leptonic channel. In addition, the case $m_{H^{\pm}} > m_{top}$ was also investigated [33]. The significance studies presented in this thesis complete the (m_A, $\tan\beta$) survey for the MSSM charged Higgs. Furthermore, in the so far uncovered 5-10 $\tan\beta$ region a significance greater than 5σ is obtained already for 10 fb^{-1} of data (corresponding to one year of running at low luminosity) with the channel studied in this work. Therefore, the discovery potential studies of ATLAS standalone and ATLAS+CMS combined for any of the different MSSM Higgs bosons (h, H, A, H^+, H^-) cover the whole MSSM (m_A, $\tan\beta$) space.

Moreover, an important aspect of this channel is that it gives the possibility to measure the mass. The light MSSM charged Higgs mass was obtained from the transverse mass

distribution (since in the $H^{\pm} \to \tau\nu$ channel there is no resonance peak) by means of a maximum likelihood method and the expected precision on this mass was also given. The error was completely dominated by systematics and a precision close to 4% could be achieved for an integrated luminosity of 10 fb^{-1}.

To conclude, the results presented in this work show that the prospects for discovering the charged Higgs at the LHC are very good. At the Tevatron Run II, this discovery is quite unlikely due to the small $t\bar{t}$ cross section, two orders of magnitude lower than that of LHC ($\sigma(p\bar{p} \to t\bar{t}) \sim 7$ pb at $\sqrt{s} = 2.0$ TeV [104]), and the limited integrated luminosity. Most likely we will have to wait for the first LHC data in order to prove the existence of the charged Higgs and get more insight in Supersymmetry.

Appendix A

Effects of the new $\tau + E_{Tmiss}$ and jet+E_{Tmiss} trigger thresholds on the discovery potential of a MSSM $H^{\pm}$ produced in top decays

As it was pointed out in section 6.4.1, at the moment of writing this thesis the thresholds of the $\tau + E_{Tmiss}$ and jet+E_{Tmiss} triggers were increased in order to reduce the final amount of data to store on tape after the Event Filter. Those new thresholds were already presented in Table 4.4. As a reminder, those changes are listed below:

- (t20xe30)→(t35xe45)
- (j60xe60)→(j70xe70)

In section 4.4.3 it was shown that the MSSM $H^{\pm}$ signature studied in this thesis had a weak dependency on the $\tau + E_{Tmiss}$ trigger thresholds since most of the τ jets produced in $H^{\pm}$ decays also fulfilled the jet+E_{Tmiss} trigger.

In order to study how these changes affected the discovery potential of the MSSM charged Higgs, the set of cuts given in section 6.4 were applied to the generated signal and background processes (see section 6.3) with the new trigger conditions, namely

(t35xe45).OR.(j70xe70). In Fig. A.1 the change in statistical significance (without taking into account systematic error effects) as well as the lost in luminosity in percent (i.e., how much the luminosity would have to be increased in order to reach the statistical significance values achieved with the old thresholds) as a function of $\tan\beta$ is represented for three different MSSM $H^{\pm}$ masses, 90, 127 and 160 GeV.

It can be seen that almost no decrease in the statistical significance is produced. Thus, only a few percent of relative additional luminosity would recover the statistical significance losses due to the new trigger menus (the negative values in the luminosity plots are due to a lack of statistics in the signal events).

This results are not surprising. In the selection cuts, already a cut on events with E_{Tmiss} >45 GeV and a τ jet of at least 25 GeV was applied. Moreover, the transverse momentum of the τ jet is really high (specially for the $\tau^{\pm}$'s produced in $H^{\pm} \rightarrow \tau^{\pm}\nu_{\tau} \rightarrow \pi^{\pm}\nu_{\tau}\bar{\nu}_{\tau}$ decays as it was already commented in section 6.3.1). Therefore, many of these τ jets (see Fig. 6.10(a)) are going to fulfill the 'j70' trigger requirement.

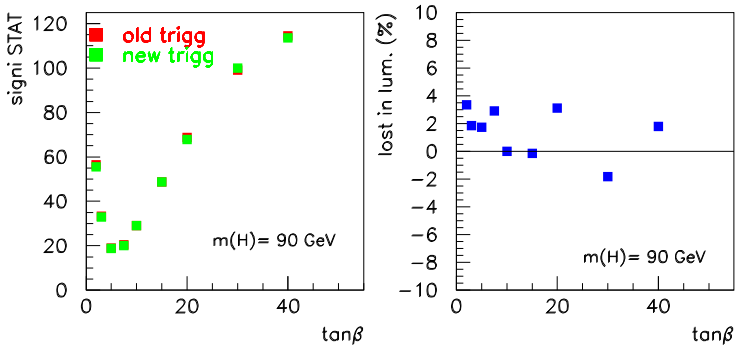

(a) $m_{H^{\pm}} = 90$ GeV

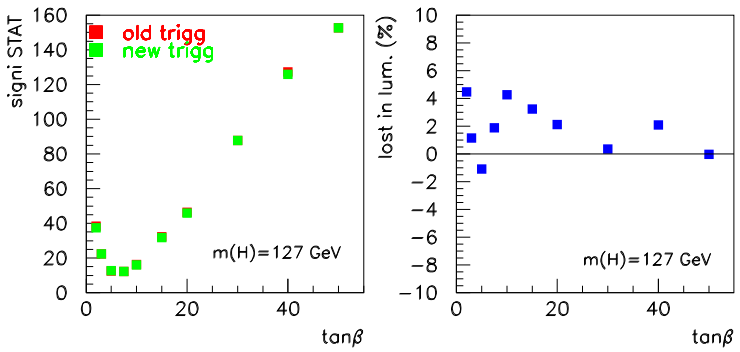

(b) $m_{H^{\pm}} = 127$ GeV

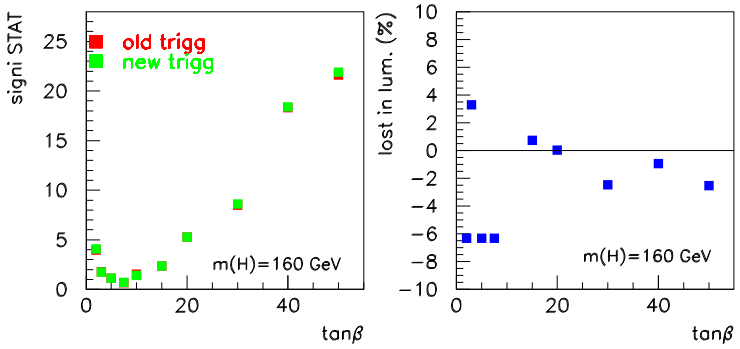

(c) $m_{H^{\pm}} = 160$ GeV

Figure A.1: Change in statistical significance and lost in luminosity when applying the new trigger thresholds, (t35xe45).OR.(j70xe70) as a function of $\tan\beta$ for three different MSSM $H^{\pm}$ masses: 90, 127 and 160 GeV.

Bibliography

[1] S.L. Glashow, Nucl. Phys. **B22** (1961) 579;
S. Weinberg, Phys. Rev. Lett. **19** (1967) 1264;
A. Salam, *Elementary Particle Theory*, ed. N. Svartholm, Almqvist and Wiksell, Stockholm (1968) 367;
S.L. Glashow, J. Iliopoulos and L. Maiani, Phys. Rev. **D2** (1970) 1285.

[2] H. Fritzsch and M. Gell-Mann, Proc. XVI Int. Conf. on High Energy Physics, eds. J.D. Jackson and A. Roberts (Fermilab 1972).

[3] L. D. Faddeev and V. N. Popov, Phys. Lett. **25B** (1967) 29

[4] P. W. Higgs, Phys. Lett. **12** (1964) 132;
F. Englert and R. Brout, Phys. Rev. Lett. (1964) 321;
G. S. Guralnik, C. R. Hagen and T. W. B. Kibble, Phys. Rev. Lett. **13** (1964) 585;
P. W. Higgs, Phys. Rev. **145** (1966) 1156;
T. W. B. Kibble, Phys. Rev. **155** (1967) 1554.

[5] B. Lee, C. Quigg and H. Thacker, Phys. Rev. **D16** (1977) 1519.

[6] The ALEPH Collaboration, Phys. Lett. **B526** (2002) 191.

[7] UA1 Collaboration, G. Arnison *et al.*, Phys. Lett. **B122** (1983) 103;
UA2 Collaboration, M. Banner *et al.*, Phys. Lett. **B122** (1983) 476.

[8] S. Myers and E. Picasso. *The design, construction and commissioning of the CERN Large Electron Positron collider.* Contemporary Physics **31** (1990) 387.

[9] Lep Design Report, vol. 1 CERN-LEP/83-29 (1983);
Lep Design Report, vol. 2 CERN-LEP/84-01 (1984).

[10] L. Maiani, Proc. Summer School on Particle Physics, Gif-sur-Yvette (1979) (IN2P3, Paris, 1980) 3;
G't Hoof *et al.*, eds., *Recent Developments in Field Theories*, Plenum Press, New York (1980);
E. Witten, Nucl. Phys. **B188** (1981) 513;
R. K. Kaul, Phys. Lett. **109B** (1982) 19.

[11] D. Dicus and V. Mathur, Phys. Rev. **D7** (1973) 3111;
B. Lee, C. Quigg and H. Thacker, Phys. Rev. **D16** (1977) 1519.

[12] Yu. A. Gol'fand and E. P. Likhtman, ZhETF Pis. Red. **13** (1971) 452 [JETP Lett. **13** (1971) 323];
D. V. Volkov and V. P. Akulov, Phys. Lett. **B46**, (1973) 109;
J. Wess and B. Zumino, Nucl. Phys. **B70** (1974) 39.

[13] R. Haag, J. Lopuszanski and M. Sohnius, Nucl. Phys. **B88** (1975) 416.

[14] E. Witten, Nucl. Phys. **B188** (1981) 513;
N. Sakai, Z. Phys. **C11** (1981) 153.

[15] S. P. Martin, *A Supersymmetry Primer in perspectives in Supersymmetry*, G. L. Kane, World Scientific, Singapore (1997); hep-ph/9709356.

[16] H. P. Nilles, Phys. Rev. **110** (1984) 1;
H. E. Haber and G. L. Kane, Phys. Rev. **117** (1985) 75;
R. Barbieri, Riv. Nuov. Cim. **11** (1988) 1.

[17] S. Dimopoulos and H. Georgi, Nucl. Phys. **B193** (1981);
N. Sakai, Z. Phys. **C11** (1981) 153.

[18] C. Carlson, P. Roy, and M. Sher, Phys. Lett. **B357** (1995) 99;
G. Bhattacharyya, hep-ph/9608415 (1996).

[19] G. R. Farrar and P. Fayet, Phys. Lett. **B76** (1978) 575;
F. Zwirner, Phys. Lett. **B132** (1983) 103;
L. Hall and M. Suzuki, Nucl. Phys. B231 (1984) 419;
J. Ellis, G. Gelmini, C. Jarlskog, G. Ross, and J. Valle, Phys. Lett. **B150** (1985) 142;
G. Ross and J. Valle, Phys. Lett. **B151** (1985) 375;

S. Dawson, Nucl. Phys. **B261** (1985) 297;
S. Dimopoulos and L. Hall, Phys. Lett. **B207** (1988) 210.

[20] R. Arnowitt, P. Nath, in Particles and Fields, Proc. of the VII J. A. Swieca Summer School, Sao Paulo, Brazil (1993) ed. O. Eboli, V. Rivelles (Word Scientific, Singapore, 1993);
Properties of SUSY particles, ed. L. Ciffarelly, V. Khoze (World Scientific, Singapore, 1993);
X. Tata, Lectures presented at TASI95, Univ. of Colorado, Boulder (1995), hep-ph/9510287.

[21] L. Hall, J. Lykken, and S. Weinberg, Phys. Rev. **D27** (1973) 2359.

[22] L. Girardello and M. Grisaru, Nucl. Phys. **B194** (1982) 65;
K. Harada and N. Sakai, Prog. Theor. Phys. **67** (1982) 67.

[23] S. Dimopoulos and D. Sutter, Nucl. Phys. **B452** (1995) 496.

[24] L. Ibáñez and G. G. Ross, Phys. Lett. **B110** (1982) 215.

[25] M. Carena *et al.*, Phys. Lett. **B355** (1995) 209.

[26] P. Chamkowski, S. Pokorski, and J. Rosiek, Phys. Lett. **B274** (1992) 191; Phys. Lett. **B281** (1992) 100.

[27] A. Brignole, J. Ellis, G. Ridolfi, F. Zwirner, Phys. Lett. **B271** (1991) 123;
A. Brignole, Phys. Lett. **B277** (1992) 313.

[28] M. A. Díaz, H. E. Haber, Phys. Rev. **D45** (1992) 4246.

[29] M. S. Alam *et al.*, Phys. Rev. Lett. **74** (1995) 2885;

[30] P. Gambino and M. Misiak, Nucl. Phys. **B611** (2001) 338.

[31] J. A. Coarasa, J. Guasch, J. Solà and W. Hollik, Phys. Lett. B442 (1998) 326.

[32] L. J. Hall, R. Rattazzi and U. Sarid, Phys. Rev. **D50** (1994) 7048.

[33] K. A. Assamagan *et al.*, EPJdirect **C9**, 1-31 (2002).

[34] M. Carena *et al.*, hep-ph/9912223 (1999).

[35] S. Dawson, *The MSSM and why it works*, 4 lectures at TASI Summer School, Boulder CO., June 2-6 (1997)

[36] ALEPH, DELPHI, L3 and OPAL Collaborations, hep-ex/0107031 (2001).

[37] ALEPH Collaboration, hep-ex/0207054 (2002).

[38] M. Carena *et al.*, *Report of the Tevatron Higgs Working Group*, hep-ph/0010338 (2000).

[39] CDF Run II TDR, Fermilab-Pub-96/390-E (1996);
D∅ Run II TDR, Fermilab-Pub-96/357-E (1996).

[40] J. F. Gunion, H. E. Haber, G. Kane and S. Dawson, *The Higgs Hunter's Guide*, Perseus Publishing, Reading, MA (2000).

[41] D∅ Collaboration, hep-ex/0102039 (2002).

[42] ATLAS Collaboration, ATLAS Detector and Physics Performance: Technical Design Report, Volume 2, report CERN/LHCC/99-15 (1999).

[43] CMS Collaboration, Technical Proposal, report CERN/LHCC/94-38 (1994).

[44] D. Cavalli *et al.*, ATLAS Internal Note ATL-PHYS-94-053 (1994).

[45] M. Dress, M. Guchait and D. P. Roy, hep-ph/9909266 (1999).

[46] K. A. Assamagan, ATLAS Internal Note ATL-PHYS-99-013 (1999).

[47] K. A. Assamagan and Y. Coadou, ATLAS Internal Note ATL-PHYS-2000-031 (2000).

[48] `http://atlas.web.cern.ch/Atlas/GROUPS/PHYSICS/HIGGS/higgs-conf/MSSMplots2002/MSSMplots2002.html` (2002).

[49] ATLAS Collaboration, ATLAS Magnet System Technical Design Report, report CERN/LHCC/97-18, (1997).

[50] ATLAS Collaboration, ATLAS Technical Proposal, report CERN/LHCC/94-43 (1994).

[51] ATLAS Collaboration, ATLAS Detector and Physics Performance: Technical Design Report, Volume 1, report CERN/LHCC/99-14 (1999).

[52] ATLAS Collaboration, ATLAS Inner Detector Technical Design Report, Volume 1, report CERN/LHCC/97-16 (1997).

[53] ATLAS Collaboration, ATLAS Inner Detector Technical Design Report, Volume 2, report CERN/LHCC/97-17 (1997).

[54] ATLAS Collaboration, ATLAS Pixel Detector Technical Design Report, report CERN/LHCC/98-13 (1998).

[55] ATLAS Collaboration, ATLAS Liquid Argon Calorimeter Technical Design Report, report CERN/LHCC/96-41 (1996).

[56] ATLAS Collaboration, ATLAS Calorimeter Performance Technical Design Report, report CERN/LHCC/96-40 (1996).

[57] ATLAS Collaboration, ATLAS Tile Calorimeter Technical Design Report, report CERN/LHCC/96-42 (1996).

[58] ATLAS Collaboration, ATLAS Muon Spectrometer Technical Design Report, report CERN/LHCC/97-72 (1997).

[59] ATLAS Collaboration, ATLAS High-Level Triggers, DAQ and DCS Technical Design Report (in preparation), (2003).

[60] M. Cobal *et al.*, ATLAS Internal Note ATL-TILECAL-95-067 (1995).

[61] W. Braunschweig *et al.* (H1 calorimeter group), Nucl. Inst. and Meth. **A265** (1988) 246;
B. Andrieu *et al.* (H1 calorimeter group), DESY 93-04 (1993).

[62] M. Bosman *et al.*, ATLAS Internal Note ATL-SOFT-98-038 (1998).

[63] D. Cavalli, ATLAS Internal Note ATL-PHYS-96-080 (1996).

[64] D. Cavalli, ATLAS Internal Note ATL-PHYS-98-118 (1998).

[65] D. Cavalli, ATLAS Internal Note ATL-PHYS-94-051 (1994).

[66] I. Gavrilenko, ATLAS Internal Note ATL-INDET-97-165 (1997).

[67] ATLAS Collaboration, ATLAS Level-1 Trigger Technical Design Report, report CERN/LHCC/98-14 (1998).

[68] HP. Beck *et al.*, HLT operational analysis and requirements to other sub-systems, http://atlas.web.cern.ch/Atlas/GROUPS/DAQTRIG/DataFlow/DataCollection/docs/DC-059/DC-059.pdf (2003).

[69] The ATLAS Collaboration, ATLAS Trigger Performance Status Report, report CERN/LHCC 98-15 (1998).

[70] Presentation given by S. Tapprogge in March 2002 LHCC open session, http://documents.cern.ch/cgi-bin/setlink?base=agenda&categ=a02381&id=a02381s3t1/transparencies (2002).

[71] Presentation given by F. Gianotti in October 2002 LHCC open session, http://documents.cern.ch/cgi-bin/setlink?base=agenda&categ=a021034&id=a021034s2t1/transparencies (2002).

[72] A. T. Watson, ATLAS Internal Note ATL-DAQ-2000-046 (2000).

[73] D. Cavalli *et al.*, ATLAS Internal Note ATL-DAQ-2000-016 (2000).

[74] T. Sjöstrand *et al.*, Computer Phys. Comm. **135** (2001) 238.

[75] E. Richter-Was, D. Froidevaux, L. Poggioli, ATLAS Internal Notes ATL-PHYS-96-079 (1996) and ATL-PHYS-98-131 (1998).

[76] R. Brun *et al.*, GEANT3, CERN/DD/EE/84-1 (1996).

[77] C. Biscarat, ATLAS Internal Note, ATL-COM-DAQ-2001-008 (2001).

[78] S. Jadach, Z. Was and J.H. Kuehn, Computer Phys. Comm. **64** (1991) 275.

[79] http://www.phys.psu.edu/~cteq/#PDFs

[80] http://atlas.web.cern.ch/GROUPS/SOFTWARE/OO/architecture

[81] E. Gamma *et al.*, *Design patterns*, Addison-Wesley (1995).

[82] http://proj-gaudi.web.cern.ch/proj-gaudi

[83] http://www.wlap.org/atlas/computing/tutorials/athena/2002/

[84] M. Bosman *et al.*, ATLAS Internal Note ATL-DAQ-2002-005 (2002).

[85] http://atlas.web.cern.ch/Atlas/GROUPS/SOFTWARE/OO/tools/cvs_server.html;
http://www.cvshome.org

[86] http://www.cmtsite.org

[87] http://www.hep.ucl.ac.uk/atlas/atlfast

[88] S. Mrenna, Computer Physics Commun., **101** (1997) 232.

[89] D. P. Roy, Phys. Lett. **B459** (1999) 607.

[90] D. Cavalli and S. Resconi, ATLAS Internal Note, ATL-PHYS-97-100 (1997).

[91] D. Froidevaux, E. Richter-Was, ATLAS Internal Note, ATL-PHYS-94-43 (1994).

[92] http://www.hep.ucl.ac.uk/%7Erms/phd/analysis/index.html

[93] R. Bonciani *et al.*, Nucl. Phys. **B529** (1998), 424.

[94] K. Hagiwara et al., Phys. Rev. D 66, 010001 (2002).

[95] M. Drees and D. P. Roy, Phys. Lett. **B269** (1991), 155;
D. P. Roy, ibid **B283** (1992), 403.

[96] ALEPH, DELPHI, L3, OPAL Collaborations and LEP Higgs Working Group, LHWG Note 2001-04 (2001).

[97] H. L. Lai *et al.* (CTEQ Collaboration), Phys. Rev. **D51** (1995) 4763.

[98] http://zebu.uoregon.edu/~parton/partongraph.html

[99] B. K. Bullock, K. Hagiwara and A. D. Martin, Nucl. Phys. **B395** (1993), 499.

[100] F. Gianotti *et al.*, ATLAS Internal Note, ATL-PHYS-99-001 (1999).

[101] UA2 Collaboration, J. Alitti *et al.*, Phys. Lett. **B280** (1992) 137.

[102] M. Hohlfeld, ATLAS Internal Note, ATL-PHYS-2001-004 (2001).

[103] V. A. Mitsou, ATLAS Internal Note, ATL-PHYS-2000-021 (2000).

[104] R. Bonciani, S. Catani, M. L. Mangano and P. Nason, Nucl. Phys. **B529** (1998), 424.